ISSN 1580-2949
UDK 669+666+678+53 MTAEC9, 46(2)93–190(2012)

MATER. TEHNOL.	LETNIK VOLUME 46	ŠTEV. NO. 2	STR. P. 93–190	LJUBLJANA SLOVENIJA	MAR.–APR. 2012

VSEBINA – CONTENTS

PREDGOVOR/FOREWORD

Vsakovrstni materiali nas obkrožajo na vsakem koraku v našem življenju. Ali se kdaj vprašamo, kako so ti materiali nastali, kdo jih je razvil in izboljšal, kako jih najboljše uporabiti in kakšna je prihodnost materialov in tehnologij? Odgovor na ta vprašanja vsekakor ni preprost, iskanje odgovorov pa omogoča nadaljnji razvoj in napredek družbe, kot tudi obstoj revije *Materiali in tehnologije*. Kot pove že njeno ime, je revija namenjena materialom in tehnologijam. Njen začetek sega v leto 1967, ko je začela izhajati kot *Železarski zbornik*, kjer so svoja dognanja objavljali predvsem strokovnjaki slovenske industrije jekla. Leta 1992 se je revija preimenovala v *Kovine zlitine tehnologije*, kjer je svoja dela objavljalo tudi vedno več slovenskih raziskovalcev. Revija se je še enkrat preimenovala leta 2000, ko je dobila današnjo obliko in ime.

Revija *Materiali in tehnologije* je prehodila že kar častitljivo pot razvoja, od svojih začetkov kot *Železarski zbornik*, pa do današnjih dni. Opažamo, da postaja cenjena v različnih strokovnih krogih, saj omogoča vpogled v dogajanje na področju kovinskih, polimernih in anorganskih materialov ter tehnologij s teh področij. Resno delo urednikov v preteklosti je omogočilo tudi vključitev revije v sistem SCI, kar ji je še povečalo dodano vrednost. Po sedanjih mednarodnih merilih se kvaliteta revije izraža s faktorjem SCI, ki je pomemben del tudi pri oceni kvalitete publikacij raziskovalcev, ki v njej objavljajo svoje članke. Povečuje se število slovenskih avtorjev, povečuje pa se tudi interes avtorjev iz tujine. To je dokaz, da gre razvoj revije v pravo smer.

Revija je pomembna tudi z nacionalnega stališča. Večina znanstvenih in strokovnih člankov je v angleškem jeziku, v slovenski jezik pa so prevedeni: naslov, povzetek, ključne besede, naslovi tabel in podnaslovi slik. To prispeva k širjenju slovenske strokovne terminologije, kar je pomembno za bogatenje in nadaljnji razvoj slovenskega jezika.

V decembru 2011 so bili imenovani nov glavni in odgovorni urednik ter člani uredniškega odbora. To postavlja pred imenovane nove izzive, ki bodo omogočili nadaljnji razvoj revije, njeno širjenje po znanstveni in strokovni javnosti ter večanje ugleda revije na področju materialov in tehnologij.

Prizadevali si bomo čim bolj skrajšati rok od sprejetja članka do njegove objave. Pri tem imajo pomembno vlogo tudi avtorji, saj kvalitetna vsebina in ustrezna tehnična priprava članka olajšata delo vsem, ki sodelujemo pri pripravi člankov za objavo.

Zahvaljujem se dosedanjemu glavnemu in odgovornemu uredniku prof. dr. Francu Vodopivcu za ves trud in prizadevanje, ki ga je vložil v revijo.

Glavni in odgovorni urednik
doc. dr. Matjaž Torkar

A wide variety of materials surround us in everyday life. However, do we always ask ourselves where these materials came from, how these materials were prepared, who developed them, who improved them, what is their best application and what is the future of materials and technologies? The answers to these questions are not easy, but the search for the answers enables the further development of society, as well as the existence of our journal – *Materials and Technology*. As is clear from the journal's name, it is devoted to materials and technology. The earliest issue dates back to 1967, when the journal was called *Železarski zbornik*: a periodical where metallurgical engineers from Slovenian steelworks could publish their results. In 1992 the journal changed its name to *Kovine zlitine tehnologije* (*Metals Alloys Technologies*) and a larger number of Slovenian researchers started to publish articles. The last change of name was in 2000, when the journal *Materiali in tehnologije* (*Materials and Technology*) took its present name and form.

Materials and Technology has come a long way from its beginnings as *Železarski zbornik*. It is clear that the journal is much appreciated in a variety of professional circles, where it provides an insight into activities in the fields of metallic materials, polymer materials and ceramic materials, as well as the technology of these fields. Intense efforts made by previous editors made it possible for the journal to enter the SCI system, which greatly increases the added value of the journal. After some recent changes the quality of the journal is now reflected in its SCI factor, which is an important element in the evaluation of the quality of researchers. The increasing number of Slovenian authors and the ever-larger number of authors from abroad are evidence that the journal is developing in the proper direction.

The journal is also important from the national point of view. Most of the articles are published in English, but with translations of the abstract, keywords, table titles, figure captions into Slovene. This helps with the spreading of Slovenian terminology, which is important for the further development and enrichment of Slovene.

A new Editor-in-Chief and Editorial Board were elected in December 2011. Their mission will be to ensure the successful development of the journal *Materials and Technology*, its broader recognition among material scientists and an increase of the journal's reputation in the field of materials and technologies.

We will strive to reduce the time from the acceptance to the publication of articles. However, an important role is also played by the authors, as the quality of the content and the technical correctness of the paper's preparation facilitates the work of all the staff included in the process of publishing the articles.

Finally, I would like to express my thanks to the former Editor-in-Chief, prof. Franc Vodopivec, for all his hard work and the effort that he put into the journal.

Editor-in-Chief
A/Prof.Dr. Matjaž Torkar

UDK 66.017:519.61/.64:620.17
Original scientific article/Izvirni znanstveni članek

ISSN 1580-2949
MTAEC9, 46(2)97(2012)

LINEAR TWO-SCALE MODEL FOR DETERMINING THE MECHANICAL PROPERTIES OF A TEXTILE COMPOSITE MATERIAL

LINEARNI DVOSTOPENJSKI MODEL ZA DOLOČITEV MEHANSKIH LASTNOSTI TEKSTILNEGA KOMPOZITA

Tomáš Kroupa[1], Petr Janda[2], Robert Zemčík[3]

[1]University of West Bohemia in Pilsen, Department of Mechanics, Univerzitní 22, 306 14, Plzeň, Czech Republic
[2]University of West Bohemia in Pilsen, Department of Machine design, Univerzitní 22, 306 14 Plzeň, Czech Republic
[3]University of West Bohemia in Pilsen, Department of Mechanics, Univerzitní 22, 306 14, Plzeň, Czech Republic
kroupa@kme.zcu.cz

Prejem rokopisa – received: 2011-02-01; sprejem za objavo – accepted for publication: 2011-10-10

The engineering mechanical constants for a description of mechanical macro-scale models of carbon and aramid textile composite materials are calculated using finite-element analyses. Two sub-scale models of representative volumes are used. The micro-scale model represents a periodically repeated volume consisting of fibers and a matrix within each interweaved yarn. The meso-scale model represents a unit cell of four interweaved yarns, which is repeated within the whole composite with the properties obtained from a micro-scale model and matrix. The finite-element models are built with the commercial packages Siemens NX 7.5 and MSC.Marc 2008r1 using subroutines.

Keywords: composite, textile, linear, carbon, aramid, epoxy, tensile, finite-element analysis

Z uporabo metode končnih elementov so izračunane inženirske konstante za opis mehanskega makrodimenzionalnega ogljik-aramidnega modela kompozita. Uporabljena sta dva poddimenzionalna modela za manjše ustrezne prostornine. Mikrodimenzionalni model je periodično ponavljanje prostornine, ki se ponavlja za ves kompozit za matico in vpleteno vlakno. Mezodimenzionalni model je spletna celica iz štirih vpletenih vlaken in se ponavlja v vsem kompozitu z lastnostmi mikromodela in matice. Modeli končnih elementov so vgrajeni v paketa Siemens NX 7.5 in MSC.Marc 2008r1 z uporabo podrutin.

Ključne besede: kompozit, tekstil, linearen, ogljik, aramid, epoksi, natezne lastnosti, končni elementi

1 INTRODUCTION

A knowledge of the precise values of the mechanical properties of materials is crucial for the capability of models to predict the behavior of analyzed structures. This is also the case for the modeling of composite materials. Several material properties of the composites can be calculated directly from experimental results (Young's moduli from tensile tests, etc.). The presented paper is aimed at a determination of the elasticity constants of textile composites using sub-scale models to determine the properties that cannot be measured and calculated directly from the experiment (shear modulus, etc.). The models were used for the prediction of the elasticity constants of two materials with a simple plain weave. This type of material was chosen because of the possibility to measure directly the Young's moduli in the principal material directions using tensile tests. Nevertheless, the shear modulus was fitted on the linear part of the measured curves using a gradient-optimization algorithm and the Poisson's ratios of the whole textile composites were identified using a digital image correlation[1]. The material data of the constituents were given by the manufacturer and the dimensions of the periodically repeated volume (unit-cell element – UCE) of the textiles were measured using a digital camera.

2 EXPERIMENT

The effective material parameters were determined using simple tensile tests performed on a Zwick/Roell Z050 test machine on thin strips with the dimensions given in **Table 1**.

Table 1: Dimensions of the strips
Tabela 1: Dimenzije traka

		Carbon	Aramid
Length	mm	100.00	100.00
Width	mm	10.00	10.00
Thickness	mm	0.30	0.35

Three types of specimens were used for each material. One of two principal directions of the textile fabric form the angles 0°, 45° and 90° with the direction of the loading force. Once the force-displacement diagrams (**Figures 1 and 2**) were measured, the Young's moduli in directions 1 and 2 and the shear modulus were fitted on the linear parts of the curves using a combination of a plane-stress finite-element (FE) model and the gradient-optimization algorithm implemented in OptiSLang software (the methodology is described in[2,3]). A digital image correlation[1] was used for the calculation

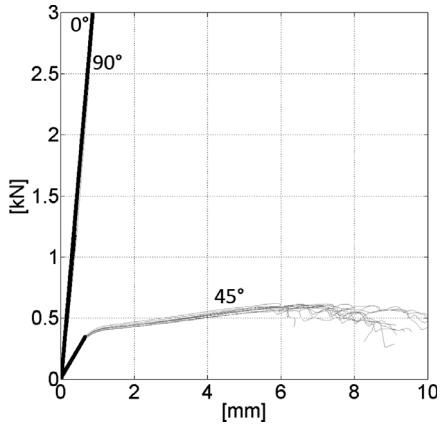

Figure 1: Force-displacement diagram (gray) for Carbon/Epoxy, with fitted parts (black)
Slika 1: Odvisnost sila – premik (sivo) za ogljik/epoksi s približki (črno)

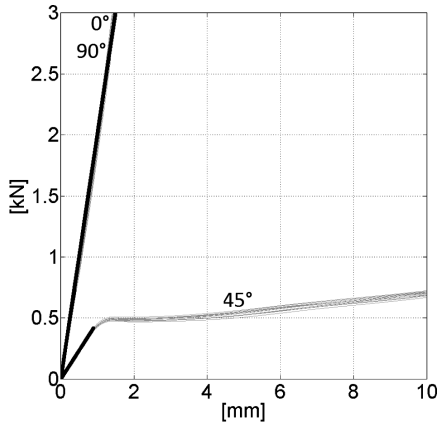

Figure 2: Force-displacement diagrams (gray) for Aramid/Epoxy, with fitted parts (black)
Slika 2: Odvisnost sila – premik (sivo) za aramid/epoksi s približki (črno)

of the Poisson's ratios. The elasticity parameters of the textiles are shown in **Table 2**.

Table 2: Elasticity parameters of textile composites
Tabela 2: Parametri elastičnosti za tekstilne kompozite

		Carbon/Epoxy	Aramid/Epoxy
E_1	GPa	31.05	15.85
E_2	GPa	29.73	15.66
G_{12}	GPa	1.83	1.24
ν_{12}	–	0.19	0.31

3 UNIT-CELL ELEMENTS

Axes orientations in UCE (**Figure 4**) are shown in **Figure 3**. Dimensionless geometry of UCE of yarns is shown in **Table 3**. The ideal distribution of fibers in the yarns, the perfect saturation of the yarns by the matrix and the volume fiber fractions $V_f = 0.6$ and $V_f = 0.7$ are considered in the calculations.

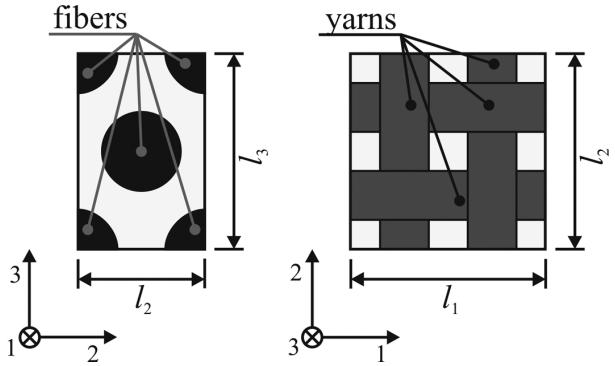

Figure 3: Material axes: yarn (left), textile (right)
Slika 3: Osi materiala: vlakno (levo), tekstil (desno)

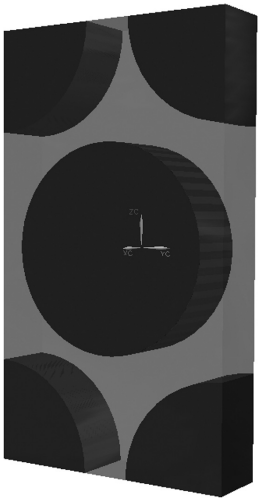

Figure 4: UCE geometry of yarn with $V_f = 0.6$ (fibers – black, matrix – gray)
Slika 4: UCE-geometrija vlakna z $V_f = 0.6$ (vlakna – črno, matica – sivo)

Table 3: Dimensions of the unit cell of the yarn
Tabela 3: Dimenzije spletne celice

l_1	[-]	1
l_2	[-]	4
l_3	[-]	$4 \cdot \sqrt{3}$

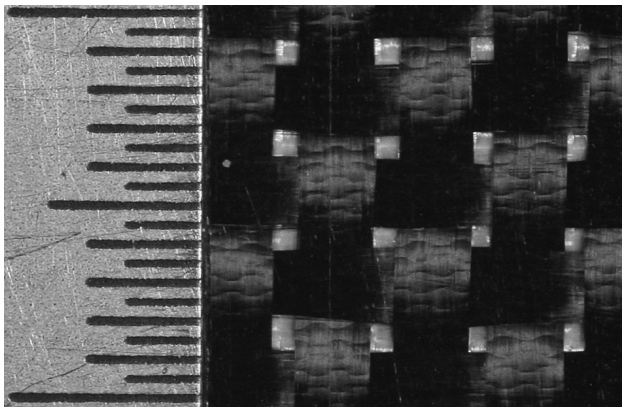

Figure 5: Photograph of Carbon/Epoxy specimen
Slika 5: Posnetek vzorca ogljik/epoksi

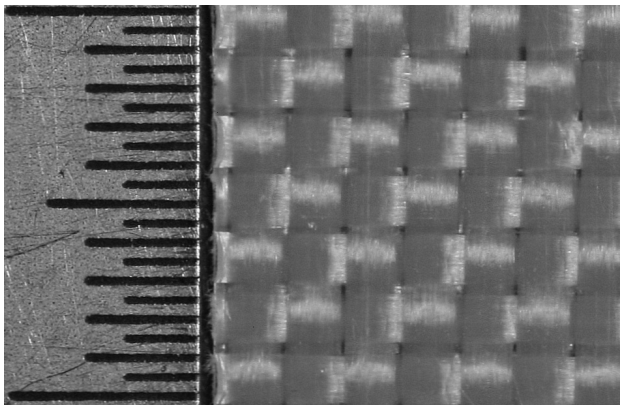

Figure 6: Photograph of Aramid/Epoxy specimen
Slika 6: Posnetek vzorca aramid/epoksi

The dimensions of the UCE of both materials, which were measured using detailed photographs provided by a Canon EOS 400D digital camera (**Figures 5 and 6**) are shown in **Table 4**.

Table 4: Dimensions of textile unit cells
Tabela 4: Dimenzije spletne celice tekstila

		Carbon/Epoxy	Aramid/Epoxy
l_1	mm	5.00	3.00
l_2	mm	5.00	3.00
l_3	mm	0.30	0.35

4 BOUNDARY CONDITIONS

In the FE model of the UCE (**Figure 7**) it is necessary to invoke pure tensile conditions or pure shear conditions to determine the elasticity parameters. Furthermore, the UCE has to be fixed in space to eliminate rigid body modes. Finally, the periodic boundary conditions have to be satisfied. The effect of the periodic boundary condition on the UCE with two periodically tied faces is sketched in **Figure 8**.

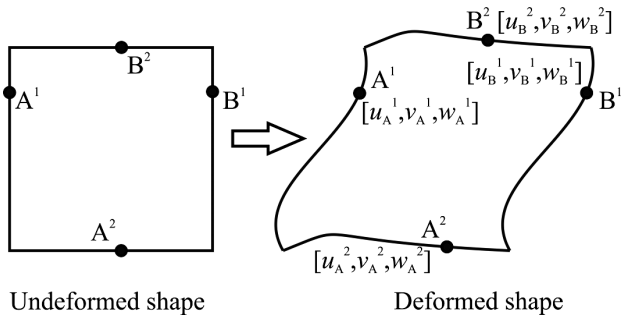

Figure 8: Scheme of the effect of the periodic boundary conditions
Slika 8: Shema učinka periodičnosti mejnih pogojev

Each corresponding pair of nodes on opposite faces of the FE model must fulfill the conditions [4–6]

$$u_{\mathrm{B}}^{i} - u_{\mathrm{A}}^{i} = d_{u}^{i},\ v_{\mathrm{B}}^{i} - v_{\mathrm{A}}^{i} = d_{v}^{i} \qquad \text{(P)}$$
$$w_{\mathrm{B}}^{i} - w_{\mathrm{A}}^{i} = d_{w}^{i} \text{ for } i=1...N$$

where i is the index of the corresponding constrained faces; N is the total number of the periodically constrained faces; u, v and w are the displacements in the 1, 2 and 3 direction; and d_u^i, d_v^i, d_w^i are displacements of the appropriate retained nodes in which the loading is applied (**Figure 9**). The UCE of the yarns is periodically tied in all three directions and the UCE of the textiles is tied in direction 1 and 2 (**Figure 9**).

For the determination of the Young's modulus E_1 and the Poisson's ratio ν_{12} of the textile composite the model is loaded with $\sigma_1 \neq 0$ and the other loadings are equal to zero. Normal strains in direction 1 and 2 are calculated as

$$\varepsilon_1 = \frac{d_1^1}{l_1},\ \varepsilon_2 = \frac{d_2^2}{l_2} \qquad \text{(e12)}$$

and the Young's modulus and Poisson's ratio are

$$E_1 = \frac{\sigma_1}{\varepsilon_1}, \nu_{12} = \frac{\varepsilon_2}{\varepsilon_1} \qquad \text{(E1}\nu\text{12)}$$

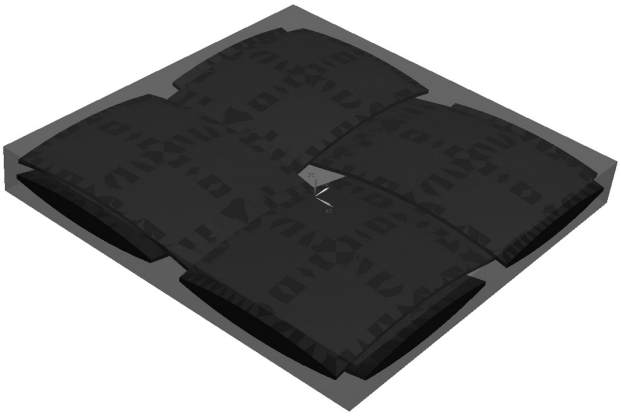

Figure 7: UCE geometry of Carbon/Epoxy textile composite (yarns – black, matrix – gray)
Slika 7: UCE-geometrija kompozita ogljik/epoksi (trakovi – črno, matica – sivo)

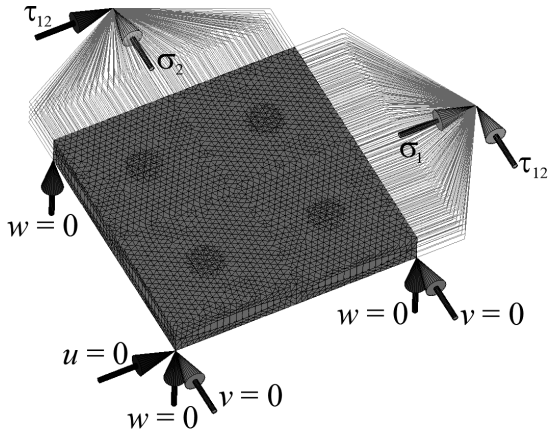

Figure 9: Boundary conditions and links used for periodic boundary conditions for UCE of Aramid/Epoxy textile
Slika 9: Mejni pogoji in povezave, uporabljene za periodične mejne pogoje za UCE aramid/epoksi tekstil

For the determination of the shear modulus G_{12} the model is loaded by $\tau_{12} \neq 0$. The other loadings are equal to zero. The shear strain in plane 12 is calculated as

$$\gamma_{12} = \frac{d_2^1}{l_1} + \frac{d_1^2}{l_2} \qquad \text{(g12)}$$

and the shear modulus is

$$G_{12} = \frac{\tau_{12}}{\gamma_{12}} \qquad \text{(G12)}$$

The same scheme is used for the determination of the elasticity constants in the other directions or planes.

5 INPUT PARAMETERS

Carbon (Toray T600) and Aramid (Twaron K1055) fibers are transversely isotropic materials. Their elasticity parameters are given in **Table 5**.

Table 5: Elasticity parameters for fibers
Tabela 5: Parametri elastičnosti za vlakna

		Carbon	Aramid
E_1	GPa	230.00	104.00
E_2	GPa	7.05	5.40
E_3	GPa	7.05	5.40
ν_{12}	–	0.30	0.40
ν_{23}	–	0.30	0.40
ν_{31}	–	0.02	0.02
G_{12}	GPa	50.00	12.00
G_{23}	GPa	50.00	12.00
G_{31}	GPa	50.00	12.00

The matrix is manufactured from epoxy resin (MGS® L 285) and hardener (MGS® 285). It is considered to be a linear isotropic material (**Table 6**).

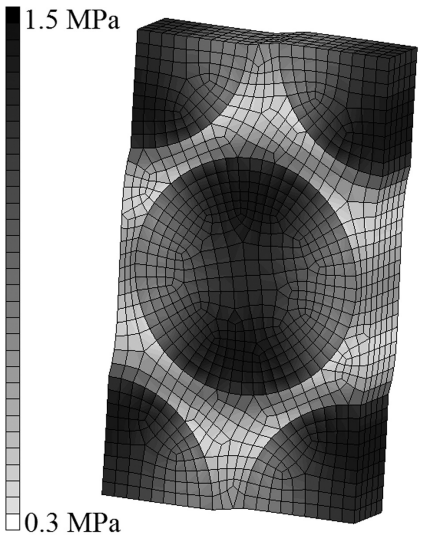

Figure 10: Deformed FE model of the UCE of yarn under shear loading in plane 23 (shown values of shear stress τ_{23})
Slika 10: Deformiran FE-model za UCE-spleta pri strižni obremenitvi v ravnini 23 (prikazane vrednosti strižne napetosti τ_{23})

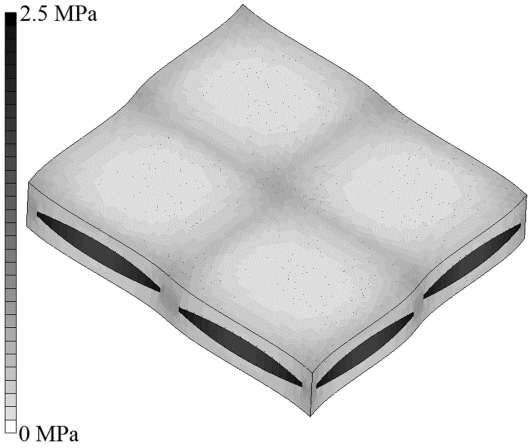

Figure 11: Deformed FE model of the UCE of the textile under shear loading in plane 12 (shown values of shear stress τ_{12})
Slika 11: Deformiran FE-model UCE za tekstil pri strižni obremenitvi v ravnini 12 (prikazane vrednosti strižne napetosti τ_{12})

Table 6: Elasticity parameters for the matrix
Tabela 6: Parametri elastičnosti za matico

		Epoxy
E	GPa	3.00
ν	–	0.30

6 RESULTS

The effect of the periodic boundary conditions is shown in **Figures 10** and **11**. Opposite faces of the UCE are deformed in the same shape. The elastic properties of the yarns are shown in **Table 7**. The results are shown for both fiber volume fractions (V_f). Similarly, the results for the textiles are shown for both V_f (**Table 8**).

Table 7: Calculated elasticity parameters of the yarns
Tabela 7: Izračunani parametri elastičnosti za spleta

		Carbon/Epoxy		Aramid/Epoxy	
V_f	–	0.60	0.70	0.60	0.70
E_1	GPa	138.87	161.54	63.46	73.55
E_2	GPa	7.05	8.33	4.36	4.60
E_3	GPa	7.05	8.33	4.36	4.60
ν_{12}	–	0.30	0.30	0.36	0.37
ν_{23}	–	0.36	0.34	0.40	0.40
ν_{31}	–	0.02	0.02	0.02	0.02
G_{12}	GPa	4.26	5.90	3.42	4.34
G_{23}	GPa	3.88	5.45	3.15	4.01
G_{31}	GPa	4.26	5.90	3.42	4.34

Table 8: Calculated elasticity parameters for textiles
Tabela 8: Izračunani parametri elastičnosti za tekstil

		Carbon/Epoxy		Aramid/Epoxy	
V_f	–	0.60	0.70	0.60	0.70
E_1	GPa	27.75	31.89	14.08	15.72
E_2	GPa	27.75	31.89	14.08	15.72
G_{12}	GPa	2.60	3.30	2.21	2.60
ν_{12}	–	0.33	0.33	0.28	0.29

7 CONCLUSION

Multi-scale models for the prediction of the elasticity constants of textile composites with a simple plain weave were developed and presented. Good agreement of the Young's moduli was achieved between the calculated and experimental values. However, the shear moduli are slightly over-predicted. The calculated Poisson's ratios were calculated with acceptable accuracy only for the Aramid/Epoxy textile. Future research will be aimed at the non-linear, plastic and damage behavior of the matrix, the damage behavior of the fibers and an investigation of the imperfections and the unit-cell element dimensions of the textiles.

Acknowledgement

The work has been supported by the projects GA P101/11/0288 and European project NTIS – New Technologies for Information Society No. CZ.1.05/1.1.00/02.0090.

8 REFERENCES

[1] R. Kottner, R. Zemčík, V. Laš, Mechanical characteristics of rubber segment – shear test. In: Experimental Stress Analysis 2007

[2] T. Kroupa, R. Zemčík, J. Klepáček, Temperature dependence of parameters of non-linear stress-strain relations for carbon epoxy composites, Mater. Tehnol., 43 (**2009**) 2, 69–72

[3] T. Kroupa, R. Zemčík, V. Laš, Improved non-linear stress-strain relation for carbon-epoxy composites and identification of material parameters, JCM, 45 (**2011**) 9, 1045–1057

[4] P. P. Camanho, C. G. Dávila, S. T. Pinho, J. J. C. Remmers, Mechanical response of Composites, ECCOMAS, Springer 2008

[5] B. Hassani, E. Hinton, Homogenization and structural topology optimization, Springer 1999

[6] R. Zemčík, K. Kunc, T. Kroupa, R. Kottner, P. Janda, Micromodel for failure analysis of textile composites, In: YSESM, Trieste, Italy, 2010, 48–51

UDK 669.715:621.95:620.179.11
Original scientific article/Izvirni znanstveni članek

ISSN 1580-2949
MTAEC9, 46(2)103(2012)

INFLUENCE OF THE PROCESS PARAMETERS AND THE MECHANICAL PROPERTIES OF ALUMINUM ALLOYS ON THE BURR HEIGHT AND THE SURFACE ROUGHNESS IN DRY DRILLING

VPLIV PARAMETROV PROCESA IN MEHANSKIH LASTNOSTI ALUMINIJEVIH ZLITIN NA VIŠINO IGLE IN HRAPAVOST POVRŠINE PRI SUHEM VRTANJU

Uğur Köklü

Department of Manufacturing Engineering, Faculty of Technology, University of Dumlupınar, 43500, Simav-Kütahya, Turkey
ugurkoklu@gmail.com

Prejem rokopisa – received: 2011-05-10; sprejem za objavo – accepted for publication: 2011-10-28

In this paper, the effect of the mechanical properties of aluminum alloys, cutting speed, feed rate and the drill diameter on burr height and surface roughness of drilling holes were investigated, using the Taguchi method. Al-2024, Al-7075 and Al-7050 were selected as the workpiece materials for experiments. The analysis of variance and signal-to-noise ratio were employed to analyze the effect of the drilling parameters. The results of the statistical analysis indicated that feed rate and cutting speed minimize significantly both the height of the exit burrs and the surface roughness. Moreover, the mechanical properties of the workpieces are different influential factors on both responses.

Keywords: drilling, burr height, surface roughness, Al-2024, Al-7075, Al-7050

Raziskan je vpliv mehanskih lastnosti aluminijevih zlitin, hitrosti rezanja in podajanja ter premera svedra na višino igle in hrapavost površine vrtane površine z uporabo Taguchi metode. Za preizkuse so bile izbrane zlitine Al-2024, Al-7075 in Al-7050. Analize variance in intenzitete signal-ozadje so bile uporabljene za določitev vpliva parametrov vrtanja. Rezultati statistične analize so pokazali, da hitrosti podajanja in rezanja zmanjšujeta višino izhodne igle in hrapavost površine. Tudi mehanske lastnosti obdelovanca imajo različen vpliv na oba odgovora.

Ključne besede: vrtanje, višina igle, hrapavost površine, Al-2024, Al-7075, Al-7050

1 INTRODUCTION

Drilling is one of the most important material removal process that has been widely used in the aerospace, aircraft and automotive industries. Although modern metal-cutting methods, including electron-beam machining, ultrasonic machining, electrolytic machining and abrasive jet machining, have improved in the manufacturing industry, conventional drilling still remains one of the most common machining processes[1,2]. Aluminum is used in many industrial areas to make different products and it is significant for the world economy. Structural components made from aluminum and aluminum alloys are vital in the aerospace industry and very important in other areas of transportation and building in which durability, strength and light weight are expected[3].

The drilling process produces burrs on both the entrance and the exit surfaces of the workpiece. The exit burr is part of the material extending off the exit surface of the workpiece. Most burr-related problems in drilling are caused by the exit burr because it is much larger than the entrance burr[4]. The presence of these exit burrs requires additional manufacturing steps for disassembly and deburring. These additional steps are typically not easy to automate and are generally performed manually[5]. Burr formation affects workpiece accuracy and quality in several ways: deterioration of the surface quality, dimensional distortion on the part edge, challenges to assembly and handling caused by burrs in sensitive locations on the work and damage done to the workpiece subsurface from the deformation associated with burr formation[6].

In several studies burr formation and surface roughness were investigated. Nouari et al.[7] examined the effect of the machining parameters on the hole-surface roughness and diameter deviations for different coated drills. The results show that, small constant feed rate, low cutting speeds are appropriate for the dry machining of AA-2024. Kilickap[6] presented an application of Taguchi and response surface methodologies for minimizing the burr height and the surface roughness in drilling Al-7075. The optimization results showed that the combination of low cutting speed, low feed rate and high point angle is necessary to minimize both burr height and surface roughness. Kurt et al.[3] investigated the role of different coatings, point angle and cutting parameters on the hole quality in the drilling of Al-2024 alloy and concluded that the cutting parameters and the coatings have different effects on hole quality. They have

obtained effective results using a low cutting speed and feed rate. Ko and Lee[8] used several materials that were drilled by several cutting conditions, velocity and feed rate. They indicated that burr formations were highly dependent on the material properties, the drill geometry and the cutting condition. Lauderbaugh[9] used simulation tools and analysis of variance to identify the influence of process parameter on the height of exit burrs and concluded that feed rate, chisel-edge-to-drill diameter ratio, drill diameter, yield strength and point angle are significant for the height of exit burrs. Ko et al.[10] carried out an experimental investigation of the role of various shapes of drills and materials (SM45C, SS400, A6061-T6 and A2024-T4) on the burr in drilling. Their experimental results showed that the burr height from ductile materials is larger than from brittle materials. Kurt et al.[11] investigated the influence of the cutting parameters and the mechanical properties of a workpiece on the burr formations in a dry drilling process. His experimental results showed that the machining parameters and the mechanical properties of a workpiece effect the burr formation. In addition to these they have classified the burrs into three types. Kalidas et al.[12] compared the performance of the three types of coatings on the hole quality under dry- and wet-drilling conditions of aluminum alloys. The result of the experiments indicates that, the use of coatings did not seem to affect the surface roughness of the hole produced.

In this study a statistical analysis of the experimental data of the cutting parameters and the mechanical properties of aluminum alloys on the burr height and surface roughness of the produced hole in the dry drilling of Al-2024, Al-7075 and Al-7050 have been investigated and analyzed with the Taguchi method.

2 MATERIALS, CUTTING CONDITIONS AND PLAN OF EXPERIMENTS

Burr height and the surface roughness of the drilled hole surface were determined by cutting condition. The drilling experiments were conducted in dry cutting conditions on a Johnford VMC model three axes CNC milling machine with a Fanuc controller. In this study, Al-2024, Al-7075 and Al-7050 were chosen as the work materials with the specimen dimensions 200 mm × 140 mm × 30 mm. The mechanical properties of the three aluminum alloys are presented in **Table 1**.

Uncoated, conventional, high-speed-steel twist drills with diameters of 8 mm, 10 mm and 12 mm were used for drilling experiment. A new drill bit was used for each drilling experiment. The burr heights (H) and surface roughness (R_a, the arithmetic average) of each drilled hole were measured by means of an optical microscope and a Mahr Perthometer surface roughness tester using a meter cut off of 5.6 mm. The burr height and the surface roughness of the machined hole measurement points of the workpiece are shown in **Figure 1**. Each specimen

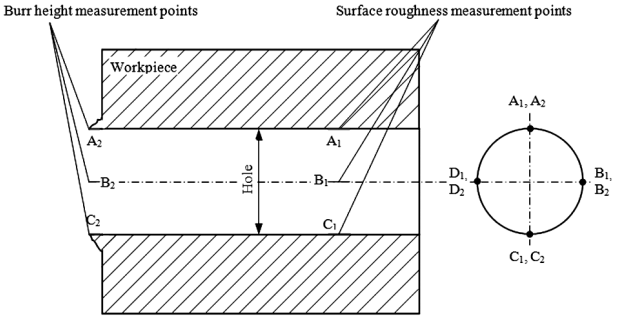

Figure 1: Burr height and surface-roughness measurement points of the produced hole
Slika 1: Točke meritev višine igle in hrapavosti površine pri izvrtinah

was measured from four different points (0°, 90°, 180° and 270°) for both, burr height and surface roughness.

The drilling experiments were planned using Taguchi's orthogonal array. Three experimental parameters were the cutting speed, feed rate and drill diameter were selected for the present investigation. Three levels of each control factor were taken into account. Taguchi's orthogonal array of L_{27} was chosen for the experimental plan. The considered experimental factors and their levels are listed in **Table 2**.

Table 1: Mechanical properties of Al-2024, Al-7075 and Al-7050 materials
Tabela 1: Mehanske lastnosti zlitin Al-2024, Al-7075 in Al-7050

Materials	Tensile Strength (MPa)	Yield Strength (MPa)	Elongation %	Hardness (HRB)
Al-2024	469	324	17	75
Al-7075	570	505	11	87
Al-7050	521	467	10	84

Table 2: Control factors and their levels used for drilling experiments
Tabela 2: Kontrolni dejavniki in njihov nivo, uporabljen pri preizkusih vrtanja

Symbol	Factors	Unit	Level		
			1	2	3
A	Cutting speed	m/min	20	30	40
B	Feed rate	mm/r	0.05	0.1	0.15
C	Drill diameter	mm	8	10	12

3 EXPERIMENTAL RESULTS AND ANALYSIS

The Taguchi method is very popular for solving optimization problems in the field of manufacturing engineering[13]. In this method, the term "signal" (S) represents the desired value and the "noise" (N) represents the undesired value. The objective of using the *S/N* ratio is a measure of the performance to develop products and processes that are insensitive to noise factors. The *S/N* ratio indicates the degree of predictable performance of a product or process in presence of noise factors. The process parameter settings with the highest *S/N* ratio always yield the optimum quality with minimum variance. The difference between the functional

Table 3: Experimental layout using L_{27} orthogonal array and experimental values
Tabela 3: Načrt preizkusov z uporabo ortogonalne razporeditve L_{27} in vrednosti preizkusov

Trial no.	Factor Level			Al-2024		Al-7075		Al-7050	
	A	B	C	*H*/mm	R_a/μm	*H*/mm	R_a/μm	*H*/mm	R_a/μm
1	1	1	1	3.29	6.200	1.43	2.967	1.14	2.042
2	1	1	2	3.32	6.188	1.55	3.061	1.45	2.275
3	1	1	3	3.54	6.484	1.68	3.073	1.60	2.352
4	1	2	1	4.27	6.395	1.64	3.112	1.22	2.331
5	1	2	2	4.40	6.580	1.88	3.335	1.55	2.422
6	1	2	3	4.51	6.934	1.92	3.429	1.65	2.421
7	1	3	1	5.28	6.883	2.76	3.265	2.21	2.487
8	1	3	2	4.84	6.930	2.59	3.312	2.25	2.529
9	1	3	3	5.06	7.234	2.62	3.451	2.45	2.587
10	2	1	1	3.04	6.847	1.73	3.088	1.28	2.242
11	2	1	2	3.22	7.090	2.12	3.208	1.89	2.421
12	2	1	3	3.30	7.158	2.30	3.322	1.31	2.582
13	2	2	1	4.04	6.906	1.87	3.457	1.98	2.627
14	2	2	2	3.81	7.120	1.98	3.742	2.42	2.728
15	2	2	3	5.27	7.476	2.88	3.751	2.38	2.838
16	2	3	1	6.28	7.118	2.44	3.634	2.11	2.854
17	2	3	2	6.44	7.515	2.65	3.361	2.20	2.975
18	2	3	3	6.61	7.700	2.93	3.814	2.56	3.081
19	3	1	1	3.51	7.322	1.93	3.676	1.72	2.679
20	3	1	2	5.75	7.441	1.93	3.332	1.45	2.751
21	3	1	3	5.01	7.397	2.13	3.751	1.97	2.883
22	3	2	1	6.21	7.809	2.92	3.209	2.21	2.667
23	3	2	2	5.57	7.930	2.78	3.831	2.55	2.948
24	3	2	3	6.31	7.974	2.42	3.928	2.22	3.027
25	3	3	1	6.58	7.970	2.97	3.287	2.63	3.031
26	3	3	2	6.42	8.114	3.75	4.107	2.67	2.942
27	3	3	3	4.89	7.939	3.78	4.321	3.53	3.288

Table 4: Response table for burr height and surface roughness
Tabela 4: ANOVA-rezultati za višino igle

Factors	Mean *S/N* ratios (dB) for *H*			Mean *S/N* ratios (dB) for R_a		
	Level 1	Level 2	Level 3	Level 1	Level 2	Level 3
Al–2024						
Cutting speed	–12.50[2]	–12.99	–14.80	–16.44[1]	–17.16	–17.80
Feed rate	–11.34[1]	–13.72	–15.23	–16.76[2]	–17.16	–17.47
Drill diameter	–13.14[3]	–13.47	–13.68	–16.94[3]	–17.13	–17.33
Al–7075						
Cutting speed	–5.813[2]	–7.181	–8.482	–10.15[1]	–10.83	–11.36
Feed rate	–5.326[1]	–6.874	–9.276	–10.28[2]	–10.94	–11.12
Drill diameter	–6.516[3]	–7.173	–7.788	–10.35[3]	–10.79	–11.20
Al–7050						
Cutting speed	–4.450[2]	–5.851	–7.073	–7.524[1]	–8.606	–9.269
Feed rate	–3.588[1]	–5.886	–7.900	–7.805[2]	–8.490	–9.103
Drill diameter	–4.924[3]	–6.002	–6.448	–8.076[3]	–8.478	–8.844

1, 2 and 3: Optimum level and Rank

value and the objective value is emphasized and identified as the loss function. The loss function is derived as Eq. (1)

$$L(y) = \frac{L''(m)(y-m)^2}{2!} = k(y-m)^2 = k(MSD) \qquad (1)$$

where *L(y)* is the loss function, *y* is the value of the quality characteristic, *m* is the target value of *y*, *k* is the commensurately constant, which depends on financial criticality of *y,* and *MSD* is the mean square deviation. Eq. (1) can be expressed by the signal-to-noise ratio (η) and can be rewritten as:

$$\eta = -10\lg_{10}(MSD) \qquad (2)$$

The value of the loss function is further transformed into a signal-to-noise (*S/N*) ratio. In the present investi-

gation, the objective is to minimize the burr height and the surface roughness; therefore, "smaller is better" as a quality characteristic is selected, which is a logarithmic function given as:

$$S/N(\eta) = -10\lg_{10}\left(\frac{1}{r}\sum_{i=1}^{r} R_i^2\right) \quad i=1,2,...,r \qquad (3)$$

where R_i is the value of the burr height or the surface roughness for the ith trial in r number of measurements[14].

The experimental values obtained from the experiments related to burr height and surface roughness are illustrated in **Table 3**. The *S/N* ratios for the burr height (H) and the surface roughness (R_a) were calculated using the output parameter values given in **Table 3**. The *S/N* ratio for each parameter level was calculated by averaging the *S/N* ratios obtained when the parameter maintained at that level. **Table 4** shows the *S/N* ratio obtained for different parameter levels.

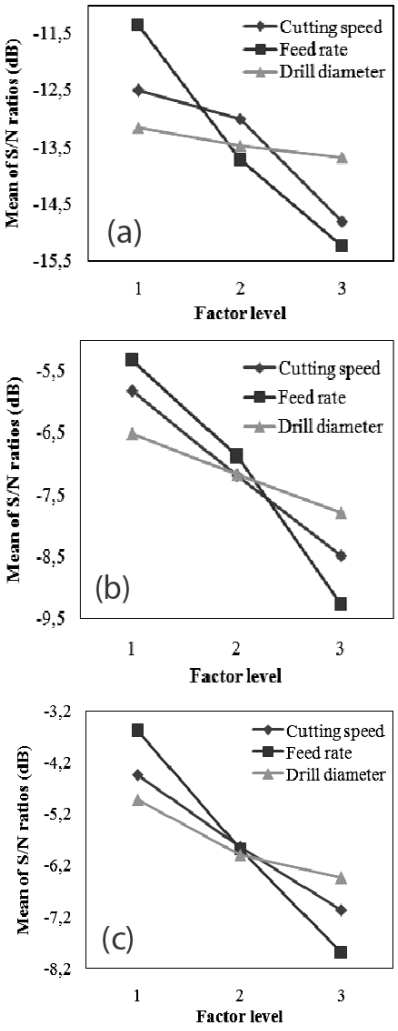

Figure 2: Effect of cutting parameters on the burr height: a) Al-2024, b) Al-7075 and c) Al-7050

Slika 2: Vpliv parametrov rezanja na višino igle: a) Al-2024, b) Al-7075 in c) Al-7050

Table 5: The result of ANOVA for burr height
Tabela 5: ANOVA-rezultati za višino igle

Factors	*Dof*	*SS*	*V*	*F*	*P*/%
Al-2024					
Cutting speed	2	8.0732	4.0366	7.60*	21.31
Feed rate	2	18.9565	9.4782	17.84*	50.04
Drill diameter	2	0.2276	0.1138	0.21	0.60
Error	20	10.6262	0.5313		28.05
Total	26	37.8834			100
Al-7075					
Cutting speed	2	2.3905	1.1953	13.76*	23.98
Feed rate	2	5.3525	2.6762	30.80*	53.68
Drill diameter	2	0.4903	0.2451	2.82	4.92
Error	20	1.7376	0.0869		17.42
Total	26	9.9709			100
Al-7050					
Cutting speed	2	1.6389	0.8194	10.37*	20.27
Feed rate	2	4.3023	2.1511	27.23*	53.19
Drill diameter	2	0.5671	0.2835	3.59*	7.01
Error	20	1.5800	0.0790		19.53
Total	26	8.0883			100

* Significant at 95 % confidence level

Table 6: The result of ANOVA for surface roughness
Tabela 6: ANOVA-rezultati za hrapavost površine

Factors	*Dof*	*SS*	*V*	*F*	*P*/%
Al-2024					
Cutting speed	2	5.6317	2.8159	131.94*	69.83
Feed rate	2	1.5560	0.7780	36.45*	19.30
Drill diameter	2	0.4501	0.2250	10.54*	5.58
Error	20	0.4268	0.0213		5.29
Total	26	8.0646			100
Al-7075					
Cutting speed	2	1.09547	0.54773	13.10*	35.90
Feed rate	2	0.56992	0.28496	6.81*	18.68
Drill diameter	2	0.54954	0.27477	6.57*	18.00
Error	20	0.83654	0.04183		27.42
Total	26	3.05146			100
Al-7050					
Cutting speed	2	1.28385	0.64192	87.02*	54.05
Feed rate	2	0.69896	0.34948	47.38*	29.43
Drill diameter	2	0.24479	0.12240	16.59*	10.31
Error	20	0.14753	0.00738		6.21
Total	26	2.37513			100

*Significant at 95 % confidence level

The response graphs for the *S/N* ratios of the burr height and the surface roughness are shown in **Figures 2** and **3**, respectively. It is observed from the *S/N* response graph that the optimum parameter level combinations for the minimum values of Al-2024, Al-7075 and Al-7050 are $A_1B_1C_1$, for both burr height and surface roughness. As shown in **Table 4** and **Figure 2**, the feed rate is the dominant parameter on the burr height followed by the cutting speed. The drill diameter has a lower effect on burr height. Although a lower burr height is always preferred, burr formation in drilling is not desirable. In

the present investigation, when cutting speed 20 m/min, feed rate 0.05 mm/r and drill diameter 8 mm are used, the burr height is minimized. The height of the exit burr increases as the feed rate, the cutting speed and the drill diameter increase. As shown in **Table 4** and **Figure 3**, cutting speed is the dominant parameter on surface roughness, followed by the feed rate. The drill diameter has a lower effect on surface roughness. In the present investigation, when applied by cutting speed 20 m/min, feed rate 0.05 mm/r and the drill diameter 8 mm, the surface roughness is minimized. The roughness of the drilled surface increases as the feed rate, the cutting speed and the drill diameter increase.

The results of the analysis of variance (ANOVA) for the burr height are presented in **Table 5**. From the analysis, for all three aluminum alloys the feed rate is a highly significant factor and plays a major role in affecting the burr height. It can be observed from **Table 5** that cutting speed also affects the burr height. The effect of the drill diameter does not make any impact on the responses, except for Al-7050. Percent (%) is described as the significance rate of the process parameters on the burr height. It can be observed from the ANOVA Table that the cutting speed, feed rate and drill diameter are effect on the burr height 21.31 %, 50.04 % and 0.60 %; 23.98 %, 53.68 % and 4.92 %; 20.27 %, 53.19 % and 7.01 % in drilling of Al-2024, Al-7075 and Al-7050, respectively.

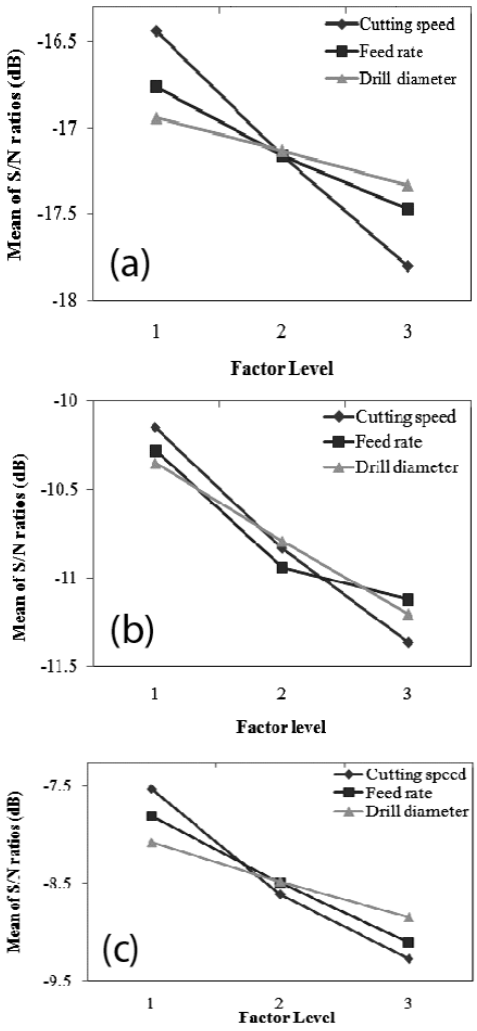

Figure 3: Effect of cutting parameters on the surface roughness: a) Al-2024, b) Al-7075 and c) Al-7050

Slika 3: Vpliv parametrov rezanja na hrapavost površine: a) Al-2024, b) Al-7075 in c) Al-7050

The results of the ANOVA for the surface roughness are presented in **Table 6**. From the analysis, for the all three aluminum alloys the cutting speed is a highly significant factor and plays a major role in affecting the surface roughness. It can be observed from **Table 6** that the feed rate and the drill diameter also affect the surface roughness. It can be observed from the ANOVA Table that cutting speed, the feed rate and the drill diameter are effect on the surface roughness 69.83 %, 19.30 % and 5.58 %; 35.90 %, 18.68 % and 18.00 %; 54.05 %, 29.43 % and 10.31 % drilling of the Al-2024, Al-7075 and Al-7050, respectively.

A series of experiment were conducted on three types of aluminum. The properties of the workpiece material have a significant influence on the burr height[15]. The burr formation process is heavily dependent on the yield strength, ultimate strength[9] and ductility[4]. Also considering the ductility of materials represented as elongation[8] in **Table 1** for the alloys Al-2024, Al-7075 and Al-7050. The higher value of elongation represents better ductility of the material. Al-2024 shows more ductility than the Al-7075 and Al-7050 alloys. The elongation percentage of workpieces used in the experiments affects the formation of the burr height and the surface roughness. The amount of burr around the hole, which is drilled in Al-2024 alloy material is greater for Al-7075 and Al-7050, because Al-2024 is more ductile than Al-7075 and Al-7050. Also the difference of burr height in Al-7075 and Al-7050 is not large, Al-7050 produces the smaller burr. As a result, much more burr occurs in ductile materials. This tendency was also mentioned by various other researchers[4,8–10]. In summary, burrs are formed as a result of plastic deformation and fracture. The final burr geometry determined by the amount of plastic deformation is determined by the ductility of the material represented as elongation[8].

Al-7050 alloy machined surface, shows a lower value of the surface roughness compared to Al-2024 and Al-7075 alloys. Higher surface roughness values of Al-2024 alloy can be explained by the highly ductile nature of the alloy, which increases the tendency to form a built-up edge (BUE). A relatively higher workpiece ductility increases the BUE formation tendency[16]. The presence of the BUE in the drilling process causes an increase in the tool wear and a rougher surface finish.

4 CONCLUSIONS

In order to minimize the burr height and the surface roughness of Al-2024, Al-7075 and Al-7050, the effects of various cutting parameters have been investigated in drilling using the Taguchi method and the analysis of variance. Based on the *S/N* ratios and the ANOVA results it is concluded that feed rate was the most influential controllable factor among input parameters which affect the burr height. The cutting speed was the second factor at burr formation. The drill diameter has the lowest effect on burr height. In view of the surface roughness, cutting speed is a dominant parameter and it is followed by feed rate and drill diameter, respectively. Moreover, the best parametric combination of the three control factors minimizing both the burr height and the surface roughness were as follows: 20 m/min cutting speed, 0.05 mm/r feed rate and 8 mm drill diameter.

The mechanical properties of the workpieces are an influential factor on burr height and surface roughness formed at the hole. Due to the ductility of the material, the amount of burr around the hole in Al-2024 alloy material is much more than in Al-7075 and Al-7050, and it can be explained with elongation. In addition, the surface roughness obtained by Al-2024 is worse than by Al-7075 and Al-7050 alloys. The higher surface roughness values of the Al-2024 alloy can be explained by the highly ductile nature of the alloy.

It is highly important to avoid burr formation, to minimize it or to take it under control as an additional manufacturing step is needed in order to be able to eliminate the burrs formed by drilling. Minimization of burr formation is an important problem of manufacturing. The analysis of variance and Taguchi techniques were applied in order to determine the effects of the drilling parameters. Through the utilizing optimal conditions obtained with S/N ratio, the burr around the hole is minimized which contibutes the reduction of the overall manufacturing cost by reducing the number of processing requirement.

5 REFERENCES

[1] M. Kurt, E. Bagci, Y. Kaynak, Application of Taguchi methods in the optimization of cutting parameters for surface finish and hole diameter accuracy in dry drilling processes, Int J Adv Manuf Technol, 40 (**2009**), 458–469

[2] E. Bagci, B. Ozcelik, Analysis of temperature changes on the twist drill under different drilling conditions based on Taguchi method during dry drilling of Al 7075-T651, Int J Adv Manuf Technol, 29 (**2006**), 629–636

[3] M. Kurt, Y. Kaynak E. Bagci, Evaluation of drilled hole quality in Al 2024 alloy, Int J Adv Manuf Technol, 37 (**2008**), 1051–1060

[4] J. Kim, S. Min, D. A. Dornfeld, Optimization and control of drilling burr formation of AISI 304L and AISI 4118 based on drilling burr control charts, Int J Machine Tools Manuf, 41 (**2001**), 923–936

[5] L. K. L. Saunders, C. A. Mauch, An exit burr model for drilling of metals, Transactions of the ASME, 123 (**2001**), 562–566

[6] E. Kilickap, Modeling and optimization of burr height in drilling of Al-7075 using Taguchi method and response surface methodology, Int J Adv Manuf Technol, 49 (**2010**), 911–923

[7] M. Nouari, G. List, F. Girot, D. Ge´hin, Effect of machining parameters and coating on wear mechanisms in dry drilling of aluminium alloys, Int J Machine Tools Manuf, 45 (**2005**), 1436–1442

[8] S. L. Ko, J. K. Lee, Analysis of burr formation in drilling with a new-concept drill, J Mater Process Technol, 113 (**2001**), 392–398

[9] L. K. Lauderbaugh, Analysis of the effects of process parameters on exit burrs in drilling using a combined simulation and experimental approach, J Mater Process Technol, 209 (**2009**), 1909–1919

[10] S. L. Ko, J. E. Chang, S. Kalpakjian, Development of drill geometry for burr minimization in drilling, CIRP Annals-Manuf Technol, 52 (**2003**), 45–48

[11] M. Kurt, Y. Kaynak, U. Köklü, B. Bakir, G. Atakök, Investigation of the effect of cutting parameters and workpiece mechanical properties on burr formation in drilling process, Proc 12th Int Materials Symposium (Denizli) 15–17 October 2008

[12] S. Kalidas, R. E. Devor, S. G. Kapoor, Experimental investigation of the effect of drill coatings on hole quality under dry and wet drilling conditions, Surface and Coatings Technol, 148 (**2001**), 117–128

[13] U. Esme, M. Bayramoglu, Y. Kazancoglu, S. Ozgun, Optimization of weld bead geometry in TIG welding process using Grey relation analysis and Taguchi method, Mater. Tehnol., 43 (**2009**) 3, 143–149

[14] K. Palanikumar, Application of Taguchi and response surface methodologies for surface roughness in machining glass fiber reinforced plastics by PCD tooling, Int J Adv Manuf Technol, 36 (**2008**), 19–27

[15] U. Heisel, M. Schaal, Burr formation in intersecting holes, Prod Eng Res Devel, 2 (**2008**), 55–62

[16] H. Demir, S. Gündüz, The effects of aging on machinability of 6061 aluminium alloy, Materials & Design, 30 (**2009**), 1480–1483

UDK 620.17:519.61/.64:669.018.95
Original scientific article/Izvirni znanstveni članek

ISSN 1580-2949
MTAEC9, 46(2)109(2012)

THE PERFORMANCE OF VARIOUS ARTIFICIAL NEURONS INTERCONNECTIONS IN THE MODELLING AND EXPERIMENTAL MANUFACTURING OF THE COMPOSITES

PREDSTAVITEV RAZLIČNIH UMETNIH NEVRONSKIH POVEZAV PRI MODELIRANJU IN EKSPERIMENTALNI IZDELAVI KOMPOZITOV

Mohsen Ostad Shabani, Ali Mazahery

Karaj Branch, Islamic Azad University, Karaj, Iran
vahid_ostadshabany@yahoo.com

Prejem rokopisa – received: 2011-05-31; sprejem za objavo – accepted for publication: 2011-07-06

This study reports the performance of different artificial neural network (ANN) training algorithms in the prediction of mechanical properties. First, an experimental investigation was carried out on the mechanical behavior of an A356 composite reinforced with B_4C particulates and then an ANN modeling was implemented in order to predict the mechanical properties, including the yield stress, UTS, hardness and elongation percentage. After the preparation of the training set, the neural network was trained using different training algorithms, hidden layers and the number of neurons in hidden layers. The test set was used to check the system accuracy for each training algorithm at the end of the learning. The results show that the Levenberg-Marquardt learning algorithm gave the best prediction for the yield stress, UTS, hardness and elongation percentage of the A356 composite reinforced with B_4C particulates.

Keywords: composite, hardness, mechanical properties, ANN

V tem delu smo najprej opredelili mehanske lastnosti, vključno z mejo plastičnosti, natezno trdnostjo, trdoto in raztezkom kompozita A356, ojačenega z delci B_4C, in nato uporabili kombinacijo umetne nevronske mreže in metode končnih elementov. Po pripravi treningpostavitve je bila nevronska mreža preizkušena z uporabo različnih algoritmov, skritih plasti in števila nevronov v skritih plasteh. Treningpostavitev je bila uporabljena za preverjanje natančnosti za vsak algoritem na koncu učenja. Rezultati kažejo, da da Levenberg-Marquardtov učni logaritem najboljšo napoved meje plastičnosti, natezne trdnosti, trdote in raztezka za kompozit A356, ki je ojačen z delci B_4C.

Ključne besede: kompozit, trdota, mehanske lastnosti, ANN

1 INTRODUCTION

Large quantities of castings are made each year from the aluminium alloy A356 (also known as Al-7Si-0.3Mg). This alloy is one of the most popular alloys used in industry due to its high fluidity and good "castability"[1–5].

The addition of hard particles to a ductile metal matrix produces a material whose mechanical properties are intermediate between the matrix alloy and the ceramic reinforcement. The casting cooling rate, the reinforcement volume fraction, size, shape, and spatial distribution are the most important parameters, playing a role in the enhancement of the composite's mechanical properties. A stronger adhesion at the particle/matrix interface improves the load transfer, increasing the yield strength and stiffness, and delays the onset of particle/matrix de-cohesion[6].

An ANN is a logical structure with multi-processing elements, which are connected through interconnection weights. The knowledge is represented by the interconnection weights, which are adjusted during the learning phase. This technique is especially valuable in processes where a complete understanding of the physical mechanisms is very difficult, or even impossible to acquire, as in the case of material properties where no satisfactory analytical model exists[7–14].

The aim of this study was to investigate the prediction performance of various training algorithms using a neural network computer program for the mechanical properties of the A356 composite reinforced with B_4C particulates. The results showed that the Levenberg-Marquardt learning algorithms gave the best result for this study.

2 EXPERIMENTAL

In this study, A356 was used as the matrix material and different volume fractions of B_4C particles (1 % to 15 % B_4C) with particle sizes ranging from 1 μm to 5 μm were used as the reinforcements.

The melt-particle slurry was produced by a mechanical stirrer. Approximately 5 kg of A356 alloy was charged into the graphite crucible and heated up to a temperature above the alloy's melting point (750 °C). The graphite stirrer, fixed on the mandrel of the drilling

machine, was introduced into the melt and positioned just below the surface of the melt. It was stirred at approximately 600 r/min and 750 °C. Then the step casting was poured into the CO_2-sand mould.

Microscopic examinations of the composites and matrix alloy were carried out using an optical microscope. The porosity measurements of the composites were obtained using Archimedes's method. Hardness and tensile tests were used to assess the mechanical behavior of the composites and the matrix alloy.

2.1 Prediction of cooling rate and temperature gradient with EEM

The numerical model is applied to simulate the solidification of binary alloys; the mathematical formulation of this solidification problem is given[15]:

$$\rho C \frac{\partial T(x,y,z,t)}{\partial t} = K\nabla^2 T(x,y,z,t) + q \quad (1)$$

where ρ/(kg/m^3) is the density, K/(W/(m K)) is the thermal conductivity, C/(J/(kg K)) is the specific heat, q/(W/m^3) is the rate of energy generation, T/K is the temperature, and t/s is the time.

The release of latent heat between the liquidus and solidus temperatures is expressed by:

$$q = \rho L \frac{\delta f_s}{\delta t} \quad (2)$$

where L/(J/kg) is the latent heat and f_s is the local solid fraction.

The fraction of solid in the mushy zone is estimated by the Scheil equation, which assumes perfect mixing in the liquid and no solid diffusion. With the liquidus and solidus having constant slopes, f_s is then expressed as:

$$f_s = 1 - \left(\frac{T_f - T}{T_f - T_{liq}} \right)^{1/(k_0 - 1)} \quad (3)$$

where T_f/K is the melting temperature, T_{Liq}/K is the liquidus temperature and k_0 is the partition coefficient. Then[15]:

$$\frac{\delta f_s}{\delta t} = \frac{1}{(k_0 - 1)(T_f - T_{liq})} \left(\frac{T_f - T}{T_f - T_{liq}} \right)^{(2-k_0)/(k_0-1)} \frac{\delta T}{\delta t} \quad (4)$$

The latent heat released during the solidification of the remaining liquid of eutectic composition was taken into account by a device that considers a temperature accumulation factor.

$$\rho C', \frac{\partial T(x,y,z,t)}{\partial t} = K\nabla^2 T(x,y,z,t) + q \quad (5)$$

where C' can be considered as a pseudo-specific heat given by:

$$C' = C_M - L \frac{\delta f_s}{\delta T} \quad (6)$$

$$C_M = (1 - f_s) C_1 + f_s C_s \quad (7)$$

where the subscripts L, S and M refer to liquid, solid and mushy, respectively. The other properties, such as the thermal conductivity and the density in the mushy zone, are described in a similar way to the specific heat:

$$K_M = (1 - f_s) K_1 + f_s K_s \quad (8)$$

$$\rho_M = (1 - f_s) \rho_1 + f_s \rho_s \quad (9)$$

The finite-element method (FEM) was used for discretization. Based on the above transient-temperature model, the FEM method is used to calculate the transient temperature, cooling rate and temperature gradient (G).

2.2 Neural network training algorithms

There are various training algorithms used in neural network applications. However, it is difficult to predict which of these will be the fastest one for any problem. Generally, it depends on some factors: the structure of the networks, in other words, the number of hidden layers, weights and biases in the network, aimed error during the learning, and application area, for instance, pattern recognition or classification or the function approximation problem. However, the data structure and the uniformity of the training set are also important factors that affect the system accuracy and performance. Some of the famous training algorithms are as follows[7–14,16–26]:

Resilient back propagation (R_{prop}): is a network training function that updates weight and bias values according to the R_{prop} algorithm.

Random order incremental training with learning functions: trains a network with weight and bias learning rules using incremental updates after each presentation of an input. Inputs are presented in a random order.

Gradient descent back propagation: is a network training function that updates weight and bias values according to the gradient descent.

BFGS quasi-Newton back propagation: is a network training function that updates weight and bias values according to the BFGS quasi-Newton method.

Bayesian regularization: is a network training function that updates the weight and bias values according to LM optimization. It minimizes a combination of squared errors and weights, and then determines the correct combination so as to produce a network that generalizes well. The process is called Bayesian regularization.

In the analysis of the performance of various training algorithms, the same prepared learning and test set were used in the training processes of each learning algorithm. The performance analyses were made from the viewpoint of training duration, error minimization and prediction achievement. The neural network predictions were directly compared with the experimentally obtained data to evaluate the learning performance. The mean square error (MSE), which is a statistical and scientific

error-computation method, was used to analyze the error[25].

3 RESULTS AND DISCUSSION

Microscopic examinations were carried out on the metal-matrix composite. **Figure 1** shows that the B_4C particles were distributed between the dendrite branches and were frequently clustered together, leaving the dendrite branches as particle-free regions in the material.

Figure 2 shows the variation of porosity with B_4C content. It indicates that an increasing amount of porosity is observed with increasing the volume fraction of the composites. The porosity level increased, since the contact surface area was increased[27–31].

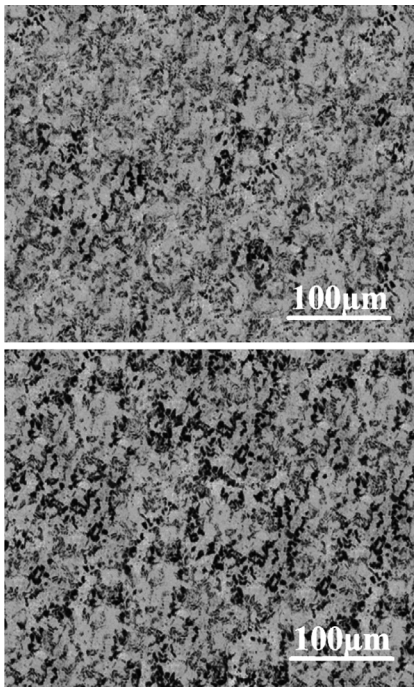

Figure 1: Typical optical micrographs: a) the composite with the volume fraction of B_4C 4 %, b) the composite with 13 % B_4C

Slika 1: Tipičen optični posnetek: a) kompozit z volumenskim deležem B_4C 2 %, b) kompozit s 15 % B_4C

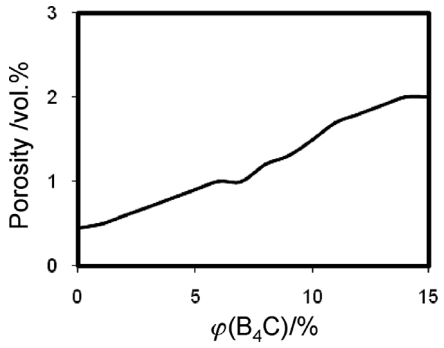

Figure 2: Variations of porosity as a function of the volume fraction of B_4C

Slika 2: Spremembe poroznosti v odvisnosti od volumenskega deleža B_4C

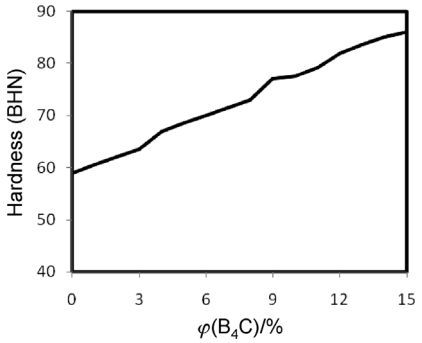

Figure 3: Variations of the hardness value of the samples as a function of the volume fraction of B_4C

Slika 3: Spremembe trdote vzorcev v odvisnosti od volumenskega deleža B_4C

Figure 3 displays the results of the hardness tests. The hardness of the MMCs increases with the volume fraction of particulates in the alloy matrix. The higher hardness of the composites could be attributed to the fact that the B_4C particles act as obstacles to the motion of dislocations[32–36]. **Figure 4** shows the typical stress-strain curves obtained from uniaxial tension tests. The considerable increase in strain-hardening observed during the plastic deformation of composites is rationalized by the resistance of the hard reinforcing particles to the slip behavior of the Al matrix. The elongation to fracture of the composite materials was found to be very low, and no necking phenomenon was observed before fracture. On the other hand, the elongation to fracture of the un-reinforced Al alloy was about 15 %.

The input and output data set of the model is illustrated schematically in **Figure 5**. In **Figure 6**, the obtained MSE values for training data were given for each training algorithm. The obtained error values for

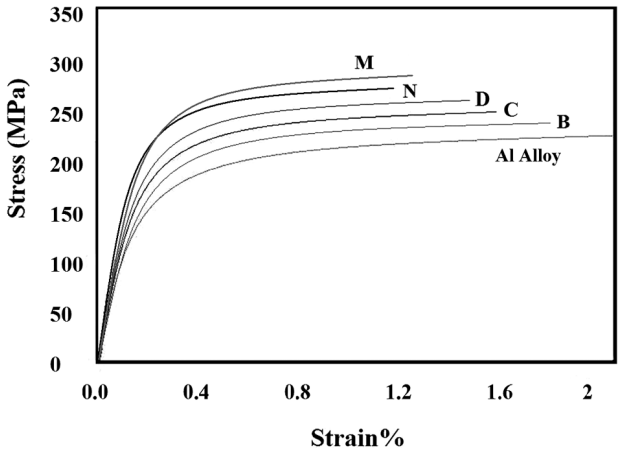

Figure 4: Stress-strain curves for volume fractions Al/ 3 % B_4C (B), Al/ 7 % B_4C (C), Al/ 10 % B_4C (D), Al/ 12 % B_4C (M) and Al/ 15 % B_4C (N)

Slika 4: Odvisnosti napetost – deformacija za volumenske deleže Al/ 3 % B_4C (B), Al/ 7 % B_4C (C), Al/ 10 % B_4C (D), Al/ 12 % B_4C (M) in Al/ 15 % B_4C (N)

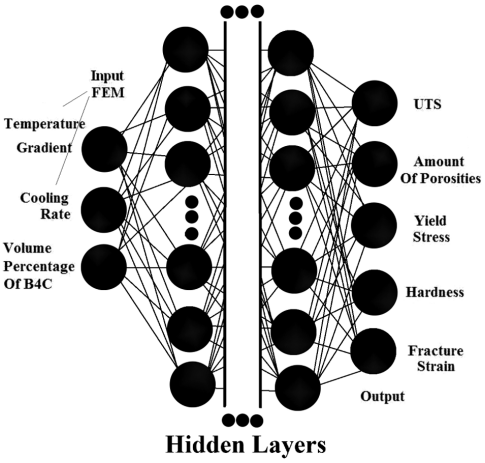

Figure 5: Schematic representation of the neural network architecture
Slika 5: Shematičen prikaz nevronske arhitekture

different numbers of neurons in the hidden layers and the number of hidden layers were analyzed and presented graphically. This figure also gives information about the accuracy of five famous training algorithms depending on the number of neurons in the hidden layers and the number of hidden layers. It is evident from this figure that the smallest error value was obtained by using the Levenberg-Marquardt training algorithm with two hidden layers and eight neurons (*MSE* = 6.4). BFGS quasi-Newton back propagation with three hidden layers and nine neurons in the hidden layers follows the

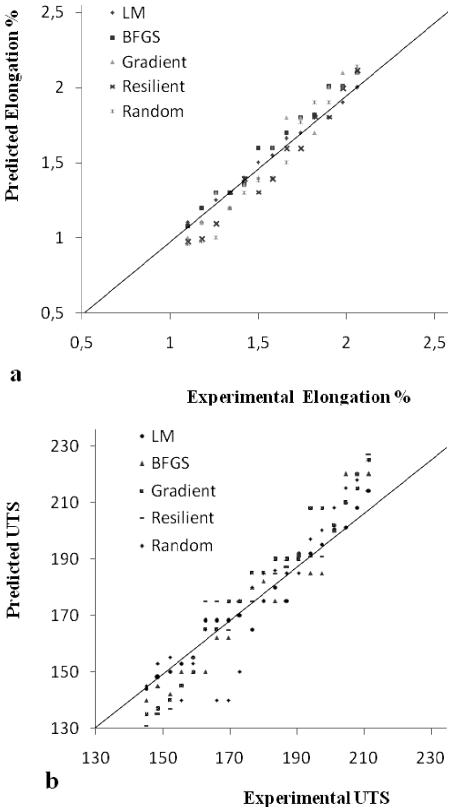

Figure 7: Comparison between the experimental and predicted values: a) elongation percentage, b) UTS
Slika 7: Primerjava med eksperimentalnimi in predvidenimi vrednostmi za: a) raztezek in b) natezno trdnost

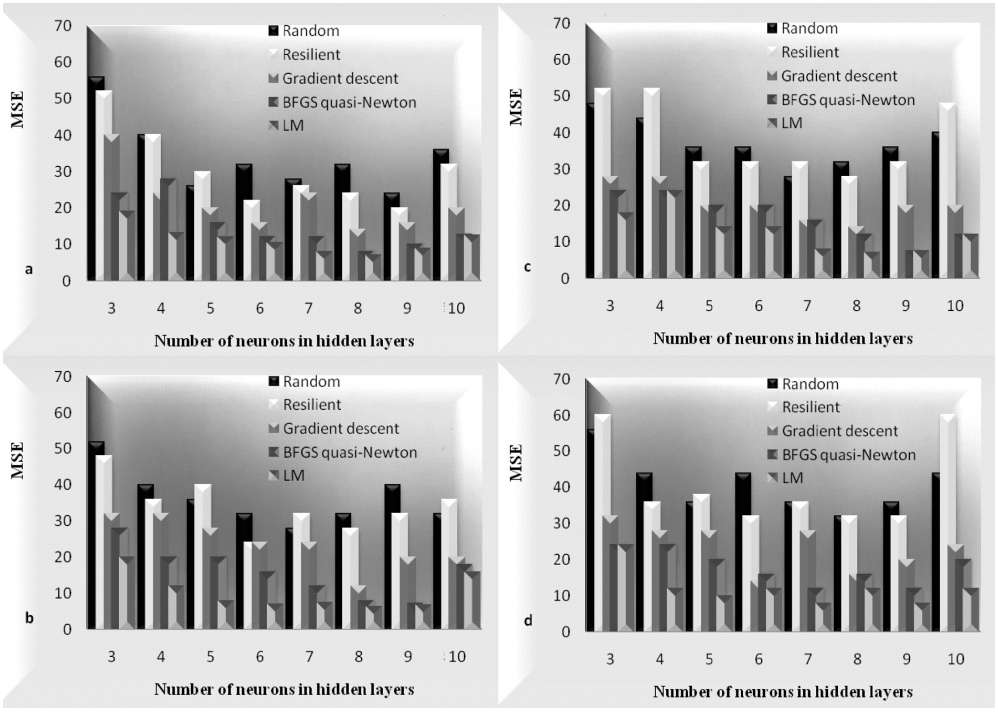

Figure 6: Evaluation of the training performance of the networks for different training algorithms according to the *MSE* values with: a) one hidden layer, b) two hidden layers, c) three hidden layers and d) four hidden layers
Slika 6: Ocena parametrov treninga mreže za različne treningalgoritme po *MSE*-vrednostih za: a) eno skrito plast, b) dve skriti plasti, c) tri skrite plasti in d) štiri skrite plasti

Levenberg-Marquardt algorithm (*MSE* = 8.1), and thirdly the gradient descent back propagation including four hidden layers and six neurons in the hidden layers has clearly much more error than the previous two cases (*MSE* = 14.4). The most error was obtained from the Resilient back-propagation training algorithm and the Random order incremental training with learning functions. The Levenberg-Marquardt training algorithm was found to be the fastest training algorithm; however, it requires more memory with the same error convergence bound compared to the training methods[25]. *MSE* is a good criterion to have information about learning performance. The iterations were continued until it is decided that the minimum *MSE* error is obtained.

Figure 7 shows the efficacy of the optimization scheme by comparing the ANN results with the experimental values. There is a convincing agreement between the experimental values and the predicted values for UTS and the elongation percentage of the A356 composite reinforced with B_4C particulates for the Levenberg-Marquardt training algorithm.

4 CONCLUSION

1) The mechanical properties modeling was developed to predict the hardness, yield stress, ultimate tensile strength and elongation percentage.
2) The effect of various training algorithms on the prediction of the mechanical properties of the fabricated A356 composite reinforced with B_4C particulates was investigated. The prediction of the ANN model was found to be in good agreement with the experimental data.
3) According to the results, the Levenberg-Marquardt learning algorithm gave the best prediction for hardness, yield stress, ultimate tensile strength and elongation percentage for the A356 composite. It is believed that an ANN with two hidden layers and eight neurons (*MSE* = 6.4) gave an accurate prediction of the mechanical properties of the fabricated A356 composite reinforced with B_4C particulates.

5 REFERENCES

[1] A. Mazahery, M. O. Shabani, J. Mater. Eng. Perform., 21 (**2012**), 247–252

[2] H. Möller, G. Govender, W. E. Stumpf, Trans. Nonferrous Met. Soc. China, 20 (**2010**), 1780-1785

[3] L. Ceschini, A. Morri, G. Sambogna, Journal of Materials Processing Technology, 204 (**2008**), 231–238

[4] M. O. Shabani, A. Mazahery, A. Bahmani, P. Davami, N. Varahram, Kovove Mater, 49 (**2011**) 4, 253–258

[5] N. Chomsaeng, M. Haruta, T. Chairuangsri, H. Kurata, S. Isoda, M. Shiojiri, Journal of Alloys and Compounds, 496 (**2010**), 478–487

[6] A. Evans, C. S. Marchi, A. Mortensen, Kluwer Academic Publishers, Dordrecht, Netherlands, 2003

[7] S. K. Singh, K. Mahesh, A. K. Gupta, Materials and Design, 31 (**2010**), 2288–2295

[8] F. Karimzadeh, A. Ebnonnasir A. Foroughi, Materials Science and Engineering A, 432 (**2006**), 184–190

[9] N. Altinkok, R. Koker, Materials and Design, 25 (**2004**), 595–602

[10] A. M. Hassan, A. Alrashdan, M. T. Hayajneh, A. T. Mayyas, Journal of Materials Processing Technology, 209 (**2009**), 894–899

[11] M. Ohlsson, Artificial Intelligence in Medicine, 30 (**2004**), 49–60

[12] S. K. Singh, K. Mahesh, A. K. Gupta, Materials and Design, 31 (**2010**), 2288–2295

[13] P. J. Lisboa, A. F. G. Taktak, A systematic review, Neural Networks, 19 (**2006**), 408–415

[14] A. M. Rashidi, A. R. Eivani, A. Amadeh, Computational Materials Science, 45 (**2009**), 499–504

[15] M. O. Shabani, A. Mazahery, Int. J. of Appl. Math and Mech, 7 (**2011**), 89–97

[16] A. Mazahery, M. O. Shabani, Powder Technology, 217 (**2012**), 558–565

[17] R. Koker, N. Altinkok, A. Demir, Materials and Design, 28 (**2007**), 616–627

[18] M. O. Shabani, A. Mazahery, Applied Mathematical Modelling, 35 (**2011**), 5707–5713

[19] L. Fratini, G. Buffa, D. Palmeri, Computers and Structures, 87 (**2009**), 1166–1174

[20] R. Hamzaoui, M. Cherigui, S. Guessasm, O. ElKedim, N. Fenineche, Materials Science and Engineering B, 163 (**2009**), 17–21

[21] N. S. Reddy, A. K. Prasada Rao, M. Chakraborty, B. S. Murty, Materials Science and Engineering A, 391 (**2005**), 131–140

[22] Z. Sterjovski, D. Nolan, K. R. Carpenter, D. P. Dunne, J. Norrish, Journal of Materials Processing Technology, 170 (**2005**), 536–544

[23] S. H. Mousavi Anijdan, A. Bahrami, H. R. Madaah Hosseini, A. Shafyei, Materials and Design, 27 (**2006**), 605–609

[24] M. O. Shabani, A. Mazahery, Synthetic Metals, 161 (**2011**), 1226–1231

[25] R. Koker, N. Altinkok, A. Demir, Materials and Design, 28 (**2007**), 616–627

[26] M. Tatlier, H. K. Cigizoglu, A. Erdem-Şenatalar, Computers and Chemical Engineering, 30 (**2005**), 137–146

[27] M. Zamzam, D. Ros, J. Grosch, Key Eng Mater, 79–80 (**1993**), 235–246

[28] M. Kok, Ph. D. Thesis, The Institute of Science and Technology of Elazig University, Turkey, 1999

[29] W. Zhou, Z. M. Xu, Casting of SiC reinforced metal matrix composites, J. Mater. Process. Technol., 63 (**1997**), 358–363

[30] S. Ray, Porosity in foundry composites prepared by vortex method, in: S. G. Fishman, A. K. Dhingra (Eds.), ASM/TMS, 1988, 77–80

[31] D. J. Lloyd, B. Chamberian, ASM, Illinois, 1988, 263–269

[32] F. M. Hosking, F. Folgar Portillo, R. Wunderlin, R. Mehrabian, Composites of aluminium alloys: fabrication and wear behaviour, J. Mater. Sci., 17 (**1982**), 477–498

[33] M. Roy, B. Venkataraman, V. V. Bhanuprasad, Y. R. Mahajan, G. Sundararajan, Metall. Trans. A, 23 (**1992**), 2833–2846

[34] S. Chung, B. H. Hwang, Tribol. Int., 27 (**1994**) 5, 307–314

[35] S. Skolianos, T. Z. Kattamis, Mater. Sci. Eng. A, 163 (**1993**), 107–113

[36] P. N. Bindumadhavan, H. K. Wah, O. Prabhakar, Wear, 248 (**2001**), 112–120

UDK 536.2
Original scientific article/Izvirni znanstveni članek

ISSN 1580-2949
MTAEC9, 46(2)115(2012)

EXPERIMENTAL AND THEORETICAL INVESTIGATION OF DRYING TECHNOLOGY AND HEAT TRANSFER ON THE CONTACT CYLINDRICAL DRYER

EKSPERIMENTALNA IN TEORETIČNA RAZISKAVA TEHNOLOGIJE SUŠENJA IN PREVAJANJA TOPLOTE NA KONTAKTNEM VALJASTEM SUŠILNIKU

Slavica Prvulović, Dragiša Tolmač, Miroslav Lambić, Dragana Dimitrijević, Jasna Tolmač

University of Novi Sad, Technical faculty "Mihajlo Pupin", Djure Djakovića bb, 23000 Zrenjanin, Serbia
prvulovicslavica@yahoo.com

Prejem rokopisa – received: 2011-06-05; sprejem za objavo – accepted for publication: 2011-11-23

An experimental and theoretical research on the technology and application of contact drying on the rotating cylinder dryer is presented. Results of measurements of drying parameters of drying starch solution in real working conditions of drying are analysed. Based on tests numerical values of the coefficient of heat transfer, heat transfer model, energy performance, curves of drying kinetics and drying kinetics equations are given, characteristic for drying technology of drying and other relevant parameters of the process.

Keywords: drying technology, heat transfer, contact cylindrical dryers

Predstavljena je eksperimentalna in teoretična raziskava tehnologije in uporabe kontaktnega sušenja na sušilniku z vrtečim se valjem. Analizirani so rezultati meritev parametrov sušenja raztopine škroba v realnih obratovalnih razmerah. Na podlagi numeričnih vrednosti koeficientov prenosa toplote so prikazani model prenosa toplote, poraba energije, krivulje kinetike sušenja in kinetične enačbe sušenja, karakteristične za tehnologijo sušenja in drugi za proces pomembni parametri.

Ključne besede: tehnologija sušenja, prenos toplote, kontaktni valjasti sušilnik

1 INTRODUCTION

Drying on the rollers is a method recognized worldwide as a continuous and very economical technology. Contact roll kiln is applied in several branches of industry, especially in chemical and food industry. It is also applied in drying powdered products in water dispersion with 35–40 % dry matter, colloidal solution and suspension, viscous liquids and pastes.[1] Different dispersions of certain powdered products unequally react by drying, which depends on the properties of the processed powdered material. Thus, it is very difficult to propose a unique technique of cylinder dryer.[2] In comparison to other systems, roller drying accommodation requires less space, service and maintenance are very simple and performed with a small labor force. These advantages, as well as the economical transfer of heat provide a low price of dried final product.

The drying time is in most cases of only a few seconds and it is very important by drying of products sensitive to heat, such as vitamins, which makes better high temperature in short period of time than lower temperatures in long period of time. For substances such as starch solutions in water, contact drying on heated rollers is a good solution of the problem of drying.

Adhesion of dried solution is intensive (in the thin layer) and the drying is done in one incomplete roll revolution. The layer thickness of dried material is regulated by the size of gap between the main and applying rollers, which usually ranges from 0.1–1.0 mm. Thanks to the principle of drying based on direct contact of heated roll and wet material, intensive exchange of heat and mass occurs.

The kiln shown in relation to other technological solutions, has better technical and economic indicators of work. In addition to work efficiency, the essential precondition for any wider application of roll drying is the relatively low specific energy consumption. This consumption by the drying roller is significantly less than by using of other drying mechanisms and spray drying, or in any other way. Generally it is in the range of 1.2–1.6 (kg steam/kg evaporated water). The revolution rate is in the range 5–25 r/min and it depends on the type of dried material. For roll heating used aerated water pressure 3–8 bar, hot water or organic liquids with high boiling temperature are used.[3,4]

The drying efficiency is estimated with the quantity of evaporated moisture, which is in range 10–60 kg h^{-1} m^{-2} depending on the size of the drying cilinder. The relatively simple construction and low specific energy consumption make these drying roll devices very attractive for applications in industry. For these contact roll dryers there are very few technical data on experimental plants which would enable exact calculations

necessary for designing of dryers. Drying on cylinder dryers is an improved drying technique. It provides high quality of dried material and high efficiency and economy of plants, i.e. the reduction of the power and investment costs.[5] Descriptions of cylinder dryers and other drying systems are found in references.[6,7]

2 EXPERIMENTAL FACILITY AND RESULTS OF MEASUREMENTS

The tests were performed on the industrial dryer with cylinder diameter d = 1 220 mm and length L = 3 048 mm, heated inside by steam vapor shown in **Figure 1**. By cylinder heating and by constant working pressure of p = 4 bar, the stationary conditions necessary in experimental measurements are obtained for a great number of rotations.

Used measuring instruments:

1) Water vapor pressure
p_p = 4 bar
2) Water vapor temperature
T_p = 140 °C
3) Number of cylinder rotations
n = 7.5 min^{-1}
4) Thickness of cylinder envelope
δ_1 = 35 mm
5) Thickness of the dried material moisture
δ_2 = 0.25 mm

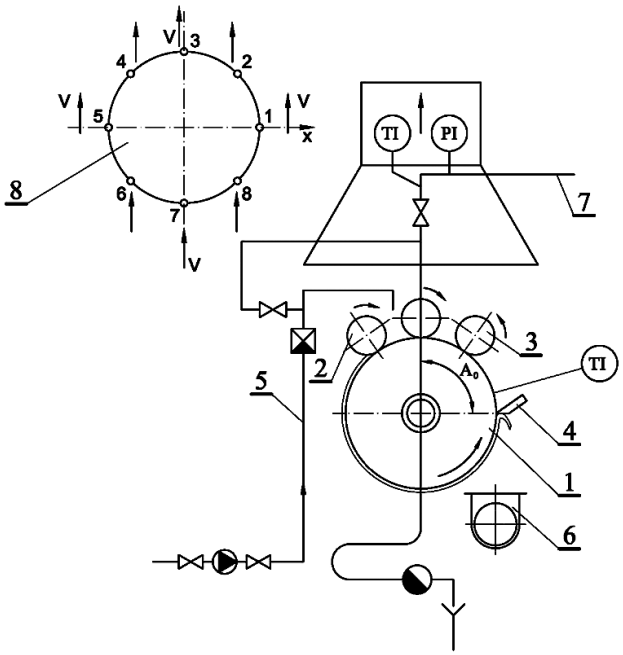

Figure 1: Scheme of experimental contact rool dryer; 1- cylinder; 2- bringing cylinders; 3- scattering cylinder; 4- knife; 5- pipeline for the wet material transporting; 6- worm conveyer; 7- steam pipeline; 8- scheme of measuring points

Slika 1. Shema eksperimentalnega kontaktnega valjastega sušilnika; 1- valj; 2- dovodna valja; 3- razpršilni valj; 4- nož; 5- cevovod za transport sušenega materiala; 6- polžasti prenosnik; 7- parni cevovod; 8- shema merilnih točk

6) Cylinder surface A = 11.5 m^2
7) Water content of dried material
– start of drying w_1 = 65 %
– end of drying w_2 = 5 %
8) Water vapor consumption m_p = 268 kg h^{-1}
9) The dried material is 35 % mass solution of potato starch in water.

For experimental measurements, the next measuring instruments and accessories were used:

1) For measuring of water pressure: membrane manometer of 0–10) bar range and precision of 1.6 %;
2) Water temperature: bimetal thermometer with range 0–200 °C and precision of ±2.5 %;
3) Cylinder surface temperature and temperatures in direct vicinity of the cylinder: digital thermometer, type KD-23; with thermo couple NiCr-Ni as sensor, with range –69–199.9 °C and ±0.1 °C precision.
4) Ambient temperature: glass mercury thermometers with range 0–50 °C.
5) Air speed in direct vicinity of the cylinder: anemometer with incandescent wire, type TA 400, Airflow Developments Canada – LTD, with range 0–2) m/s and precision of ±0.02 m s^{-1}.
6) Moisture of drying material: digital meter for humidity, type Metler-LP16 and precision of ±0.1 %.

Table 1: Average values of the results of temperature measuring of drying material T_m/°C and content of moisture, w/%

Tabela 1: Povprečne vrednosti izmerjenih temperatur sušenega materiala T_m/°C in vsebnost vlage v masnih deležih, w/%

Measuring place, according to the **Figure 1**	Average values of the temperature dried material, T_m/°C	Moisture of the dried material, w/%	Time drying t/s
3	–	65	0
4	80	54	1
5	81	41	2
6	82	29.5	3
7	84	18.5	4
8	89	10	5
1	96	5	6

Table 2: Results of temperature measuring in drying material layer on the cylinder surface, T/°C

Tabela 2: Povprečne temperature v plasti sušenega materiala na površini valja, T/°C

Number of measure-ment points	Distance from cylinder; x/m				
	0	0.005	0.01	0.02	0.03	0.04
1.	96	65	43.5	39.8	37.2	35.0
2.	98	59	40	38	37	35.5
3.	–	–	–	–	–	–
4.	80	53	42.0	40.0	31.0	30.0
5.	81	48	35.0	31.0	30.0	29.0
6.	82	45	36.0	28.5	38.0	27.0
7.	84	43	30.0	27.3	26.0	25.0
Mean value T/°C	85.0	50.4	37.8	34.2	31.6	30,2

7) Water power consumption: measurement of condensate mass out of the dryer with the balance "Scalar 100" with the range of 0–100 kg.

The results of temperature measuring with dried materials layer on cylinder surface, and dried material moisture are given in **Table 1**. The measuring was performed in the plane of cylinder cross-section according to experimental points marked in **Figure 1**.

The results of temperature measuring with dried materials layer on cylinder surface are given in **Table 2.**

3 DETERMINATION OF HEAT TRANSFER COEFFICIENT

The overall heat flux from vapor into surrounding air can be calculated as:

$$q_u = U\,(T_p - T) \tag{1}$$

For great cylinder diameters and with relation to envelope thickness, it is possible with great accuracy use the term for the coefficient of heat transfer as for the flat wall the Eq. (2). The difference of heat transfer coefficient for flat wall and for the cylinder diameter d = 1 220 mm and cylinder wall thickness δ_1 = 35 mm is of 1.66 % with regard heat transfer coefficient for cylinder body. Because of simpler form, for calculation of the total coefficient of heat transfer Eq. (2) will be applied[8].

When in the cylinder surface is covered by a layer of drying material, the overall heat transfer coefficient is defined according to equation (2):

$$U = \frac{1}{\frac{l}{h_1} + \frac{\delta_1}{k_1} + \frac{\delta_2}{k_{2m}} + \frac{1}{h_{com}}} \tag{2}$$

The influential parameter of the mechanism of heat transfer is the combined coefficient of heat transfer (h_m), **Table 3** and value of Nussle's number is defined with the equation.

$$Nu = \frac{h_c d}{k_a} = BRe^c \tag{3}$$

On the basis of grouping influential parameters that influence the most coefficient of heat transfer, the results of experimental and theoretical researches are being correlated using the equation of Nussle's type[9–11].

$$h_c = \frac{k_a}{d} B \left(\frac{dG}{\mu} \right)^c \tag{4}$$

The constants (B) and (c), are defined by the method of the least squares.

4 RESULTS AND DISCUSSION

Applying correlation theory on experimental results of measuring empirical equations of drying kinetics were dedeuced.[12,13]

In the initial drying period the dependence of moisture versus drying time is almost linear with initial of drying at t = 0–1) s (**Figure 2**). Thus, in the initial period the drying rate is constant. In the second period of drying in temporal interval t = 1–6 s, the drying dependence changes to a second rank polio. At the end of drying, the content of moisture is of w_2 = 5 %.

In **Figure 3**, the drying rates curves are presented. Initially, the drying rate is constant, and in the second period the drying rate decreases. When the content of moisture is reduced to that of balanced moisture w = 5 %, the evaporation rate is dw/dt = 0.06 (kg water/ kg dried solid).

The presented thermal drying curve in **Figure 4** corresponds to a dependence of polio of second rank. The initial drying temperature is of 80 °C and in the end of drying it is of 96 °C.

Using the method of smallest squares in processing the experiment data the next empiric equations were derived:

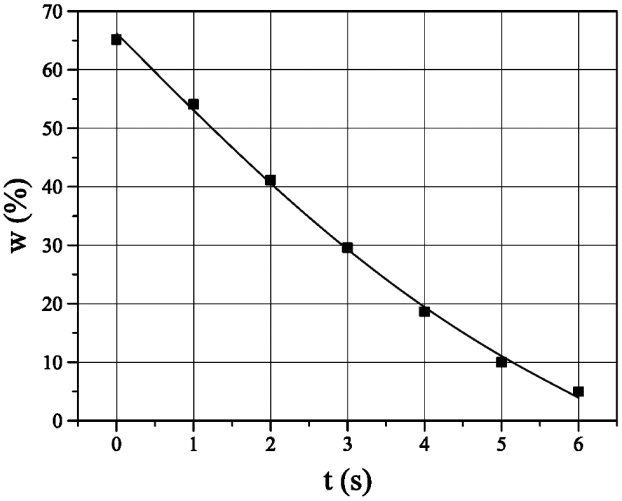

Figure 2: Dependence content of moisture and drying time
Slika 2: Odvisnost vsebnosti vlage od časa sušenja

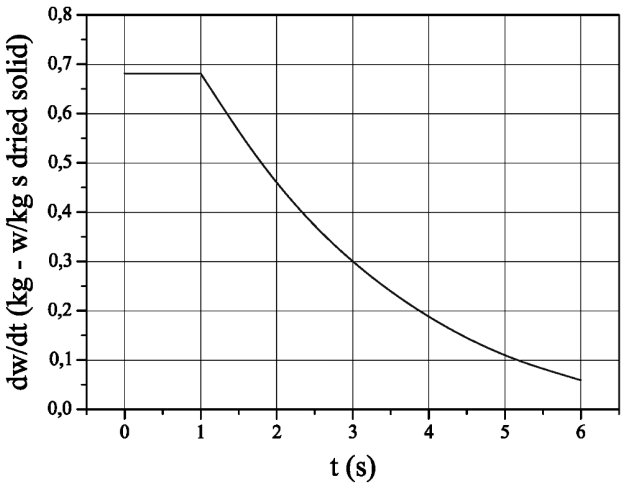

Figure 3: Dependence quantity of dried solid and drying time
Slika 3: Odvisnost količine trdnega materiala od časa sušenja

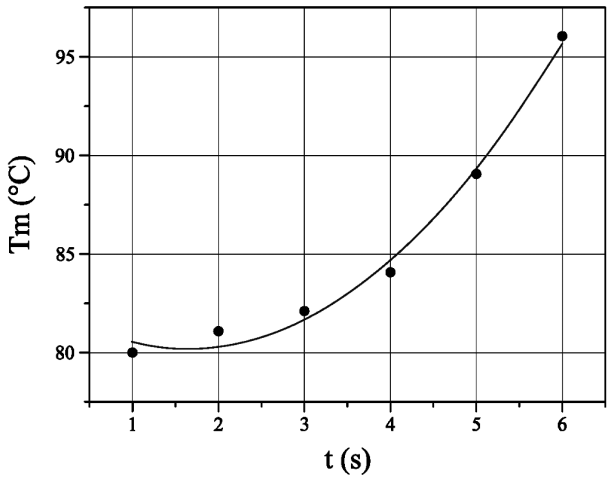

Figure 4: Dependence temperature of drying layer and time
Slika 4: Odvisnost temperature v sušeni plasti od časa sušenja

– dependence content of moisture material and drying time (**Figure 2**):

$$w = 66.166 - 14.196\ t + 0.636\ t^2 \quad (5)$$

– dependence drying rate and drying time (**Figure 3**):

$$\mathrm{d}w/\mathrm{d}t = 0.744 - 0.168\ t + 0.008\ t^2 \quad (6)$$

– drying temperature and drying time (**Figure 4**):

$$T_\mathrm{m} = 82.40 - 2.721\ t + 0.821\ t^2 \quad (7)$$

These empiric equations for drying are obtained from experimental data, they define the character of the drying process and are in accord with previous researches.[14,15]

In the initial period of drying, the surface of dried material with high content of moisture is covered by a thin layer of water, it behaves as free moisture and the evaporation is accelerated also with taking up physically tied moisture (**Figure 3**). In the second period, the drying rate is lower, also for tied moisture.

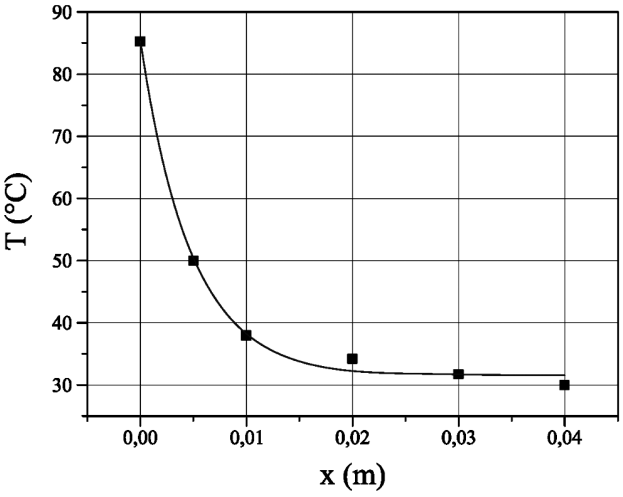

Figure 5: Dependence of temperature in the plane of central cross and distance from cylinder surface
Slika 5: Odvisnost temperature v ravnini srednjega prereza od razdalje do površine valja

Applying the correlation theory for experimental results we obtained empirical equations for change of temperature (T) in function of distance (x), for distance of cylinder surface in every measuring point. The temperature in the plane of the central cross-section of cylinder with consideration of standard deviations is given in **Figure 5**.

The empiric equation for the dependence of mean temperature and distance x (m), from the cylinder surface (**Figure 5**), is:

$$T = 75.50 - 3\ 611.88x + 64\ 595.87x^2 \quad (8)$$

Based on the results of experimental and theoretical investigation[16,17] the following correlative equations were deduced:

$$N_u = 0.569\ Re^{0.691} \quad (9)$$

$$h_c = 0.569\ Re^{0691}\ (k/d) \quad (10)$$

$$q_m = -\ 3.29\ (\mathrm{d}T/\mathrm{d}x)_{x\,=\,0} \quad (11)$$

In the layer of drying material, the total heat flux consists of part of flux equal to the product of heat conductivity of humid material and temperature gradient and of the flux part equal to the product of material flux of humidity, specifically the humidity enthalpy, i.e. the flux originating from evaporation of humidity. The intensity of this flux is a relevant factor in total heat flux by drying the material on the surface.

On the basis of local temperature, the heat flux is variable along the rim of the rotating cylinder. In the second drying period, and especially at the end of drying, the temperature gradient has a rising tendency. During the drying process on cylinder dryers, humidity remnants near the end of drying are evaporated at rising temperature on material surface and cause higher variables of temperature gradient.

Table 3: Combined heat transfer coefficient (h_com), heat transfer coefficient with convection (h_c), heat transfer coefficient with radiation (h_r) and heat transfer coefficient by evaporation of humidity (h_w)
Tabela 3: Kombinirani koeficient prenosa toplote (h_com), koeficient prenosa toplote s konvekcijo (h_c), koeficient prenosa toplote s sevanjem (h_r) in koeficient prenosa toplote z izparevenjem vlage (h_w)

Number of measuring place	Convective heat transfer coefficient h_c / (W m^{-2} K^{-1})	Radiation heat transfer coefficient h_r / (W m^{-2} K^{-1})	Evaporation heat transfer coefficient h_w / (W m^{-2}K^{-1})	Combined coefficient of heat transfer h_com / (W m^{-2}K^{-1}) = $h_\mathrm{c} + h_\mathrm{r} + h_\mathrm{w}$
4	15.0	7.0	475	497
5	15.8	7.2	335	358
6	17.0	7.1	189	214
7	17.8	7.2	128	153
8	14.7	7.3	87	109
1	16.9	7.1	41	65
Mean value	15.8	7.2	210	233

In **Table 3**, are given the results of deduction of heat transfer coefficient with convection (h_c), heat transfer coefficient with radiation (h_r), heat transfer coefficient with evaporation of humidity (h_w) and combined heat transfer coefficient (h_{com}). The heat transfer coefficient with convection from drying material layer in air is variable along the cylinder rim.

The mean value of heat transfer coefficient is 15,8 W m^{-2} K^{-1}. The maximal value of heat transfer coefficient found in the lower zone of cylinder is 17.8 W m^{-2} K^{-1}. To greater values of Reynolds's number, correspond the higher temperature gradient, greater values of heat transfer with convection and higher Nussle's number (**Figure 6**).

The investigated drying process is in reality a natural air streaming around a rotating cilinder with low streaming speed measured at eight measuring points in close aproximity of the cilinde. The air streaming combines natural flux and flux due to the cylinder rotation with rotation rate set for an optimal drying. Since the Raynolds's number depends on air streaming speed, it changes in a given interval, presented on **(Figure 6)**.

According to **Figure 6**, the Reynolds's number is lower than $R_{ek} = 5 \cdot 10^5$ and indicates to a laminar convection in direct vicinity of the cylinder surface.

The thermal resistance consisting of combined coefficients of heat transfer ($1/h_{com}$) has an important effect on the overall heat transfer coefficient (U), as shown in **Table 4**.

The mean value for thermal resistance of heat transfer of $\Sigma R = 8.26 \cdot 10^{-3}$ m^2 K W^{-1} agrees to the mean value of overall heat transfer coefficient U = 118 W m^{-2} K^{-1}, (**Table 4).** According to data from,[18,19] heat transfer coefficient is in the range of 105–345 W m^{-2} K^{-1}.

Taking into account the local values of combined heat transfer coefficients (h_m), (**Table 4),** the variation along the cylinder size indicates to changes of technical resistances of heat transfer from the cylinder to air

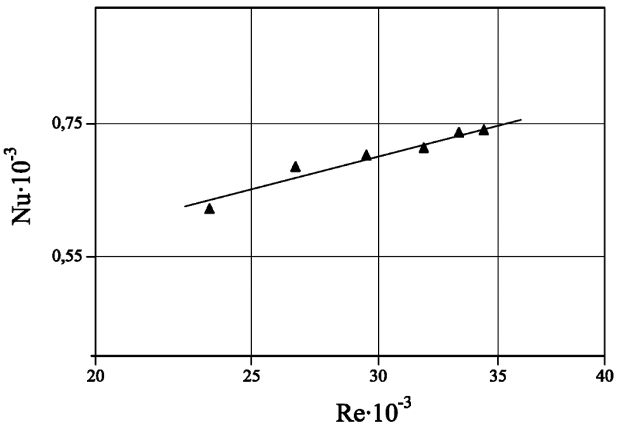

Figure 6: Dependence of change of Nussle's and Raynolds's number with cylinder (d = 1 220 mm, v = 0.35 m/s, T_m = 85 °C)
Slika 6: Odvisnost spremembe Nusslevega in Raynoldsovega števila pri valju (d = 1 220 mm, v = 0.35 m/s, T_m = 85 °C)

Table 4: Overall heat transfer coefficient (U)
Tabela 4. Splošni koeficient prenosa toplote (U)

Measuring point	Thermal resistance of heat transfer 10^3 (m^2 K W^{-1}) $\Sigma R = (1/h_1 + \delta_1/k_1 + \delta_2/k_{2m} + 1/h_{com})$				Overall heat transfer coefficient U/(W m^{-2} K^{-1})
4	0.1	0.76	3.1	2.0	167
5	0.1	0.76	3.1	2.7	150
6	0.1	0.76	3.1	4.6	117
7	0.1	0.76	3.1	6.5	96
8	0.1	0.76	3.1	9.1	76
1	0.1	0.76	3.1	15.3	52
Mean value	0.1	0.76	3.1	4.3	118

($1/h_{com}$) and also originate changes of overall heat transfer coefficient (U) along the cylinder circumference.

The dominant effect on changes of overall heat transfer coefficient (U) is due to changes of coefficients of heat transfer with evaporation of humidity (**Table 4**). This effect is represented as thermal resistance of heat transfer ($1/h_{com}$). The research results for these dryers include various values of Reynolds's number, which cover air convection speeds from 0.1 m/s to 1 m/s i.e. Re = 10000–34500 by standard cylinder size of d = 1 220 mm.

The overall energy of vapour as thermal flux is:

$$q_p = \frac{m_p \cdot r}{A} \tag{12}$$

The energy balance is presented in order to check the acquired results. For the value of temperature gradient $(dT/dx)_{x=0}$ = –3 611 Eq. (8), heat flux is q_m = 11 880 W m^{-2}, Eq.(11). The overall energy of vapour as thermal flux is q_p = 13 825 W m^{-2}, Eq. (12).

The difference of both values is 1 945 W m^{-2}, and it is heat loss. Thermal degree of energy use is η_T = 0.859. During contact drying there is high degree of heat use due to direct contact of drying material layer and the cylinder heated surface.

The evaluation of uncertainty is an ongoing process consuming time and resources. It consists of:

(a) Uncertainty value is from the surface of cylinder temperature and temperatures in direct vicinity of the cylinder and uncertainty of the digital thermometer, type KD-23; and thermo couple NiCr-Ni.
(b) Uncertainty value is from air speed in direct vicinity of the cylinder.

Uncertainty of the anemometer with incandescent wire, type: TA 400, 0–2 m s^{-1}.

Applying the correlation theory to measurement results we have obtained the empirical Eq. (8), (9), (10), (11) with a high coefficient of correlation, equation (8): R = 0.985, eq. (9), (10): R = 0.963, eq. (11): R = 0.978, therefore, the total uncertainty is of 5–7.8 %. The uncertainty analysis of the whole work shows that

temperature and air speed measurements have a relatively little influence on the accuracy of results. Thus it is concluded that the obtained results can be used in practice.

5 CONCLUSIONS

On the basis of experimental results and their analysis, the following conclusions are proposed:

- Local values of temperature, heat flux and heat transfer coefficient are different along the cylinder rim;
- maximal values of heat flux originate in the upper cylinder zone (i.e. in initial drying period);
- The values of heat transfer complex coefficient from the surface of drying material on surrounding air produce changes of thermal resistances and heat transfer and cause variations of total heat transfer coefficient along the cylinder rim. The greatest is the effect of heat transfer coefficient with humidity evaporation.
- On the basis of the research results, the mean value of overall heat transfer coefficient U = 118 W m^{-2} K^{-1} was obtained.
- On the basis of experimental and theoretical results the thermo dynamical analysis of the problem was performed and temperature gradients, heat flux and heat transfer coefficients were calculated. In this way, a new approach is given to the drying theory in the last fifteen to twenty years;

The obtained results can be used:

- For defining the essential dependences and parameters of heat transfer with rotating cylinders heated inside by vapor;
- For the design and development of new drying cylinders or selection of optimal parameters of heat transfer.
- The research results can be used because of experimental data taken at real plant as base. For this reason, the results can be useful for: researchers, designers and manufacturers of such and similar drying systems, as well for educative purposes.
- The determined relevant parameters of heat transfer have had as objective a more complete energy description of rotating cylinders for cylinder dryers and drying and to complement the existing knowledge and explanations of some, so far incompletely explained phenomena in simpler devices.

6 REFERENCES

[1] L. Renshu, W. Weihong, H. Jun, A Study on contact drying with flexible screen, Journal of Forestry Research, 11 (**2000**) 1, 51–53

[2] M. W. Meshram, V. V. Patil, S. S. Waje, B. N. Thorat, Simultaneous gelatinization and drying of maize starch in a single-screw extruder, Drying Technology, 27 (**2009**) 1, 113–122

[3] S. Prvulovic, D. Tolmac, M. Lambic, Z. Blagojevic, Researching results of contact drying, Energetic Technologies, 5 (**2008**), 3–6

[4] D. Tolmac, M. Lambic, Heat transfer through rotating rol of contact dryer, Int. Comm. in Heat and Mass Transfer, 24 (**1997**), 569–573

[5] S. Prvulovic, D. Tolmac, M. Lambic, Convection drying in the food Industry, Agricultural Engineering International the CIGR E journal, 9 (**2007**), 1–12

[6] T. Aihara, W. S. Fu, Y. Suzuki, Numerical analysis of heat and mass transfer from horizontal cylinders in downward flow of air-water mist, Journal of Heat Transfer, 112 (**1990**), 472–478

[7] N. L. Yong, W. J. Minkowycz, Heat Transfer characteristics of the annulus of two coaxial cylinders with one cylinder rotating, Heat and Mass Transfer, 32 (**1989**), 711–721

[8] D. Tolmac, S. Prvulovic, M. Lambic, The Mathematical model of the heat transfer for the contact dryer, FME Transactions, 35 (**2007**), 5–22

[9] D. Maillet, A. Degiovanni, R. Pasquetti, Inverse heat conduction applied to the measurement of heat transfer coefficient on a cylinder, Journal of Heat Transfer, 113 (**1991**), 549–557

[10] A. Sakurai, M. Shiatsu, K. Hata, A General correlation for pool film boiling heat transfer from a horizontal cylinder to sub cooled liquid, Journal of Heat Transfer, 112 (**1990**), 441–450

[11] D. Tolmac, Determination of heat transfer coefficient of contact dryer's rotating cylinder, Ph. D. dissertation, University of Novi Sad, Zrenjanin, Serbia, 1995

[12] D. Hez, Comparison of processing economics of different starch dryers. Journal of Starch/Strake, 36 (**1984**), 369–373

[13] D. Tolmac, M. Lambic, The mathematical model of the temperature field of the rotating cylinder for the contact dryer, Int. Comm. in Heat and Mass Transfer, 26 (**1999**), 579–586

[14] H. H. Cho, S. Y. Lee, J. H. Won, D. H. Rhee, Heat and mass transfer in a two-pass rotating rectangular duct, Heat and Mas transfer, 40 (**2004**) 6–7, 467–475

[15] C. Y. Song, S. T. Lin, G. J. Hwang, An Experimental study of convective heat transfer in radial rotating rectangular ducts, Journal of Heat Transfer, 113 (**1991**), 604–611

[16] L. Fue-Sang, C. Tsar-Ming, C. Chao-Kuang, Analysis of a free convection micro polar boundary layer about a horizontal permeable cylinder at a no uniform thermal condition, Journal of Heat Transfer, 112 (**1990**), 504–506

[17] S. Prvulovic, D. Tolmac, M. Lambic, Lj. Radovanovic, Efects of heat transfer in a horizontal rotating cyilinder of the contact dryer, Facta Universitatis, 5 (**2007**), 47–61

[18] H. H. Cho, S. Y. Lee, D. H. Rhee, Effects of cross ribs on heat and mass transfer in a two-pass rotating duct, Heat and Mass Transfer, 40 (**2004**) 10, 743–755

[19] Y. Mori, I. Hosokawa, H. Koizumi, Control of the formation of Benard cells in a horizontal rectangular duct heated from below, Heat and Mass Transfer, 27 (**1992**) 4, 195–200

List of symbols

d/m – roll diameter
n/(r/min) – number of roll rotations
p/bar – pressure
T/°C – temperature
q/(W m^{-2}) – heat flux
x/m – distance
Nu – Nuselts number
Re – Reynolds number
A/m^2 – the cylinder surface
G/(kg s^{-1} m^{-2}) – mass speed stream warm air
μ/(kg s^{-1} m^{-1}) – dynamic viscosity warm air
(dT/dx)/K m^{-1} (or °C m^{-1}) – temperature gradient
w/% – moisture

T_p/°C – water vapor temperature for cylinder heating
r/(kJ kg $^{-1}$) – heat evaporation steam water
U/(W m $^{-2}$ K^{-1}) – overall heat transfer coefficient from condensing vapor in cylinder interior on surrounding air
k_a/(W m^{-1} K^{-1}) – termical conductivity of air
h_1/(W m^{-2} K^{-1}) – coefficient of heat transfer from condensing vapor on cylinder wall
δ_1/m – thickness of cylinder envelope
δ_2/m – mean thickness of drying material layer
k_1/(W m^{-1} K^{-1}) – thermo conductivity of cylinder envelope
k_{2m}/(W m^{-1} K^{-1}) – mean thermo conductivity of material at drying
h_{com}/(W m^{-2} K^{-1}) – combined coefficient of heat transfer
ΣR/(m^2 K W^{-1}) – thermical resistance of heat transfer

UDK 577.1:616.314-76/-77
Original scientific article/Izvirni znanstveni članek

ISSN 1580-2949
MTAEC9, 46(2)123(2012)

AN RE/RM APPROACH TO THE DESIGN AND MANUFACTURE OF REMOVABLE PARTIAL DENTURES WITH A BIOCOMPATIBILITY ANALYSIS OF THE F75 Co-Cr SLM ALLOY

RE/RM-PRIBLIŽEK, NAČRTOVANJE IN IZDELAVA SNEMLJIVIH DELOV ZOBOVJA Z ANALIZO BIOKOMPATIBILNOSTI ZLITINE F75 Co-Cr SLM

Danimir P. Jevremović[1], Tatjana M. Puškar[2], Igor Budak[3], Djordje Vukelić[3], Vesna Kojić[4], Dominic Eggbeer[5], Robert J. Williams[5]

[1]Clinic for Prosthodontics, School of Dentistry, Pančevo, University Business Academy, Novi Sad, Serbia
[2]Clinic for Prosthodontics, Medical Faculty – Department of dentistry, University of Novi Sad, Serbia
[3]Faculty of Technical Sciences, University of Novi Sad, Serbia
[4]Oncology Institute of Vojvodina, Sremska Kamenica, Serbia
[5]Centre for Dental Technology and the National Centre for Product Design and Development Research, Cardiff Metropolitan University, Cardiff, United Kingdom
budaki@uns.ac.rs

Prejem rokopisa – received: 2011-07-14; sprejem za objavo – accepted for publication: 2011-08-24

The implementation of computer-aided technologies and systems has paved the way towards a significant advancement of the conventional modelling and manufacture of dental replacements. In this research the focus is on approach that combines reverse engineering as a modelling technique and rapid manufacture, i.e., selective laser melting, as the manufacturing technology, with special emphases on material selection in the fabrication of removable partial dentures. The paper presents the results of a biocompatibility analysis of the F75 Co-Cr dental alloy using the MTT eluate test.

Keywords: reverse engineering, rapid manufacturing, selective laser melting, removable partial dentures, biocompatibility, Co-Cr alloys, MTT eluate test

Uporaba računalniških tehnologij in sistemov je odprla pot do pomembnega napredka konvencionalnega modeliranja in izdelave snemljivih zobnih nadomestkov. Težišče te raziskave je približek, ki kombinira obratno inženirstvo kot tehniko modeliranja in hitre izdelave z laserskim taljenjem kot izdelavno tehnologijo s posebnim poudarkom na izbiri materiala za snemljive dele zobovja. V članku so predstavljeni rezultati analize biokompatibilnosti zobne zlitine F75 Co-Cr z MTT-preizkusom eluiranja.

Ključne besede: obratno inženirstvo, hitra izdelava, selektivno lasersko taljenje, snemljivi deli zobovja, biokompatibilnost, Co-Cr zlitina, MTT-preizkus eluiranja

1 INTRODUCTION

Dental prosthetics (also known as prosthodontics) has always maintained close relationships with engineering disciplines, relying mostly on production engineering. The rapid development of computer-aided (CA) technologies, which completely transformed production engineering, also left an indelible mark on dental prosthetics. Striving towards its primary goal – *primum non nocere* (in English, 'Above all, do not harm!'), the area of dental prosthetics has introduced numerous novel technologies and methods that allow the manufacture of precision, custom-made, optimal dental replacements. During the past decade, efforts have been concentrated towards an advancement of the modelling and manufacture of dental replacements by introducing modern CA systems, state-of-the-art materials and machining technologies, as opposed to the traditional way of manual manufacture, which is prone to numerous subjective errors.[1] Amongst modern CA systems that have found broad application in this area, the most widely used are 3D-digitization systems, CAD and reverse engineering (RE), CAE, CAM, rapid manufacture (RM) (or additive manufacture that become the adopted term in the sector) and rapid prototyping (RP). The development and implementation of such technologies and systems have paved the way towards a significant advancement in conventional modelling, manufacture and the inspection of dental replacements.[1–6]

Different dental substrates may have special requirements related to their modelling and manufacture. Removable partial dentures (RPDs) represent a special type of denture, designed for partially edentulous patients who cannot have a fixed partial denture, i.e., a bridge. This type of prosthesis is referred to as removable, as patients can remove and reinsert it when required without professional help. Traditionally, RPD frameworks are manufactured through the so-called lost-wax technique, where a wax pattern burns out in a preheating unit followed by an immediate casting of the melted alloy. Though in use for decades, this technique is sensitive and prone to human-induced errors.[1,6]

In this research the focus is on an approach that combines RE as a modelling technique, and RM i.e., selective laser melting (SLM), as the manufacturing technology, with a special emphasis on material selection in the fabrication of RPD frameworks.

The virtual design of dental restorations today almost always requires the application of RE modelling. RE, a modelling technique widely used in different engineering fields, has been increasingly applied in the field of prosthodontics during the past several years, mainly because of the rapid development of dental 3D digitization systems and the corresponding modelling software[2,3]. RM is no exception and its results in the field of prosthodontics significantly depend on RE modelling. Realizing the benefits of RE and RM, recently there have been several research works related to the possible use of these technologies in the design and manufacturing of RPD frameworks.[1,3,7–9]

SLM, an RM technique, is based on a layer-wise material addition that allows the generation of complex 3D parts by selectively melting successive layers of metal alloy powder on top of each other. As presented by Eyers and Dotchev in[5] and Vandenbroucke and Kruth in,[10] SLM is very suitable for dental and medical applications, due to the complex geometry of the produced parts. A pilot study presented by Williams et al.[9] showed that an RPD framework produced by SLM techniques was comparable to conventional frameworks in terms of accuracy, quality of fit and function. However, this conclusion is based on a single study and much work needs to be completed before a final conclusion can be reached.

A very important issue in prosthodontics is the material used, i.e., the alloy.[10–13] This issue is even more important in RPD framework manufacturing as the application is limited to cobalt-chromium (Co-Cr) alloys due to the low rigidity of titanium (Ti) alloys, as described by Aridome et al. in[14], and the unfavourable characteristics of gold (Au) alloys, that are otherwise widely used in the fabrication of other dental restorations. The application of SLM in the manufacturing of RPD, brings some additional material requirements related to mechanical properties[10,14] and biocompatibility.[15,16] Although a dental prosthesis fabricated by SLM showed the potential of SLM as manufacturing technique, there are still very few reports of SLM application in the manufacture of RPDs from Co-Cr alloys. Though Co-Cr alloys have been used in dentistry for years, little is known about the influence of the SLM process on the alloys' biocompatibility and mechanical behaviour.

This paper, with regards to the above discussion, focuses on the applicability and possible benefits of the application of RE and RM techniques in the design and manufacture of RPD frameworks. Moreover, special attention in this research has focused on the material properties related to SLM application in the manufacture of RPD frameworks. The paper also presents the results of an analysis of biocompatibility conducted with an MTT eluate test of the F75 Co-Cr dental alloy.

2 RE/RM IN DESIGN AND MANUFACTURING OF RPD FRAMEWORKS

The RE and RM combination has been recognized as fully compatible and very effective. Potential advantages include: a decrease of manufacturing time, an inherent repeatability, and the achievement of high quality through eliminating operator variations that are usually connected with the conventional (manual) design and manufacture of an RPD (**Figure 1**).

The application of RM, i.e., SLM in an RPD framework fabrication implicates the workflow presented in **Figure 2**. This workflow clearly presents three main phases:

1. RE modelling (of the patient's cast),
2. virtual design of the RPD framework,
3. RM of RPD framework.

The first two phases are frequently unified and denominated in references as the CAD phase, while the third is often described as the CAM phase.[1,3,5,7–10]

The RE phase starts with the 3D digitization of the patient's cast. This usually includes acquiring a dental

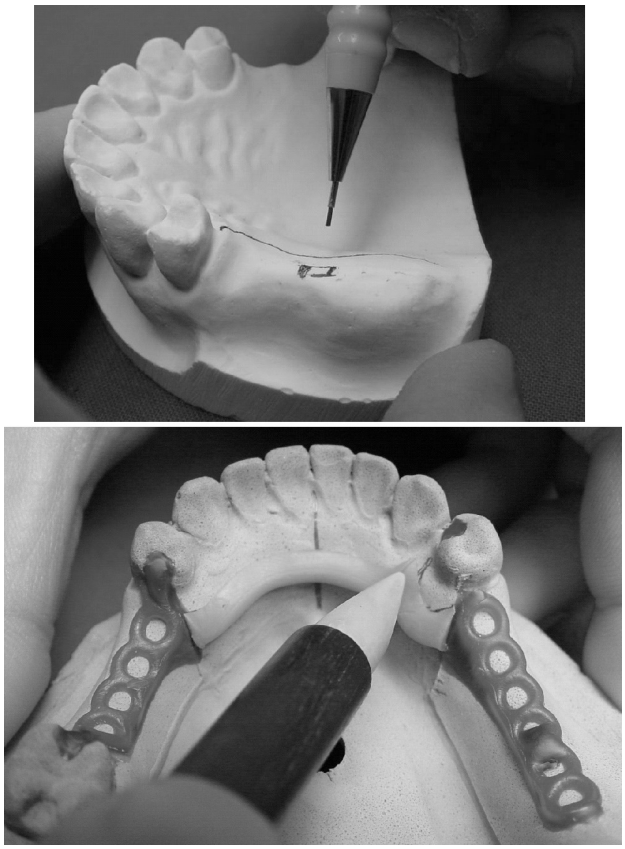

Figure 1: Conventional (manual) design of RPD
Slika 1: Konvencionalno (ročno) načrtovanje RPD

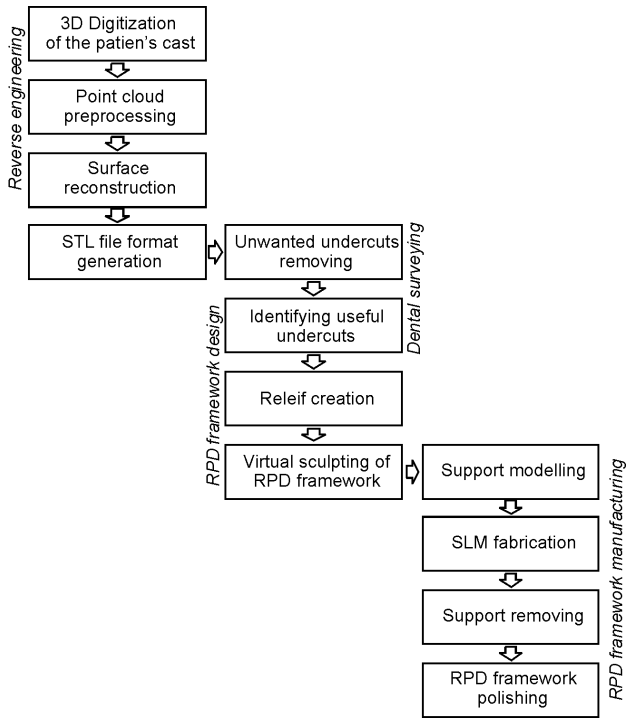

Figure 2: The typical workflow of an RE/RM approach in RPD framework fabrication
Slika 2: Značilen tok RE/RM približka v okviru RPD-izdelave

impression and extra oral scanning of a gypsum model produced from the impression (**Figure 1**).[1,6] However, the process could replace the need for an impression by the application of intra-oral scanning[2] or CT.[6,17,18] The point cloud obtained almost always needs to be pre-processed in order to insure a high-quality surface reconstruction, i.e., a credible CAD model. Regarding the applied 3D digitization technique/system, the pre-processing step can include different processes, such as noise filtering, data reduction, segmentation of the point cloud parts or assembling.[19] The obtained surface model (the reference model or the "buck") is usually exported to an STL file format based on triangular polygons, which is a suitable format for virtual dental surveying and virtual sculpting environments.[8]

The initial step of the RPD framework-design phase is the virtual dental surveying that is needed to identify areas of undercut present on the CAD model of the patient's teeth and soft tissues (**Figure 3a**). Unwanted undercuts have to be removed in order to ensure an unobstructed withdrawal of the RPD from the patient's orifice.[1,8] However, there are some useful undercuts that need to be retained and their identification and measurement are important as they serve as secure holders of flexible clasps that provide reliable retention.[1] The next step is the modelling of reliefs – the parts of a model that prevent the RPD framework from resting on the surfaces of soft tissues (**Figure 3b**).[1] After the reliefs have been added, virtual sculpting of the RPD framework elements (1-occlusal rest, 2-polymeric retention frame, 3-lingual bar, 4-acrylic line, 5-non-active clasp, 6-guide plate) may begin (**Figure 3c**).

The virtual sculpting stage is based on software tools enabling analogous work to that used in physical sculpting. This is enabled through a haptic interface that incorporates positioning in 3D space and allows rotation and translation in all axes, transferring hand movements into the virtual environment (**Figure 4**). Moreover, haptic systems enable the operator to feel contact with the object that is the subject of the modelling. Besides this usage of the haptic arm in a freehand manner, the process of virtual sculpting also allows the application of standard CAD parametric features based on sizes, shapes, relations and positions.[1,8]

Once the CAD model of the RPD framework is obtained, it can be passed to the SLM after its preparation in appropriate software. This preparation primarily involves the creation of an adequate support (**Figure 5**) that acts as a firm base for the RPD framework to be built onto and which also conducts heat away during the sintering processes. As the supports need to be removed after the solidification of the part, it is important to avoid placing them on the fitting surface of the RPD.[8]

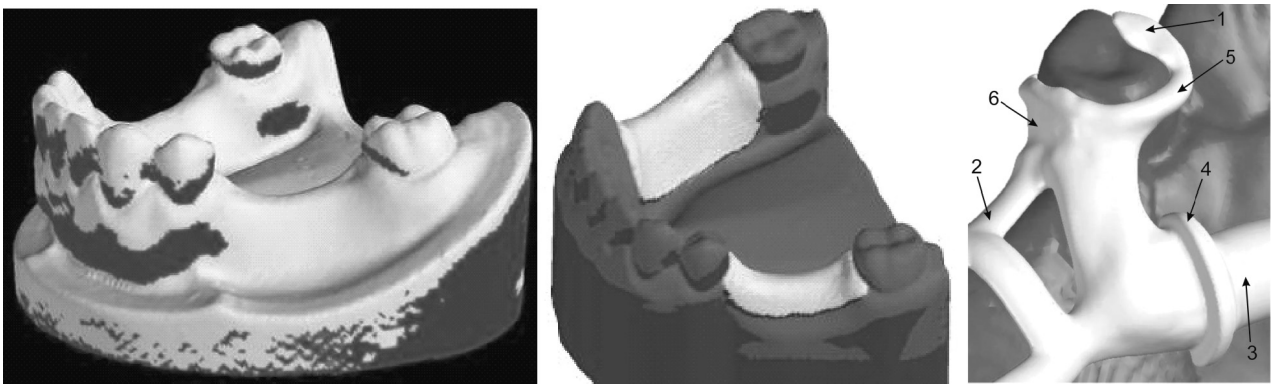

Figure 3: RPD framework design phase – the main steps: a) Identification of undercuts, b) Relief modelling, c) RPD framework elements
Slika 3: Okvir faze RPD-načrtovanja – glavni koraki: a) identifikacija spodnjih prerezov, b) modeliranje reliefa, c) elementi okvirja RPD

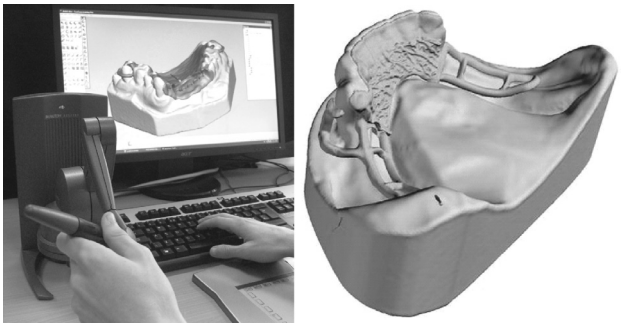

Figure 4: Virtual design of RPD frameworks
Slika 4: Virtualno načrtovanje podlag RPD

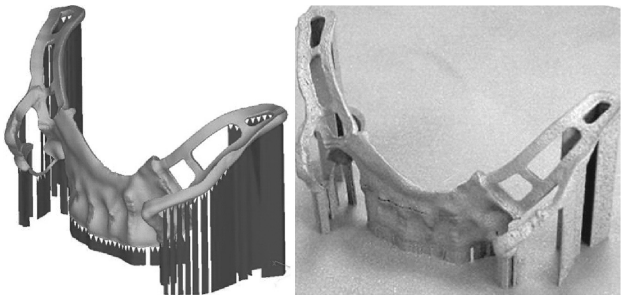

Figure 5: Support in SLM manufacturing of RPD frameworks
Slika 5: Podlaga pri SLM-izdelavi RPD-podlage

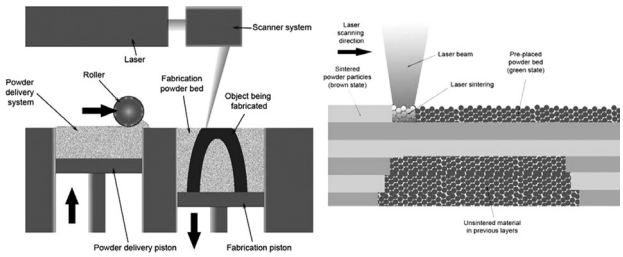

Figure 6: Principle of the SLM process
Slika 6: Princip SLM-procesa

During the SLM process, powdered material is spread by a hopper and wiper mechanism. To accommodate a new layer of the material, the build platform has to move down by one layer thickness. Subsequently, the powder is deposited incrementally on top of each solidified layer, and the process is repeated (**Figure 6**).

The manufactured RPD framework needs to be finished and polished and this is performed using traditional dental laboratory procedures.[8,9] Finally, the finished RPD framework has to be evaluated on the patient's cast. This is performed by a prosthodontic expert, who will assess the quality of fit according to recommended practice.[8]

3 BIOCOMPATIBILITY TESTING OF THE SLM Co-Cr ALLOY F75 (BY MTT ELUATE TEST)

One of very important issues that need to be investigated is the biocompatibility of the specific Co-Cr alloy used for SLM, since – to the best of authors' knowledge – there are no known published conclusions about biocompatibility. Though the basic chemical elements in alloys used for SLM (F75) and conventional investment casting, also known as the lost-wax technique (Remanium 380+) generally match, they differ by a small percentage due to the specific requirements needed by the process (**Table 1**). However, it has been shown that a modification in composition and pre-treatment can influence the cytotoxicity of an alloy on a large scale.[20,21]

The previous discussion motivated the authors to start research related to the biocompatibility testing of the specific Co-Cr alloy used for SLM.

In biocompatibility evaluations of alloys, cell culture studies are the usual starting point as they enable an investigation of the toxicity in a simplified system that minimizes the effect of confounding variables.[21] Thus, within this study a murine fibroblast cell line (L929) was used in accordance with the requirements of the ISO standard 7405 (ISO 2008).[15] The cytotoxicity determination of the Co–Cr alloy used for the fabrication of an SLM RPD framework was based on the MTT eluate test method.

3.1 Sample preparation

The investigation included the fabrication of two groups of test samples – the first from the SLM and the second from conventional investment casting (**Figure 7**).

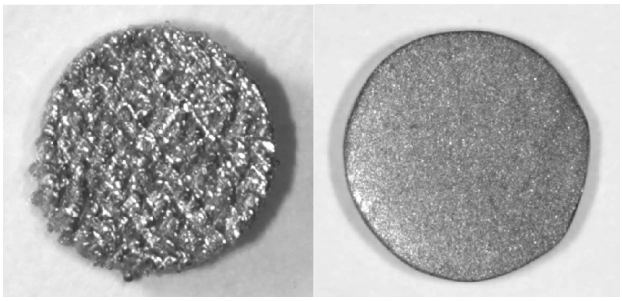

Figure 7: Test samples obtained by SLM (left) and by vacuum casting (right)
Slika 7: Preizkušanci SLM (levo) in vakuumskega taljenja (desno)

Table 1: Composition of the Remanium GM 380+ and Sandvik Osprey F75 alloys in mass fractions, *w*/%
Tabela 1: Sestave zlitin Remanium GM 380+ in Sandvik Osprey F75 v masnih deležih, *w*/%

Ingredients, *w*/%	Co	Cr	Mo	Si	Mn	N	C	Fe	Ni
Remanium GM 380+	64.6	29	4.5	<1	<1	<1	<1	/	/
Sandvik Osprey F75	Balance	27–30	5–7	<1	<1	/	<0.35	<0.75	<0.5

Figure 8: SLM system – Realiser MTT-Group, UK
Slika 8: SLM-sistem Realiser MTT-grupe, VB

The first group of samples was manufactured by the SLM system *Realiser MTT-Group* (**Figure 8**) and the software was *Magics* 9.5, *Materialise NV.* The Co-Cr layer thickness was 0.075 mm, the laser's maximum scan speed was 300 mm/s, and the beam diameter was 0.150–0.200 mm. The F75 Co-Cr alloy (Sandvik Osprey Ltd., UK) used in this study is a spherical powder with a maximum particle size of 0.045 mm (particle size range 0.005–0.045, mean size approx. 0.030 mm). After the SLM process was completed and specimens' supports were removed, the discs were finished by polishing according to the usual dental laboratory procedure.

The second group of samples – four disc specimens with a radius of 5 mm and thickness of 1 mm – were fabricated from a non-precious Co-Cr alloy *Remanium GM380+* (Dentaurum, Ispringen, Germany) containing no Ni, Be or Fe, and widely used for RPD framework casting. The discs were obtained from wax patterns, invested in *Rema dynamic* (Dentaurum, Ispringen, Germany) investment, and vacuum casted in a *Nautilus CC* (Bego, Bremen, Germany) system (**Figure 9**). After casting, the discs were divested and blasted with 100-µm aluminium oxide particles, and then polished with silicon carbide papers in the sequence 320, 400, 600, 1200, 1500 and 2000. The final polishing was performed using oxide pastes.

Figure 9: Nautilus CC system for vacuum casting
Slika 9: Nautilusov sistem za vakuumsko taljenje

3.2 MTT eluate testing

The test performed was the MTT (tetrazolium colorimetric assay) eluate test, widely used for the quantitative evaluation of cell proliferation and survival.[16,20] The assay depends on the cleavage of tetrazolium salt 3-[4,5–dimethylthiazol–2–yl]-2,5-diphenyltetrazoliumbromide (MTT) to purple formazan crystals by mitochondrial dehydrogenases in viable cells.[21] The assay detects living but not dead cells and the rate of MTT reduction to formazan products. It is also dependent on the degree of cell activation. Therefore, the assay is suitable for measuring cytotoxicity, proliferation and activation.[16]

Eluates of both the CM and SLM disc samples were prepared. The samples were extracted with 10 mL of Dulbecco's modified Eagle's medium (DMEM) without serum for 48 h. The extraction was performed in an atmosphere of 5 % CO_2 and 95 % air at 37 °C. All the extracts were filtered for sterilization and used as a culture medium for L-929 cells. MTT assays with L-929 cells treated with different eluates were completed after 48 h of incubation. The experiment was repeated twice (thus eight CM and eight SLM samples were tested in two independent experiments).

The cells (L929) were cultured in Petri dishes containing eluates of the CM or SLM alloy discs (**Figure 10**). They were incubated for (3, 5, 7 and 9) d at 37 °C in 95 % air and 5 % CO_2. The control samples contained a regular culture medium. After the incubation, the cells were detached using enzymatic digestion and counted in a counting chamber using trypan blue. Briefly, 5×10^3 cells were seeded to a 96-well plate and cultured for 48 h at 37 °C in 95 % air and 5 % CO_2.

After the incubation period, 20 µL of MTT solution were added to each well and incubated for another 3 h. The purple formazan product was dissolved in 100 µL of

Figure 10: MTT eluate testing
Slika 10: MTT preizkus eluiranja

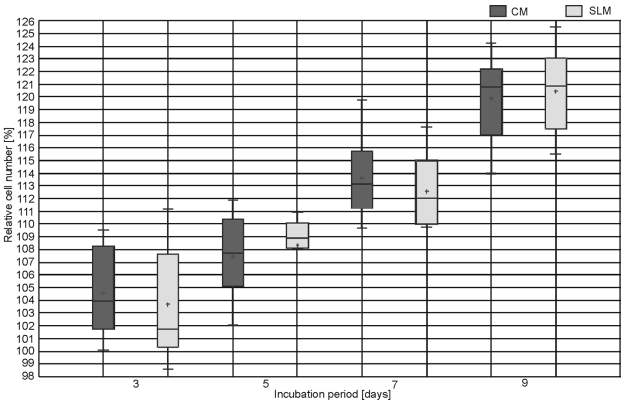

Figure 11: MTT test results for CM and SLM alloy after different incubation periods – graphical review of the confidence intervals
Slika 11: Rezultati MTT-preizkusov CM- in SLM-zlitine po različnih dobah inkubacije – grafična predstavitev intervalov zanesljivosti

0.04-M hydrochloric acid in isopropanol. The reduced MTT was then measured spectrophotometrically in a dual-beam, microtiter plate reader *Multiscan MCC/340* at 540 nm with a 690-nm reference. The optical density values of the experimental groups were divided by the control and expressed as a percentage of the control.

3.3 Statistical results of the MTT eluate testing

A statistical analysis was carried out using the Statgraphics Centurion program. The data were evaluated statistically using the Student's t-test and a value of $p < 0.05$ was considered to be statistically significant. The results of the MTT eluate testing of the disc samples that were taken after an extraction period of (3, 5, 7 and 9) d are listed in **Table 2**, and graphically presented in **Figure 11**.

Of particular interest was the confidence interval evaluation for the difference between the means. Since all four intervals contain the value 0, there is no statistically significant difference between the means of the CM and SLM samples at the 95 % confidence level. Furthermore, a t-test was used for testing a specific hypothesis about the difference between the means of the populations from which the two samples come. In this case, the test was constructed to determine whether the difference between the two means equals 0.0 (null hypothesis: mean1 = mean2) versus the alternative hypothesis that the difference does not equal 0.0 (mean1 ≠ mean2). Since the computed P-values are not less than 0.05 in all four cases, the null hypothesis cannot be rejected.

4 DISCUSSION

Publications investigating the corrosion of dental alloys give information firstly about the release of potentially harmful ions from the dental device. Cell-culture tests give an insight into whether the released ions in a cell-culture medium imitating the oral environment could have a negative effect on the biological system. The results of the MTT eluate testing with the SLM samples do not show significant cellular damage potential. Statistical analyses carried out showed that the alloys did not release harmful material that could cause acute effects against L929 cells under the given experimental conditions. Furthermore, the MTT test showed no permanent damage to the cell function. The viability was much higher than 50 % after all the extraction periods for both the CM and SLM alloy. Replication during an extended contact period with

Table 2: Results of statistical analysis of MTT eluate testing of CM and SLM disc samples
Tabela 2: Rezultati statistične analize MTT-preizkusa eluiranja CM- in SLM-vzorcev

	Period of cell incubation in d	*3*		*5*		*7*		*9*	
Descriptive statistics	Technology	CM	SLM	CM	SLM	CM	SLM	CM	SLM
	Count	8	8	8	8	8	8	8	8
	Average % of relative cell No.	104.655	103.639	107.604	108.364	113.73	112.694	119.778	120.525
	Standard deviation	3.62557	4.56325	3.43234	2.94701	3.34183	2.92113	3.45744	3.58149
	Coeff. of variation,%	3.4643	4.40303	3.18979	2.71955	2.93839	2.5921	2.88655	2.97158
	Minimum	100.05	98.64	102.04	101.54	109.78	109.78	114.01	115.61
	Maximum	109.45	111.23	111.97	111.02	119.74	117.64	124.31	125.64
Comparison of means	95 % CIM*	104.655 +/– 3.03106	103.639 +/– 3.81498	107.604 +/– 2.86951	108.364 +/– 2.46377	113.73 +/– 2.79385	112.694 +/– 2.44213	119.778 +/– 2.8905	120.525 +/– 2.99421
	95 % CIDM**	1.01625 +/– 4.41952		–0.76 +/– 3.43048		1.03625 +/– 3.36576		–0.7475 +/– 3.77485	
	t	0.493186		–0.475165		0.660339		–0.424715	
	P-value	0.629527		0.641997		0.519754		0.6775	

* CIM – Confidence Interval for Means, ** CIDM – Confidence Interval for the difference between the Means assuming equal variances

potential toxic substances, however, showed good biocompatible properties of the chosen SLM alloy. Additionally, the negative effect decreased with time for both the examined substances. Therefore, both alloys can be rated as non-cytotoxic.

It has, however, to be noted that SLM, as a complex thermo-physical process, produces a variation in the final product depending on several factors, such as the material, laser, scan and parameters of the environment used.[10] Changeable variables include: laser power, layer thickness, scan speed and hatch spacing. With the current settings, as can be seen from the study, the final product complies with the required biocompatibility standards, showing no potentially harmful effect. However, those values can be adjusted accordingly, optimizing some aspects that can have a negative effect on the materials' properties, such as porosity. For example, for a low energy input, successive scan tracks may not be fully molten, leaving large pores along the scan lines, as seen in the mentioned study. If so, a combination other parameters might change the surface properties, which might also result in changes in the ion release and therefore require separate biocompatibility studies. This study has, however, showed that the initial screening gave positive results and the F75 SLM alloy can be subjected to further tests.

The study concerning the ion release from the cast and SLM samples, presented in,[10] revealed the more favourable behaviour of the SLM specimens. The main ion detected was cobalt, since the corrosion of the alloy is determined by the main component, and the passivating effect of chromium. The SLM test specimens showed lower emissions than the cast specimens, probably because the laser-melted material is more homogeneous, contains fewer pores and has a finer microstructure. This also highlights the importance of the finishing procedure, which still has to be conducted manually.

Another physical factor that might influence the biocompatibility 'in vivo' is the surface roughness[21]. The changes in this parameter can be explained by the so-called stair effect, inherent to the layer-wise production of SLM. In the oral environment, this might increase plaque retention, leading to the formation of acidic micro-fields that might change the metallic ion release unfavourably. This effect can be reduced by decreasing the layer thickness or by increasing the sloping angle[10].

5 CONCLUSION

This paper shows that a complete RE/RM procedure for RPD framework fabrication should bring significant advantages both to practitioners and patients. Special attention was focused on the biocompatibility analysis of the dental alloys used with the SLM. Moreover, the paper presents a biocompatibility evaluation of the F75 SLM dental alloy using the MTT eluate test. On the basis of the obtained results, within the limitations of the study, it can be concluded that the RE/RM procedure showed a promising potential in RPD framework fabrication, as well as that the F75 alloy used for SLM manufacturing showed positive initial results regarding its biocompatibility. However, further studies, including in vivo tests and tests of mechanical properties, have to be conducted before the final release of the alloy for mass production.

6 REFERENCES

[1] D. Eggbeer, R. Bibb, R. Williams, Proc. Inst. Mech. Eng. Part H-J. Eng. Med., 219 (**2005**) 3, 195–202

[2] I. Budak, B. Trifkovic, T. Puskar, M. Hadzistevic, D. Vukelic, J. Hodolic, Application and accuracy of 3D-digitization systems in the field of dentistry, Proceedings of the 6th International Working Conference Total Quality Management – Advanced and Intelligent Approaches, 2011, 409–414

[3] M. Germani, R. Raffaeli, A. Mazzoli, Rapid Prototyping J., 16 (**2010**) 5, 345–355

[4] A. Cernescu, N. Faur, C. Bortun, M. Hluscu, Eng. Fail. Anal., 18 (**2011**) 5, 1253–1261

[5] D. Eyers, K. Dotchev, Assem. Autom., 30 (**2010**) 1, 39–46

[6] A. Azari, S. Nikzad, Rapid Prototyping J., 15 (**2009**) 3, 216–225

[7] R. Bibb, D. Eggbeer, R. J. Williams, Rapid Prototyping J., 12 (**2006**) 2, 95–99

[8] R. J. Williams, R. Bibb, D. Eggbeer, J. Collis, J. Prosthet. Dent., 96 (**2006**) 2, 96–99

[9] R. J. Williams, R. Bibb, D. Eggbeer, Pract. Proced. Aesthet. Dent., 20 (**2008**) 6, 349–351

[10] B. Vandenbroucke, J. P. Kruth, Rapid Prototyping J., 13 (**2007**) 4, 196–203

[11] R. Rudolf, T. Zupancic Hartner, L. Kosec, A. Todorovic, B. Kosec, I. Anzel, Metalurgija, 47 (**2008**) 4, 317–323

[12] K. Raic, R. Rudolf, A. Todorovic, D. Stamenkovic, I. Anzel, Mater. Tehnol., 44 (**2010**) 2, 59–66

[13] A. Todorovic, K. Radovic, A. Grbovic, R. Rudolf, I. Maksimovic, D. Stamenkovic, Mater. Tehnol., 44 (**2010**) 1, 41–47

[14] K. Aridome, M. Yamazaki, K. Baba, T. Ohyama, J. Prosthet. Dent., 93 (**2005**) 3, 267–273

[15] ISO 7405:2008, Dentistry – Evaluation of biocompatibility of medical devices used in dentistry.

[16] ISO 10993-5:2009, Biological evaluation of medical devices – Part 5: Tests for in vitro cytotoxicity.

[17] R. Bibb, D. Eggbeer, P. Evans, A. Bocca, A. Sugar, Rapid Prototyping J., 15 (**2009**) 5, 346–354

[18] R. Bibb, J. Winder, Radiography, 16 (**2010**) 1, 78–83

[19] I. Budak, M. Sokovic, J. Kopac, J. Hodolic, Strojniski Vestn. – J. Mech. Eng., 55 (**2009**) 12, 755–765

[20] T. Mosmann, J. Immunol. Methods, 65 (**1983**) 1–2, 55–63

[21] A. Naji, M. F. Harmand, J. Biomed. Mater. Res., 24 (**1990**) 7, 861–871

UDK 621.357:591.18
Original scientific article/Izvirni znanstveni članek

ISSN 1580-2949
MTAEC9, 46(2)131(2012)

INFLUENCE OF TRANSIENT RESPONSE OF PLATINUM ELECTRODE ON NEURAL SIGNALS DURING STIMULATION OF ISOLATED SWINISH LEFT VAGUS NERVE

VPLIV PREHODNEGA ZNAČAJA PLATINASTE ELEKTRODE NA ŽIVČNI SIGNAL MED STIMULACIJO IZOLIRANEGA ŽIVCA VAGUSA SVINJE

Polona Pečlin[1], Franci Vode[2], Andraž Mehle[1], Igor Grešovnik[3], Janez Rozman[1]

[1]ITIS, d. o. o., Ljubljana, Centre for implantable technology and sensors, Lepi pot 11, 1000 Ljubljana, Slovenia
[2]Institute of metals and technology, Lepi pot 11, 1000 Ljubljana, Slovenia
[3]Faculty of Natural Sciences and Mathematics, University of Maribor, Koroška cesta 160, 2000 Maribor, Slovenia
polona.peclin@gmail.com

Prejem rokopisa – received: 2011-07-29; sprejem za objavo – accepted for publication: 2011-12-16

The main aim of the work was to measure transient response characteristics of interface between platinum stimulating electrodes and isolated swinish left cervical vagus nerve (segment), when electrical stimulating pulses are applied to preselected locations along the segment and elicited neural signals, also described as compound action potentials (CAPs), are recorded from particular compartments of the nerve.
The stimulating system was manufactured as a silicone self-coiling spiral cuff (cuff) with embedded matrix of ninety-nine rectangular electrodes (0.5 mm in width and 2mm in length), made of 45 μm thick annealed platinum ribbon (99.99 % purity), and a geometric surface of 1 mm^2.
For electrical stimulation, a current quasitrapezoidal, asymmetric and biphasic pulses with frequency of 1 Hz, were used. To test an influence of stimulating pulses having different parameters and waveforms on elicited CAPs, various degree of imbalance between an electric charge (charge) injected in cathodic phase as well as charge injected in anodic phase of a biphasic stimulating pulse, were deployed and compared.
To identify the differences in elicited CAPs however, an integral of the CAP cathodic phase as well as integral of the CAP anodic phase of stimulating pulse, were calculated and compared.
Results showed a strong component superimposed in the CAPs, considered as an ensemble artefact which greatly obscured the components of the CAPs, and various components did overlap.
Results also showed that stimulating pulses, having preset certain degree of imbalance between charge injected in cathodic and charge injected in anodic phase, elicited a slight change in a positive waveform deflection of CAP manifested under a cathodic phase as well as slight change in a negative waveform deflection of CAP manifested under an anodic phase. Furthermore, slight difference was observed in a CAP, expressed as integral cathodic positive deflection and as integral anodic negative deflection. However, it could be concluded that measured CAPs are not greatly influenced by the imbalance between a charge injected in cathodic and anodic phase of quasitrapezoidal, asymmetric and biphasic stimulating pulses.

Keywords: electrical stimulation, platinum electrodes, left vagus nerve, electrochemistry, electrical charge

Glavni namen dela je bil izmeriti prehodni značaj na prehodu med platinasto stimulacijsko elektrodo in delom izoliranega levega vratnega prašičjega živca vagusa (segment) med dovajanjem stimulacijskih impulzov na izbrana mesta vzdolž živca in hkratnim merjenjem živčnega signala, imenovanega sestavljeni akcijski potencial (CAP) na določenih predelih živca.
Stimulacijski sistem je bil izdelan v obliki silikonske spiralne objemke (cuff) z vdelano matriko devetindevetdestih pravokotnih elektrod (širina 0,5 mm in dolžina 2 mm), izdelanih iz žarjenega platinastega traku (čistost 99,99 %) in geometrijsko površino 1 mm^2.
Za električno stimulacijo so bili uporabljeni tokovni kvazitrapezni, asimetrični in izmenični impulzi frekvence 1 Hz.
Za preizkušanje vpliva stimulacijskih impulzov z različnimi parametri in oblikami na izzvani CAP je bila med katodno in anodno vneseni električni naboj uvedena določena stopnja neuravnoteženosti. Katodno in anodno vnesena naboja sta bila za izbrane impulze med seboj primerjana.
S ciljem ugotavljanja razlik v izzvanem CAP-u pa sta bila izračunana in med seboj primerjana integrala tako CAP-a, prisotnega pod katodno fazo, kot CAP-a, prisotnega pod anodno fazo zgoraj omenjenega stimulacijskega impulza.
Rezultati so pokazali močno komponento, položeno na CAP, ki je sestavljena motnja in ki znatno zamegli ter prekrije posamezne komponente CAP-a.
Rezultati so tudi pokazali, da zgoraj omenjeni stimulacijski impulzi s prednastavljeno določeno stopnjo neravnotežja med nabojem, vnesenim v katodni fazi, ter nabojem, vnesenim v anodni fazi, izzovejo majhne spremembe pri pozitivnem odklonu CAP-a, prisotnega pod katodno fazo, kakor tudi majhne spremembe v negativnem odklonu CAP-a, prisotnega pod anodno fazo.
Nadalje so bile opažene tudi majhne razlike v CAP-ih, izražene kot integral pod katodnim pozitivnim odklonom in kot integral pod anodnim negativnim odklonom.
Končno je mogoče skleniti, da neravnotežje med katodno in anodno vnesenim nabojem ni znatno vplivalo na izmerjene CAP-e.

Ključne besede: električna stimulacija, platinaste elektrode, levi živec vagus, elektrokemija, električni naboj

1 INTRODUCTION

In the past few decades, vagus nerve stimulation (VNS) has been the subject of considerable research with the goal to be used as method to treat a number of nervous system disorders, neuropsychiatric disorders, eating disorders, sleep disorders, cardiac disorders, endocrine disorders, and pain, among others.[1–3] In practically all studies in humans, VNS refers to non-selective stimulation of the cranial nerve X, known as the left vagus nerve, using specific electrode devices which development was based on different models provided by various research groups.The frequent result of non-selective stimulation however, is the occurrence of undesirable side effects.[4–6]

Peripheral nerve stimulation however, often requires the development of electrode systems that stimulate selectively a certain group of fibers in a nerve trunk without excitation of other nerve fibers.

However, the long-term use of such electrical stimulation requires that it is applied selectively and without tissue injury. Tissue injury and the corrosion of the stimulating electrode are both associated with high charge density stimulation.[7,8] For this reason, long-term stimulation of the nervous tissue requires the absence of irreversible electrochemical reactions such as electrolysis of water, evolution of chlorine gas or formation of metal oxides.

For a given electrode, there is a limit to the quantity of charge that can be injected in either anodic or cathodic direction with reversible surface processes. This limit depends upon the parameters of the stimulating waveform, the size of the electrode, and its geometry.[9–11] Namely, at the electrode-electrolyte interface there are capacitive mechanisms (charging and discharging of the electrode double layer, no electron transfer) and Faradaic mechanisms (chemical oxidation or reduction, reversible or irreversible).[12–14] If the voltage across the electrode-tissue interface is kept within certain limits, then chemical reactions can be avoided, and all charge transfer will occur by the charging and discharging of the double-layer capacitance. However, in many instances, the electrode capacitance is not sufficient to store the charge necessary for the desired excitation without the electrode voltage reaching levels where reactions could occur.[11,15]

The principal approach to control the interface voltage has been the use of charge-balanced biphasic stimuli that have two phases that contain equal and opposite charge. However, even with charge-balanced stimulating pulses it is possible that the interface voltage may reach levels where electrochemical reactions can occur.[16,17]

Platinum is among commonly used stimulating electrode materials that are capable of supplying high-density electrical charge to effectively activate neural tissue.[11] However, stimulation with a high charge density, pH shifts causing irreversible changes in tissue proteins, metallic dissolution products, gross hydrogen and oxygen gas bubbles, and oxidized organic and inorganic species, could occur[18]. Therefore, some platinum toxicity interactions in the body, actually not conclusively proven in human, could be expected. Namely, tests on laboratory mammals showed that soluble platinum compounds are much more toxic than insoluble ones while solid platinum wire or foil is considered to be biologically inert. Complexes with other dangerous metals and chemicals in the human body such as platinum salts, can cause several health effects, such as: DNA alterations, cancer, allergic reactions of the skin and the mucous membrane, damage to organs, such as intestines, kidneys and bone marrow and hearing damage.[19,20]

In the area of Functional Electrical Stimulation (FES) cuffs have been used in neuroprosthetic applications as stimulation electrodes as well as electrodes for the recording of the electroneurogram (ENG) for more than 35 years.[21] Twenty years later, this method was used for the first time in a chronic implantation in human subjects for the recording of the ENG for the use of feedback signal in a system for the correction of foot-drop.[22] While the time was passing, theoretical considerations and different models have stimulated and accompanied the development of cuffs[23,24] promoting them as the most successful biomedical electrodes for selective stimulation of different superficial regions of a peripheral nerve.[25,26] However, the long-term effectiveness and potential harmful effects of the cuffs on neural tissue in various applications is still not completely defined.

The present study addressed the mechanisms that could be involved in the modulation of recruitment properties of nerve fibres, and thus, in the modulation of CAP induced by both, the cathodic and anodic charge injected during selective stimulation of the isolated vagus nerve with developed cuffs and imbalanced quasitrapezoidal stimulating pulses having different parameters.

2 METHODS

The cuff was designed taking into consideration the results of histological examination of the swinish left vagus nerve, the model of selective electrical stimulation of particular superficial regions of the nerve and the model of selective stimulation of nerve fibers with different diameters.[27–29] The cuff and physical dimensions of the cuff were actually devised so to induce as low as possible radial pressure when installed on the nerve. Therefore, minimum mechanically induced nerve damage might be expected.

The cuff was manufactured by bonding two 0.05 mm thick silicone sheets together (Medical Grade Silicone Sheeting, Non-Reinforced, 6" × 8" × 0.002" Matt, SH-20001-002, BioPlexus Corporation, 1547 Los Ange-

les Avenue #107, Ventura, California 93004. USA.). At room temperature one sheet, stretched and fixed in that position, was covered with a layer of adhesive (RTV Adhesive, Acetoxy, Implant Grade, Part Number 40064, Applied Silicone Corporation, 270 Quail Court, Santa Paula, CA 93060, USA). A second un-stretched sheet was placed on top of the adhesive and the composite was compressed to a thickness of 0.15 mm until the whole curing process was completed. In normal laboratory conditions, the curing process was completed within 24 h. When released, the composite curled into a spiral tube as the stretched sheet contracted to its natural length.[26,27] As a result, the composite is soft self-sizing and flexible self-coiling spiral tube. When instaled on the nerve, the cuff wraps around the nerve and, because of its self-coiling property, adjusts automatically its inner diameter to the size of the nerve.

Ninety-nine rectangular electrodes with a width of 0.5 mm and length of 2 mm (geometric surface g = 1 mm^2, real surface area ≈ 1.4 mm[13], made of 45 μm thick annealed platinum ribbon (99.99 % purity), were then under microscope mechanically mounted on the third silicone sheet with a thickness of 0.05 mm. They were arranged in nine parallel groups each containing eleven electrodes, thus forming a matrix of ninety-nine electrodes.[28,29]

Afterwards, the electrodes were connected individually to the high frequency miniature and highly flexible isolated, multi-stranded and enameled finest copper wires (CU-lackdraht DIN 46 435, Φ 12 × 0.04 mm, Elektrisola, Reichshof-Eckenhagen, Germany). For experimental purpose, the junctions between platinum electrodes and multi-stranded wires were implemented using a special tin alloy. The multi-stranded wire was used, since it has the same average fatigue life as their individual constituent strands but the variance of that life is smaller. To maximize service life, it was concluded that wire strands should be manufactured at the smallest diameter possible (without introducing structural flaws). It was assumed that multi-stranded wires to the stimulating electrodes if routed carefully would play a minimal role on rotation of the cuff around the logitudinal axis and on translation in a longitudinal direction. Therefore, to ensure that the multi-stranded wires would not be the possible source of mechanical damage to the nerve, special care should be taken during instalation to route them so that enough slack would be left to avoid mechanical tensions being transmitted to the cuff. Afterwards, a self-coiling tube was mechanically opened and the silicone sheet with the matrix of electrodes was adhered onto an inner side of the tube.

In fabricted cuff, when the matrix was spirally rolled up, the longitudinal separation between nine parallel groups of electrodes was 2 mm and the circumferential separation between electrodes was 0.5 mm.

The dimensions of the nerve considered in cuff design were the:

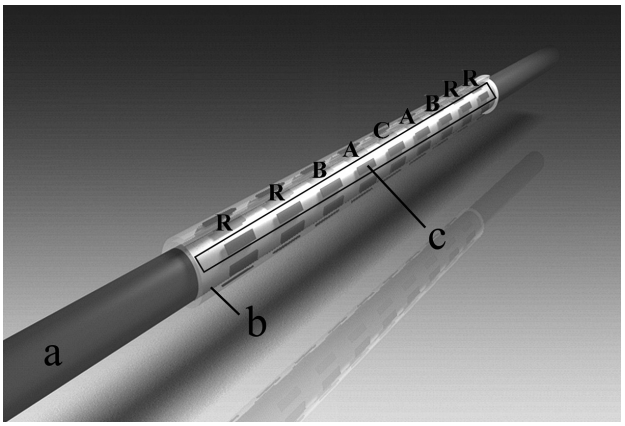

Figure 1: A perspective illustration of the the nerve segment (a) instaled into the 99-electrode cuff (b) and a position of specific electrodes within an arbitrary chosen longitudinal row of platinum electrodes (c). A-C-A represents triplets of electrodes within the stimulating section, B-represents blocking electrodes and R–R represents bipolar couples of electrodes for measurement of a CAP.

Slika 1: Prostorska risba segmenta živca (a) vstavljenega v 99-elektrodno objemko (b) in položaj posamezne platinaste elektrode v naključno izbrani vzdolžni vrsti elektrod (c). A-C-A je trojček elektrod v stimulacijski sekciji, B sta "bloking" elektrodi in R–R je bipolarni par elektrod v sekciji za merjenje CAP-a.

d – nominal diameter of the nerve: 2.5 mm
c – circumference of the nerve: 7.85 mm
l – total length of the cuff: 38 mm
w – approximate width of opened cuff: 12 mm

Figure 1 shows a finished ninety-nine-electrode cuff of 44 mm in total length and 2.5 mm in diameter (inner diameter of the first layer) and had 2.25–2.75 turns, snugly fitting the nerve in its resting position.

From the electrochemical point of view, a very important factor considered in the design of the cuff from different metals, was the stability of electrochemical potentials and the galvanometric behavior of stimulating electrodes in physiological media.

To supervise the electrode-electrolyte interface, the parameters of the stimulating waveform, injected via the stimulating electrode, were interchanged so to intentionally exceed the limits for reversible charge injection.[9,10,18]

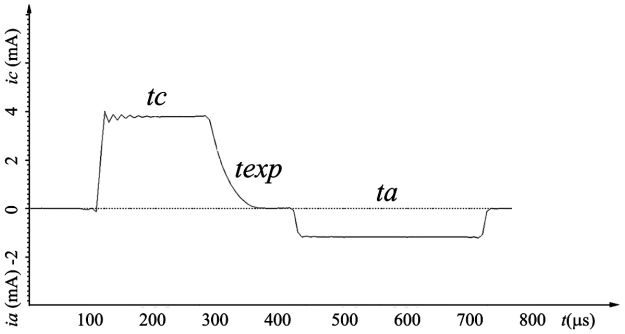

Figure 2: Parameters and waveform of the stimulating pulse

Slika 2: Parametri in oblika stimulacijskega impulza

Precisely, the absence or presence of both, reversible as well as irreversible electrochemical reactions, was controled exclusively via the imbalance between cathodically and anodically injected charge by the biphasic stimulating waveform.[7]

The stimulating pulse used in the study and shown in **Figure 2**, was current, biphasic, charge balanced and asymmetric pulse consisting of a precisely determined quasi-trapezoidal cathodic phase with a square leading edge with intensity i_c, a plateau with width t_c and exponentially decaying phase t_{exp}, followed by a wide rectangular anodic phase t_a/μs of a magnitude i_a.

To stimulate a determined group fibres within a particular compartment of a segment, stimulating pulses at frequency of 1 Hz were applied via stimulating cathode to preselected location.

An isolated, about 8 cm long segment of a swinish mid-cervical left vagus nerve, was installed within the cuff and mounted into the experimental chamber (**Figure 3**), according to the protocol approved by the ethics committee at the Veterinary Administration of the Republic of Slovenia, Ministry of Agriculture, Forestry and Food (VARS).

To maintain simulated physiological thermal conditions, the body of a measuring chamber machined out from Plexiglas, was heated to 37 °C using precision water circulator with range of control: ±0.003 °C .

To prevent extensive drying of the segment and maintain a natural "wet" surrounding of the nerve, the segment was occasionally flooded by the simulated cerebral perfusion fluid consisting of (in mM): MgCI2 2, CaCI2 2, KCI 2.5, NaCl 126, glucose 10, NaH2PO4·H2O 1.25, NaHCO3 26. At the same time, an interface between the stimulating electrode and neural tissue was maintained to closely mimic the physiological conditions.

The experiment consisted of four tests referred to as Test1-4, where given quasitrapezoidal stimulating pulses with preset parameters and waveform were delivered from a single channel precision custom designed stimulator to the triplet 5 in the stimulating section (ACA) of the cuff. A specific waveform and parameters of the individual pulses (1 Hz), were chosen by manual manipulation of the dials on the stimulator.

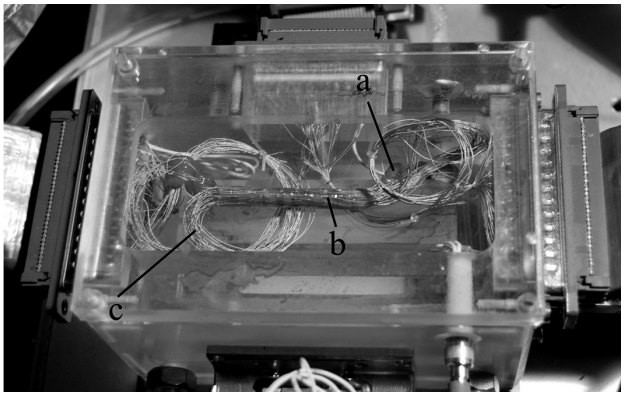

Figure 3: An isolated nerve segment (a), installed within the cuff (b) and multi-stranded copper wires (c), mounted into the experimental chamber

Slika 3: Izolirani segment živca (a), vstavljen v spiralno objemko (b), in bakrene pletenice (c), zmontirani v poskusno celico

In the Test 1, the parameters and waveform were the following: i_c = 1.84 mA, t_c = 185 μs,

t_{exp} = 100 μs, τ_{exp} = 35 μs and i_a = 0.79 mA.

In the Test 2, the parameters and waveform were the following: i_c = 1.71 mA, t_c = 65 μs,

t_{exp} = 100 μs, τ_{exp} = 35 μs and i_a = 0.74 mA.

In the Test 3, the parameters and waveform were the following: i_c = 4.07 mA, t_c = 155 μs,

t_{exp} = 105 μs, τ_{exp} = 60 μs and i_a = 1.77 mA.

In the Test 4, the parameters and waveform were the following: i_c = 3.9 mA, t_c = 265 μs,

t_{exp} = 105 μs, τ_{exp} = 35 μs and i_a = 1.67 mA.

In the first three out of four stimulation tests, the CAP was measured simultaneously from the right end of the segment with with the couple of electrodes in the recording section (R–R) of the cuff, having the same longitudinal position as appointed triplet5 within the stimulating section (A-C-A).[30,31] In the Test 4 however, a selected recording couple was located at circumferentially opposite site according to an appointed triplet5.

In measurements of CAPs, signals recorded with an appointed couple of electrodes were delivered to a custom designed differential amplifier and amplified (A = 100).

The analogous signals of both, stimulating pulses and measured CAP signals, were digitized via an analogue-digital conversion board (DEWE-43, high performance data acquisition system designed and manufactured by the company DEWESOFT using data acquisition software DEWESoft 7.0.2 and stored on a Lenovo T420 portable computer).

To supervise the electrode-electrolyte interface established upon intentionally exceeded limits for reversible charge injection by different values of parameters and waveforms of selectively delivered stimulating pulses, a charge Q_c injected in cathodic phase as well as charge Q_a injected in anodic phase within precisely defined stimulus as shown above, were calculated and compared to each other. For this purpose, an integral of the i_c under a cathodic phase Q_c as well as the integral of the i_a under an anodic phase of the stimulus Q_c, were calculated. By doing this, the influence of the different stimuli on the offsets in the measured CAPs that might be elicited due to an imbalance between Q_c as well as Q_a, could be identified. Since all the stimuli were current pulses expressed in milliamperes, the corresponding charges Q_c *and* Q_a were expressed in nAs.

However, to identify the differences in CAPs, elicited by electrode-electrolyte interface established upon intentionally exceeded limits for reversible charge

injection by different values of parameters and waveforms of selectively delivered stimulating pulses, an integral of the CAP in cathodic phase as well as integral of the CAP in anodic phase of stimuli were calculated and compared to each other. Since all the CAPs were voltage signals expressed in milivolts, the corresponding integrals were expressed in nV s.

All the offline signal analyses were performed on a Lenovo T420 portable computer using the Matlab R2007a programming tool.

3 RESULTS

Figure 4 shows measured CAPs while the segment was stimulated using quasitrapezoidal stimulus output waveforms and parameters, namely i_c, t_c, t_{exp}, *tau*, t_a and i_a, specifically preset in the abovementioned four tests. As could be seen in recorded CAPs, the **Figure 4** shown waveforms and values of the CAP were slightly obscured by stimulus artefacts and the transient response characteristics of an electrode/neural tissue interface and that of an inherent capacitance of the segment.

Table 1, however shows numerical values of calculated charge Q_c injected in cathodic phase as well as charge Q_a injected in anodic phase of precisely defined quasitrapezoidal stimuli selectively delivered to the triplet5 in Tests1–4. **Table 1** shows also values of calculated integral of corresponding CAPs in cathodic phase as well as in anodic phase of selectively delivered stimulating pulses.

A Test 4 however, was considered only in the sense of charge calculations while in a sense of integral calculation it was not considered. Namely, in the Test 4, corresponding CAP was measured using the couple of electrodes localed at circumferentially opposite site according to an triplet 5. Therefore, measured CAP could not contain action potentials of nerve fibres activated with an appointed triplet 5.

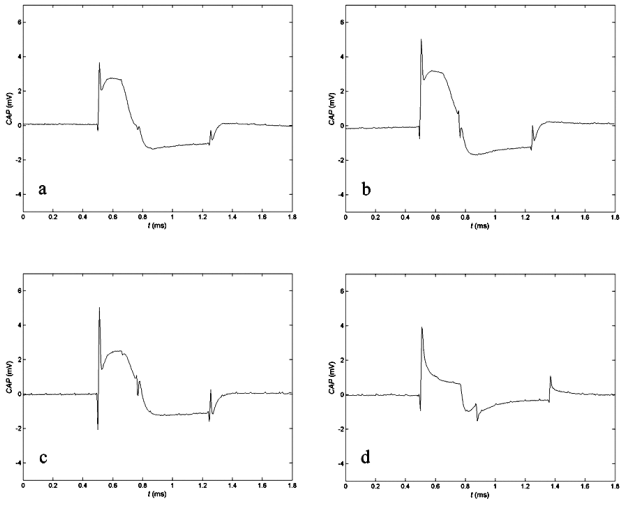

Figure 4: Specific waveform and values of CAPs measured in aforementioned four tests: a) CAP measured in the Test 1; b) CAP measured in the Test 2; c) CAP measured in the Test 3 and d) CAP measured in the Test 4

Slika 4: Oblika in vrednosti CAP-ov, izmerjenih v zgoraj omenjenih štirih preizkusih: a) CAP, izmerjen v testu 1; b) CAP, izmerjen v testu 2; c) CAP, izmerjen v testu 3 in d) CAP, izmerjen v testu 4

Table 1: Values and differences of cathodic Q_c and anodic Q_a charges and values and differences of Integrals1 of the CAP manifested under a cathodic phase and Integrals2 of the CAP manifested under an anodic phase of the stimulating pulses in Tests1-4

Tabela 1: Vrednosti in razlike katodnih Q_c in anodnih nabojev Q_a ter vrednosti in razlike Integrala 1 CAP-ov, zmontiranih pod katodno fazo in Integrala 2 CAP-ov, izraženih pod anodno fazo stimulusa pri testih 1–4

Variable	Test 1	Test 2	Test 3	Test 4
Q_c /(nA·s)	376.30	151.93	799.13	1107.82
Q_a /(nA·s)	376.42	352.63	832.27	803.42
ΔQ /(nA·s)	0.12	200.7	33.14	-304.4
Integral 1 /(nV·s)	250.57	113.01	665.22	300.38
Integral 2 /(nV·s)	59.85	61.50	76.15	44.95
ΔIntegral /(nV·s)	190.72	51.51	589.07	255.43

As result, **Table 1** shows the difference ΔQ of a cathodic Q_c and of an anodic charge Q_a as well as the difference of Integral1 of the CAP for cathodic phase and Integral2 of the CAP for anodic phase of the stimululating pulse for Tests1-4. Regardingly, in the Test2, for instance, a charge Q_c = 151.93 nAs was injected in cathodic phase and a charge Q_a = 352.63 nA s was injected in anodic phase, yielding a positive difference Q_{diff} = 200.7 nA s. This positive difference, being relatively high, could expectedly elicit some positive offset in the recorded CAP. In the Test4 however, a charge Q_c = 1107.82 nA s was injected in cathodic phase and a charge Q_a = 803.42 nA s was injected in anodic phase, yielding a negative difference Q_{diff} = –304.4 nA s. This negative difference, being also relatively high, could expectedly elicit some negative offset in the recorded CAP. Fortunately, it could be seen in **Figure 4**, that offset in all four measured CAPs, which could arise as a consequence of predefined imbalance in injected Q_c and Q_a, was not significant.

From the electrochemical point of view, it seems that all the reactions that occured at the cathode (A in **Figure 1**) due to a charge Q_c, injected via an i_c in the cathodic phase within a time t_c, were reversed, in part or in full, by the charge Q_a, injected via the anodic phase i_a within a time t_a. At each of the two triplet anodes in the same longitudinal row of electrodes (A–A in **Figure 1**), however, both the current and charge density would be equal to one fourth of the current and charge density occurring at the cathode. Namely, according to the model not presented in the paper, both of the triplet anodes and the two corresponding blocking electrodes (B–B in **Figure 1**), were electrically connected. Therefore, the electrochemical reactions that would occur at the single anode could not be of the irreversible type.

However, this pattern would inevitable worsen in case of stimulation in clinical practice where trains of repetitive stimulating pulses are applied. In this case,

excursions of potential of electrodes within stimulating section due to predefined charge imbalance are additive in each stimulating pulse and the resulting excursion and consequently arised offset coud be significant.

4 DISCUSSION

An aim of the work was to contribute to the development of models and multi-electrode cuffs to be used for efficient and safe selective stimulation of autonomous peripheral nerves and for selective recording of CAPs at the same time.

The key developments in this technology were a cuff that can expand and contract to provide a snug yet non-compressing fit to the nerve, and a distributed matrix of platinum stimulating electrodes which made the performance of the cuff independent of it's positioning around the nerve. This design has strong potential for applications in neuro-prosthetic technology in future[9]. Namely, it would be very desirable to control different internal organs such as cardio-vascular system in patients with heart failure or atrial fibrillation by only one implanted system, e.g. on the lef cervical vagus nerve.

However, it is unavoidable to understand the response of peripheral nervous system elements to stresses that may occur in the complex interactions that take place between electrode and nerve secondary to VNS.

From CAP recording poinf of view, clinical use of implanted electrodes is hampered by a lack of reliability in chronic recordings, independent of the type of electrodes used. Namely, persistent presence of the electrode close to the neural tissue, causes a progressive local neurodegenerative disease-like state surrounding the electrode and is a potential cause for chronic recording failure.

However, from stimulation point of view, nerve fibers are located close to the stimulating electrode and also at a certain distance from it, the electrode should be able to inject enough charge to activate these fibers.[25,27] However, for multielectrode stimulating systems, containing miniature stimulating electrodes working at relatively high charge densities, it is very important that they are safe and electrochemically stable. Namely, to avoid harm to the vagus nerve in clinical use of the cuff, an inevitable requirement is the absence of irreversible electrochemical reactions such as electrolysis of water, evolution of chlorine gas or formation of metal oxides that could cause severe tissue injury associated with high charge density stimulation.[16,17]

Regarding both points of view, changes in the complex impedance of stimulating and recording electrodes in the cuff, chronically instaled onto a vagus nerve, should be characterized in a series of animal experiments.[32]

One weakness of a cuff manufacturing was a technically demanding and a time consuming process. Another weakness of a cuff was the use of a tin alloy at the junctions between platinum electrodes and multi-stranded wires. As this solution is not appropriate for a clinical practice, a mechanical connection as a more appropriate solution for further development of cuffs is in preparation. Beside, a perfect electrical isolation of all metals except electrode material is crucial for the life time of the system, othervise the mentioned reactions could occur.

Directions that our further work would be the following:

- Further development of the cuff for given clinical applications and accomplishment of electrochemical measurements under realistic conditions using the method of cyclic voltammetry, implementing the Ag/AgCl reference electrode.
- Development of the strategies to enhance a capability to obtainreliable long-term bipolar recordings of a CAP from a particular couple of platinum electrodes within the cuff.

It could be expected that mentioned directions, when performed, will lead to an additional enhancement of the cuff efficiency and to an overall more efficient and effective implantable devices.

5 CONCLUSIONS

The most important findings of the present study are the following:

- The strong component superimposed in the CAP was an ensemble artefact which came exclusively from the stimulating pulse via the transient response characteristics of an electrode/neural tissue interface and in part from an inherent capacitance of the segment.
- One could speculate that stimulus artefact traveled exclusively along the nerve surface via a capacitive nature of an interface, while recording electrodes measured an elicited voltage drop at the surface on the nerve.
- Single stimulating pulses, having preset certain degree of imbalance between a charge injected in cathodic phase Q_c and charge injected in anodic phase Q_a, elicited a slight change in a positive waveform deflection of CAP manifested under a cathodic phase as well as slight change in a negative waveform deflection of a CAP manifested under an anodic phase of the stimulating pulse.
- Measured CAPs are not greatly influenced by the imbalance between a charge injected in cathodic and anodic phase of quasitrapezoidal, asymmetric and biphasic stimulating pulses.
- The reactions that occured at the cathode due to an injected charge Q_c were reversed, in part or in full, by the charge Q_a.
- The electrochemical reactions that occured at the single anode could not be of irreversible type.

Acknowledgements

This study was supported in part by the Ministry of Higher Education and Science, Republic of Slovenia, Research Program P3-0171 and in part by the ITIS, d. o. o., Ljubljana, Centre for Implantable Technology and Sensors.

6 REFERENCES

[1] A. V. Zamotrinsky, B. Kondratiev, J. W. de Jong, Vagal neurostimulation in patients with coronary artery disease, Auton. Neurosci., 88 (**2001**), 109–116

[2] G. M. De Ferrari, A. Sanzo, P. J. Schwartz, Chronic vagal stimulation in patients with congestive heart failure, Conf Proc IEEE Eng Med Biol Soc., Minneapolis, MN, Sept. 3.–6., 2009, 2037–2039

[3] J. Rozman, P. Pečlin, I. Kneževič, T. Mirkovič, B. Geršak, M. Podbregar, Heart function influenced by selective mid-cervical left vagus nerve stimulation in a human case study, Hypertens. res., 32 (**2009**) 11, 1041–1043

[4] A. B. Setty, B. V. Vaughn, S. R. Quint, K. R. Robertson, J. A. Messenheimer, Heart period variability during vagal nerve stimulation, Seizure, 7 (**1998**), 213–217

[5] D. M. Labiner, G. L. Ahern, Vagus nerve stimulation therapy in depression and epilepsy: therapeutic parameter settings, Acta Neurol. Scand., (**2007**), 23–33

[6] C. Heck, S. L. Helmers, C. M. DeGiorgio, Vagus nerve stimulation therapy, epilepsy, and device parameters: scientific basis and recommendations for use, Neurology, 59 (**2002**), 31–37

[7] W. F. Agnew, D. B. McCreery, Considerations for safety with chronically implanted nerve electrodes, Epilepsia, 31 (**1990**), Suppl. 2, 27–32

[8] L. S. Robblee, T. L. Rose, The electrochemistry of electrical stimulation. Proc. 12th Ann. Conf. IEEE Eng. in Med. & Biol. Soc., Philadelphia, PA, November 1.–4., 1990, 1479–1480

[9] J. T. Mortimer, Motor Prostheses. Pages 155–187 in Handbook of Physiology, Section 1. J. B. Brookhart, V. B. Mountcastle, (section eds.), V. B. Brooks (volume ed.), S. R. Geiger (executive ed.), American Physiological Society, Bethesda, MD., 1981

[10] W. F. Agnew, D. B. McCreery (Editors), Neural Prostheses, Fundamental Studies, Prentice-Hall, Inc., A Division of Simon & Shuster, Englewood Cliffs, New Jersey, 1990

[11] S. B. Brummer, M. J. Turner, Electrochemical considerations for safe electrical stimulation of the nervous system with platinum electrodes, IEEE Trans. Biomed. Eng., 24 (**1977**), 59–63

[12] D. B. McCreery, W. F. Agnew, T. G. H. Yuen, L. Bullara, Charge density and charge per phase as cofactors in neural injury induced by electrical stimulation, IEEE Trans. Biomed. Eng., 37 (**1990**), 996–1001

[13] S. B. Brummer, M. J. Turner, Electrical stimulation with Pt electrodes, I. A method for determination of "real" electrode areas, IEEE Trans. Biomed. Eng., 24 (**1977**), 436–439

[14] M. D. Bonner, M. Daroux, T. Crish, J. T. Mortimer, The pulse-clamp method for analyzing the electrochemistry of neural stimulating electrode, J. Electrochem. Soc., 140 (**1993**), 2740–274

[15] L. S. Robblee, T. L. Rose, Electrochemical guidelines for selection of protocols and electrode materials for neural stimulation, In Neural Prostheses: Fundamental Studies. W. F. Agnew, D. B. McCreery, Eds. Englewood Cliffs, Nj: Prentice-Hall, 1990, 25–66

[16] D. B. McCreery, W. F. Agnew, T. G. H. Yuen, L. A. Bullara, Relationship between stimulus amplitude, stimulus frequency and neural damage during electrical stimulation of sciatic nerve of cat, Med. Biol. Eng. Comput., 33 (**1995**) 3, 426–429

[17] T. G. H. Yuen, W. F. Agnew, L. A. Bullara, S. Jacques, D. B. McCreery, Histological evaluation of neural damage from electrical stimulation, considerations for the selection of parameters for clinical application, Neurosurgery, 9 (**1981**) 3, 292–299

[18] B. Onaral, H. H. Sun, H. P. Schwan, Electrical properties of bioelectrodes, IEEE Trans Biomed Eng, 31 (**1984**) 12, 827–832

[19] P. Kopf-Maier, Complexes of metals other than platinum as antitumour agents, Eur J Clin Pharmacol, 47 (**1994**) 1, 1–16

[20] R. Osterauer, L. Marschner, O. Betz, M. Gerberding, B. Sawasdee, P. Cloetens, N. Haus, B. Sures, R. Triebskorn, H. R. Köhler, Turning snails into slugs, induced body plan changes and formation of an internal shell, Evolution & Development, 12 (**2010**), 474–483

[21] R. B. Stein, D. Charles, L. Davis, J. Jhamandas, A. Mannard, T. R. Nichols, Principles underlying new methods for chronic neural recording, Can J Neurol Sci, 2 (**1975**), 235–244

[22] M. K. Haugland, T. Sinkjær, Cutaneous whole nerve recordings used for correction of footdrop in hemiplegic man, IEEE Trans Rehabil Eng, 3 (**1995**), 307–317

[23] J. J. Struijk, The Extracellular Potential of a Myelinated Nerve Fiber in an Unbounded Medium and in Nerve Cuff Models, Biophysical Journal, 72 (**1997**) 6, 2457–2469

[24] J. Taylor, N. Donaldson, J. Winter, Multiple-electrode nerve cuffs for low-velocity and velocity-selective neural recording, Med Biol Eng Comput, 42 (**2004**), 634–643

[25] G. G. Naples, J. T. Mortimer, T. G. H. Yuen, Overview of peripheral nerve electrode design and implantation, In Neural Prostheses, Agnew W. F., McCreery, D. B., Eds. Englewood Cliffs, NJ: Prentice Hall, 1989, 108–145

[26] G. G. Naples, J. D. Sweeny, J. T. Mortimer, Implantable cuff, Method and manufacture, and Method of installation, U. S. Patent #4, 1986, 602–624

[27] D. R. Mc Neal, B. R. Bowman, Selective activation of muscles using peripheral nerve electrodes, Med. & Biol. Eng. & Comput., 23 (**1985**), 249–253

[28] G. G. Naples, J. T. Mortimer, A nerve cuff electrode for peripheral nerve stimulation, IEEE Trans. Biomed. Eng., BME-35, (**1988**), 905–916

[29] J. D. Sweeney, D. A. Ksienski, J. T. Mortimer, A nerve cuff technique for selective excitation of peripheral nerve trunk regions, IEEE Trans. Biomed. Eng., BME-37, (**1990**), 706–715

[30] S. C. Ordelman, L. Kornet, R. Cornelussen, H. P. Buschman, P. H. Veltink, An indirect component in the evoked compound action potential of the vagal nerve, J Neural Eng, 7 (**2010**) 6, 066001

[31] I. F. Triantis, A. Demosthenous, N. Donaldson, On cuff imbalance and tripolar ENG amplifier, IEEE Trans Biomed Eng, 52 (**2005**), 314–320

[32] J. C. Williams, J. A. Hippensteel, J. Dilgen, W. Shain, D. R. Kipke, Complex impedance spectroscopy for monitoring tissue responses to inserted neural implants, J Neural Eng, 4 (**2007**), 410

UDK 681.7.026.6:539.23:669.75
Original scientific article/Izvirni znanstveni članek

ISSN 1580-2949
MTAEC9, 46(2)139(2012)

EFFECT OF THE ANTIMONY THIN-FILM DEPOSITION SEQUENCE ON COPPER-SILICON INTERDIFFUSION

VPLIV ZAPOREDJA NANOSA TANKIH PLASTI ANTIMONA NA INTERDIFUZIJO BAKER-SILICIJ

Menni Nasser[1], Boudissa Mokhtar[1], Benkerri Mahfoud[2], Reffas Mounir[2], Zekkar Fouzia[1], Benazzouz Chaouki[3]

[1]ENMC Laboratory, F. Abbas University, Algeria
[2]LESIMS Laboratory, F. Abbas University, Algeria
[3]Nuclear research Center, 16000Algiers, Algeria
nacermenni@yahoo.fr

Prejem rokopisa – received: 2011-08-22; sprejem za objavo – accepted for publication: 2011-08-27

In this work we present a study of the effect of an antimony layer on the interdiffusion and formation of copper silicides while inverting the sequence of Cu and Sb deposition on Si(111) substrates. Thermal evaporation was used to deposit Cu/Sb and Sb/Cu bilayers on a Si(111) substrate heated at 100 °C, without breaking the vacuum. XRD and RBS analysis showed, for samples heat treated at 200 °C and 400 °C, a segregation of the three elements (i.e., Cu, Sb and Si) to the surface and diffusion in bulk ending in the formation of a layer made of a mixture containing the three elements at the samples' surface. After 200 °C annealing, in the Cu/Sb/Si system, we observed the formation of only Cu_2Sb, and for the Sb/Cu/si system, there is the formation of the Cu_3Si and Cu_2Sb phases; after 400 °C annealing, the Cu-Sb-Si mixture is formed by the cohabitation of the Cu_3Si silicide and the Cu_2Sb intermetallic compound in the Cu/Sb/Si sample and only Cu_2Sb in the Sb/Cu/Si sample. For the Cu/Sb/Si sample, annealed at 400 °C, the SEM micrographs exhibit compound formation with crystallites that have a trapezoidal shape.

Keywords: thin film, PVD, diffusion, copper-antimony compound, copper silicide, Rutherford backscattering, scanning electron microscopy, X-ray diffraction

V delu predstavljamo študijo vpliva plasti antimona na interdifuzijo in formiranje bakrovih silicidov pri inverziji zaporedja nanosa Cu in Sb na Si(111)-podlago. Nanos plasti Cu/Sb in Sb/Cu je bil izvršen s termičnim izhlapevanjem na Si(111)-substrat pri 100 °C brez prekinitve vakuuma. XRD- in RBS-analize vzorcev, žarjenih pri 200 °C in 400 °C, so pokazale segregacijo treh elementov (Cu, Sb in Si) na površini podlage in difuzijo masivnega materiala s tvorbo plasti zmesi treh elementov na površini podlage. Po žarjenju sistema Cu/Sb/Si pri 200 °C je bil opažen nastanek Cu_2Sb, v sistemu Sb/Cu/Si pa nastanek faz Cu_3Si in Cu_2Sb. Po žarjenju pri 400 °C je bilo ugotovljeno sobivanje silicida Cu_3Si in intermetalne spojine Cu_2Sb pri vzorcu Cu/Sb/Si in samo Cu_2Sb pri vzorcu Sb/Cu/Si. Pri vzorcu Cu/Sb/Si, žarjenem pri 400 °C, SEM-posnetki kažejo nastanek spojin s kristali trapezoidne oblike.

Ključne besede: tanke plasti, PVD, difuzija, spojina baker-antimon, bakrov silicid, Ruthefordovo povratno sipanje, vrstična elektronska mikroskopija, difrakcija rentgenskih žarkov

1 INTRODUCTION

Antimony and copper are important elements for the design of silicon-based electronics devices; indeed, copper is predominant in interconnect metallization material for deep sub-micrometer technology due to its relatively low resistivity and electromigration resistance[1–3], and antimony is most frequently used as an n-type doping element during silicon crystal growth[3,4]. Unfortunately, the extensive diffusion of Cu in Si is detrimental to the electrical performance of devices, because Cu can form recombination-generation centers in the active regions of Si. Additionally, it reacts with silicon at very low temperatures, even below 150 °C, forming Cu-Si silicides[5–10] hence, diffusion barriers (e.g., an Sb layer) are necessary between the metallization copper and Si substrate. To the best of our knowledge, no study on the Cu-Sb-Si thin film system has been published in the literature so far, though a study of the Cu-Sb thin-film system deposited on glass substrate, annealed up to 600 °C, has shown that during annealing at up to 300°C, only the Cu_2Sb compound is formed. During subsequent heat treatments from 350 °C to 600 °C, the Cu_9Sb_2 phase nucleates and grows at the expense of the Cu_2Sb phase[11]. In a previous work[12,13], the effect of temperature and doping-element redistribution on atomic interdiffusion between a thin copper layer and monocrystalline silicon, implanted and Sb^+ unimplanted with different doses, was investigated. The results show the growth and formation of Cu_3Si and Cu_4Si silicides under crystallites shape dispatched on the sample surface, independently of the implantation dose. On the other hand, it was established that the copper layer is less and less consumed as the antimony dose increases, resulting in an accumulation of Sb ions at the silicide/Si interface and in the silicide layer close to the surface. However, the low antimony quantity in the presence has not led to an understanding of the reactions which could take place between the three elements and the inter diffusion mechanism involving the Sb and Cu layers and the Si substrate.

In the present study, we focus on copper, antimony and silicon atoms' interdiffusion in the Cu-Sb-Si thin-layers system, while inverting the sequence of evapo-

ration of the Cu and Sb thin films on monocrystalline (111) Si. Indeed, from a metallurgical point of view, it is very interesting to study the Sb/Cu/Si and Cu/Sb/Si sequences in order to obtain some information about the influence of Sb on the diffusion process and on the formation of the different phases.

2 EXPERIMENTAL PROCEDURES

N-type monocrystalline(111)-oriented silicon wafers with a resistivity of 1–3 Ω cm were used as substrates. In order to eliminate as far as possible the residual layer of silicon oxide, the wafers were etched in 10 % hydrofluoric (HF) acid for 20 s and rinsed in de-ionized water prior to loading into the vacuum system. Copper and antimony thin films were thermally evaporated alternatively, Cu/Sb as well as Sb/Cu, onto the Si(111) substrate heated at 100 °C for a better adhesion of the antimony layer. These evaporations were performed without breaking the vacuum of $5.23 \cdot 10^{-7}$ mbar obtained with a turbomolecular pump. An in-situ quartz crystal oscillator allows measurement of the thickness of the copper and antimony layers, which were 70 nm and 30 nm, respectively, in the Cu/Sb systems, and 100 nm and 30 nm, respectively, in Sb/Cu layers. In order to promote diffusion, conventional annealing treatments were performed at temperatures of 200 °C and 400 °C, for 45 min, in a quartz tube, under a vacuum of about $2.66 \cdot 10^{-7}$ mbar. It is important to note that the first steps range of the reaction at the different interfaces happen at these temperatures of annealing.

The surface morphology characterization of the samples, before and after the heat treatments, was carried out using a JEOL JSM-6460 scanning electron microscope with an accelerating voltage of 20 kV and an EDX analyzer. The primary energy of the electron beam is chosen to be equal to 10 keV in order to limit the analyzed depth to about 300 nm into the surface. A

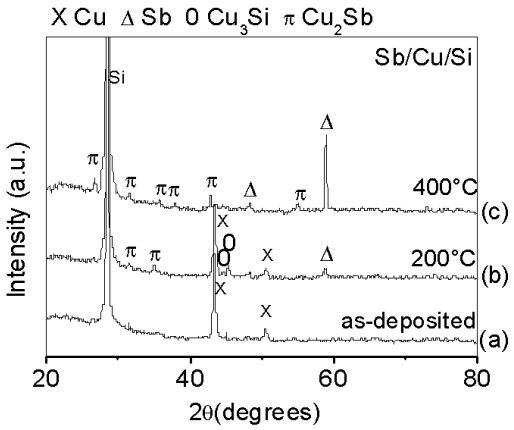

Figure 1: X-ray diffraction patterns of Sb/Cu bilayers on Si(111) substrate heated at 100 °C: a) as-deposited and annealed at b) 200 °C and c) 400 °C

Slika 1: Rentgenski uklonski spektri Sb/Cu-plasti na Si(111)-podlago pri 100 °C: a) naneseni in žarjeni pri b) 200 °C in c) 400 °C

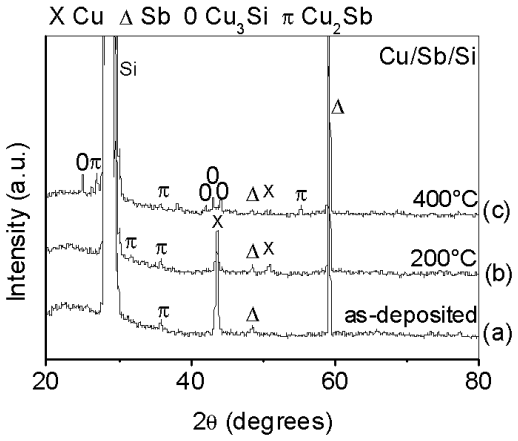

Figure 2: X-ray diffraction patterns of Cu/Sb bilayers on Si(111) substrate heated at 100 °C: a) as-deposited and annealed at b) 200 °C and c) 400 °C

Slika 2: Rentgenski uklonski spektri Cu/Sb-plasti na Si(111)-podlago pri 100 °C: a) naneseni in žarjeni pri b) 200 °C in c) 400 °C

Siemens D5000 diffractometer, in θ–2θ mode, was used to identify the formed compounds. The concentration profiles of the Cu, Sb and Si were determined with the help of spectra simulated with the RUMP program by fitting the experimental RBS spectra recorded at (2 MeV, $^4He^+$) with the detector positioned at 160° relative to the beam.

3 RESULTS AND DISCUSSION

Typical X-ray diffraction patterns corresponding to the Sb/Cu/Si(111) and Cu/Sb/Si(111) systems, as deposited, are shown in **Figures 1a** and **2a**, respectively. The nominal preheating of the substrate at 100 °C was used during evaporation in order to enhance the in-surface adhesion. On the XRD diagram corresponding to th Sb/Cu bilayers deposited on the Si(111), there is

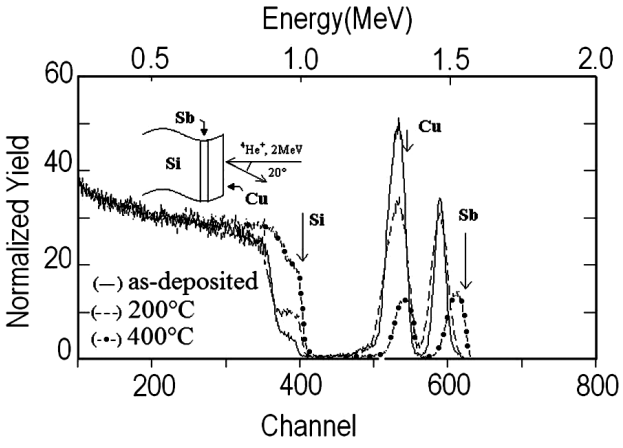

Figure 3: Rutherford backscattering spectra of Cu/Sb bilayers on silicon substrate heated at 100 °C: as-deposited and annealed at 200 °C and 400°C

Slika 3: Spektri Ruthefordovega povratnega sipanja za Cu/Sb-plasti na Si(111)-podlagi pri 100 °C: naneseni in žarjeni pri 200 °C in 400 °C

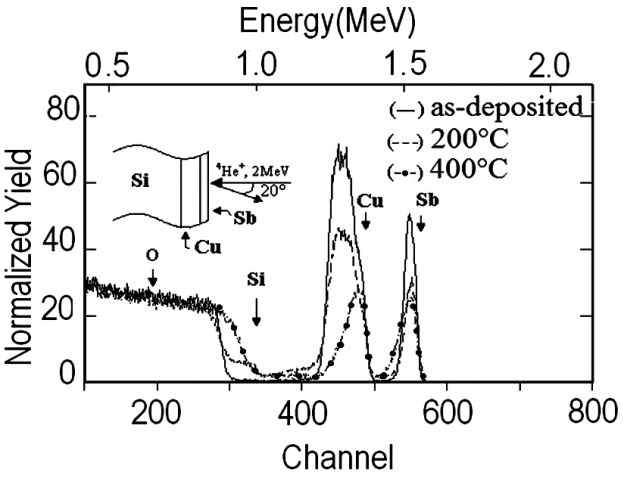

Figure 4: Rutherford backscattering spectra of Sb/Cu bilayers on silicon substrate heated at 100 °C: as-deposited and annealed at 200 °C and 400 °C

Slika 4: Spektri Ruthefordovega povratnega sipanja za Sb/Cu-plasti na Si(111)-podlagi pri 100 °C: naneseni in žarjeni pri 200 °C in 400 °C

clear evidence of the main (111)Cu and (200)Cu reflection lines, and the absence of that of the evaporated antimony layer, which could be amorphous or formed from nanometric grains. In the Cu/Sb/Si sample, in addition to the high texturization of the antimony layer, we can see, before any annealing, the apparition of the Cu_2Sb intermetallic compound. RBS spectra, for both as-deposited samples, shown in **Figure 3** and **Figure 4**, reveal that the different interfaces are not abrupt. This means that the preheating of the substrate during evaporation has already led to atomic interdiffusion at the different interfaces. Particularly in the Cu/Sb/Si sequence case, where the RBS spectrum shows a slight shift of the silicon signal towards the high-energies side, with a 30 %. Si concentration in the outer layer. This is synonymous with the silicon atoms segregation to the sample surface, which has as a consequence the beginning of the asperities formation shown on the corresponding micrograph, (**Figure 5a**). On the other hand, in the Sb/Cu/Si system, we can see the displace-

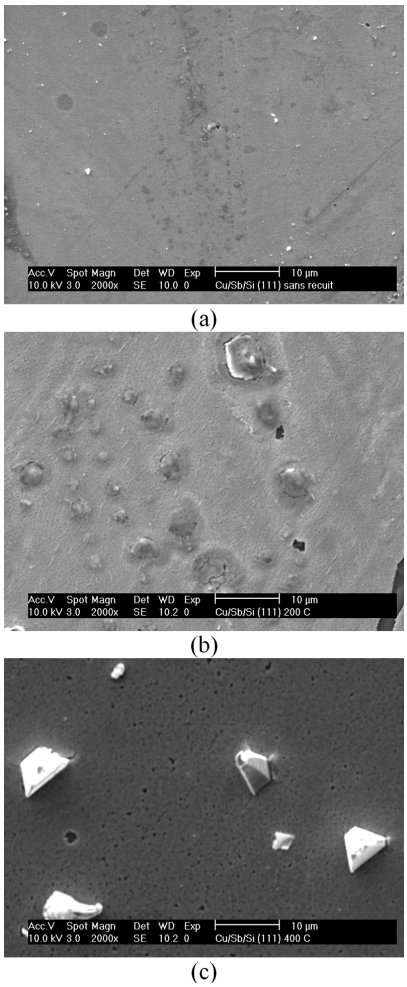

Figure 5: SEM micrographs from the surfaces of Cu/Sb bilayers on silicon substrate heated at 100 °C: a) as-deposited and heat treated at b) 200 °C and c) 400 °C

Slika 5: SEM-posnetki površine plasti Cu/Sb na Si(111)-podlagi pri 100 °C: a) naneseni in žarjeni pri b) 200 °C in c) 400 °C

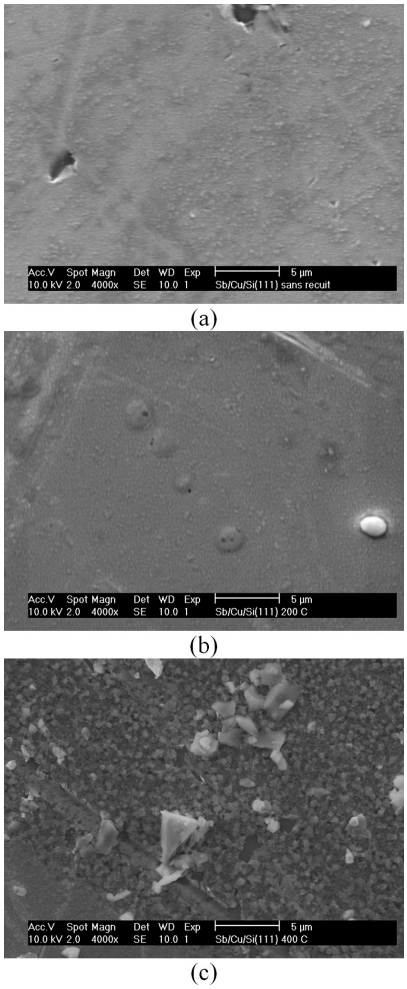

Figure 6: SEM micrographs from the surfaces of Sb/Cubilayers on silicon substrate heated at 100 °C: a) as-deposited and heat treated at b) 200 °C and c) 400 °C

Slika 6: SEM-posnetki površine plasti Sb/Cu na Si(111)-podlagi pri 100 °C: a) naneseni in žarjeni pri b) 200 °C in c) 400 °C

ment of the Cu RBS spectrum to lower energy, due to its diffusion into the silicon substrate. Again, a shoulder appears on the right-hand side of the Cu spectrum, which means that an appreciable amount of the mole fraction of Cu (x = 68 %) has already segregated to the surface through the antimony top layer. In this latter case, the diffusion of copper atoms is favored. In this pre-reactional diffusion, the displacement of Sb atoms appears timorous because of the low diffusion coefficient of Sb into Si. Indeed, according to Fahey et al.[14], the Sb diffusion coefficient in Si, under equilibrium conditions, is $1.2 \cdot 10^{-19}$ cm^2/s. However, in the solid state, antimony is partially soluble in copper, with the solubility decreasing with temperature, and, it is more plausible that Cu atoms dissolve in the antimony layer rather than the opposite, because the atomic radius of Cu (0.128 nm) is smaller than that of Sb (0.145 nm).

After 200 °C annealing (**Figure 1b**), X-ray diffraction patterns for the Sb/Cu/si system show that in the inner copper layer the copper reacted with Si and Sb to give reflection lines corresponding to the Cu_3Si and Cu_2Sb phases. Whereas in the outer copper layer system (Cu/Sb/Si) we see the formation of only Cu_2Sb, which leads to a decrease of the (111) and (100)Cu reflection lines' intensities, as indicated in **Figure 2b)**. For this latter case, the surface morphology shows that the asperities of the as-deposited samples have served as nucleation sites for the first diffusion steps on the sample surface (**Figure 5b**). According to the RBS signals of the silicon, for both samples at 200 °C annealing, the evolution of an enhanced silicon concentration in the surface is very easily seen. When copper is the first deposited layer onto the silicon, an important quantity of copper (x(Cu) = 63 %) has diffused in the bulk as a consequence of its exceptionally fast diffusivity in the Si substrate. Copper is known as the fastest diffusing element in silicon among all the transition metals, for depths of a few micrometers. For instance, the Cu diffusion coefficient in Si is $1.4 \cdot 10^{-6}$ cm^2/s at 400 °C and copper atoms move interstitially in the lattice to form an interstitial solid solution[15,16]. For the Cu/Sb/Si sample heat treated at 200 °C, (**Figure 3**), the RBS signal of antimony seems to decrease in terms of yield intensity versus the diffusion of silicon and the presence of copper atoms at the surface, to form the mole fractions 39 % Cu, 15 % Sb and 45 % Si mixture layer that is 140 nm thick. This phenomenon is more pronounced during 400 °C annealing, for both samples, where the heights of the copper and antimony signals have drastically decreased due to the transport of the three elements, (**Figures 3** and **4)**. Besides, the rear edges for both metallic peaks have extended to lower channel numbers, while the front edge of the silicon signal has extended to the higher channel numbers. This clearly indicates that intermixing has occurred across the different interfaces and in the surface. In both cases, the formed alloy is evaluated from the slopes of the rear edge of the metal layers from the metallic signals, and it is evident from the RBS spectra of the Sb/Cu/Si sample, that the slopes of the rear edges of the Cu and Sb are more important than in the Cu/Sb/Si sample. These rear edges of the Cu and Sb RBS signals were simulated while taking the 12 % Cu, 5 % Sb, 83 % Si and 26 % Cu, 6 % Sb, 68 % Si for Cu/Sb and Sb/Cu bilayers, respectively. For both systems, the diffusion of all the elements is clearly visible and is also dramatic on the signals' shape with a perturbation of the silicon substrate over about 1300 nm in depth. This Cu-Sb-Si mixture is really formed by the cohabitation of the Cu_3Si silicide and the Cu_2Sb intermetallic compound in the Cu/Sb/Si and only the Cu_2Sb in the Sb/Cu/Si sample, after 400 °C annealing **Figures 1c** and **2c**. In this latter case, the disappearance of Cu_3Si silicide to the benefit of the Cu_2Sb phase is foreseeable owing to the fact that the growth and formation of the second compound is energetically more favorable, as will be argued later in this paper. The persistence of the two compounds in the Cu/Sb/Si sample means that the reaction is less pronounced than in the Sb/Cu/Si sample.

Equilibrium phase diagrams of the Sb-Si[2], Cu-Sb[4] and Cu-Si[17] binary alloys, which bind the ternary Cu/Sb/Si system, have been well known for a long time. Among the binary systems with an important segregation, Cu–Sb and Cu-Si are particularly interesting for their strong tendency to form ordered compounds And it is known that Sb/Si is a simple eutectic system, which induces a low limited mutual solubility of Sb and Si and, with no intermediate phase formation because Sb has a high mass and low diffusivity in Si. Indeed, the solid solubility of Sb in Si is very low: the maximum equilibrium solubility of Sb in Si is 0.1 % during an equilibrium processes, whereas that of silicon in Sb is negligible. In the solid state, antimony is partially soluble in copper, with the proportion decreasing with temperature. The solid solubilities of 1.5 % and 3 % Sb in Cu are reached at temperatures of 250 °C and 300 °C, respectively. A maximum solubility of 5.8 % antimony in a copper matrix is reached at a temperature of 645 °C[8]. On the other hand, the copper atoms' diffusion in Si is essentially interstitial with an activation energy of 0.43 eV and a limited solubility of about $1 \cdot 10^{15}$ cm^{-3} at 600 °C[18,19]. In addition, Cu-Sb and Cu-Si couples are completely miscible with the formation of ordered compounds, such as Cu_2Sb, Cu_3Sb, $\eta Cu_{11}Sb_2$, Cu_9Sb_2 and Cu_3Si, Cu_4Si, $Cu_{0.83}Si_{0.17}$, Cu_5Si, respectively, depending on the composition in the solid solution. However, it is reported as the growth and formation, as the first phases of Cu_2Sb and Cu_3Si in their corresponding binary systems, respectively. This formation of Cu_3Si and Cu_2Sb phases in our case is in conformity with results reported in the literature[11,20] and is in agreement with both the prediction[21] and the thermodynamic minimization of the free enthalpy ΔH. From the Cu-Sb system, the reported free energies of formation of the Cu_2Sb, Cu_9Sb_2, $\eta Cu_{11}Sb_2$ intermetallic compounds are

(–4.23, –0.54 and –0.29) kJ/mol, respectively[22], whereas from the Cu-Si system, those of the Cu_3Si, Cu_4Si, and Cu_5Si silicides are (–4.1, –3.4, and –2.9) kJ/mol, respectively[23]. Thermodynamically, the formation of the first stable compound at the interface requires the lowest free enthalpy and is consequently favored. In other words, the Cu_2Sb and Cu_3Si compounds have the lowest heat of formation of their mother compounds and are energetically more favorable. While adopting the same argumentation, if these two compounds are in competition, it is clear that the formation of Cu_2Sb is more favorable than that of Cu_3Si. Indeed, these results confirm that copper atoms are the dominant diffusion species in both compounds, which is in agreement with the rule that stipulates that the majority of atoms in the formed phase should be more mobile than the minority atoms[24]. The observed compounds' compositions (XRD spectra) in the *equilibrated* mixture (RBS spectra) show that an equilibrium exists between the Cu_3Si and Cu_2Sb phases, starting from 200 °C. This temperature of formation, surprisingly low compared to those leading to the formation of silicides and intermetallic compounds of refractory metals, can be attributed to the high diffusivity of the copper in both the antimony and silicon matrices[25].

Figure 5 illustrates the evolution of the surface morphology with temperature, examined by scanning electron microscope, for the Cu/Sb/Si(111) sample. The first micrograph (magnif. 2000-times) of the as-deposited sample shows some asperities, probably due to the preheating of the silicon substrate; this contrasts with the presupposed uniform aspect that the evaporated metallic layer on the cold substrate should have. Starting from 200 °C, as seen in **Figure 5b**, crystallites sprinkled on the samples' surface, begin to take shape according to the same oblique lines. After the 400 °C annealing (**Figure 5c**) we can see large white crystallites with a micrometric dimension of the trapezoidal shape, grown at surface as consequence of the great interdiffusion between the three elements. This is due to the segregation and coalescence of the elements above the sample surface, leading to the growth and formation of Cu_2Sb and Cu_3Si crystallites with heights of over one micrometer, which is equivalent to the simulated thickness of the coalesced metal layers. Particularly for the Cu_3Si silicide, a similar epitaxial growth has already been reported in n octahedral shape on Si(100)[26] and different shapes with and without an intermediate metallic layer[9]. In this study, such oriented crystallites' formation was not observed for the Sb/Cu/Si(111) sequence, in spite of enlargement of 4000-times, (**Figure 6**). Indeed, in this case, according to X-ray diffraction diagram, there is no formation of the Cu_3Si phase at 400 °C.

4 CONCLUSION

The XRD, RBS and SEM techniques have been used to investigate atomic interdiffusion in Cu/Sb and Sb/Cu bilayers deposited on monocrystalline silicon with a (111) orientation. In the Cu/Sb/Si sample, in addition to the high texturization of the antimony layer, we already se, before any annealing, the appearance of Cu_2Sb intermetallic compound due to substrate heating at 100 °C. Heat treatments of 200 °C and then 400 °C, reveal a strong Cu-Sb-Si intermixing between the three elements for both systems, resulting in compounds formation. After the 200 °C annealing, in the Cu/Sb/Si system, we see the formation of only Cu_2Sb, and for the Sb/Cu/si system, there is the formation of the Cu_3Si and Cu_2Sb phases. After 400 °C annealing, the Cu-Sb-Si mixture is formed by the cohabitation of the Cu_3Si silicide and the Cu_2Sb intermetallic compound in Cu/Sb/Si and only Cu_2Sb in the Sb/Cu/Si sample. For both systems, the diffusion of all elements is clearly visible and is also dramatic on the RBS signals' shape with a perturbation of silicon substrate of about 1300 nm in depth. Indeed, at 400 °C, SEM micrographs for Cu/Sb/Si sample show the formation of Cu_2Sb and Cu_3Si crystallites with heights of over one micrometer, which is comparatively equivalent to the simulated thickness of the coalesced metal layers. In this study, such oriented crystallites formation were not observed for the Sb/Cu/Si(111) sequence in spite of the SEM micrograph enlargement of 4000-times.

5 REFERENCES

[1] S. M. Murarka, I.V. Verner, R. J. Gitmann, Copper – Fundamental Mechanisms for Microelectronic Applications, Ed., John Wiley and Sons, New York, 2000, chapter I

[2] J. F. Gui Llaumond, Étude de la résistivité et de l'é lectromigration dans les interconne xions destiné es aux technologies des nœuds 90 nm – 32 nm Ph.D. Thesis, Universite Joseph Fourier – Grenoble 1, 2005

[3] A. R. Powell, R. A. A. Kubiak, S. M. Newstead, C. Parry, N. L. Mattey, D. W. Smith et al., Elemental boron and antimony doping of MBE Si and SiGe structures grown at temperatures below 600 °C, Journal of Crystal Growth, 111 (**1991**) 1–4, 907–911

[4] A. Csik, G. A. Langer, G. Erdélyi, D. L. Beke, Z. Erdelyi, K. Vad, Investigation of Sb diffusion in amorphous silicon, Vacuum Volume 82, Issue 2, 29 October 2007, Pages 257–260 Proceedings of the 11th Joint Vacuum Conference (JVC-11)

[5] M. Uekubo, T. Oku, K. Nii, M. Murakami, K. Takahiro, S. Yamaguchi, T. Nakano, T. Ohta, WNx diffusion barriers between Si and Cu, Thin Solid Films, 286 (**1996**) 1–2, 170–175

[6] V. V. Jain, Microstructure and properties of copper thin films on silicon substrates. M. S. dissertation, Texas A&M University, 2007

[7] N. Benouattas, A. Mosser, A. Bouabellou, Surface morphology and reaction at Cu/Si interface – Effect of native silicon suboxide, Applied Surface Science, 252 (**2006**), 7572

[8] N. Benouattas, L. Osmani, L. Salik, C. Benazzouz, M. Benkerri, A. Bouabellou, R. Halimi, Epitaxial growth of copper silicides by bilayer technique on monocrystalline silicon with native SiOx, Materials Science and Engineering B, 132 (**2006**), 283

[9] C. Benazzouz, N. Benouattas, A. Bouabellou, Competitive diffusion of gold and copper atoms in Cu/Au/Si and Au/Cu/Si annealed

systems, Nuclear Instruments and Methods in Physics Research B, 230 (**2005**), 571

[10] C. Benazzouz, N. Benouattas, S. Iaiche, A. Bouabellou, Study of diffusion at surface of multilayered Cu/Au films on monocrystalline silicon, Nuclear Instruments and Methods in Physics Research B, 213 (**2004**), 519

[11] R. Halimi, A. Merabet, Kinetics of compound formation in Cu-Sb thin films, Surface Science, North-Holland, Amsterdam 223 (**1989**), 599–606

[12] M. Benkerri, R. Halimi, A. Bouabellou, N. Benouattas, Effect of Sb+ implantation on copper silicides formation and morphology after annealing of Cu/Si structures, Materials Science in Semiconductor Processing, 7 (**2004**), 319–324

[13] M. Benkerri, R. Halimi, A. Bouabellou, Antimony dopant redistribution during copper silicide formation, International Journal of Inorganic Materials, V3(8) (**2001**), 1299

[14] P. M. Fahey, P. B. Griffin, J. D. Plummer, Point Defects and Dopant Diffusion in Silicon, Review of Modern Physics, 61 (**1989**) 2, 289–384

[15] Y. G. Celebi, Copper Diffusion in silicon, Ph.D dissertation Texas Tech University USA 1998

[16] T. Heiser, A. Mesli, Determination of the copper diffusion coefficient in silicon from transient ion-drift, Applied Physics A: Materials Science & Processing, 57 (**2004**) 4, 325–328

[17] M. Hansen, Constitution of Binary Alloys, Ed. McGraw-Hill, New York, 1958

[18] H. Bracht, Copper related diffusion phenomena in germanium and silicon, Materials Science in Semiconductor Processing, 7 (**2004**) 3, 113–124

[19] E. R. Weber, Transition metals in silicon Applied Physics A: Materials Science & Processing, 30 (**2004**) 1, 1–22

[20] H. Bryngelsson, J. Eskhult, L. Nyholm, K. Edström, Thin films of Cu2Sb and Cu9Sb2 as anode materials in Li-ion batteries, Electrochimica Acta, 53 (**2008**), 7226–7234

[21] S. S. Lau, B. X. Liu, M. A. Nicolet, Ion mixing and phase diagrams, Nuclear Instruments and Methods in Physics Research, 209–210 (**1983**) 1, 97–105

[22] C. J. Smithells, Metals Reference Book, 5th Ed. Butterworths, London, 1976

[23] M. A. Nicolet, S. S. Lau, VLSI Electronics: Microstructure Science, Vol. 6, ed. by NG Einspruch, Materials and Process Characterization, ed. by NG Einspruch and GB Larrabee, Academic Press, New York 1983, Chap 7

[24] F. M. D'Heurle, P. Gas, The formation of Cu3Si: Marker experiments, J. Mater. Res. Soc., 1 (**1986**), 205

[25] C. A. Chang, High-temperature interaction studies of C/Cu/SiO2/Si and related structures, J. Appl. Phys., 66 (**1989**) 3, 1163

[26] D. Viale, G. Weber, B. Gillot, Growth of Cu3Si from CuCl vapor deposition on Si(100) oriented wafers, Journal of Crystal Growth, 102 (**1990**) 1–2, 269–280

UDK 691.5:691.26:620.187
Original scientific article/Izvirni znanstveni članek

ISSN 1580-2949
MTAEC9, 46(2)145(2012)

LIME-METAKAOLIN HYDRATION PRODUCTS: A MICROSCOPY ANALYSIS

PRODUKTI HIDRACIJE APNO-METAKAOLIN: MIKROSKOPSKA ANALIZA

André Leal Gameiro[1], Antonio Santos Silva[1], Maria do Rosário Veiga[1], Ana Luísa Velosa[2]

[1]National Laboratory of Civil Engineering, Av. do Brasil, 101, Lisbon, Portugal
[2]Department of Civil Engineering, Geobiotec, University of Aveiro, Aveiro
agameiro@lnec.pt

Prejem rokopisa – received: 2011-10-01; sprejem za objavo – accepted for publication: 2011-12-02

Metakaolin (MK) is nowadays a well-known pozzolanic material being used in cement-based materials, like mortars and concretes. The reaction of MK with calcium hydroxide yields cementitious products, being calcium silicate hydrate (CSH), stratlingite (C_2ASH_8) and tetra calcium aluminium hydrate (C_4AH_{13}) the main phases formed at ambient temperature. The transformation of stratlingite and C_4AH_{13} into hydrogarnet at long term is an important issue that may result in an increase in the porosity and a loss of compressive strength that can induce a complete material degradation.
With the objective of studying the compounds formed in lime/MK pastes and their stability during time, blended pastes were prepared with several substitution rates (in weight) of lime by MK, and maintained at RH > 95 % and 23 ± 2 °C. XRD and TGA-DTA were used to follow the kinetics of the lime/MK hydration as well the reaction products. Microscopic tests (SEM-EDS) results are performed and compared with the thermal and mineralogical data. The results obtained show that the quantity of the hydration products formed changes with the lime replacement, being the aluminum and calcium silicates more abundant in the higher MK content pastes, and C_4AH_{13}, C_4ACH_{11} and C_2ASH_8 the major phases formed up to 90 days of curing.

Keywords: microscopy, XRD, TGA-DTA, lime, metakaolin

Metakaolin (MK) je danes dobro poznan pocolanski material in se uporablja v gradivih na podlagi cementa, npr. malta in beton. Reakcija MK s kalcijevim hidroksidom ustvari cementne proizvode: kalcijev silikatni hidrat (CSH), stratlingit (C_2ASH_8) in tetra kalcij aluminijev hidrat(C_4AH_{13}) kot glavne faze, ki nastanejo pri temperaturi okolice. Transformacija stratlingita in C_4AH_{13} v hidrogarnet po dolgem času je proces, ki lahko poveča poroznost in zmanjša tlačno trdnost ter lahko povzroči popolno degradacijo materiala.
S ciljem raziskave spojin, ki so nastale v zmeseh apno-MK, in njihove časovne stabilnosti smo pripravili mešane mase z več deleži zamenjave (v masi) apna z VK in zorili pri RH > 95 % in 23 ± 2 °C. XRD in TGA-DTA so bile uporabljene za spremljanje kinetike hidracije apna-MK in reakcijskih produktov. Rezultate mikroskopskih opazovanj (SEM-EDS) smo primerjali s termalnimi in mineraloškimi podatki. Dobljeni rezultati kažejo, da količina hidracijskih produktov z nadomestitvijo količine apna količina aluminijevih in kalcijeviih silikatov raste z vsebnostjo MK v masi in so C_4AH_{13}, C_4ACH_{11}, C_2ASH_8 glavne faze, nastale po 90 dneh zorenja.

Ključne besede: mikroskopija, XRD, TGA-DTA, apno, metakaolin

1 INTRODUCTION

During the past decade, metakaolin (MK), a thermally activated aluminosilicate material ($Al_2O_3{\cdot}2SiO_2$) obtained by calcination of clay or soil rich in kaolinite ($Al_2(OH)_4Si_2O_5$), within the temperature range of 700–850 °C [1], has been the objective of several research studies, mainly due to its capacity to react vividly with calcium hydroxide (pozzolanicity). Recent studies[2] showed that MK is a very effective pozzolan, altering the pore structure of the lime and cement pastes and greatly improving its resistance to the transport of water and diffusion of harmful ions through the matrix, supporting the idea of its beneficial addition in blended mortars, cement pastes and concrete.

The reaction between MK, calcium hydroxide and water results in the formation of hydraulic products. At ambient temperature the main phases/products formed are calcium silicate hydrate gel (CSH), stratlingite (C_2ASH_8) and tetra calcium aluminium hydrate (C_4AH_{13}). According to literature[3], it is possible to assume that these hydration phases are linked to lime/MK ratio, temperature, and also to the presence of various activators. However, reference to variations regarding these phase's stability has been shown in literature[4]. As stated by P. S. Silva and Glasser, transformation of stratlingite and C_4AH_{13} into hydrogarnet (C_3AH_6) at long term may lead to a volume reduction, producing an increase in porosity and a loss of microstructural compactness, i.e., less mechanical strength.

Having the aim of studying the compounds obtained in lime/MK pastes and their stability overtime, it is important to discuss a possible conversion of metastable hexagonal hydrates (C_2ASH_8 and C_4AH_{13}) to stable cubic phase (siliceous hydrogarnet with variable composition, $C_3AS_xH_{6-2x}$), when samples are submitted to ambient curing temperatures at long term ages, negatively influencing the performance of MK blended matrixes, especially on durability[5].

Most of the works published up to now on lime/MK systems are focused on reaction kinetics and on its interaction with Portland cement[3,5,6]. However, there is

little information on microstructure and mechanical characteristics of the lime/MK pastes[6].

In order to study the development of hydration phases of the lime/MK systems, pastes with different mixing mass ratios of lime/MK were prepared and afterwards cured at 23 °C and RH > 95 %.

At certain curing ages, XRD and TGA-DTA were used to follow the kinetics of the blended MK pastes as well the reaction products formed, while microscopic tests (SEM-EDS) results are performed and compared with the thermal and mineralogical data.

2 EXPERIMENTAL

The mix procedure consisted in mixing the amount of lime with the total amount of water, which was stirred for about 3 min using an external mixer, after which MK was added slowly, maintaining the mixing for further 20 min.[7] The pastes were then stored in open plastic containers and introduced in a sealed chamber at RH > 95 % and 23 ± 2 °C, to maintain on-going hydration reactions. The hydration was stopped after each predetermined curing time, subjecting the samples to acetone for complete removal of the free water, after which they were then dried at 40 °C, in order to be tested by XRD, TGA-DTA and SEM-EDS. The metakaolin used was ARGICAL M1200S from IMERYS with the mass fractions $SiO_2 \approx 55$ % and $Al_2O_3 \approx 39$ % regarding chemical composition, while the lime used was a commercial Portuguese (Lusical H100) hydrated lime with a chemical composition of $Ca(OH)_2 \geq 93$ and MgO ≤ 3, with classification CL90, according to the NP EN 459-1(2002) standard.

The evolution of the kinetic reactions as well as the phases formation was evaluated by X-ray diffractometry (XRD), thermogravimetric and differential thermal analysis (TGA-DTA) and scanning electron microscopy with X-ray microanalysis (SEM-EDS). The experimental conditions used are previously published[8].

3 RESULTS AND DISCUSSION

In order to illustrate the main results obtained two pastes were selected with lime/MK mass ratios of 1/1 and 1/0.2.

3.1 X-ray diffraction analysis (XRD)

XRD patterns are illustrated in **Figures 1a** and **b**. A peak attributed to stratlingite (C_2ASH_8) is noted for paste MK1. The stratlingite tends to increase with the curing time, becoming the dominant phase, whereas significant amounts of monocarboaluminate ($C_4A\overline{C}H_{11}$), quartz, calcite, calcium silicate hydrates (CSH) and calcium aluminate hydrates (C_4AH_{13}) are observed. Although in paste MK02 stratlingite is not detected by XRD, it is possible that it may be present in very low, undetected quantity. An interesting result was also observed in paste MK1 up to 28 d of curing regarding the presence of calcium aluminates hydrates ($C_4A\overline{C}H_{11}$ and C_4AH_{13}), whereas at further ages (56 d and 90 d) only traces of these compounds are identified, presumably signifying that a decomposition of these phases may have occurred. Traces of crystallized CSH were detected in higher MK mixes.

In MK02 paste high amounts of portlandite (CH) are observed, however a maximum peak is noticed for 56 d and 90 d of reaction, possibly due to the decomposition of C_4AH_{13} and monocarboaluminate, liberating more portlandite to the system, also observed for paste MK1. The XRD confirms also up to 90 d the non-formation of hydrogarnet phase for both pastes, which can be explained due to the fact that this compound is associated with higher curing temperatures. Reports of the absence of hydrogarnet until 270 d of curing time are shown by other authors[6].

An important reference must be attributed to the fact that for both pastes the calcite ($CaCO_3$) content tends to increase up to 90 d of curing.

Several studies have reported the appearance C_4AH_{13} or $C_4A\overline{C}H_{11}$ and C_2ASH_8 and CSH at 20 °C[5] as the reaction products of the lime/MK hydration reaction. In other studies[4], C_2ASH_8 and CSH are considered the main phases formed, however in this research, the formation

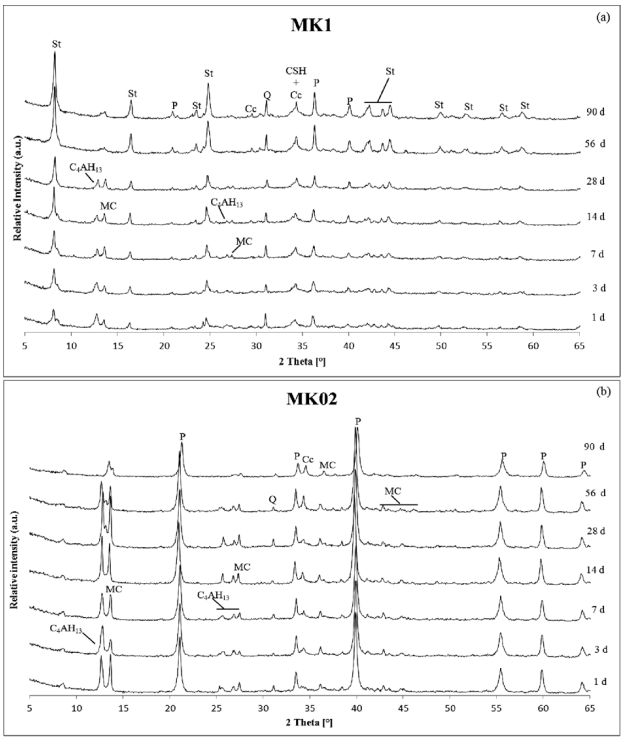

Figure 1: XRD patterns for a) MK1 and b) MK02; Cc – calcite; P – portlandite; MC – monocarboaluminate; St – stratlingite; CSH – calcium silicate hydrate; C_4AH_{13} – tetracalcium aluminium hydrate

Slika 1: XRD-spektri za a) MK1 in b) MK02; Cc – kalcit, P – portlandit, MC – monokarboaluminat, St – stratlingit, CSH – kalcijev silikat hidrat, C_4AH_{13} – tetrakalcij aluminijev hidrat

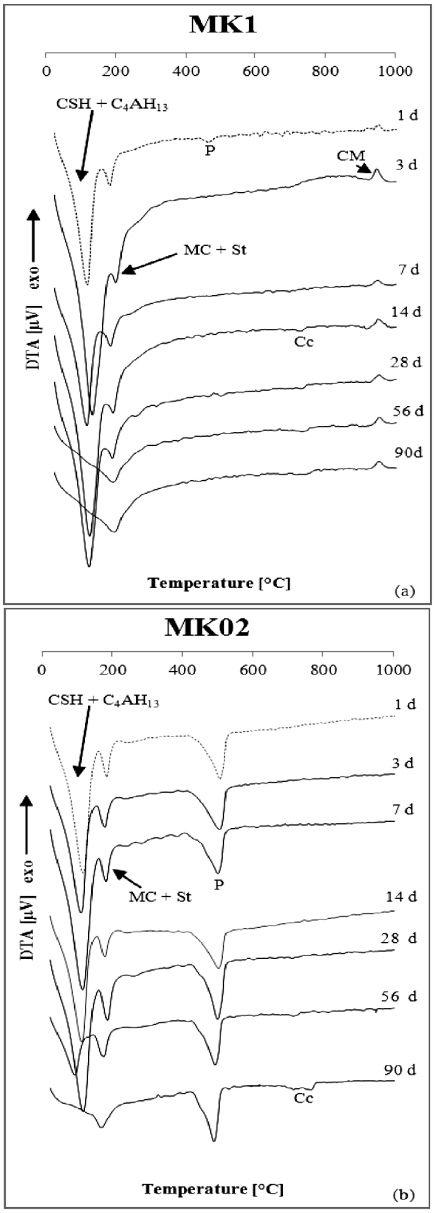

Figure 2: DTA curves for a) MK1 and b) MK02; P – portlandite; CM – cristoballite and mullite; St – stratlingite; CSH – calcium silicate hydrate; Cc – calcite; MC – monocarboaluminate; C_4AH_{13} – tetracalcium aluminum hydrate

Slika 2: DTA-spektri za a) MK1 in b) MK02; P – portlandit, CM – kristobalit in mulit, St – stratlingit, CSH – kalcijev silikat hidrat, Cc – kalcit, MC – monokarboaluminat, C_4AH_{13} – tetrakalcijev aluminijev hidrat

of CSH, C_4AH_{13}, $C_4A\overline{C}H_{11}$ and C_2ASH_8 have been identified.

3.2 TGA-DTA analysis

Figures 2a and **b** present the DTA curves of MK1 and MK02. The sharp peak observed at about 110 °C can be attributed to the presence of CSH and C_4AH_{13}, being sharper for 28 d, disappearing after 90 d of reaction. The characteristic peak of stratlingite, which appears as a sharp peak at about 190 °C, can be observed for MK1,

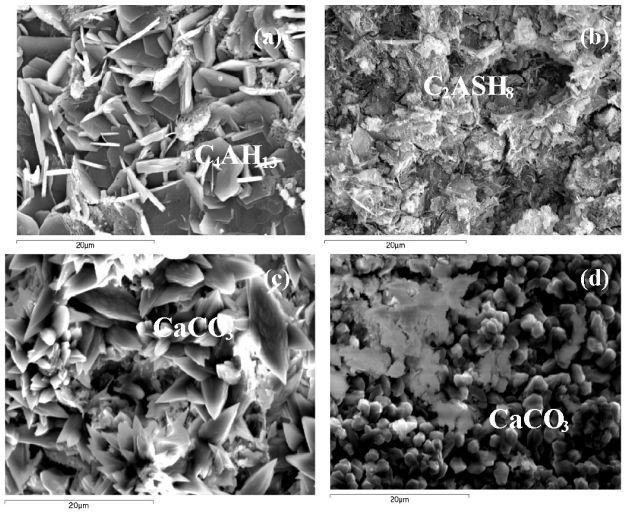

Figure 3: SEM micrographs of MK1 and MK02 at ages 28 d and 90 d: a) SEM image of MK1 paste at 28 d where the presence of hexagonal C_4AH_{13} is visible; b) SEM image of MK1 at 90 d where is visible the predominance of C_2ASH_8; c) SEM image of MK02 at 28 d of curing; revealing the presence of $CaCO_3$; d) SEM image of MK02 paste at 90 d of curing where is visible an increase in the paste carbonation rate

Slika 3: SEM-posnetki MK1 in MK02 po zorenju 28 d in 90 d: a) SEM-posnetek MK1-mase po 28 d, kjer je viden heksagonalni C_4AH_{13}, b) SEM-posnetek MK1 po 90 d, kjer je vidna prevlada C_2ASH_8, c) SEM-posnetek MK02 po 28 d, ki dokazuje prisotnost $CaCO_3$, d) SEM-posnetek MK02, kjer se v masi vidi rast hitrosti karbonacije

however, a broader peak after 90 d of curing. In the same range of temperature (≈160–220 °C) the dehydration of $C_4A\overline{C}H_{11}$ (monocarboaluminate) occurs.

For paste MK1 a small broad peak at about 480 °C is present at 1 d reaction, indicative of the existence of free portlandite, being almost consumed after 1 d of curing (**Figure 2a**). Instead, for paste MK02, a sharper band can be seen at approximately 500 °C (**Figure 2b**), due to free portlandite in the reaction.

As referred above at about 950 °C, a sharp exothermic peak was only observed for paste MK1, attributed to the formation of high-temperature phases such as mullite and cristobalite, as described by Bakolas, appearing due to the existence of "free" MK. These peaks do not appear in paste MK02 due to the total amount of MK being rapidly consumed.

3.3 SEM results

Figures 3a, b, c and **d** show the main results of the SEM-EDS. Paste MK1 at 28 d of reaction presents (**Figure 3a**) a well-crystallized matrix, with large amounts of C_4AH_{13}; instead at 90 d of curing (**Figure 3b**) the paste matrix is more "densified" and less crystalline with a large presence of stratlingite. In paste MK02 (**Figures 3c** and **d**), the microstructure "evolution" does not vary like in MK1 from 28 d to 90 d, remaining as a crystalline microstructure, revealing high amounts of calcite.

4 CONCLUSIONS

The influence of the lime/MK ratio was studied at ambient temperature and RH > 95 %. According to the results obtained the products formed are the same for all blended mixes, while the amount formed changes with the MK content, being the aluminum (C_4AH_{13}, $C_4A\overline{C}H_{11}$) and calcium silicates (C_2ASH_8) more abundant in the higher MK content pastes. SEM results show that for MK1 at 28 d the microstructure consists essentially of C_2ASH_8 and C_4AH_{13} and $C_4A\overline{C}H_{11}$, while at 90 d of curing there is a significant decrease of the presence of calcium aluminate hydrates, and a predominance of stratlingite. On the contrary, the MK02 paste reveals a highly crystalline microstructure, with predominance of calcite. Up to 90 d of curing time, no hydrogarnet presence is detected, in any of the blended pastes studied. A decrease in the amount of C_4AH_{13} and $C_4A\overline{C}H_{11}$ with curing time is verified, not followed by a decrease in microstructural porosity, that may influence for mixtures with low MK content a decrease in the mechanical resistance of the blended lime/MK mixes. The results show the formation of hydration products that may confer mechanical resistance to lime/MK mortars.

Acknowledgments

The authors wish to acknowledge the Fundação para a Ciência e Tecnologia (FCT) for the financial support under project METACAL (PTDC/ECM/100431/2008) and to the enterprises Lusical and IMERYS for the supply of the lime and metakaolin used in this work.

5 REFERENCES

[1] C. S. Poon, L. Lam, C. S. Kou, Wong, Y. L., Wong, Ron, Rate of pozzolanic reaction in high-performance cement pastes, Cement and Concrete Research, 31 (**2001**), 1301–1306

[2] S. S. Sabir, S. Wild, J. Bai, Metakaolin and calcined clays as pozzolans for concrete: a review, CEm. Concr. Compos., 23 (**2001**), 441–454

[3] J. Cabrera, M. Frías, Influence of MK on the reaction kinetics in MK/lime and MK-blended cement systems at 20 °C, Cement and Concrete Research, 31 (**2001**), 519–527

[4] P. S. De Silva, F. G. Glasser, Phase relation in the system $CaO\text{-}Al_2O_3\text{-}SiO_2\text{-}H_2O$ relevant to metakaolin-calcium hydroxide hydration, Cem. Concr. Res., 23 (**1993**) 3, 627–639

[5] M. Frías Rojas, Study of hydrated phases present in a MK-lime system cured at 60 °C and 60 months of reaction, Cement and Concrete Research, 36 (**2006**), 827–831

[6] A. Bakolas, E. Aggelakopoulou, A. Moropoulou, S. Anagnostopoulou, Evaluation of pozzolanic activity and physico-mechanical characteristics in metakaolin-lime pastes, Journal of Thermal Analysis and Calorimetry, 84 (**2006**) 1, 157–163

[7] A. Moropoulou, A. Bakolas, E. Aggelakopoulou, Evaluation of pozzolanic activity of natural and artificial pozzolans by thermal analysis, Thermochimica Acta, 420 (**2004**), 135–140

[8] A. Gameiro, A. Santos Silva, R. Veiga, A. Velosa, Phase and microstructural characterization of lime-MK blended mixes, Proc. of the VI International Materials Symposium MATERIAIS 2011, April 2011; 6 pages

UDK 621.77
Original scientific article/Izvirni znanstveni članek

ISSN 1580-2949
MTAEC9, 46(2)149(2012)

THE IMPACT OF DIE ANGLE ON TOOL LOADING IN THE PROCESS OF COLD EXTRUDING STEEL

VPLIV KOTA MATRICE NA OBREMENITEV ORODJA PRI HLADNI EKSTRUZIJI JEKLA

Saša Randjelović[1], Miodrag Manić[1], Miroslav Trajanović[1], Mladomir Milutinović[2], Dejan Movrin[2]

[1]University of Niš, Faculty of Mechanical Engineering, Serbia
[2]University of Novi Sad, Faculty of Technical Science, Serbia
sassa@masfak.ni.ac.rs

Prejem rokopisa – received: 2011-10-20; sprejem za objavo – accepted for publication: 2011-12-08

This paper presents an analysis of tool loading in the technology of the cold forward extrusion of steel. In the process of plastic deformation it is necessary to know the contact stress as a prerequisite for a more accurate analysis of the stress and strain on the internal structure of the continuum. In this way, accurate boundary conditions at the contact surfaces are obtained for the achieved conditions of deformation, which represent the starting values for generating numerical approximations of the plasticity parameter changes within the deformable volume. In the process of the forward extrusion of steel the workpiece material is exposed to all-round pressure during the entire process. Due to the high surface pressure at the head of the punch and the solid walls of the die, the material flows in the direction of the opening of the exchangeable conical surfaces of the die. During the extrusion process, the greatest resistance occurs in the direction of the axis displacement, i.e., the head punch, while the walls of the tools suffer considerably smaller loads. However, this has crucial importance for the accuracy and the quality of the finished part.

Keywords: cold extrusion, angle die, contact stress, FEM

V članku je opisana analiza obremenitve orodja pri hladni ekstruziji jekla v smeri naprej. Pri procesu plastične deformacije je treba poznati kontaktno napetost, ki je prvi pogoj za bolj natančno analizo napetosti in deformacije na notranjo strukturo kontinuuma. Tako je mogoče doseči natančne mejne razmere na kontaktnih površinah pri določenih pogojih deformacije, ki so začetne vrednosti za generiranje numeričnih približkov spremembe parametrov plastičnosti v deformabilnem volumnu. Pri ekstruziji materiala v smeri naprej je prešanec med celotnim procesom izpostavljen okolišnjemu pritisku. Zaradi visokega površinskega pritiska na čela trna in trdne stene valjastega orodja material teče v smeri premika osi, torej čela trna, medtem ko je obremenitev stene orodja mnogo manjša, vendar je zelo pomembna za natančnost in kakovost iztiskanca.

Ključne besede: hladna ekstruzija, kot matrice, kotaktna napetost, FEM

1 INTRODUCTION

Analyses of the uni-directional extrusion process have been made by many authors. First of all, this is a process of volume deforming in which the workpiece material is subjected to overall pressure throughout the entire process. Due to the high surface pressure on the extruder head and on the rigid matrix walls, the material flows towards the opening on the conical matrix surfaces. During the extrusion process the greatest forces occur in the extrusion axis direction, i.e., on the punch head and on the matrix walls.

Many examples from industry show, in a clear manner, that realistic lifetime calculations for cold-forging tools should be focused on the accurate prediction of the number of load cycles until the appreciable continual damage or the initiation of fatigue cracks.

In addition, the results gained from previous investigations show that lifetime predictions only based on finite-element analyses are characterised by intolerable inaccuracies[1].

2 EXPERIMENTAL SET-UP

The satisfying experimental matrix rigidity and annulling of high pressure in the radial direction can be achieved in two ways. One of them is to increase the matrix-wall thickness up to a certain limit, thus obtaining the required matrix rigidity. The other solution is installing the clamping-ring application, thus bringing the matrix body into a pre-stress state of the opposite sign with respect to the stresses occurring during the extrusion process itself.

If, in the first case, we regard the receiver as a fairly thick pipe of outer diameter D_1, under high inner pressure loading, then its walls are subjected to a radial stress of pressure R_r and tangential extension stress R_t whose greatest value is on inner receiver diameter D_0.

$$R_r = -p,\ R_t = \frac{a^2+1}{a^2-1} \cdot p = C \cdot p \qquad (1)$$

where $a = D_1/D_0$.

By superposition these two stresses, according to the plastic yield hypothesis, the following overall stress is obtained:

$$R_u = \sqrt{R_r^2 + R_t^2 - R_r R_t} = p \cdot \sqrt{1 + C + C^2} \qquad (2)$$

Assuming that, for instance, the outer receiver diameter is four times larger than the inner diameter, i.e., $a = 4$, we find that $R_u = 1.85 \cdot p$.

Along with the further increase of the outer diameter, the overall stress reduction in the receiver walls is not adequate. In the case when $a = 10$, which is not quite justified in real exploitation conditions, $C = 1.02$ and $R_u = 1{,}75p$ is obtained, i.e., the overall stress reduction is 9.5 % along with an outer receiver dimension increase of 2.5 times. Since the receiver must remain in the elasticity range, i.e., since there must be no plastic deformation ($R_u < R_e$) throughout the process, we can approximately determine the greatest value of the working pressure in the receiver made of alloyed tool steel submitted to heat treatment:

$$R_e \approx 2\ 000 \text{ MPa}, \; p_{max} = 1\ 100 \text{ MPa}$$

The above-presented analysis has been used as the basis for experimental tool design for the forward-extrusion procedure. Unlike the exploitation tools, these tools, **Figure 1**, enable an extrusion force measurement on the punch as well as that of the radial forces in the lower part of the tool on the receiver wall.

The extrusion force on the punch can be measured in many ways. In this investigation, the choice of measurement procedure is made by means of the universal force transducer (2 000 kN), which can be placed either in the upper or the lower part of the tool, as is our case, through which the overall loading is transmitted along the extrusion axis. For the measurement of the radial forces, the measuring pin load-cell method (**Figure 2**), ascribed Plancak et al.[2], is the most suitable for this kind of plastic metal-deforming process.

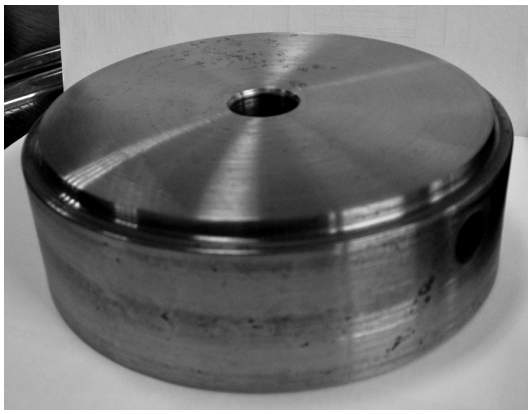

Figure 1: Experimental tool, receiver
Slika 1: Eksperimentalno orodje: prejemnik

Figure 2: Measuring pin load-cell for radial forces
Slika 2: Merilna celica s trni za radialne sile

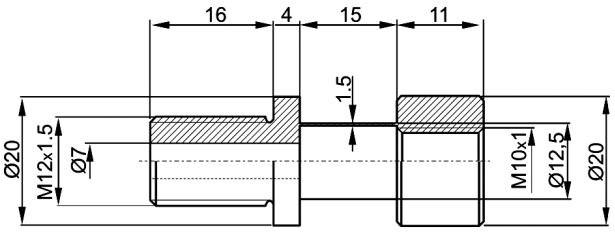

Figure 3: Measuring capsule
Slika 3: Merilni valj

The loading due to the contact between the workpiece and three measuring pins is transmitted to the measuring capsule (**Figure 3**) placed on the outer matrix wall.

The extension of the measuring wall of the capsule which is 1.5 mm thick, due to the radial forces in the receiver tool, actually yields the loading magnitude on the matrix walls. On each capsule wall there are two measuring bands HBM (measurement and compensation ones) glued and joined into a semi-bridge (Wheatstone) necessary to carry out their calibration with a known loading and thus set up a relation between the capsule wall elongation and the force being transmitted.

In order to obtain complete information about the magnitude and the kind of stress throughout the extrusion process, the measuring pins distribution is defined by the matrix geometry as well as the workpiece size. For these reasons, there are three measuring pins

Figure 4: Experimental tool, receiver with three measuring pin load-cells
Slika 4: Eksperimentano orodje: prejemnik s tremi merilnimi trni

placed in radial way in the extrusion matrix body at an angle of 120° to the measuring pin that is in direct contact with the workpiece during the extrusion process. In order to obtain complete information about the loading magnitude during the process, the measuring pins are placed at various heights in the material receiver (**Figure 4**).

In order to provide for variants of the presented tool solution, the very deformation focus (conical matrix part) and calibration zone are made in special dies introduced into the matrix body. The characteristic conical tool surface, on the given matrices, has three values of the angle, i.e., 60°, 90° and 120° (**Figure 5**), which will directly affect both the extrusion forces and the radial forces in the tool.

The material of the workpiece was low-carbon steel Ck 10 (DIN) for cold forging[3]. The flow stress at room temperature was modeled by the strain hardening function $K = 285 + 539.7 \cdot \varphi^{0.304}$ MPa, obtained from the Rastegaev compression test according reference[3]. The Young's modulus and the Poisson's ratio were 210 GPa and 0.3, respectively. FEM analysis was performed on a constant friction model, with the friction factor $m = 0.5$ K.[4]

3 SIMULATION RESULTS AND FEM ANALYSES

The coordinate system for presenting the results comprises a time x-axis with the number of readings equal to 800 with a step, the time interval between two signals of 0.003 s as well as the *y*-axis with the force in kN on the x-axis one part is singled where the workpiece extrusion process and the extruded-part ejection process are marked.

The measurement results show a certain regularity (**Figures 6, 7** and **8**) and similar effects can be noticed in all the extrusion processes. The force upon the punch shows, before the very extrusion process, a marked instability as well as a very high increase, after which it drops to its minimal value throughout the overall

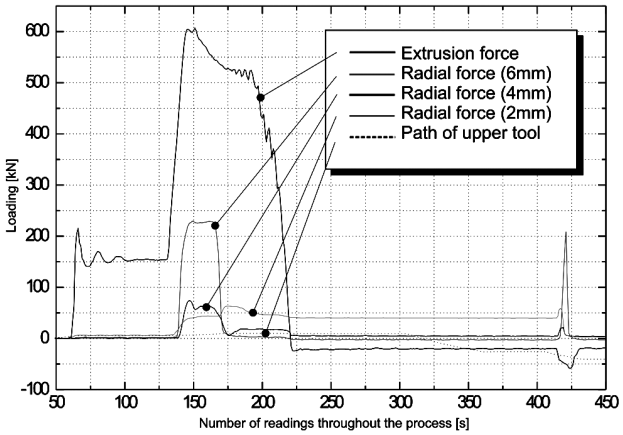

Figure 6: Force distribution at a die angle of 60°
Slika 6: Sile pri kotu matrice 60°

deforming process. The force instability, as well as its increase, can be explained by considering the most favorable initial position of the workpiece in the tool and by the needed – relatively high – force for the very beginning of the material flow on the matrix insert walls. A marked force drop shows that the first phase is completed, that the material filled up the input part of the cone; after that the force starts to increase rapidly to a maximum, after which the material flow on the conical tool parts begins. The maximum value has a marked increase along with the matrix-angle increase.

In all diagrams the radial forces are denoted by the relative height at which they were measured. Namely, as there is a difference regarding the height of the place at which the pin contact to the workpiece; at every 2 mm from the upper edge of the matrix insert, at mutual matrix angles of 120°, there is a different increase in the given forces recorded. In the beginning of the process, the maximum radial force is achieved at the highest pin with respect to the matrix insert at the moment when the extrusion force achieves its maximum value, i.e., when the initial unstable phase is completed and the material

Figure 5: Extrusion matrices with various cone angles
Slika 5: Ekstruzijske matrice z različnimi koti

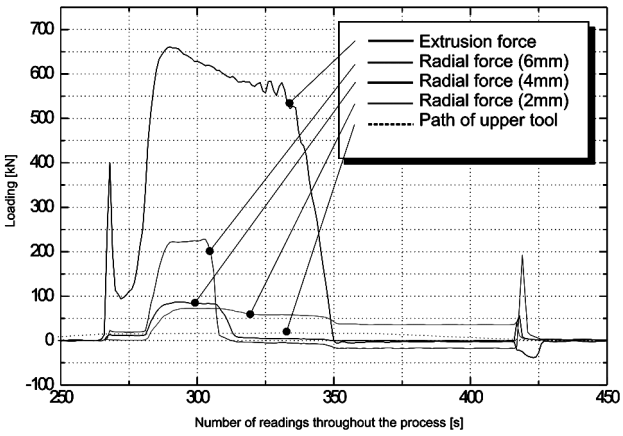

Figure 7: Force distribution at a die angle of 90°
Slika 7: Sile pri kotu matrice 90°

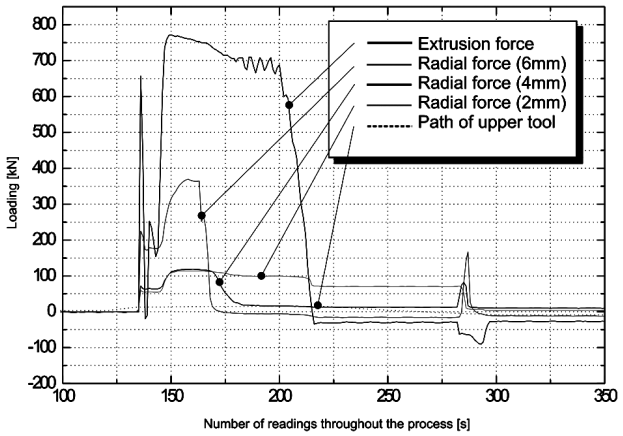

Figure 8: Force distribution at a die angle of 120°
Slika 8: Sile pri kotu matrice 120°

flowness has already started. This is explained by the very workpiece itself at this particular moment (barrel-like form in the receiver) and immediately after it, when the workpiece material filled up the whole material receiver volume and when its "maximum diameter slides" along the matrix walls. After reaching its maximum value as well as its retention, this force drops to almost a zero value. A less distinct maximum is reached by the radial force on the second pin, at the height of 4 mm from the die insert, but in an almost identical period of time when the first radial force reaches its maximum. The lowest pin with respect to the matrix pickup records almost the same magnitude of radial force as that on the second pickup, but it can clearly be seen that it preserves this value, with some slight decline, until the end of the extrusion process, since the non-extruded volume of the material from the receiver also remains at its height.

The extrusion force on the extruder has values ranging from 560 kN to 600 kN in the matrix with the smallest cone angle of 60°, i.e., 660 kN to 690 kN for the matrix with a cone angle of 90°, or to 720–790 kN in the

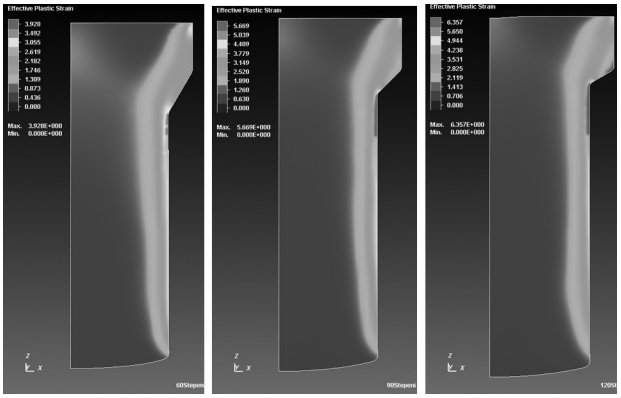

Figure 9: Field of efective plastic strain at three die angles: 60°, 90° and 120°
Slika 9: Polje efektivnih plastičnih deformacij pri treh kotih matrice 60°, 90° in 120°

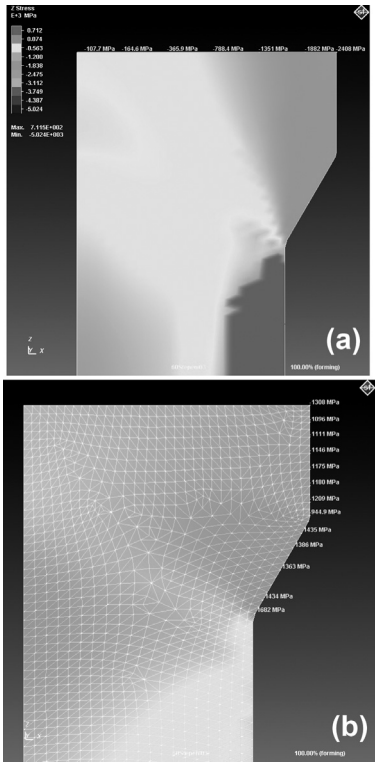

Figure 10: Contact stress at a die angle of 60°: a) on the punch and b) on the receiver wall in the radial direction
Slika 10: Kontaktne napetosti pri kotu 60°: a) na batu in b) na steni prejemnika v radialni smeri

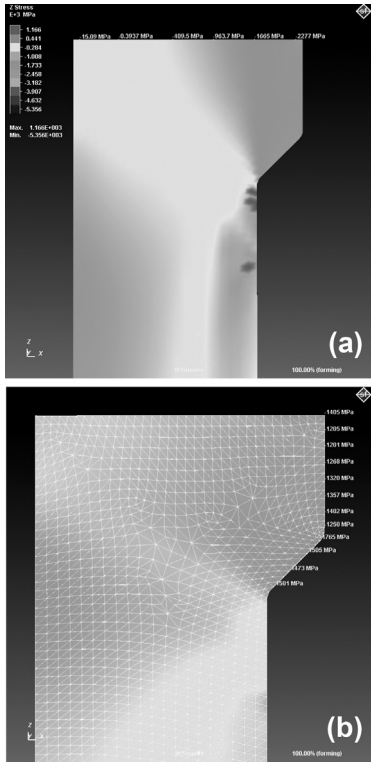

Figure 11: Contact stress at a die angle of 90°: a) on the punch and b) on the receiver wall in the radial direction
Slika 11: Kontaktne napetosti pri kotu 90°: a) na batu in b) na steni prejemnika v radialni smeri

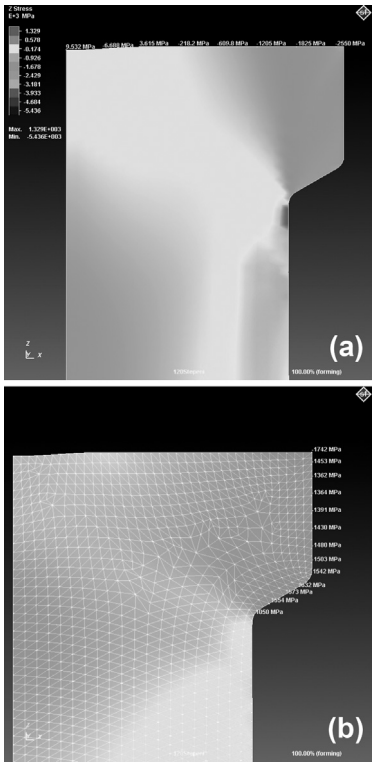

Figure 12: Contact stress at a die angle of 120°: a) on the punch and b) on the receiver wall in the radial direction

Slika 12: Kontaktne napetosti pri kotu 120°: a) na batu in b) na steni prejemnika v radialni smeri

matrix with a cone angle of 120°. Reduced to the cross-sectional area of the workpiece, over which this force is transmitted, working pressures of 1900–2500 N/mm^2 occur in the extrusion process. The radial force on the matrix wall, depending on the cone angle, moves in the interval from 50 kN to 230 kN for 60°, i.e., from 70 kN to 230 kN for 90° and 100 kN to 350 kN for 120°. The force increase follows the height of the measurement place on the receiver wall. In the radial direction there are considerably smaller pressures and they move within the limits from 945 N/mm^2 to 1742 N/mm^2.

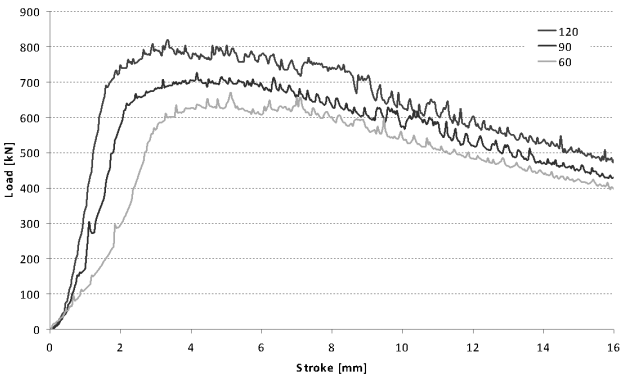

Figure 13: Loading distribution during the working stroke

Slika 13: Razporeditev obremenitev med delovnim ciklom

On the right-hand side of all the diagrams, there is a marked instability of all the forces associated with the ejection phase of the extruded piece from the die and the matrix itself.

A numerical 2D Finite-Element Method (FEM) analysis of the investigated models of forward extrusion was performed using Simufact. Forming 10.0 software package[5]. The commercial FEM package enabled the entire forming process to be simulated, while simultaneously predicting a large number of parameters at both the workpiece and the tool[6]. In this paper the FEM is employed to predict stress-strain state, the forming load and the geometry of the workpiece. To simulate the process, a model of elastic-plastic material for the workpiece was chosen, as the die and punch are considered to be rigid bodies. Due to the axial-symmetry of the deformation process, only one-half of the workpiece was modeled. The displacement of the punch is defined to be 16 mm and the punch velocity as 0.1 mm/s.

The workpiece model was initially meshed with advancing front quad elements with a size of 0.3 mm, the total number of which was 2 220. In the simulation, the remeshing of the starting elements was executed in the most highly deformed zones of the workpiece. The remeshing procedure was performed at every five increments in order to minimize the effect of the tool penetration through the elements due to large workpiece deformations.

Stress-strain components within the workpiece volume obtained by the FE analysis are shown in **Figures 9, 10, 11** and **12**. It is significant that the stress-strain state is very heterogeneous[7].

The FEA-simulation-predicted load-stroke diagram closely resembles the ones obtained experimentally (**Figure 13**). Initially, the load increases quickly up to 1.8 mm (120°), 2.2 mm (90°) and 3.4 mm (60°) of the punch stroke. As the punch stroke progresses further, the load continues to increase gradually. The final phase is marked by a noticeable load decrease.

4 CONCLUSIONS

The analysis of the tool loading points to the order of the loading magnitude as well as the force effect distribution over time during the process. The tool loading is of a variable character and the order of magnitude directly depends on the workpiece diameter, the finished part diameter and the extrusion angle in the deformation focus. The measurement itself aims at pointing to the loading magnitude at the contact surfaces, while, in further work, this could serve as input data for solving the stress-distribution equations with respect to the volume of the extruded part.

A special set of interchangeable tools, with three different angle dies, condition different values and levels of change in the radial force, as well as the degree of damage to the tools, which directly affect its service life,

is used. The change of radial force in time points to the changeable shape of the workpiece during the process and to the surface of contact within the receiver tool.

Acknowledgement

This paper is part of the project III41017 Virtual human osteoarticular system and its application in preclinical and clinical practice, funded by the Ministry of Education and Science of the Republic of Serbia (http://vihos.masfak.ni.ac.rs).

5 REFERENCES

[1] B. Falk, U. Engel, M. Geiger, Fundamental aspects for the evolution of the fatigue behaviour of cold forging tools, Journal of Materials Processing Technology, (**2001**), 158–164

[2] M. Plancak, A. N. Bramley, F. H. Osman, Some observations on contact stress measurement by pin load cell in bulk metal forming, Journal of Materials Processing Technology, (**1996**), 339–342

[3] Steels for cold forging – their behaviour and selection, ICFG document No.11/01, ISBN 3-87525-148-2, 2001

[4] K. H. Jung, H. C. Lee, J. S. Ajiboye and Y. T. Im, Characterization of Frictional Behavior in Cold Forging, Tribology Letters, 37 (**2010**), 353–359

[5] Simufact.Forming. 10.0. Documentation

[6] J. Kusiak, M. Pietrzyk, J. L. Chenot, Die Shape Design and Evaluation of Microstructure Control in the Closed die Axisymetric Forging by Using FORGE2 Program, ISIJ International, 34 (**1994**) 9, 755–760

[7] Z. Peng, T. Sheppard, A study on material flow in isothermal extrusion by FEM simulation, Modelling and simulation in materials science and engineering, 12 (**2004**), 745–763

UDK 621.74.047:536.421.4:519.61/.64
Original scientific article/Izvirni znanstveni članek

ISSN 1580-2949
MTAEC9, 46(2)155(2012)

FINAL-STRUCTURE PREDICTION OF CONTINUOUSLY CAST BILLETS

NAPOVED KONČNE MIKROSTRUKTURE KONTINUIRNO ULITIH GREDIC

Josef Štětina, Lubomír Klimeš, Tomáš Mauder, František Kavička

Brno University of Technology, Technická 2, 616 69 Brno, Czech Republic
stetina@fme.vutbr.cz

Prejem rokopisa – received: 2011-10-20; sprejem za objavo – accepted for publication: 2012-01-09

In steel production, controlling and monitoring quality, grade and structure of final steel products are very important issues. It has been shown that the temperature distribution, the magnitude of temperature gradients, as well as the cooling strategy during the continuous steel casting have a significant impact on material properties, the structure and any defect formation of cast products. The paper describes an accurate computational tool intended for investigating the transient phenomena in continuously cast billets, for developing the caster control techniques and also for determining the optimum cooling strategy in order to meet all quality requirements. The numerical model of the temperature field is based on the finite-difference implementation of the 3D energy-balance equation using the enthalpy approach. This allows us to analyse the temperature field along the entire cast billet. Since the steel billets are produced constantly 24 hours per day, the transient temperature field is being computed in a non-stop trial run. It enables us to monitor and investigate the formation of the temperature field in real time within the mould, as well as the secondary and tertiary cooling zones, where the observed information can be immediately utilized for the caster-control optimization with respect to the whole machine or just an individual part. The application of the presented model is demonstrated with two examples including the steelworks in Třinec, Czech Republic, and in Podbrezová, Slovakia. To consider different operational conditions, the influences of the secondary-cooling setting on the surface and the inner defects formation, and on the final structure of the 150 × 150 mm billet are also discussed.

Keywords: concast billet, numerical model, solidification

Pri proizvodnji jekla je pomembno izvajanje kontrole kvalitete, vrste in mikrostrukture končnih proizvodov. Prikazano je, da ima razporeditev temperature, razpon temperaturnega gradienta, kot tudi strategija ohlajanja med kontinuirnim ulivanjem pomemben vpliv na lastnosti materiala, mikrostrukturo in možnost nastanka napak v litem proizvodu. V članku je predstavljeno natančno računalniško orodje za preiskave prehodnih pojavov v kontinuirno uliti gredici. Orodje je namenjeno razvoju kontrolne tehnike in tudi za določanje optimalne strategije ohlajanja za doseganje zahtevane kakovosti. Numerični model temperaturnega polja temelji na uporabi končnih diferenc 3D-enačbe energijskega ravnotežja z uporabo entalpije. Omogoča analizo temperaturnega polja vzdolž celotne lite gredice. Ker je proizvodnja gredic stalna, 24 ur na dan, je bilo prehodno temperaturno polje izračunano za neprekinjeno preskusno obratovanje. Omogočena je kontrola in preiskava nastanka temperaturnega polja v realnem času v kokili, v sekundarni in terciarni hladilni coni. Ugotovljena informacija se lahko neposredno uporabi za optimiranje celotne livne naprave ali pa samo posameznega dela. Uporaba predlaganega modela je prikazana za dva primera iz železarne Třinec na Češkem in železarne Podbrezová na Slovaškem. Prikazan je tudi vpliv nastavitve sekundarnega ohlajanja na nastanek površinskih in notranjih napak na gredici 150 mm × 150 mm pri različnih obratovalnih razmerah.

Ključne besede: kontinuirno ulite gredice, numerični model, strjevanje

1 NUMERICAL MODEL OF THE TEMPERATURE FIELD OF A CONCAST BILLET

The presented in-house model of the transient temperature field of the blank from a billet caster (**Figure 1**) is unique. In addition to being entirely 3D, it can operate in real time. It is possible to adapt its universal code and use it for any billet caster. The numerical model covers the temperature field of the entire length of a blank (i.e., from the meniscus inside the mould all the way down to the cutting torch) with up to one million nodes.

The solidification and cooling of a blank and the simultaneous heating of the mould is a case of the 3D transient heat and mass transfer in a system comprising a blank-mould ambient and, after leaving the mould, only a blank ambient[1]. If mass transfer is neglected and if only conduction is considered as being decisive, then the heating up of the mould is described by the Fourier Equation (1). The solidification and the cooling of a blank is described by the Fourier-Kirchhoff Equation (2),

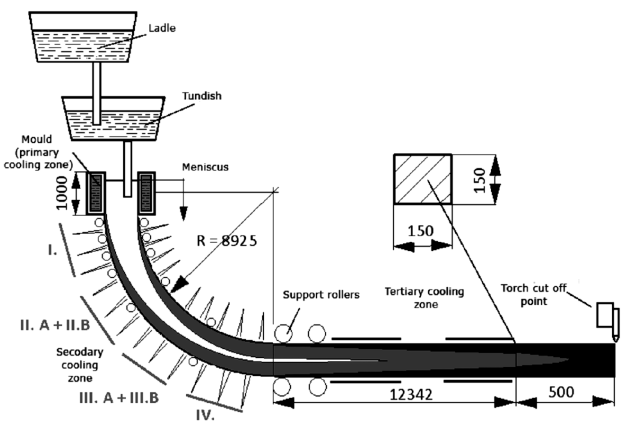

Figure 1: A billet caster
Slika 1: Shematski prikaz kontinuirnega ulivanja gredic

which contains the components describing the heat flow from the melt flowing with a velocity v, and the component including the internal source of latent heats of phase or structural changes $\dot{Q}_{\text{source}}$.

$$\rho \cdot c \frac{\partial T}{\partial \tau} = \frac{\partial}{\partial x}\left(k \frac{\partial T}{\partial x}\right) + \frac{\partial}{\partial y}\left(k \frac{\partial T}{\partial y}\right) + \frac{\partial}{\partial z}\left(k \frac{\partial T}{\partial z}\right) \quad (1)$$

$$\rho \cdot c \frac{\partial T}{\partial \tau} = \frac{\partial}{\partial x}\left(k \frac{\partial T}{\partial x}\right) + \frac{\partial}{\partial y}\left(k \frac{\partial T}{\partial y}\right) + \frac{\partial}{\partial z}\left(k \frac{\partial T}{\partial z}\right) + + \rho \cdot c\left(u \frac{\partial T}{\partial x} + v \frac{\partial T}{\partial y} + w \frac{\partial T}{\partial z}\right) + \dot{Q}_{\text{source}} \quad (2)$$

Figure 2 shows the temperature balance of an elementary volume representing the general node of the mesh *(i,j,k)* inside the mould. The heat conductivities *VX*, *VY* and *VZ* along the main axes are:

$$VX_{i,j,k} = k_i \frac{A_x}{\Delta x} \qquad VX_{i-1,j,k} = k_{i-1} \frac{A_x}{\Delta x} \quad (3a)$$

$$VY_{i,j,k} = k_j \frac{A_y}{\Delta y} \qquad VY_{i,j-1,k} = k_{j-1} \frac{A_y}{\Delta y} \quad (3b)$$

$$VZ_{i,j,k} = k_k \frac{A_z}{\Delta z} \qquad VZ_{i,j,k-1} = k_{k-1} \frac{A_z}{\Delta z} \quad (3c)$$

The heat flows *QX*, *QY* and *QZ* through the elementary volume along the main axes are:

$$QX = VX_{i,j,k}(T^{(\tau)}_{i+1,j,k} - T^{(\tau)}_{i,j,k}) \quad (4a)$$

$$QY_i = VY_{i,j,k}(T^{(\tau)}_{i,j+1,k} - T^{(\tau)}_{i,j,k}) \quad (4b)$$

$$QX1 = VX_{i-1,j,k}(T^{(\tau)}_{i-1,j,k} - T^{(\tau)}_{i,j,k}) \quad (4c)$$

$$QY1_1 = VY_{i,j-1,k}(T^{(\tau)}_{i,j-1,k} - T^{(\tau)}_{i,j,k}) \quad (4d)$$

$$QZ_{i,j} = VZ_{i,j,k}(T^{(\tau)}_{i,j,k+1} - T^{(\tau)}_{i,j,k}) \quad (4e)$$

$$QZ1_{i,j} = VZ_{i,j,k-1}(T^{(\tau)}_{i,j,k-1} - T^{(\tau)}_{i,j,k}) \quad (4f)$$

The temperature balance of the general node is:

$$(QZ1_{i,j} + QZ_{i,j} + QY1_{i,j} + QY_{i,j} + QX1 + QX) = = \frac{\Delta x \cdot \Delta y \cdot \Delta z \cdot \rho \cdot c}{\Delta \tau}(T^{(\tau+\Delta\tau)}_{i,j,k} - T^{(\tau)}_{i,j,k}) \quad (5)$$

where the right-hand side expresses the accumulation (or loss) of heat in the node *i,j,k* during the time step $\Delta\tau$. The unknown temperature of the general node of the mesh inside the mould in the following instant ($\tau + \Delta\tau$) is therefore given by the explicit formula:

$$T^{(\tau+\Delta\tau)}_{i,j,k} = T^{(\tau)}_{i,j,k} + (QZ1_{i,j} + QZ_{i,j} + QY1_{i,j} + QY_{i,j} + QX1 + QX) \cdot \cdot \frac{\Delta\tau}{\Delta x \cdot \Delta y \cdot \Delta z \cdot \rho \cdot c} \quad (6)$$

The temperature field of the blank passing through a radial caster of a large radius can be simplified by the Fourier-Kirchhoff equation where only the v_z component of the velocity is considered. Equation (2) is therefore reduced to:

$$\rho \cdot c \frac{\partial T}{\partial \tau} = \frac{\partial}{\partial x}\left(k \frac{\partial T}{\partial x}\right) + \frac{\partial}{\partial y}\left(k \frac{\partial T}{\partial y}\right) + \frac{\partial}{\partial z}\left(k \frac{\partial T}{\partial z}\right) + + \rho \cdot c \cdot w \frac{\partial T}{\partial z} + \dot{Q}_{\text{source}} \quad (7)$$

Equation (7) must cover the temperature field of the blank in all three stages: above the liquidus temperature (i.e., the melt), in the interval between the liquidus and solidus temperatures (i.e., the so-called mushy zone) and beneath the solidus temperature (i.e., the solid phase). It is therefore convenient to introduce the thermodynamic function of specific volume enthalpy $H_v = c\rho T$, which is dependent on temperature, and also includes the phase and structural heats (**Figure 3**).

Heat conductivity k, specific heat capacity c and density ρ are thermophysical properties that are also functions of temperature. Equation (7) therefore takes on the form:

$$\frac{\partial H_v}{\partial \tau} = \frac{\partial}{\partial x}\left(k \frac{\partial T}{\partial x}\right) + \frac{\partial}{\partial y}\left(k \frac{\partial T}{\partial y}\right) + \frac{\partial}{\partial z}\left(k \frac{\partial T}{\partial z}\right) + w \frac{\partial H_v}{\partial z} \quad (8)$$

The heat balance of the elementary node is:

$$(QZ1_{i,j} + QZ_{i,j} + QY1_{i,j} + QY_{i,j} + QX1 + QX) = = \frac{\Delta x \cdot \Delta y \cdot \Delta z}{\Delta \tau}(T^{(\tau+\Delta\tau)}_{vi,j,k} - T^{(\tau)}_{vi,j,k}) \quad (9)$$

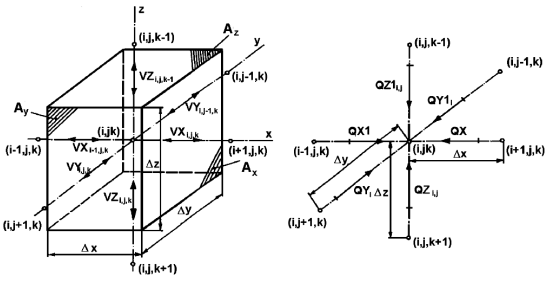

Figure 2: Heat balance of the general node of the mesh
Slika 2: Diagram toplotnega ravnovesja v splošni točki mreže

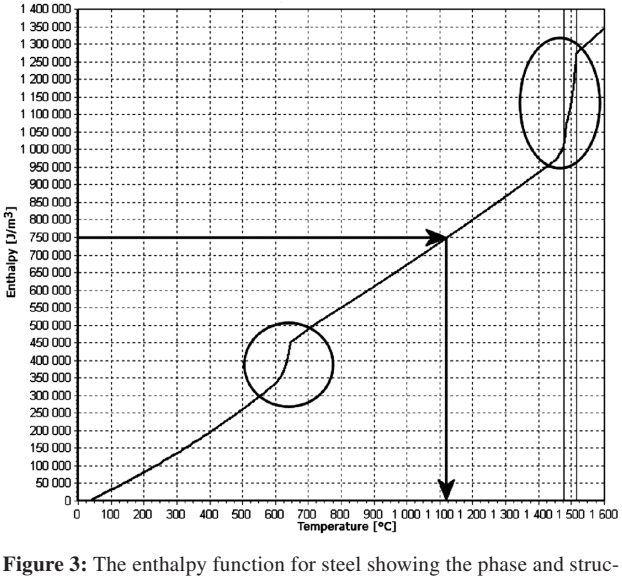

Figure 3: The enthalpy function for steel showing the phase and structural changes
Slika 3: Entalpijska funkcija za jeklo s fazno in strukturno premeno

where the heat flow $QZ_{i,j}$ must now also include the enthalpy of the incoming volume of melt:

$$(QZ1_{i,j} = QZ_{i,j}(T^{(\tau)}_{i,j,k+1} - T^{(\tau)}_{i,j,k}) - A_z \cdot w \cdot H^{(\tau)}_{vi,j,k} \quad (10)$$

The unknown enthalpy of the general node of the blank in the following instant ($\tau + \Delta\tau$) is given by the explicit formula, similar to Equation (6):

$$H^{(\tau+\Delta\tau)}_{vi,j,k} = H^{(\tau)}_{vi,j,k} + (QZ1_{i,j} + QZ_{i,j} + QY1_{i,j} + QY_{i,j} + QX1 + QX) \cdot \cdot \frac{\Delta\tau}{\Delta x \cdot \Delta y \cdot \Delta z} \quad (11)$$

Figure 3 indicates how the temperature model for the calculated enthalpy in Equation (11) determines the unknown temperature.

The next task is to choose a suitable coordinate system and a mesh. This paper deals with the symmetrical half of one cross-section of a blank from the meniscus inside the mould down to the cutting torch. The origin of the coordinate system is positioned on the small radius in the centre of the width (**Figure 4**). This enables all coordinates to be positive, which facilitates the software programming. In the region of the radius, the Cartesian coordinates are transformed into the cylindrical ones (i.e., y is the radius and z is the angle). The mesh is generated automatically and the model supports all densities of the mesh introduced in **Figure 4**. All the results presented in this paper are based on a mesh of 573,594 nodes (11 in the x-direction, 21 in the y-direction and 1861 in the z-direction) and a 7.5 mm × 7.5 mm × 15 mm elementary volume.

All thermodynamic properties of the cast steel, dependent on its chemical composition and the cooling rate, enter the calculation as functions of temperature[2]. This is therefore a significantly non-linear task because, even with the boundary conditions, their dependence on the surface temperature of the blank is considered here.

Regarding the fact that the task can be considered symmetrical along the axis (**Figure 4**), it is sufficient to deal with only one half of the cross-section. The boundary conditions are therefore as follows:

1. $T = T_{\text{cast}}$ the level of the steel (12a)

2. $-k\frac{\partial T}{\partial n} = 0$ the plane of symmetry (12b)

3. $-k\frac{\partial T}{\partial n} = htc \cdot (T_{\text{surface}} - T_{\text{amb}})$ inside the mould (12c)

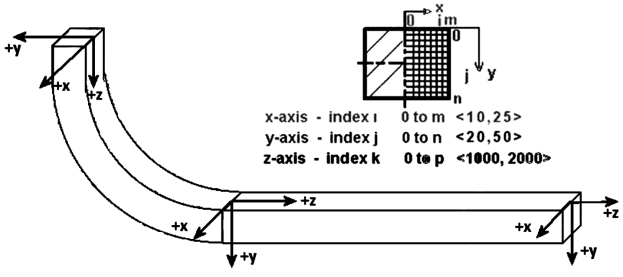

Figure 4: The mesh and the definition of the coordinate system
Slika 4: Mreža in opredelitev koordinatnega sistema

4. $-k\frac{\partial T}{\partial n} = htc \cdot (T_{\text{surface}} - T_{\text{amb}}) + \sigma\varepsilon(T^4_{\text{surface}} - T^4_{\text{amb}})$ within the secondary and tertiary zones (12d)

5. $-k\frac{\partial T}{\partial z} = \dot{q}$ beneath the rollers (12e)

The boundary conditions are divided into the area of the mould, the area of the secondary cooling and the area of the tertiary cooling.

The initial condition for the investigation is the setting of the temperature in individual points of the mesh. A suitable temperature is the highest possible temperature, i.e., the pouring temperature. The explicit difference method is used for solving this problem. The principle of this method is that the stability of the calculation is dependent on the magnitude of the time step. The model has incorporated a method for adapting the time step, i.e., the time step entered by the operator is merely a recommendation and the software modifies it throughout the calculation.

2 HEAT TRANSFER COEFFICIENT ALONG THE ENTIRE CASTER

The cooling by the water nozzles has the main influence and it is therefore necessary to devote much attention to establishing the relevant heat-transfer coefficient of the forced convection. Commercially sold models of the temperature field describe the heat-transfer coefficient beneath the nozzles as a function of the incident quantity of water per unit area. They are based on various empirical relationships. This procedure is undesirable. The model discussed in this paper obtains its heat-transfer coefficients from the measurements of spraying characteristics of all nozzles used by the caster on the so-called hot plate in an experimental laboratory[3,4] and for a sufficient range of operational pressures of water, as well as for a sufficient range of casting speeds of the blank (i.e., casting speed). This approach represents a unique combination of an experimental measurement in a laboratory and a numerical model for calculating the non-linear boundary conditions beneath the cooling nozzle.

Figure 5 presents the measured values of the heat-transfer coefficients processed by the temperature-model software. For the nozzle configuration, there is a graph of the heat-transfer coefficient beneath the nozzle. These graphs are plotted for a surface temperature of 1000 °C.

The resultant heat-transfer coefficient is determined by adding up the partial coefficients. This basically entails the total heat-transfer coefficient because even radiation, with the introduction of the "reduced heat-transfer coefficient from radiation", was converted to convection. On the areas of the blank, where the natural convection and radiation occur, the total coefficient is given by the sum of the reduced coefficient from radiation and the coefficient of the actual natural convection.

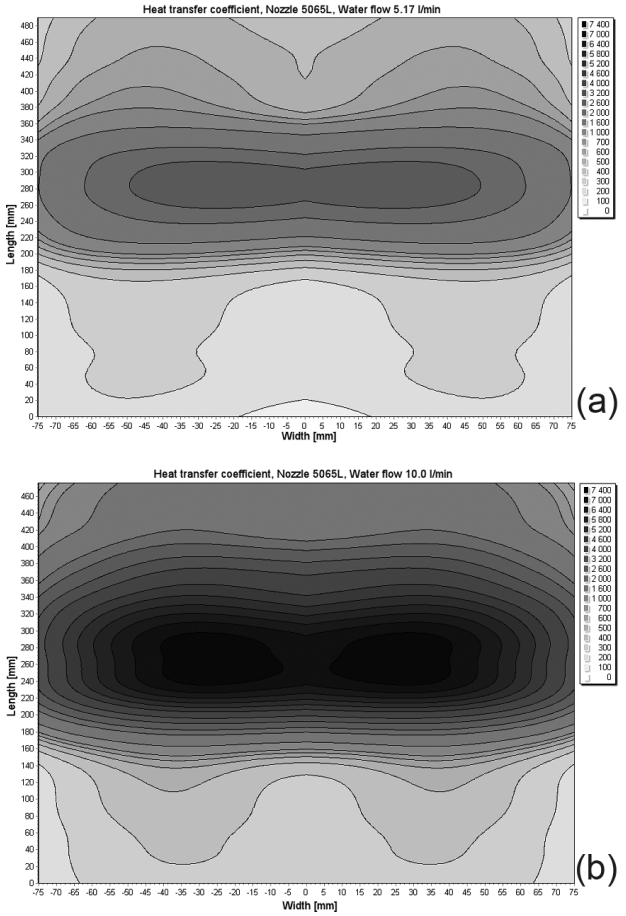

Figure 5: The heat-transfer coefficient for the 5065l nozzle: a) flow through a nozzle at 5.17 L/min, b) flow through a nozzle at 10.00 L/min

Slika 5: Koeficient prehoda toplote za šobo 50651: a) pretok skozi eno šobo pri 5,17 L/min, b) pretok skozi eno šobo pri 10,00 L/min

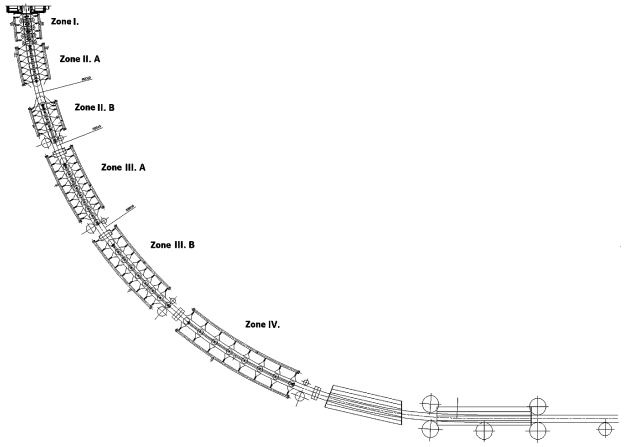

Figure 6: Positions of the nozzles along the billet caster in 6 individual zones

Slika 6: Pozicije hladilnih šob vzdolž naprave za ulivanje gredic v 6 območjih

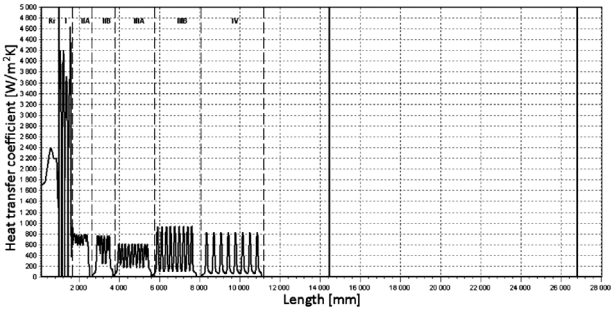

Figure 7: The resultant heat-transfer coefficient along the small radius of the billet caster

Slika 7: Dobljeni koeficienti prehoda toplote vzdolž notranjega radija naprave za ulivanje gredic

In the area beneath the nozzle, the resultant heat-transfer coefficient is obtained as the sum of the forced-convection coefficient gained from the laboratory-temperature measurement and the reduced heat-transfer coefficient from radiation[2].

On a specific caster, the nozzles of the secondary cooling are divided into several independent regulation zones, enabling the formation of the temperature field of the blank. **Figure 6** shows the 6 individual regulation zones and **Figure 7** shows the courses of the resultant heat-transfer coefficients along the small radius of the billet caster. On a specific caster, the nozzles of the secondary cooling are divided into several independent regulation zones (I, IIA, IIB, IIIA, IIIB and IV), enabling the formation of the temperature field of the blank.[5]

3 EFFECT OF THE SECONDARY COOLING

The setting of the secondary cooling and its optimization is a very complicated problem[6]. In a real operation specific intensity of cooling is characterized by the consumption of the cooling water per 1 kg of cast steel. On the basis of the curves indicating various consumptions of cooling water per unit of the mass of cast steel varying from 9 L/kg to 18 L/kg, the temperature of the blank was calculated and presented in **Figure 8**. These cooling curves are established for the given caster referring to six cooling zones I, IIA, IIB, IIIA, IIIB and IV.

4 ON-LINE MODEL OF THE TEMPERATURE FIELD

A temperature model can be considered to be successfully implemented if it is integrated into the existing information and control systems of a caster. The users (i.e., technologists) can record the real-time data from the on-line model into their off-line model of the temperature field, carry out any necessary changes in the input parameters (e.g., alter the secondary cooling or the casting speed). After a simulation on the off-line model, it is possible to determine how the temperature field will change after the implementation of the changes. Another application of the off-line version is in the occurrence of defects on/in the actual slab or sheet steel. The user can

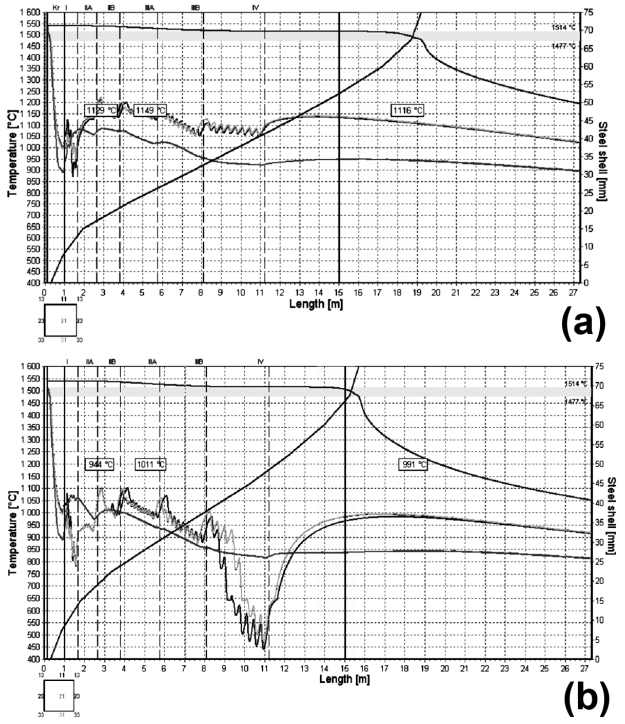

Figure 8: A comparison of the temperature fields with different intensities of secondary cooling: a) cooling curve 9 L/kg, b) cooling curve 18 L/kg

Slika 8: Primerjava temperaturnih polj pri različni intenzivnosti sekundarnega hlajenja: a) krivulja ohlajanja pri 9 L/kg, b) krivulja ohlajanja pri 18 L/kg

read the temperature field from the archive server using the dynamic model and – using the off-line model – analyse any likely causes of defects and prepare the necessary measures for the defects never to occur again. The off-line model will (in future) enable the reading of quantities and their dependences from the application server and, using statistical methods and the relationships among these quantities and defects, will look for the cause in the original temperature field of the concasting from a specific melt. However, this will be the task of the mathematical-stochastic prediction model.

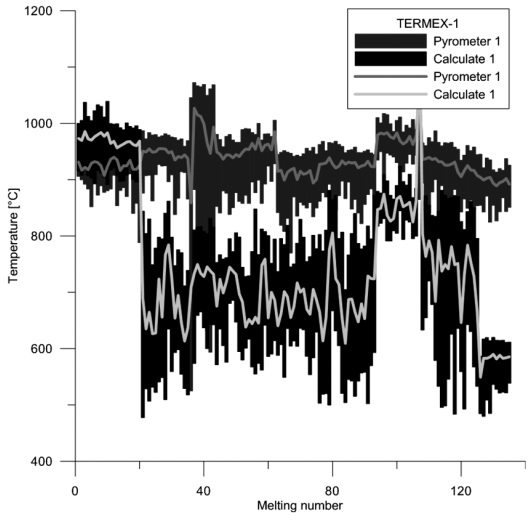

Figure 9: The measured and calculated temperatures of a billet

Slika 9: Izmerjene in izračunane temperature gredice

Figure 9 compares the average values of the measured surface temperatures in the same points. Comparing the absolute values, it is possible to see that there are long intervals where the deviation is significant and, on the other hand, there are intervals where the values are identical.

5 CONCLUSIONS

This paper presents a 3D numerical model of the temperature field (for concasting of steel) in the form of an in-house software that has been implemented in the operation of TŘINECKÉ ŽELEZÁRNY, Czech Republic and in Podbrezová, Slovakia. The model deals with the main thermodynamic transfer phenomena during the solidification of concasting.

Our analysis proved the usefulness of the model for real applications, as well as the reliability and robustness of the used numerical methods and other software. The model has been applied in the calculation and setting of the constants of the caster control system, including the simulation of the caster operation under non-standard situations (e.g., partial failures of the secondary cooling during an unexpected slowing down of the casting), in the planned maintenance of the machine or its structural improvements, in the utilization of the information that helps the operator to make spontaneous changes to the control of the machine, in the utilization of monitoring and controlling the quality, in the direct control of the casting speed and in the flow of water in individual zones of the secondary cooling of the prediction system[7].

Acknowledgments

This analysis was conducted by using a program devised within the framework of the project GA CR No. 106/08/0606, 106/09/0940 and P107/11/1566, NETME centre – New Technologies for Mechanical Engineering CZ.1.05/2.1.00/01.0002, Specific research BUT BD13102003 and the co-author, the holder of Brno PhD Talent Financial Aid sponsored by Brno City Municipality.

Nomenclature

A/m^2 – area
c/(J/kg K) – specific heat capacity
htc/(W/m^2 K) – heat transfer coefficient
H_v/(J/m^3) – volume enthalpy
k/(W/mK) – heat conductivity
T/K – temperature
T_{amb}/K – ambient temperature
T_{cast}/K – melt temperature
$T_{surface}$/K – temperature in unbending part

$\dot{q}$/(W/m^2) – specific heat flow
QX/W, QY/W, QZ/W – heat flows
$\dot{Q}_{source}$/(W/m^3) – internal heat source
x/m, y/m, z/m – axes in given direction
u/(m/s), v/(m/s), w/(m/s) – casting speed in given direction
VX/(W/K), VY/(W/K), VZ/(W/k) – heat conductivity
ρ/(kg/m^3) – density
σ/(W/m^2 K^4) – Stefan-Boltzmann constant
ε – emissivity
τ/s – time

6 REFERENCES

[1] J. K. Brimacombe, The Challenge of Quality in Continuous Casting Process, Metallurgical and Materials Trans. B, 30B (**1999**), 553–566

[2] J. Miettinen, S. Louhenkilpi, J. Laine, Solidification analysis package IDS. Proceeding of General COST 512 Workshop on Modelling in Materials Science and Processing, M. Rappaz and M. Kedro eds., ECSC-EC-EAEC, Brussels, Luxembourg, 1996

[3] M. Prihoda, J. Molinek, R. Pyszko, M. Velicka, M. Vaculík, J. Burda, Heat Transfer during Cooling of Hot Surfaces by Water Nozzles, Metalurgija = Metallurgy, 48 (**2009**) 4, 235–238

[4] J. Horsky, M. Raudensky, Measurement of Heat transfer Characteristics of Secondary Cooling in Continuous Casting. In Metal 2005. Ostrava: TANGER, 2006, 1–8

[5] A. Richard, Kai Liu Harding, Ch. Beckermann, A transient simulation and dynamic spray cooling control model for continuous steel casting, Metallurgical and materials transactions, 34B (**2003**), 297–302

[6] F. Kavička, J. Stetina, B. Sekanina, K. Stransky, J. Dobrovska, J. Heger, The optimization of a concasting technology by two numerical models, Journal of Materials Processing Technology, 185 (**2007**) 1–3, 152

[7] B. G. Thomas, R. J. O'Malley, D. T. Stone, Measurement of temperature, solidification, and microstructure in a continuous cast thin slab. Paper presented at Modeling of Casting, Welding and Advanced Solidification Processes VIII, San Diego, CA, TMS 1998

UDK 533.5:669.14.018.8:669.788
Original scientific article/Izvirni znanstveni članek

ISSN 1580-2949
MTAEC9, 46(2)161(2012)

OUTGASSING OF HYDROGEN FROM A STAINLESS STEEL VACUUM CHAMBER

RAZPLINJEVANJE VODIKA IZ NERJAVNEGA JEKLA

Sefer Avdiaj[1,3], Bojan Erjavec[2]

[1]University of Prishtina, Faculty of Natural Sciences and Mathematics, Mother Teresa Av. 3, Prishtina 10000, Kosova
[2]Institute of Metals and Technology, Lepi pot 11, 1000 Ljubljana, Slovenia
[3]Lotrič, d.o.o., Selca 163, 4227 Selca, Slovenia
sefer.avdiaj@uni-pr.edu

Prejem rokopisa – received: 2012-02-07; sprejem za objavo – accepted for publication: 2012-02-22

Due to outgassing from the walls of vacuum calibration chambers, the generation of the calibration pressure in primary vacuum calibration systems operating below 10^{-6} Pa becomes un-accurate. Austenitic stainless steel (SS) is the most common construction material for ultrahigh vacuum (UHV) and extremely high vacuum (XHV) chambers. Hydrogen is the predominant residual gas at very low pressures in SS vacuum systems, i.e., in the UHV and XHV range. Therefore, the reduction of the hydrogen outgassing rate is the most challenging problem in achieving pressures in those ranges. In this paper, a vacuum chamber with a wall thickness of 2.62 mm and made from AISI type 304 L SS was examined with the aim of mitigating the outgassing rate. The heat treatments were carried out at 250 °C for 380 h and at 350 °C for 140 h. After baking at 250 °C for 380 h (corresponding to a dimensionless time $Fo = 3.09$), an outgassing rate $q = 2.86 \times 10^{-13}$ mbar L s^{-1} cm^{-2} was achieved at room temperature (RT). This RT outgassing rate was further reduced to $q = 5.7 \times 10^{-14}$ mbar L s^{-1} cm^{-2} after baking for another 140 h at 350 °C ($Fo = 8.66$, resulting in a total dimensionless time $\Sigma Fo = 11.75$).

Keywords: hydrogen outgassing, stainless steel, dimensionless time, pressure-rise method, throughput method, gas-flow calibration coefficient

Zaradi razplinjevanja sten vakuumskih kalibracijskih posod postane vzpostavitev kalibracijskega tlaka v primarnih kalibracijskih vakuumskih sistemih, delujočih v tlačnem območju manjšem od 10^{-6} Pa, nenatančna. Avstenitno nerjavno jeklo je najprimernejši material za gradnjo ultra visokovakuumskih (UVV) in ekstremno visokovakuumskih (EVV) posod. Pri zelo nizkih tlakih v UVV- in EVV-področju je vodik prevladujoč rezidualni plin v vakuumskih sistemih, narejenih iz nerjavnega jekla. Tako je zmanjšanje razplinjevanja vodika najpomembnejše za doseganje nizkih tlakov v naštetih področjih. V tem članku je predmet raziskav vakuumska posoda z debelino stene 2,62 mm, ki je narejena iz nerjavnega jekla AISI type 304 L. Postopki pregrevanja vakuumske posode so se izvajali pri 250 °C 380 h in pri 350 °C 140 h. Po pregrevanju pri 250 °C 380 h (kar ustreza brezdimenzijskemu času $Fo = 3{,}09$) je bila pri sobni temperaturi dosežena gostota pretoka razplinjevanja $q = 2{,}86 \times 10^{-13}$ mbar L s^{-1} cm^{-2}. Z nadaljnjim pregrevanjem pri 350 °C 140 h ($Fo = 8{,}66$, kar rezultira v celotni brezdimenzijski čas $\Sigma Fo = 11{,}75$) se je gostota pretoka razplinjevanja pri sobni temperaturi zmanjšala na $q = 5{,}7 \times 10^{-14}$ mbar L s^{-1} cm^{-2}.

Ključne besede: razplinjevanje vodika, nerjavno jeklo, brezdimenzijski čas, metoda naraščanja tlaka, pretočna metoda, kalibracijski koeficient za plinski pretok

1 INTRODUCTION

The development of the science and technology of ultrahigh vacuum (UHV) and extremely high vacuum (XHV) devices has been strongly coupled to the development of increasingly larger and more sophisticated devices for physics research, such as particle accelerators, magnetic fusion devices, gravity wave observatories and many surface analysis techniques. Scientific advancements in the understanding of the outgassing limits in UHV/XHV conditions are associated with these technological developments.

Outgassing refers to the spontaneous liberation of gases from the walls of a vacuum chamber or other components placed inside the vacuum chamber. This gas release results from two processes:[1]

- Gas diffusion from the interior of vacuum chamber walls to their inner surface. This is followed by gas desorption into the chamber volume that contributes to the vacuum system outgassing.
- Release of gases or vapours previously adsorbed onto the inner surface of the vacuum chamber walls. These gases may have adsorbed onto the chamber inner surface while it was exposed to the environment and then slowly released as the pump removed the gas from the vacuum chamber.

The performance of a vacuum system is limited because it is impossible to eliminate all of the gas sources. Outgassing occurs even in the best-designed vacuum systems for UHV/XHV. The ultimate pressure in the system is related to the magnitude of the gas load; therefore, the measures taken to reduce outgassing are critical for the production of UHV/XHV. These effects extend the time required to reach UHV/XHV.

Due to the vaporisation or sublimation of atoms and molecules from some materials with a vapour pressure higher than or comparable to the residual pressure within a vacuum chamber, these materials will increase outgassing. Thus, not all types of materials can be used to build vacuum systems, and sometimes it is difficult to select appropriate materials that will fulfil the requirements of different processes. Among technical alloys, austenitic stainless steel (SS) offers several advantages compared to other alloys, and it is the most widely used

construction material for building vacuum chambers, instruments and components. SS is the most important construction material for UHV/XHV systems because of its good vacuum and mechanical properties.[2] It is non-magnetic, corrosion resistant and chemically inert. At room temperature (*RT*), SS exhibits negligible vapour pressure and negligible permeation of atmospheric gasses.[3] SS is relatively cheap, and it can be machined and welded by standard procedures.

In the high-vacuum range, the predominant gas is usually water vapour resulting from the exposure of the system to humid air.[4] The outgassing of hydrogen from SS is the main gas load in UHV/XHV systems,[5] particularly in large systems (i.e., accelerators and storage rings). Thus, hydrogen outgassing is the most significant limiting factor in reaching outgassing rates below 10^{-12} mbar L s^{-1} cm^{-2} in SS vacuum systems.[6] By reducing the hydrogen content in the bulk, the hydrogen outgassing rate can be reduced.

Many techniques have been reported that mitigate outgassing in vacuum systems, but reducing the outgassing rates of SS remains a challenge. These outgassing techniques include the following:

a) Surface treatments to reduce surface roughness, such as electro-polishing and surface machining under special conditions [3]
b) Surface treatments to create oxide films to act as a barrier to the diffusion of hydrogen from the bulk[3]
c) High-temperature bake-out (vacuum firing) to reduce the amount of dissolved H (for SS as high as 1 000 °C)[4,7]
d) Baking the vacuum system to remove water vapour, which has to be performed at 150–450 °C[4]
e) Degreasing and chemical cleaning[4]
f) Deposition of thin films to serve as a barrier layer on inner surfaces[8]
g) Choosing metals with a low solubility for hydrogen (e.g., copper)[4]
h) Reduction of hydrogen surface mobility by introducing surface trapping to reduce recombination[8]
i) Thin-film getter coatings to serve as a pump for hydrogen diffusing from the bulk[9]

The typical outgassing rate of vacuum components made from SS is on the order of 10^{-11} mbar L s^{-1} cm^{-2} without additional processing. An outgassing rate of 10^{-13} mbar L s^{-1} cm^{-2} is "routinely" achievable with a sufficient bake-out treatment. Outgassing rates lower than 10^{-14} mbar L s^{-1} cm^{-2} are achievable only with exceptional care, particularly in thin-wall vessels.[8] Until now, several reports have been published describing the reduction of SS outgassing rates by conventional bake-out or vacuum firing, but the resulting outgassing rates are not consistent: similar bake-out temperatures and times gave significantly different numerical values for the outgassing rates.

In 1967, Calder and Levin[10] published a paper on the reduction of outgassing of hydrogen from metals. They proposed the diffusion-limited model (DLM), which means that the atomic hydrogen concentration at the surface is zero and the hydrogen atoms desorb and recombine as molecules as soon as hydrogen reaches the surface. However, their assumption was not correct for lower outgassing rates, whereas their assumption was reasonable for higher outgassing rates. The experimental values obtained by Calder and Levin were two orders of magnitude larger than expected according to the DLM.[2] Therefore, their assumption that the surface density of hydrogen when solving the diffusion equations is always zero is questionable. To overcome this problem, Moore[11] calculated the outgassing rate using a recombination-limited model (RLM). Moore assumed that the surface density can never be zero and that the boundary conditions must be included when solving the diffusion equation.

Nemanič, Šetina, Bogataj and Zajec[12–14] used very thin-wall vessels instead of using thicker materials to reduce the outgassing rate. They also introduced a Fourier number (or dimensionless time) *Fo* to describe the heat treatment intensity. They reported extremely low outgassing rates of approximately 10^{-15} mbar L s^{-1} cm^{-2}, which were achieved using thinner materials.[12] Therefore, the use of thin materials is more efficient and economically suitable because shorter baking times can be used. However, the insufficient mechanical strength of very thin walls may make them unsuitable for the practical realisation of a vacuum chamber.

1.1 Measuring of outassing flux and outgassing rate

The outgassing flux of a SS sample can be measured by two general methods[4]. In the first method, the pressure increase is measured as a function of time in a closed vacuum chamber after its evacuation to a low pressure. This method is called the rate-of-rise (RoR) method or the gas-accumulation method. The outgassing flux Q is obtained as

$$Q = V \frac{\mathrm{d}P}{\mathrm{d}t} \tag{1}$$

where V is the chamber volume and $\mathrm{d}P/\mathrm{d}t$ is the measured rate of the pressure change in a closed chamber at a constant temperature.

In the second method, the vacuum test chamber is pumped through an orifice of known conductance, and the pressure drop across the orifice is measured. This method is known as the throughput method or the orifice method. The outgassing flux Q is expressed as

$$Q = C\Delta P \tag{2}$$

where C is the conductance and ΔP is the pressure difference.

In both methods, the outgassing rate q of the sample is obtained by dividing the measured outgassing flux Q by the surface area A of the sample: $q = Q/A$. The measured outgassing rate is the net rate of the difference

between the intrinsic outgassing rate of the surface and the readsorption rate.[15]

A common problem of both methods is that the test sample is placed in a vacuum measurement chamber whose walls also outgas during the measurement. Thus, the background outgassing flux of the empty chamber must be measured and subtracted from the measured outgassing flux of the sample in the chamber.

The presence of a hot cathode residual gas analyser (RGA) or ion gauge in the test chamber can cause additional outgassing, and the residual gas can react with the hot filament. Because they exhibit a certain pumping speed, RoR measurements can only be obtained with an inert vacuum gauge, such as a spinning rotor gauge (SRG).[1]

2 EXPERIMENTAL SETUP AND SAMPLE DESCRIPTION

We measured the time dependence of the outgassing rate of SS during bake-outs at 250 °C and 350 °C. Our main goal was to determine the time needed to reach the outgassing rate below 10^{-13} mbar L s^{-1} cm^{-2} at these bake-out temperatures.

We made two simple cylindrical chambers to serve as the outgassing samples (**Figure 1**). Each chamber was assembled from a CF 16 flange and had a short connection tube with an inner diameter of 16 mm and a wall thickness of 1.5 mm. The circular end plates had a thickness of 2 mm, and the cylindrical body had an inner diameter d_i = 108.7 mm and a wall thickness of 2.62 mm. The only difference between the two chambers was the cylindrical body length. The length of the body of chamber V1 was l_1 = 10 mm, and the length of the body of chamber V2 was l_2 = 210 mm.

The chambers were connected to a vacuum measurement system, as shown in **Figure 2**. The system was pumped by a turbomolecular pump and was equipped with a quadrupole mass spectrometer (QMS), a Bayard-Alpert gauge (BAG) and an SRG. The SRG was connected to a small chamber V0 that was made of a standard CF16 4-way cross and a CF16 T-piece. The chamber V0 can be isolated from the pump by a valve (E0). The chambers V1 and V2 were symmetrically connected to V0 through the bake-proof CF16 all-metal valves E1 and E2, respectively. The calibration gas was introduced into V0 through valve E3.

For the modelling of the outgassing behaviour of SS by DLM and RLM, the thickness of the sample is an important parameter. The same reduction in the outgassing rate of a plane sheet takes 4 times longer time if the sample is 2 times thicker. The entire measurement sample chamber was constructed from AISI type 304 L SS, but we were unable to make the whole chamber from the same sheet of SS. Additionally, each part had a different thickness. However, the measurement procedure was designed so that we could easily calculate the outgassing rate of the cylindrical body (which has a well-defined thickness) from the separate measurements of the outgassing flux of each chamber.

The chambers V0, V1 and V2 were placed in an oven where they could be uniformly heated up to 350 °C. Additional vacuum measurement instruments (BAG and QMS) were mounted outside the oven due to the

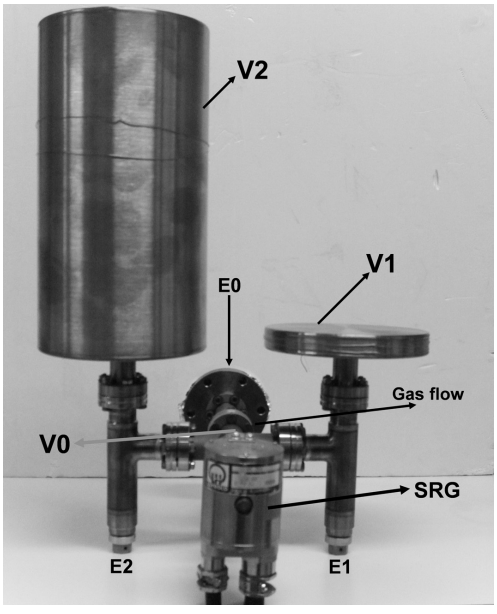

Figure 1: A photo of two SS cylindrical vacuum chambers used for the outgassing rate study

Slika 1: Fotografija dveh cilindričnih vakuumskih posod iz nerjavnega jekla, namenjenih za študij razplinjevanja

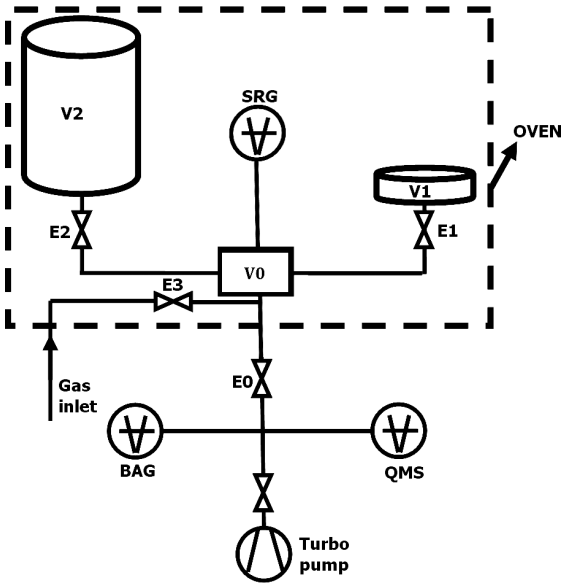

Figure 2: A schematic of the outgassing measurement system: QMS – quadrupole mass spectrometer; SRG – spinning rotor gauge; BAG – Bayard-Alpert gauge; E0, E1, E2 and E3 – bake-proof vacuum valves; V0, V1 and V2 – measuring volumes

Slika 2: Shema vakuumskega sistema za meritve razplinjevanja: QMS – kvadropolni masni spektrometer; SRG – viskoznostni merilnik z lebdečo kroglico; BAG- Bayard-Alpertova trioda; E0, E1, E2 in E3 – pregrevni vakuumski ventili; V0, V1 in V2 – merilni volumni

limitation of their operational temperature. During the bake-out, the SRG suspension head was removed, and only a thimble with a rotor was baked with the other parts.

The outgassing flux measurements at ambient temperature were performed using the RoR method. The outgassing flux measurements while baking the vacuum system (at temperatures of either 250 °C or 350 °C) were performed using the throughput method, which is described in Section 2.2.

2.1 Measuring of outassing flux using the RoR method

By closing valves E0, E2 and E3 and opening valve E1, we measured the pressure increase in chambers V0 + V1 with the SRG and used this reading to calculate the outgassing flux $Q_1 = Q_{V0} + Q_{V1}$. With the same SRG, we also measured the pressure increase in chambers V0 + V2 when valve E1 was closed and E2 was opened. This measurement gave $Q_2 = Q_{V0} + Q_{V2}$. In both cases, Q_{V0} was the same because of the symmetrical configuration of the connection with V1 and V2. By subtracting the two measured outgassing fluxes, the outgassing flux of V0 can be eliminated: $Q_2 - Q_1 = Q_{V2} - Q_{V1}$. The difference is equal to the outgassing flux from the major part of the cylindrical body of chamber V2 having a surface area $A = \pi d_i \times (l_2 - l_1)$.

To calculate the outgassing flux by the RoR method following Equation 1, we need to know the volume of the measurement system. The volumes V1 and V2 can be calculated from geometrical measurement because they are composed of simple cylindrical parts. The volume V0 has a more complicated geometrical shape because it includes the inner volume of the CF16 valves. Its volume can be determined by the static gas-expansion method. The calculated surface areas of V1 and V2 are accurate. However, we can only estimate the surface area of V0. The volumes and the surface areas for the 3 parts of the vacuum system are given in **Table 1**.

Table 1: The geometrical surface areas and volumes of particular parts of the vacuum measurement system, including their ratios

Tabela 1: Geometrijska površina *A* in volumen *V* posameznih delov vakuumskega merilnega sistema, vključujoč njihovo razmerje

	Geometrical surface area A (cm^2)	Volume V (L)	Ratio (V/A) (L cm^{-2})
V0	475 (rough estimate)	0.1206	2.54×10^{-4}
V1	247	0.1046	4.23×10^{-4}
V2	931	1.962	2.11×10^{-3}
V_{tot}	1653	2.1872	1.32×10^{-3}

2.2 Measuring of outassing flux using throughput method

To measure the outgassing flux of the test chambers during baking, the use of the SRG is not possible because the operating temperature for the measuring head of the SRG only ranges from 10 °C to 50 °C.[16] As a consequence, the RoR method cannot be used. Therefore, an adapted throughput measurement method that differs from the orifice method was used.

The steady-state outgassing flux from chamber V1 can be calculated by measuring the pressure difference ΔP_1, as measured by the BAG or QMS while opening and closing valve E1. By knowing the effective pumping speed S at the point where the BAG or QMS are connected to the vacuum system, we can calculate the corresponding outgassing flux $Q_1 = S \times \Delta P_1$. Similarly, by opening and closing E2, we can determine ΔP_2, and the outgassing flux $Q_2 = S \times \Delta P_2$. Also, the difference between the two fluxes is the outgassing flux from the major part of the cylindrical body of chamber V2, which has a surface area $A = \pi d_i \times (l_2 - l_1)$, as in the case of RoR measurements.

We were primarily interested in the outgassing of hydrogen from SS, so we used a QMS tuned to the mass number 2 (H_2 peak) for the ΔP measurements. The basic output signal of the QMS is an ion current of a particular gas. The ion current I_i^+ as a function of the partial gas pressure P_i is given by $I_i^+ = g_i \times P_i$, where g_i is the sensitivity coefficient, which depends on the gas type, the QMS geometry and the settings of various operational parameters. For accurate measurements, g_i must be determined experimentally (calibrated *in situ*) for each instrument and each gas. Therefore, to measure the outgassing flux of hydrogen, the sensitivity coefficient of the QMS g_{H2} and the effective pumping speed S_{H2} had to be determined. For hydrogen, the outgassing flux Q equals

$$Q = \frac{S_{H_2} \Delta I^+_{H_2}}{g_{H_2}} \tag{3}$$

To more easily determine the outgassing rate $q = Q/A$, we combined the effective pumping speed and the sensitivity coefficient into a single calibration coefficient K_{H2}:

$$K_{H_2} = S_{H_2} / g_{H_2} \tag{4}$$

The calibration coefficient K_{H2} can be determined experimentally in a straightforward manner and is described in the following section.

2.3 Determination of calibration coefficient

We can introduce a known flow of a calibration gas through valve E3, which is an adjustable leak valve. By closing valves E0, E1 and E2, the flow rate of the calibration gas Q_{cal} into the volume V0 can be measured by the RoR method using the same SRG as for the outgassing flux measurement. After the flow of calibration gas is determined, we can measure the difference in the hydrogen ion current ΔI_{H2}^+ by opening valve E0. Because the calibration gas flow was introduced to the QMS from the same direction as the outgassing flux from the measuring chambers, the calibration coefficients for the calibration gas flow and the outgassing flux

have similar values. The calibration coefficient can be calculated by rearranging Equation 3:

$$K_{H_2} = \frac{Q_{cal}}{\Delta I^+_{H_2}} \quad (5)$$

The measurements of $\Delta I_{H2}{}^+$ have been performed for a wide range of calibration gas flows Q_{cal}. **Figure 3** shows that when the Q_{cal} (measured by the SRG) increases, the $\Delta I_{H2}{}^+$ (measured by the QMS) increases proportionally.

From the data in **Figure 3** and with Equation 5, we have calculated the calibration coefficient. The calculated values are given in **Table 2**. The mean value of the calibration coefficient K of the QMS for hydrogen was 1.12×10^5 mbar L A^{-1} s^{-1}, and the relative standard deviation was $\sigma(K)/K = 3.61$ %.

Table 2: The calibration coefficients of QMS for hydrogen while measuring outgassing flux by the throughput method
Tabela 2: Kalibracijski koeficient QMS pri merjenju pretoka razplinjevanja vodika s pretočno metodo

I^+ (A)	K_{H2} (mbar L A^{-1} s^{-1})
1.21×10^{-10}	116998
1.10×10^{-10}	118505
3.63×10^{-11}	114295
2.37×10^{-11}	115234
1.47×10^{-11}	113737
1.42×10^{-11}	110694
1.41×10^{-11}	110739
5.54×10^{-12}	106750
1.83×10^{-12}	107483
1.24×10^{-12}	107763
1.21×10^{-12}	108467
1.20×10^{-12}	108439

The final equation to calculate the outgassing rate is

$$q = \frac{K}{A}(\Delta I_{V2} - \Delta I_{V1}) \quad (6)$$

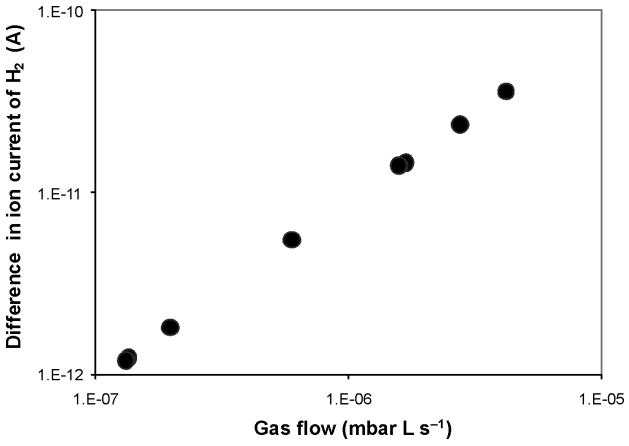

Figure 3: The difference in the hydrogen ion current, measured by QMS (using the throughput method), as a function of the hydrogen gas flow, measured by SRG (using the RoR method)
Slika 3: Razlika v ionskem toku vodika (ki je bil izmerjen s pretočno metodo in uporabo QMS) v odvisnosti od pretoka vodika (izmerjenega z metodo hitrosti naraščanja tlaka in uporabo SRG)

where ΔI_{V1} and ΔI_{V2} are the changes in the hydrogen ion current when closing valves E1 and E2, respectively.

3 RESULTS AND DISCUSSION

3.1 Time dependence of H_2 outgassing rate during bake-out at 250 °C

The measuring chambers were first baked at 250 °C for 380 h. The bake-out temperature was increased to 350 °C, and baking continued for an additional 140 h. The chambers were baked by keeping the outer side of the chamber wall in air while the inner side was under vacuum.

During the bake-out at 250 °C, we performed several measurements of the outgassing rate at the bake-out temperature using the throughput method. The heat treatment intensity expressed as a Fourier number, the baking time of the system and the outgassing rates during the heat treatment are given in **Table 3**.

Table 3: The measured hydrogen outgassing rate of the SS vacuum chamber during the bake-out. All of the outgassing rates were measured at a temperature of 250 °C.
Tabela 3: Izmerjena gostota pretoka razplinjevanja vodika vakuumske komore iz nerjavnega jekla med pregrevanjem pri 250 °C

ΣFo	t (h) at 250 °C	q (mbar l s^{-1} cm^{-2})
0.20	24	2.6×10^{-8}
0.77	95	1.10×10^{-8}
0.77	95.2	1.12×10^{-8}
0.78	96	1.19×10^{-8}
0.88	108	8.20×10^{-9}
0.89	110	8.40×10^{-9}
0.91	112	8.80×10^{-9}
1.54	190	4.20×10^{-9}
1.59	196	3.90×10^{-9}
1.71	211	2.90×10^{-9}
1.72	211.5	2.95×10^{-9}
1.72	212	3.00×10^{-9}
1.84	227	2.50×10^{-9}
1.86	228.5	2.40×10^{-9}
1.87	230	2.30×10^{-9}
2.06	254	2.00×10^{-9}
2.07	255	2.05×10^{-9}
2.08	256	2.08×10^{-9}
2.26	278	1.80×10^{-9}
2.27	279	1.85×10^{-9}
2.84	350	1.00×10^{-9}
2.85	351	1.05×10^{-9}
3.06	376	6.90×10^{-10}
3.07	378	7.30×10^{-10}

The Fourier number (or dimensionless time) $Fo = 4Dtd^{-2}$ is a characteristic quantity for describing and modelling diffusion. It was used to compare the outgassing rates for different experiments.[17] To determine the dimensionless time Fo, the following must be known: the diffusion constant D for hydrogen at temperature T, the processing time t and the wall thickness d.

The parameters t and d are measured directly. The temperature dependence of D is given by

$$D = D_0 \exp\left(\frac{-E_a}{kT}\right) \quad (7)$$

Typical values for the diffusion pre-exponential factor (D_0 = 0.012 cm^2 s^{-1}) and the activation energy (E_a = 0.57 eV)[18] were used to calculate the *Fo* values.

The bake-out at 250 °C was interrupted a few times to cool the chambers and to measure the outgassing rates at RT. The time course was as follows: bake-out at 250 °C for 24 h, interrupt baking for the RT measurement, bake-out at 250 °C for 73 h, interrupt baking for the RT measurement and bake-out at 250 °C for 284 h followed by an RT measurement. The temperature was then raised to 350 °C, and baking was performed for additional 140 h. The system was then cooled again, and the last RT measurement was performed. The results of the hydrogen outgassing rate measurements at RT, which were performed using the RoR method, are summarised in **Table 4**.

Table 4: The hydrogen RT outgassing rates of SS after the indicated bake-out treatment

Tabela 4: Gostota pretoka razplinjevanja vodika iz nerjavnega jekla pri sobni temperaturi po navedenem postopku pregrevanja

T (°C)	Incremental time Δt (h)	Fo (Δt)	ΣFo	q (mbar L s^{-1} cm^{-2})
250	24	0.19	0.19	2.10 × 10^{-12}
250	73	0.59	0.78	
250	284	2.31	3.09	
350	140	8.66	11.75	

A comparison of our results of the RT outgassing rate with the results obtained by Park et al.[19] is shown in **Figure 4**. The Fourier numbers for the data from Park et al. were recalculated using our activation energy for the diffusion E_a = 0.57 eV (instead of E_a = 14.5 kcal mol^{-1} ≈ 0.622 eV, which was used by Park et al.). Our results agree and are within a factor 3 to 4 of the results of Park et al.

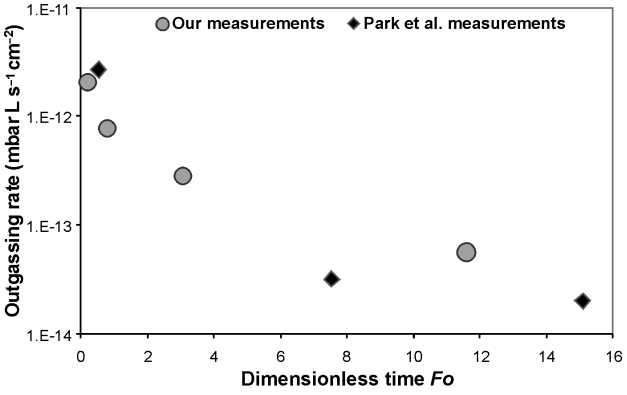

Figure 4: A comparison of the hydrogen outgassing rates between our measurements and the measurements of Park et al.[17], which were performed after the system was cooled to RT

Slika 4: Primerjava gostote pretoka razplinjevanja vodika iz nerjavnega jekla med našimi meritvami in meritvami Parka et al.[17], ki so bile izvedene po ohladitvi sistema na sobno temperaturo

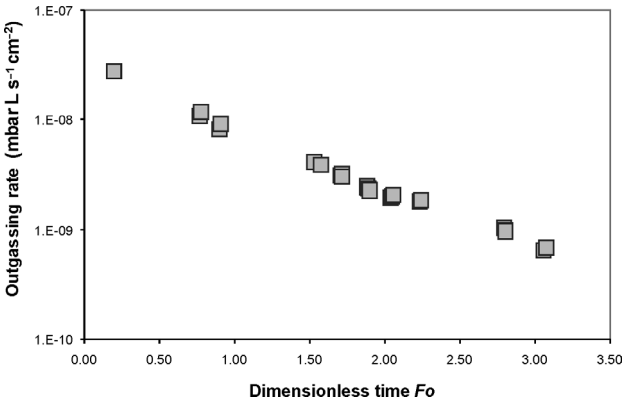

Figure 5: The hydrogen outgassing rate of SS as a function of the dimensionless time *Fo* during the heat treatment at 250 °C

Slika 5: Gostota pretoka razplinjevanja vodika iz nerjavnega jekla v odvisnosti od brezdimenzijskega časa *Fo* med postopkom pregrevanja pri 250 °C

A graphical representation of the results (taken from **Table 3**) of the outgassing rates measured at 250 °C as a function of dimensionless time *Fo* is shown in **Figure 5**.

In **Figure 6,** the same measured outgassing rates as a function of the bake-out time are presented and compared with the calculations based on the DLM.[1,6] The outgassing rate predicted by diffusion theory for t = 380 h is $q = 5 \times 10^{-11}$ mbar L s^{-1} cm^{-2}, which is 15 times lower than the measured value $q = 7 \times 10^{-10}$ mbar L s^{-1} cm^{-2}. In the early stage of bake-out, until approximately 100 h at 250 °C, the predicted curve according to the DLM and the measured data agree. However, discrepancies start to emerge after 100 h. For $Fo > 0.8$, the atomic hydrogen recombination on the SS surface is assumed to become a rate-limiting step. When a hydrogen atom has moved from the bulk to the surface/vacuum interface, it needs to find another hydrogen atom on the surface to recombine.

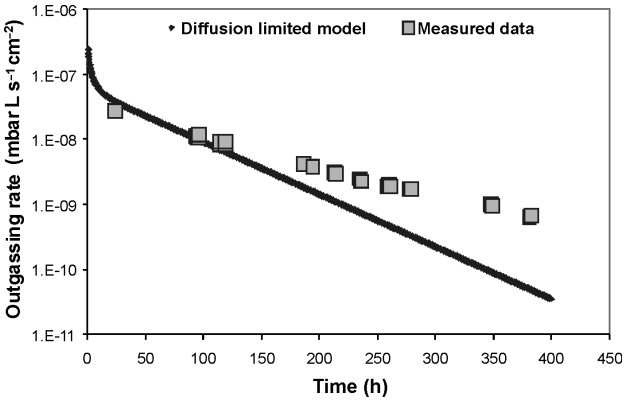

Figure 6: A comparison of the DLM-predicted hydrogen outgassing rate of SS and the measured data during the heat treatment at 250 °C as a function of the bake-out time

Slika 6: Primerjava gostote pretoka razplinjevanja vodika iz nerjavnega jekla, predvidenega na osnovi modela DLM, z merilnimi rezultati v odvisnosti od časa pregrevanja pri 250 °C

As the number of freely diffusing hydrogen surface atoms is reduced, recombination becomes less likely. Thus, when the diffusion of hydrogen atoms to the surface become small, the recombination of the hydrogen atoms might be the rate-limiting step, i.e., outgassing from the surface is described by the rate at which the hydrogen atoms can be recombined, not the bulk diffusion rate.

4 CONCLUSIONS

The determination of the calibration coefficient K for the BAG and QMS allowed us to measure the outgassing rate during the heat treatment without stopping the heating process. The DLM governs the initial removal of hydrogen from SS, and it is assumes that hydrogen surface recombination plays an important role in the outgassing rate at lower hydrogen concentrations. To compare the different outgassing treatments, the Fo number appears to be a good choice because it can be accurately calculated for any processing time and temperature. The Fo number is a parameter that shows the level of heat treatment of SS, and it is related to the diffusion of hydrogen atoms in SS.

An outgassing rate $q = 2.86 \times 10^{-13}$ mbar L s^{-1} cm^{-2} at RT was achieved for AISI type 304 L SS after baking the system at 250 °C for 380 h (conversion to dimensionless time gives Fo = 3.09). This outgassing rate was further reduced to $q = 5.7 \times 10^{-14}$ mbar L s^{-1} cm^{-2} by baking for another 140 h at T = 350 °C (Fo = 8.66, total dimensionless time ΣFo = 11.75).

Acknowledgement

S. Avdiaj acknowledges partial financial support by the European Union, European Social Fund. The study was implemented in the framework of the Operational Programme for Human Resources Development for the period 2007–2013.

5 REFERENCES

[1] K. Jousten, Thermal outgassing, Proceedings of the CERN Accelerator School, Snekersten, Denmark, CERN report, edited by S. Turner, 1999, 111–125

[2] Y. Ishikava, V. Nemanic, Vacuum, 69 (**2003**), 501–512

[3] M. Leich, Hydrogen outgassing of stainless steel, our present knowledge, Proceedings of the 1st Vacuum Symposium, UK, 2010 (http://www.ss.dsl.pipex.com/rgaug/pdfs/ vs1/Leisch.pdf)

[4] J. Lafferty, Foundations of Vacuum Science and Technology, John Wiley & Sons, New York 1998, 625–652

[5] P. A. Redhead, Extreme high vacuum, Proceedings of the CERN Acceleration School, Snekersten, Denmark, CERN report, edited by S. Turner, 1999, 213–227

[6] M. Bernardini et al., J. Vac. Sci. Technol., A 16 (**1998**), 188–193

[7] B. Zajec, V. Nemanič, Mater. Tehnol., 35 (**2001**) 5, 259–264

[8] R. Reid, Outgassing Surface Conditioning, 2009, (www.stfc.ac.uk/resources/pdf/ronreid25209.pdf)

[9] C. Benvenuti, P. Chiggiato, F. Cicoira, V. Ruzinov, Vacuum, 50 (**1998**), 57–63

[10] R. Calder, G. Lewin, Br. J. Appl. Phys., 18 (**1967**), 1459

[11] B.C. Moore, J. Vac. Sci. Technol., A 13 (**1995**), 545–548

[12] V. Nemanic, J. Setina, J. Vac. Sci. Technol., A 17 (**1999**), 1040–1046

[13] V. Nemanic, T. Bogataj, Vacuum, 50 (**1998**), 431–437

[14] V. Nemanic, B. Zajec, J. Setina, J. Vac. Sci. Technol., A 19 (**2001**), 215–222

[15] P. A. Redhead, Hydrogen in vacuum systems; an Overview, Proceedings of the First International Workshop on Hydrogen in Materials and Vacuum Systems, AIP Conference Proceedings, Volume 671, 2003, 243–254, (http://adsabs.harvard.edu/abs/2003AIPC..671..243R)

[16] www.mksinst.com

[17] V. Nemanič, T. Bogataj, Kovine zlitine tehnologije, 32 (**1998**) 3–4, 249–253

[18] D. M. Grant et al., J. Nucl. Mater., 149 (**1987**), 180–191

[19] Park et al., J. Vac. Sci. Technol., A 26 (**2008**), 1166–1171

UDK 669.18(437.3)
Professional article/Strokovni članek

ISSN 1580-2949
MTAEC9, 46(2)169(2012)

THE QUALITY OF SUPER-CLEAN STEELS PRODUCED AT ŽĎAS, inc.

KAKOVOST SUPERČISTIH JEKEL, IZDELANIH V PODJETJU ŽĎAS, inc.

Martin Balcar[1], Ludvík Martínek[1], Pavel Fila[1], Jaroslav Novák[1], Jiří Bažan[2], Ladislav Socha[2], Danijela Anica Skobir Balantič[3], Matjaž Godec[3]

[1]ŽĎAS, a. s., Strojírenská 6, 591 71 Žďár nad Sázavou, Czech Republic
[2]VŠB – Technical University of Ostrava, 17. listopadu 15/2172, 708 33 Ostrava-Poruba, Czech Republic
[3]Institute of Metals and Technology, Lepi pot 11, 1000 Ljubjana, Slovenia
martin.balcar@zdas.cz

Prejem rokopisa – received: 2011-05-30; sprejem za objavo – accepted for publication: 2011-08-24

The production of Super-Clean Steels for the rotor forgings of compressors and generators for gas-turbine units started at ZDAS with the use of secondary metallurgy processes, a ladle furnace and vacuum degassing. The development and optimization of Super-Clean Steel production technology enables effective molten metal manufacture, conforming to the requirements for chemical composition and micro-cleanness. According to the results of the current production, the effective production of rotor forgings requires new technological steps in ingot casting.

Keywords: super-clean steel, steelmaking, secondary metallurgy, ingot casting

Proizvodnja superčistih jekel za odkovke rotorjev kompresorjev in generatorjev za plinske turbine se je začela z začetkom uporabe procesov sekundarne metalurgije, s ponovčno pečjo in z vakuumsko degazacijo. Razvoj in optimizacija tehnologije superčistih jekel omogočata učinkovito izdelavo taline z upoštevanjem kemične sestave in mikročistosti. Glede na rezultate sedanje proizvodnje so za učinkovito izdelavo rotorjev potrebne tehnološke izboljšave litja ingotov.

Ključne besede: superčisto jeklo, izdelava jekla, sekundarna metalurgija, litje ingotov

1 INTRODUCTION

The production of rotors at ZDAS consists of medium-weight forgings for equipment to generate electric power, gas turbines of the type GT – 009 with a maximum output of 11.7 MW and a gas temperature at the outlet up to 580 °C.[1]

In the frame of the production of a trial series of forgings for compressor and generator rotors in ZDAS, samples of steel were taken during the forging of ingots 8K10.0 and 8K13.0 from the steel grade 26NiCrMoV115.

The analyses of the chemical composition and the evaluations of the results from the viewpoint of the achieved parameters of chemical cleanliness, as well as from the viewpoint of the influence of casting and solidification on the differences between the chemical composition of the melt and the forging, make it possible to interpret the stability of the production process. The analyses of forging defects provided sufficient information about the possible causes of defects.

2 CHEMICAL COMPOSITION OF A FORGING MADE OF SUPER-CLEAN STEELS

Table 1 summarises the requirements for the chemical composition of super-clean steel (SCS) for

Table 1: Chemical composition of steel 26NiCrMoV115 in mass fractions, *w*/%
Tabela 1: Kemična sestava jekla 26NiCrMoV115 v masnih deležih, *w*/%

A	C	Mn	Si	P	S	Cr	Ni	Mo	V	Al	Cu	As	Sn	Sb
	(*w*/%)											(μg/g)		
min.	0.26	max.	max.	max.	max.	1.40	2.80	0.30	max.	max.	max.	max.	max.	max.
max.	0.32	0.30	0.07	0.007	0.005	1.70	3.00	0.45	0.15	0.010	0.12	100	100	50

Table 2: Chemical composition of steel 26NiCrMoV145 in mass fractions, *w*/%
Tabela 2: Kemična sestava jekla 26NiCrMoV145 v masnih deležih, *w*/%

B	C	Mn	Si	P	S	Cr	Ni	Mo	V	Al	Cu	As	Sn	Sb	X factor
	(*w*/%)											(μg/g)			
min.	0.26	max.	max.	max.	max.	1.60	3.50	0.30	max.	max.	max.	max.	max.	max.	max.
max	0.32	0.04	0.04	0.004	0.004	1.90	3.80	0.45	0.15	0.015	0.12	80	50	20	7.0

Table 3: Average content of elements in the heats of steel grade 26NiCrMoV115 in mass fractions, *w*/%
Tabela 3: Povprečna vsebnost elementov v talinah jekla 26NiCrMoV115 v masnih deležih, *w*/%

A	C	Mn	Si	P	S	Cr	Ni	Mo	V	Al	Cu	As	Sn	Sb
	(*w*/%)											(μg/g)		
AVG	0.295	0.210	0.023	0.0043	0.0028	1.588	2.913	0.390	0.106	0.0063	0.080	49.4	58.5	29.3
s	0.011	0.031	0.017	0.0008	0.0014	0.035	0.033	0.013	0.009	0.0020	0.024	7.7	15.1	2.5

Table 4: Average content of elements in the heats of steel grade 26NiCrMoV145 in mass fractions, *w*/%
Tabela 4: Povprečna vsebnost elementov v talinah jekla 26NiCrMoV145 v masnih deležih, *w*/%

B	C	Mn	Si	P	S	Cr	Ni	Mo	V	Al	Cu	As*	Sn*	Sb*	X factor
	(*w*/%)											(μg/g)			
AVG	0.293	0.032	0.012	0.0032	0.0044	1.809	3.714	0.395	0.108	0.008	0.014	31.1	32.1	<20	5.81
s	0.012	0.010	0.004	0.0006	0.0039	0.046	0.040	0.0011	0.008	0.003	0.008	18.6	17.6	–	1.10

* Concentration of elements below the detection limits

Table 5: Correlation coefficients of elements (sample of the melt / forging)
Tabela 5: Korelacija kemične sestave talin in odkovkov

Elements	**Ni**	**Cu**	**Mn**	**Si**	**Cr**	**V**	**S**	**Ca**	**Al**	**C**	**Mo**	**P**	**N**	**O**
X (*w*/%) forging	0,99	0,99	0,99	0,98	0,97	0,92	0,89	0,85	0,78	0,78	0,75	0,60	0,46	0,05

compressor and generator rotors and **Table 2** for the discs of turbine and generator wheels.

The average contents of the alloying and tramp elements of 87 heats of steel grade 26NiCrMoV115 (A) and 19 heats of steel grade 26NiCrMoV145 (B) are given in **Tables 3** and **4**.

On the basis of the ordinary production of forgings a complete chemical composition was determined for 44 samples of steel from the forgings, i.e., for 44 ingots from various heats of the steel grade 26NiCrMoV115. **Figures 1** to **4** show the distribution of the content of the elements P, S, O and N.

For the monitored 44 heats the average content of phosphorus is 37.1 μg/g and the standard deviation is 7.65 μg/g. The contents vary in the range from 20 μg/g to 60 μg/g.

The average content of sulphur was of 29.3 μg/g, with the variation in the range from 10 μg/g to 50 μg/g and a standard deviation of 12.08 μg/g.

The distribution of oxygen content is shown in **Figure 3**. The average content of oxygen was 20.6 μg/g

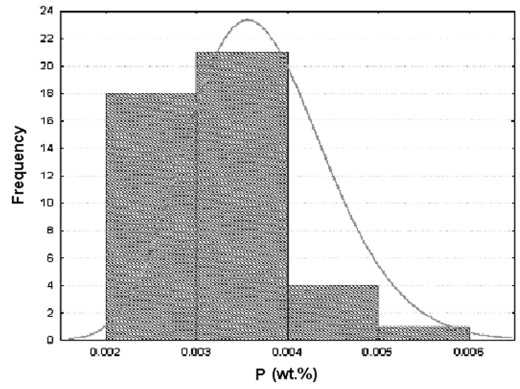

Figure 1: Phosphorus content – forging
Slika 1: Vsebnost fosforja v odkovkih

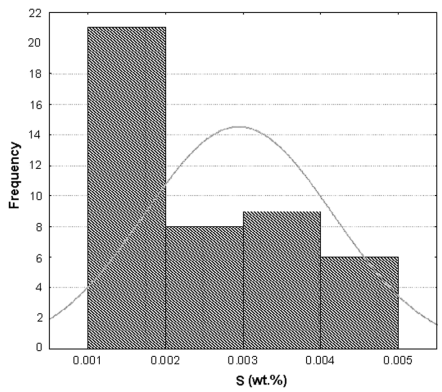

Figure 2: Sulphur content – forging
Slika 2: Vsebnost žvepla v odkovkih

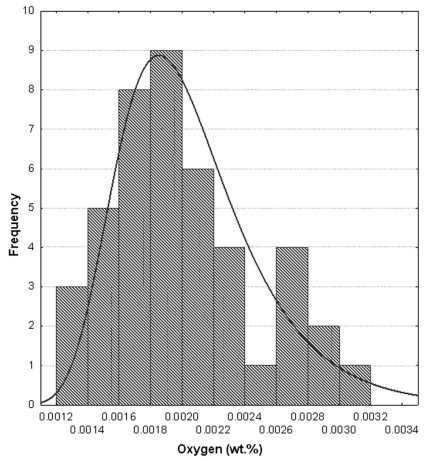

Figure 3: Oxygen content – forging
Slika 3: Vsebnost kisika v odkovkih

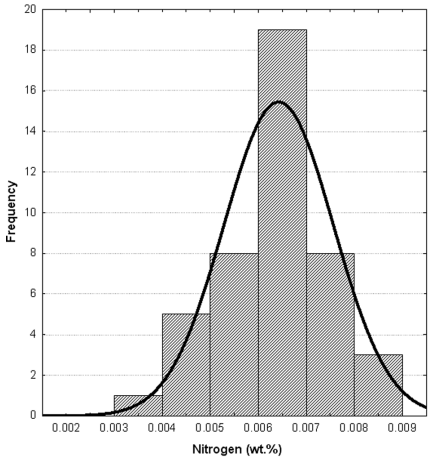

Figure 4: Nitrogen content – forging
Slika 4: Vsebnost dušika v odkovkih

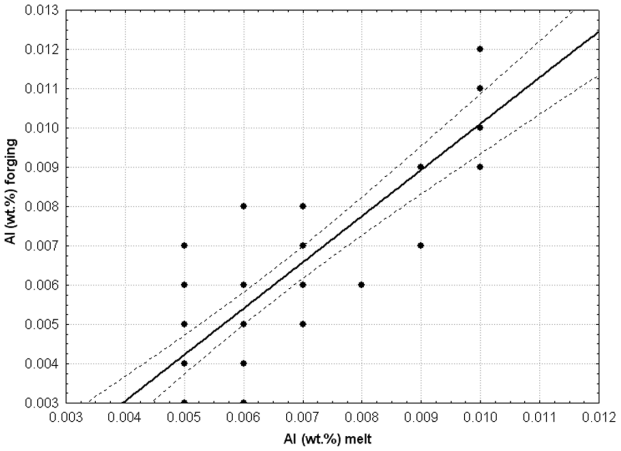

Figure 6: Aluminium content – melt / forging
Slika 6: Vsebnost aluminija – talina/odkovek

and the standard deviation was 4.56 µg/g. The oxygen content in the forgings varied in the range from 12 µg/g to 32 µg/g. The average content of nitrogen in **Figure 4** was 64.0 µg/g and the standard deviation was 11.36 µg/g. The nitrogen content in the forgings varied in the range from 34 µg/g to 84 µg/g.

3 AGREEMENT OF THE CHEMICAL ANALYSIS OF THE MELT WITH THE ANALYSIS OF THE FORGING

The results of the chemical composition of the samples of steel forgings were compared with the results of the chemical analysis of the melt to verify the agreement of both chemical analyses. The correlation coefficients of the individual elements in descending agreement are shown in **Table 5**.

The results in **Table 5** suggest that the agreement of the chemical composition of the forgings and the melts depends on the place in the sample ingot where the measurement was made. If we consider the position of the analysed sample is below the ingot head, which is the place of its biggest cross-section, and simultaneously the latest solidification part of the ingot body, it may be expected that due to segregations, the concentrations of some elements may be influenced during the ingot's solidification.

This assumption is confirmed by the order of the correlation coefficients of chromium, vanadium and molybdenum, i.e., elements that form carbides. Phosphorus and sulphur show a high degree of segregation and the low correlation coefficient suggests the segregation of nitrogen and aluminium, which have a great mutual affinity.

The lowest correlation coefficients according to **Table 5** were calculated for the gases, oxygen and nitrogen, while the correlation coefficient for the oxygen concentrations is negligible. In **Figures 5** to **8** the dependence of selected elements, i.e., calcium, aluminium, nitrogen and oxygen, is shown.

The disagreement in the oxygen and nitrogen contents is apparently related to the casting process and the sampling of metal for the analysis of both elements

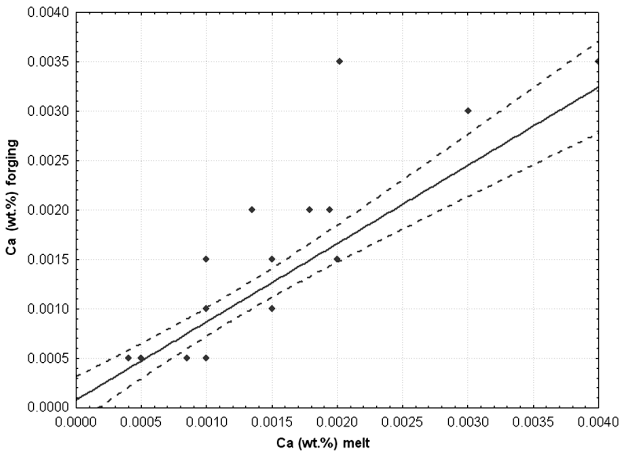

Figure 5: Calcium content – melt / forging
Slika 5: Vsebnost kalcija – talina/odkovek

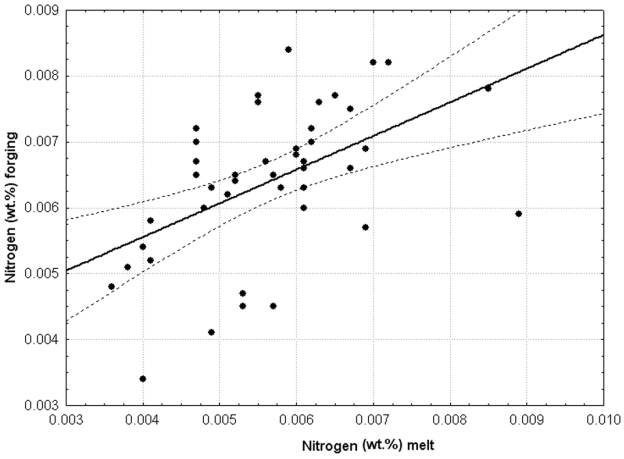

Figure 7: Nitrogen content – melt / forging
Slika 7: Vsebnost dušika – talina/odkovek

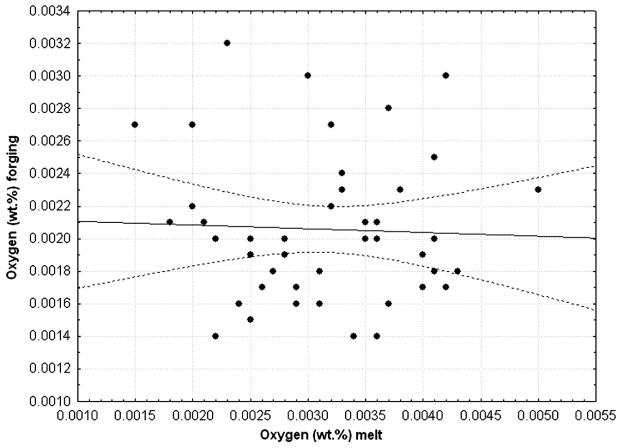

Figure 8: Oxygen content – melt / forging
Slika 8: Vsebnost kisika – talina/odkovek

from the melt. The sampling occurs by taking a small amount of melt from the flow of metal under the slide gate into the steel ladle, from which the metal is afterwards poured again into the ingot mould. This process occurs with considerable contact of the melt with surrounding atmosphere, which creates good conditions for the saturation of the degassed melt with oxygen and nitrogen.

For the oxygen content, we consider the concentration determined by the chemical analysis of the sample taken from the forging to be realistic one. On the basis of the results of the analyses it is possible to discuss the potential control of the steel's chemical composition, as well as possibility of verifying the obtained individual elements concentrations already during hot-metal production. Namely, the prediction of oxygen and nitrogen contents in the production of hot metal appears to be rather problematic with respect to the final forging contents. This suggest that the existing methodology for taking samples of melts by pouring for a determination of the gas contents in steel of the type 26NiCrMoV115 and 26NiCrMoV145 is unsatisfactory.

The solution to this issue may be the realisation of equipment that can take samples with the elimination of the earlier mentioned influence of the atmosphere, i.e., preferably by sampling directly from the ladle at the end of the treatment by the VD or VCD process and from the ingot, either already during pouring or after its completion.

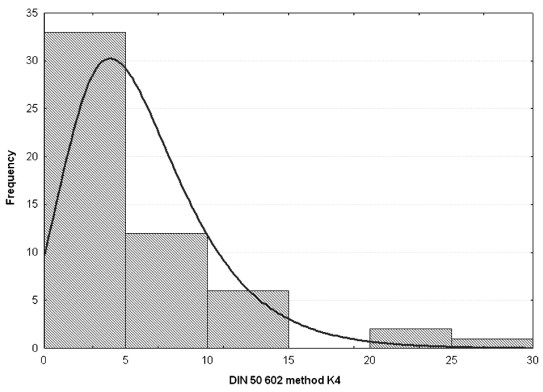

Figure 9: Micro-cleanness DIN50602, method K_4
Slika 9: Mikročistost po DIN50602, metoda K_4

4 METALLOGRAPHIC CLEANLINESS OF SUPER-CLEAN STEEL FORGINGS

The metallographic cleanliness of steel in conformity with the standard DIN 50602 was determined according the method K4 for 44 heats from identical samples, as for previous examinations, and for an additional 10 heats using samples taken in a similar manner. Thus there was a total of 54 heats.

The distribution of micro-cleanness determined according the standard DIN 50602 method K4 is shown in **Figure 9** interlaid with the curve of the normal distribution with the exclusion of the extreme values of $K_4 > 20$. The average micro-cleanness $K_4 = 6.3$ with a standard deviation of 5.61 was calculated for 54 heats. The values of K_4 were in the range from 0 to 29.

From the viewpoint of the current requirements for the cleanliness of steel the values $K_4 > 10$ can be considered as deteriorated and $K_4 > 20$ as unsatisfactory. However, the limits stipulated in this manner are relative and they are based on the assumption that the deteriorated micro-cleanness will considerably influence the mechanical properties, particularly the strength characteristics and the transition temperature or the creep resistance of the forgings.

In accordance with the defined measures, very good micro-cleanness was found for 45 heats (83.3 %) out of the 54 examined heats, while 6 heats (11.1 %) had worse micro-cleanness, and an unsatisfactory micro-cleanness was found for 3 heats, i.e., in 5.6 % of production.

In spite of the deteriorated parameters of the metallographic purity of the steels for some heats, the forgings passed the required tests of mechanical properties, even without special measures concerning their heat treatment. It is therefore possible to consider the achieved metallographic cleanliness of super-clean steels is acceptable. However, the objective should be to achieve the value of $K_4 < 10$.

The measures aimed at ensuring the required cleanliness may be the optimisation of slag mode or its possible modification. Due to the occurrence of exogenous inclusions it is not possible to also exclude the casting technology, including issues related to the ceramics used for pouring.[2]

5 ANALYSIS OF THE DEFECTS IN SUPER-CLEAN STEEL FORGINGS

Altogether, 122 shafts were produced until 2006, out of which 18 shafts were classified as unsatisfactory due to the occurrence of undesirable ultrasonic defects. A

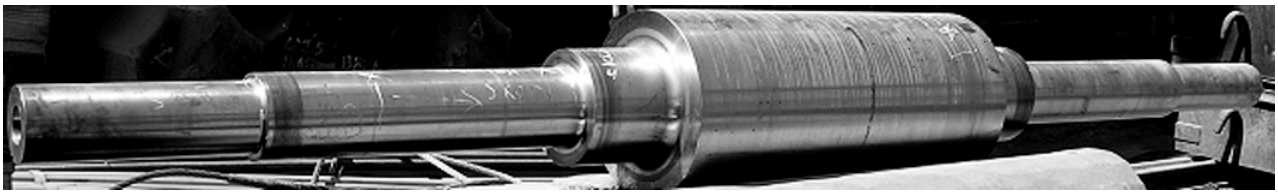

Figure 10: Defective generator rotor shaft – forging No. 447 660
Slika 10: Defektna gred rotorja generatorja – odkovek št. 447 660

Figure 11: Detail of extent and location of the defect on the generator rotor shaft – forging No. 447 660
Slika 11: Velikost in mesto napake na gredi rotorja generatorja – odkovek št. 447 660

total of 14.8 % of the total number of produced shafts was rejected. Altogether, 63 pieces of shafts were made from the ingots 8K10,0 and 59 shafts from the ingots 8K13,0, while 10 pieces of rejected shafts were made from the ingots 8K10,0 and another 8 pieces of rejected shafts were made from the ingots 8K13,0 [3].

Figure 12: Forging No. 447 660. Macro-shape of the sample at the place of defect location.
Slika 12: Odkovek št. 447 660. Vzorec z mestom napake.

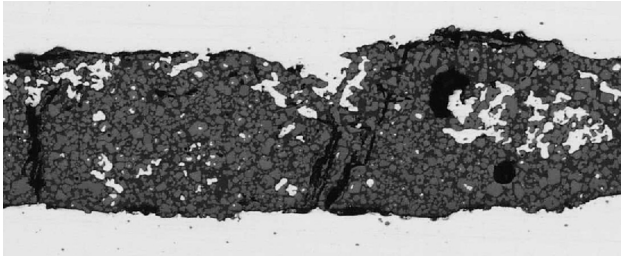

Figure 13: Micro-shape of the large part of inclusion (500-times)
Slika 13: Mikrooblika večjega dela vključka (povečava 500-kratna)

Defective forgings were submitted to a metallographic investigation and in the following review documents the results of the analysis of the forging No. 447 660 of the generator rotor shaft are presented. The shaft with a diameter of 270 mm ingot heel in **Figures 10** and **11** did not pass the ultrasonic test performed on the roughed piece prior to drilling of straight-through hole with a diameter of 95 mm. It was expected that with drilling of the hole the defects will be removed. After drilling and heat treatment an areal defect KSR 1 to 4 mm was detected at a depth of 60 mm to 75 mm in the central part of the piece.

A sample was taken from the forging in the transversal direction and the exact position of the defect was localised by repeated ultrasonic testing. A sample for metallographic analysis was taken from the place of the defect and after completion of the section at the location of the defect longitudinally with respect to the axis of the original forging continuous non-metallic inclusions was discovered on the full length of the sample (24 mm) of width of 1 mm. The macro-shape of the inclusion is shown in **Figure 12** and its micro-shape in **Figures 13** and **14**. The steel microstructure consisted predominantly of sorbite and bainite.

More analyses were performed in collaboration with the Institute of Metals and Technology Ljubljana. An identical sample was analysed by emission electron microscope JEOL JSM 6500F and an energy-dispersive spectroscope – EDS INSA CRYSTAL 300. In **Figure 15** the points of the analyses and in **Table 6** the results of the analyses are shown.

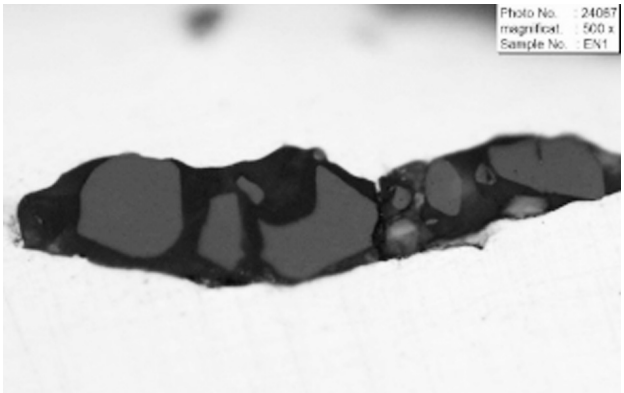

Figure 14: Shorter rows of oxides were near the large inclusion (500-times)
Slika 14: Krajši oksidni vključek blizu večjega (povečava 500-kratna)

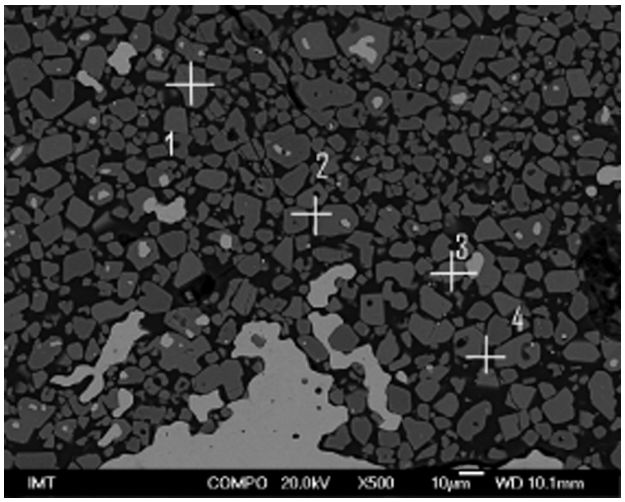

Figure 15: Points of analysis of inclusion
Slika 15: Mesta analize vključka

The chemical composition of the non-metallic–ceramic materials used during the production of steel was made for a comparison with the results of the analysis of the chemical composition of the inclusions – see **Table 7**.

On the basis of a comparison of the results of the analysis in **Tables 6** and **7** and the content of the basic elements Si, Na and K it is possible to consider the analyses on points 2 and 4 as inclusions based on the casting powder PC20. Spectre 1 and 3 correspond to the slide gate sand fill Chromix 8/5. Similar conclusions were drawn also in the other 6 cases of unsatisfactory shafts. From the description and the set of data for the chemical composition of the impurities found in the forgings for the shafts of steel 26NiCrMoV115, as determined by emission electron microscope JEOL JSM 6500F and by energy dispersive spectroscope EDS INSA CRYSTAL 300, it was determined that the main cause of the unacceptable defects of the forgings was the occurrence of non-metallic particles with a chemical composition corresponding to the casting powder PC 20 and to the slide gate fill sand Chromix 8/5. The determination of the real causes of the occurrence of this combination of non-metallic materials in ingots and forging is the subject of further tests and investigations.

6 CONCLUSIONS

In this work the production of super-clean steels at ZDAS from the perspective of chemical composition is evaluated. The chemical analyses of the melts steel were compared with the chemical composition of the forgings.

Table 6: Chemical composition in the analysed points shown in **Figure 15**
Tabela 6: Kemična sestava v točkah, označenih na **sliki 15**

Spectre	O	Al	Si	K	Mg	Na	Ca	Cr	Ti	V	Mn	Fe	Total
	(*w*/%)												
1	32.78	8.16	0.32	–	6.78	–	–	32.02	–	–	–	19.93	100
2	44.93	9.00	24.85	0.73	3.61	2.77	1.26	0.56	0.57	–	11.72	–	100
3	29.87	10.20	0.47	–	5.79	–	–	33.77	0.57	2.26	13.49	3.56	100
4	37.17	11.24	31.08	1.09	1.65	2.57	2.23	–	–	–	11.56	1.40	100

Spectre 1 – order of elements: Cr > Fe > Al > Mg > Si + O
Spectre 2 – order of elements: Si > Mn > Al > Mg > Na > Ca > K > Ti > Cr + O
Spectre 3 – order of elements: Cr > Mn > Al > Mg > Fe > V > Ti > Si + O
Spectre 4 – order of elements: Si > Mn > Al > Na > Ca > Mg > Fe > K + O

Table 7: Chemical composition of non-metallic materials used during the production of steel
Tabela 7: Kemična sestava nekovinskih materialov, uporabljenih pri izdelavi jekla

Sample	O	Al	Si	K	Mg	Na	Ca	Cr	P	S	Mo	Ti	Fe	Total
	(*w*/%)													
Refining slag VD-EU2	45.2	8.2	0.9		1.3		43.0						1.3	100
Refractory shotcrete of ref. ladle – Kalinovo	55.2	22.9	6.8		3.0		9.6						2.5	100
Sand in slide gate Chromix 8/5	30.2	8.3	1.5		7.5			33.6		0.2			18.7	100
Pouring channel – main gate of the system	55.1	21.0	19.5	1.7								1.0	1.8	100
Mortar for gluing of pouring channels – Regnalit	57.7	12.5	26.0	1.7								0.6	1.6	100
Mortar for gluing of pouring channels – ŽĎAS	52.9	16.4	24.2	0.7		4.7						0.6	0.8	100
Sand SiO_2	58.8	0.2	40.5									0.2	0.3	100
Sand SiO_2 – recycled	58.2	0.6	38.4	0.3				1.0					1.6	100
Casting powder PC 20	51.3	13.8	20.7	2.4	0.5	2.4	1.9		0.6		1.7	1.2	3.6	100

The agreement of both is acceptable for all elements, with the exception of the contents of nitrogen and particularly of oxygen. It can be concluded that the difference could be resolved by a change of methodology of taking the samples for a determination of the contents of gases in the hot metal.

On the basis of the evaluation of the micro-cleanness of the steel according to the standard DIN 50 602 by method K4, a very good micro-cleanness $K_4 < 10$ was assessed for 45 heats out of 54 heats, thus for 83.3 % of the production.

The metallographic analyses of 7 rejected rotors with use of the electron microscope showed that 6 shafts out of 7 were unsatisfactory due to the presence of isolated massive rows of clusters of non-metallic particles with lengths up to 15 mm consisting of 2 phases – casting powder and chromite sand (Cr_2O_3), which was used as fill sand for refining the ladle slide gate.

The measures for ensuring the stable level of metallographic cleanliness and for the prevention of the occurrence of exogenous inclusions may consist of the optimisation of slag mode or in its possible modification, as well as of interventions into casting technology, including the solution of the issues for ceramics used for the pouring and filtration of steel.

Acknowledgement

The investigations were performed within the EUREKA program of the E!3192 ENSTEEL project, identification number 1P04EO169 and project FR-TI1/222.

7 REFERENCES

[1] M. Balcar, R. Železný, L. Martínek, J. Bažan, Modelling of solidification process and chemical heterogeneity of 26NiCrMoV115 steel ingot. 7th International Symposium Materials and Metallurgy, Croatia, Šibenik, 2006, Metalurgija, 45 (**2006**) 3, 229

[2] J. Bažan, L. Socha, Evaluation of corrosion of refractory materials by molten steel. 7th International Symposium Materials and Metallurgy, Croatia, Šibenik, 2006, Metalurgija, 45 (**2006**) 3, 232

[3] P. Fila, M. Balcar, L. Martínek, Náhled na oblast neúplných vlastních nákladů ve vazbě na některé technologické postupy výroby elektrooceli [Insight into incomplete factory costs in relation to some technological processes for production of electrical steel], 22nd National conference with foreign participants : Teorie a praxe výroby a zpracování oceli [Theory and practice of production and treatment of steel], 4th – 5th April 2006, Rožnov pod Radhoštěm. Tanger spol. s. r. o. Ostrava, 2006, 257–261

UDK 621.74.043:669.71'782'3:539.21
Professional article/Strokovni članek

ISSN 1580-2949
MTAEC9, 46(2)177(2012)

SIMULATIONS OF THE SHRINKAGE POROSITY OF Al-Si-Cu AUTOMOTIVE COMPONENTS

MODELIRANJE KRČILNE POROZNOSTI Al-Si-Cu AVTOMOBILSKIH ULITKOV

Lejla Lavtar[1], Mitja Petrič[2], Jožef Medved[2], Boštjan Taljat[1], Primož Mrvar[2]

[1]STEEL, d. o. o., Litostrojska cesta 60, SI-1000 Ljubljana, Slovenia
[2]Department of Material Science and Metallurgy, Faculty of Natural Sciences and Engineering, University of Ljubljana, Aškerčeva cesta 12, SI-1000 Ljubljana, Slovenia
lavtar@steel.si

Prejem rokopisa – received: 2011-08-17; sprejem za objavo – accepted for publication: 2011-12-01

The 3D shoot-sleeve and shrinkage-porosity simulations of a high-pressure die-casting (HPDC) process are presented using the ProCast casting-simulation software. The porosity was studied during the casting and solidification of aluminium-silicon-copper alloy components in an H13 steel die. Excellent agreement between the simulated and experimental results was observed.

Keywords: high-pressure die casting, aluminium-silicon-copper alloy, shrinkage porosity, ProCast software

V tem prispevku je prikazano 3D-modeliranje pomika bata in krčilna poroznost procesa visokotlačnega litja (HPDC) z uporabo programskega paketa ProCast. Študija poroznosti je prikazana na aluminij-silicij-bakrovih ulitkih, litih v orodje iz jekla H13. Analiza je pokazala zelo dobro ujemanje med modeliranimi in eksperimentalno ugotovljenimi rezultati.

Ključne besede: visokotlačno litje, aluminij-silicij-bakrova zlitina, krčilna poroznost, ProCast

1 INTRODUCTION

To manufacture a large variety of products with high dimensional accuracy using the process of high-pressure die casting (HPDC) the fast and economical production of aluminium automotive components has been developed.[1] In the past two decades the rapid development of numerical simulation methodology and the solidification simulation of castings have been introduced as an effective tool for modeling the casting process and improving the quality of castings.[2,3] The use of simulation software saves time and reduces the costs of the casting-system design and of the materials used.

The physical, mechanical and esthetic properties directly depend on the metallurgical operating conditions during casting. The combination of the mechanical properties of the die-cast product, such as the die temperature, the gate metal velocity, the applied casting pressure, the cooling rate during die casting, the geometrical complexity of the parts and the mold-filling capacity, all affect the integrity of the cast components. If these parameters are not controlled properly, various defects in the finished component are to be expected. The applied casting pressure is crucial during the solidification of high-integrity parts. The effects of process variables on the quality of cast components with in-cavity pressure sensors, delay time and casting velocity were examined by Dargusch in 2006. He found that the porosity decreased with increasing intensification pressure and increased with a higher casting velocity.[1,4]

The porosity of castings can be examined with destructive testing, with visual observation after machining and non-destructing testing, like X-ray microscopy and image-processing technology, which can provide more detailed information about the pores. It is also observed that the chemical composition of the alloy affects the porosity of the cast components, the grain refinement and the modification.[5,6] Now it is commonly accepted that the shrinkage and the gas are the two major causes of porosity. The shrinkage porosity is associated with the "hot spots" in the casting. The gas porosity is caused by entrapped air in the injection system and the cavity, the gas generated from burned lubricants, the water in the cavity and hydrogen. The entrapped air is the unwanted product of the high velocity of the alloy caused by the turbulent flow during the injection process.

The paper describes a simulation of the HPDC of an Al-Si9Cu3 casting in an H13 steel die and the comparison between the simulated and the experimental porosity.

2 EXPERIMENTAL

2.1 Material and casting system

The alloy used for the die casting was an aluminium-silicon-copper alloy (**Table 1**). The alloy is less prone to shrinkage and internal shrinkage cavities and has a very good castability. The ALSI H13 chromium hot-work tool steel was used for the die. This steel has a higher resistance to the heat cracking and die wear caused by the thermal shock associated with the

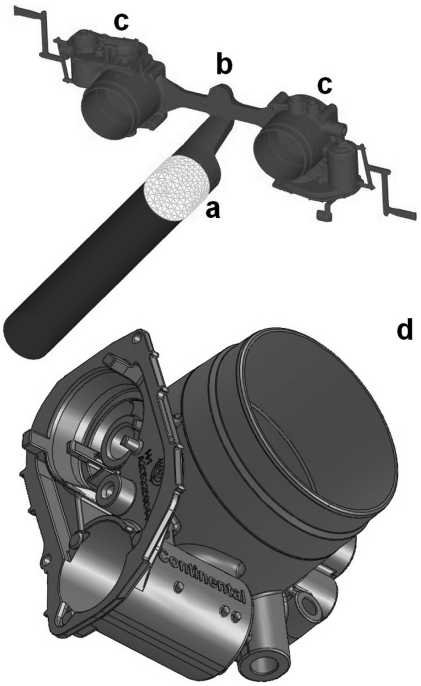

Figure 1: Casting system: a) shot sleeve with plunger, b) gates and runner system, c) the two cavities left and right and d) the casting component

Slika 1: Ulivni sistem: a) livna komora z batom, b) ulivni in dovodni kanal, c) dve livni votlini leva in desna in d) ulitek

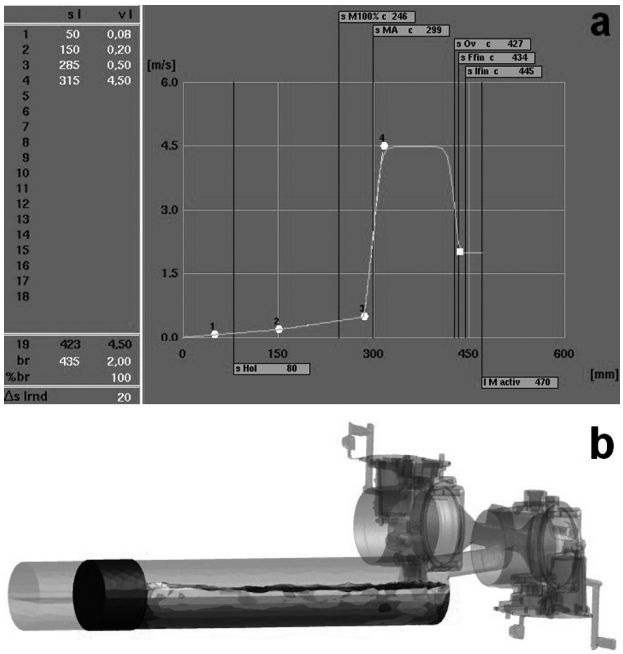

Figure 2: a) Shot profile with four different plunger speeds and b) volume fraction picture of the alloy and the empty space in the shot sleeve

Slika 2: a) Diagram pomika bata s štirimi različnimi hitrostmi in b) slika volumenskega deleža zlitine in atmosfere v livni komori

die-casting process.[7] The casting system with a shot sleeve and a plunger are presented in **Figure 1a**. The gates and runner system with two cavities are presented in **Figures 1b** and **1c**. The final product is an automotive component (**Figure 1d**).

Table 1: Chemical composition in mass fractions of the Al-Si9Cu3 alloy, *w*/%

Tabela 1: Kemijska sestava Al-Si9Cu3 zlitine v masnih deležih, *w*/%

Si	Cu	Fe	Mn	Mg	Zn	Ni	Cr
10.38	2.73	0.82	0.25	0.34	0.82	0.04	0.04

2.2 HPDC process

The casting process can be divided into four phases: the pre-filling, the shot, the final pressure phase and the ejection phase. In the pre-filling phase, the molten metal is injected by a plunger, which forces the metal with a low velocity through a horizontally mounted cylindrical shot sleeve up to the gate. Usually, the shot sleeve is partially filled with molten metal, the amount of which depends on the cast component volume. The remaining volume is empty. Previous research work has shown that the fluid flow and the amount of empty space are affected by the plunger motion, the shot-sleeve dimensions and the amount of metal in the sleeve.[8] In the short-shot phase the plunger is accelerated to high velocity and so any venting of the die cavity is practically impossible. In the final pressure phase, solidification of the casting is completed and in the ejection phase, the moulded part is removed, the die halves are sprayed and positioned back to repeat the cycle.

The industrial HPDC process for casting an automotive component starts with a plunger that has four

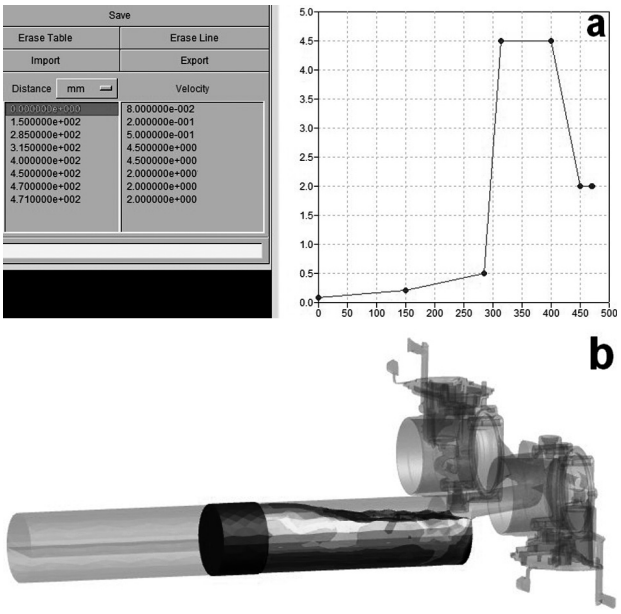

Figure 3: a) Shot profile with three different plunger speeds and b) volume fraction picture of the alloy and the empty space in the shot sleeve

Slika 3: a) Diagram pomika bata s tremi različnimi hitrostmi in b) slika volumenskega deleža zlitine in atmosfere v livni komori

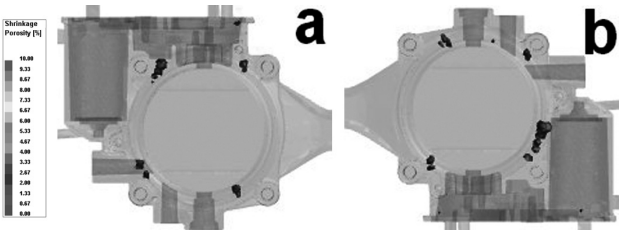

Figure 4: Shrinkage porosity simulation of: a) left and b) right castings
Slika 4: Simulacija krčilne poroznosti a) na levem in b) desnem ulitku

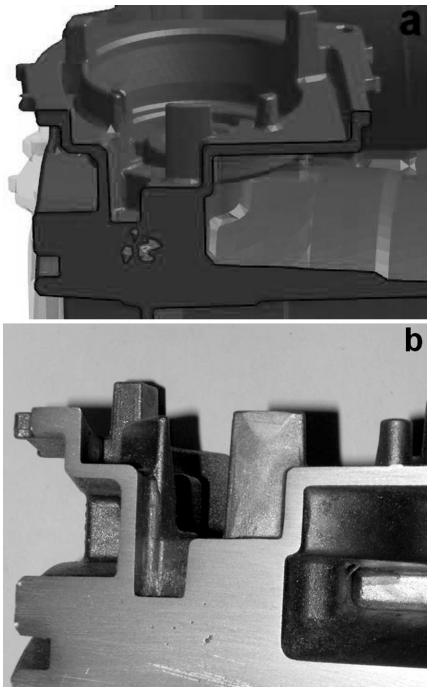

Figure 5: Shrinkage porosity in left casting at spot 1: a) simulation, b) cut section
Slika 5: Krčilna poroznost v levem ulitku na mestu 1: a) modeliranje, b) prerez

different speeds, as shown on the shot profile in **Figure 2a**. The volume fraction in **Figure 2b** shows that there was no wave and no air entrapment.

3 RESULTS AND DISCUSSION

3.1 The shot-sleeve simulation

The same industrial HPDC process was then simulated with the FEM-based software called ProCast. The movement of the plunger was simulated using three different plunger speeds. The simulation is shown on the shot profile in **Figure 3a**. The volume fraction in **Figure 3b** shows no wave and no air entrapment.

The set-up time was minimized, the plunger speed increased and the industrial HPDC process was shortened by 0.48 s.

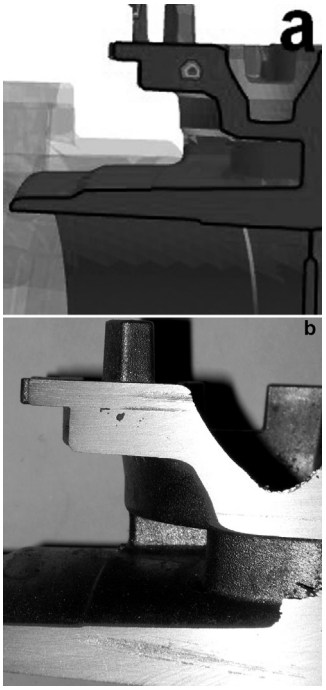

Figure 6: Shrinkage porosity in left casting at spot 3: a) simulation, b) cut section
Slika 6: Krčilna poroznost v levem ulitku na mestu 3: a) modeliranje, b) prerez

3.2 The shrinkage-porosity simulations

The shot-sleeve simulation results were used as the boundary conditions for the cavity-filling simulations and the shrinkage-porosity simulations, as the basic study in this paper was the shrinkage porosity. **Figure 4** shows the simulated shrinkage porosity "red spots" in the left and right castings were the porosity spots are marked with numbers. After nine cycles of casting constant conditions in the die were established and after ten cycles in the left-side casting two red spots of simulated shrinkage porosity were examined (**Figures 5** and **6**) and in the left casting (**Figures 5b** and **6b**) a good agreement with the simulated results of shrinkage porosity was found (**Figures 4, 5a** and **6a**).

4 CONCLUSIONS

In the present work the porosity of automotive components was analyzed with ProCast, FEM-based software. The most important conclusions that can be drawn are:

- The shot-sleeve simulation gives valuable information for the final quality of the components by minimizing the volume fraction of the empty space during the first stage of the HPDC process. The volume fraction shows no wave and no air entrapment.
- The shot-sleeve simulation gives savings in cycle time by minimizing the set-up time during the shot

stage of the HPDC process. The shot stage of the HPDC process set-up time was shortened by 0.48 s.

- The shot-sleeve simulation also gives information about the shrinkage-porosity location in castings, called "red spots". The shrinkage porosity on the sections of spots 1 and 3 in the left-side casting is in good agreement with the simulated results.

5 REFERENCES

[1] M. S. Dargusch, G. Dour, N. Schauer, C. M. Dinnis, G. Savage, J. Mater. Process. Technol., 180 (**2006**), 37–43

[2] T. R. Vijayaram, S. Sulaiman, A. M. S. Hamuda, J. Mater. Process. Technol., 178 (**2006**), 29–33

[3] L. A. Dobrzanski, M. Krupinski, J. H. Sokolowski, J. Mater. Process. Technol., 167 (**2005**), 456–462

[4] K. J. Laws, B. Gun, M. Ferry, Mater. Sci. Eng., A425 (**2006**), 114–120

[5] P. W. Cleary, J. Ha, M. Prakash, T. Nguyen, Appl. Math. Model., 30 (**2006**), 1406–1427

[6] M. Petrič, J. Medved, P. Mrvar, Metalurgija, 50 (**2011**) 2, 127–131

[7] http://www.cintool.com/catalog/mold_quality/H13. pdf

[8] W. Thorpe, V. Ahuja, M. Jahedi, P. Cleary, N. Stokes, Trans. 20th int. die casting cong. & expo NADCA, Cleveland, 1999, T99-014

UDK 621.793:539.231
Professional article/Strokovni članek

ISSN 1580-2949
MTAEC9, 46(2)181(2012)

WEAR-RESISTANT INTERMETALLIC ARC SPRAY COATINGS

OBRABNA OBSTOJNOST INTERMETALNIH PREVLEK, NAPRŠENIH V ELEKTRIČNEM OBLOKU

Ekrem Altuncu[1-3], Sedat Iriç[2], Fatih Ustel[3]

[1]Kocaeli University, Machine-Metal Tech., Kocaeli, Turkey,
[2]Sakarya University, Machine Eng. Dept., Sakarya, Turkey
[3]Sakarya University, Metall.-Materials Eng. Dept., Thermal Spray Center, Sakarya, Turkey
altuncu@kocaeli.edu.tr

Prejem rokopisa – received: 2011-10-20; sprejem za objavo – accepted for publication: 2011-12-08

The twin-wire electrical arc spraying (TWAS) process is widely used for worn-out surface restoration and the corrosion protection of metallic constructions. The industrial benefit of arc spray coatings is the possibility of cost-effective coating solutions to minimize corrosion problems. However, the wear resistance of metallic (such as Al, Cu and its alloys) arc sprayed coatings is inadequate. Alloys including Cu-Al intermetallic coatings are new candidates for use in tribological environments because of the combination of low cost and a remarkable resistance to abrasion under different working conditions. In this study the tribological properties of Al-Cu twin-wire arc-spray coatings are investigated in dry sliding test conditions depending on the load and the sliding distance.

Keywords: TWAS, intermetallic coatings, wear resistance

Elekrično naprševanje z dvojno žico (TWAS) se široko uporablja za popravilo obrabljenih površin in protikorozijsko zaščito kovinskih konstrukcij. Industrijska prednost postopka je priprava poceni prevlek za zmanjšanje korozijskih težav. Vendar obrabna obstojnost kovinskih (Al, Cu in zlitine) napršenih prevlek ni primerna. Intermetalne zlitine so nove kandidatke za uporabo v triboloških okoljih, ker združujejo nizko ceno in pomembno odpornost proti abrazivni obrabi. V tem delu so opisane tribološke lastnosti prevlek, napršenih z dvojno žico AlCu pri drsnem preizkusu v odvisnosti od obremenitve in drsne razdalje.

Ključne besede: TWAS, intermetalne prevleke, obrabna odpornost

1 INTRODUCTION

Wear-resistant coatings are used to reduce the damage caused by abrasion, erosion, cavitation, and fretting, also potentially associated with corrosion, and in some cases to reduce friction[1–3]. The optimal wear protection of light metallic substrates can be provided by a cost-effective thermal spray coating process and composition, depending on the operating environment and working conditions[4–9]. Intermetallic coatings, alloy coatings or metal-ceramic composite coatings can be obtained by wire arc spraying with cored wires or pre-alloyed wires. Cu-Al intermetallic systems were actively researched for applications in the aviation, automobile, naval, construction and defense sectors. The Cu-Al alloy system has long been used for wheel bearings for airplanes and screws for ships because of its resistance to abrasion, corrosion, and heat[7]. The purpose of this work is to develop an economical and effective deposition method for copper-aluminum intermetallic coatings to improve the wear resistance of light alloys. The sliding wear resistance of Al-Cu intermetallic arc spray coatings was investigated depending on load and sliding distance. The crystal structure and composition of the alloys were studied by x-ray diffraction.

2 EXPERIMENTAL DETAILS

The Sulzer Metco smart arc spray system we used consists of a power supply, a control unit and a robot-controlled arc spray gun. AISI 1020 low-carbon steel and AlSi alloys with a thickness of 3 mm were used in this study, and all the specimens to be coated were pretreated by grit blasting. Aluminum and copper wires with a diameter of 1.6 mm were sprayed with air used as an atomizing gas (**Table 1**). The sliding wear test (ASTM G133) conditions were as follows: sliding stroke, 20 mm; sliding frequency, 5 Hz; and normal

Table 1: Arc Spray Process Parameters
Tabela 1: Parametri napršev anja v električnem obloku

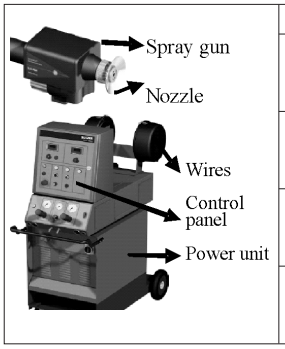

Smart ArcSpray (Sulzer)	
Current (Ampere)	205–210
Voltage (Volt)	26–28
Spray Distance (mm)	120–150
Gas Pressure (bar)	4

loads, 10 N to 30 N. The resulting sliding distances were 200 m to 1 600 m. The thickness loss and weight loss were measured on all the specimens under dry conditions. The weight loss of the specimen after the test was measured by an electronic analytical balance with a minimum reading of 0.01 mg. The friction coefficients of the coatings were measured using a ball-on-disc test in a CSM tribotester.

3 RESULTS AND DISCUSSION

3.1 Microstructure of the coatings

Surface and cross-sectional SEM micrographs of the arc-sprayed Cu-Al intermetallic coatings are shown in **Figure 1**. It is clear that the coating is a mixture of white and gray regions, which were identified as Cu and Al, respectively, by EDS analysis. The microhardness of the gray regions was found to be higher than that of the white regions.

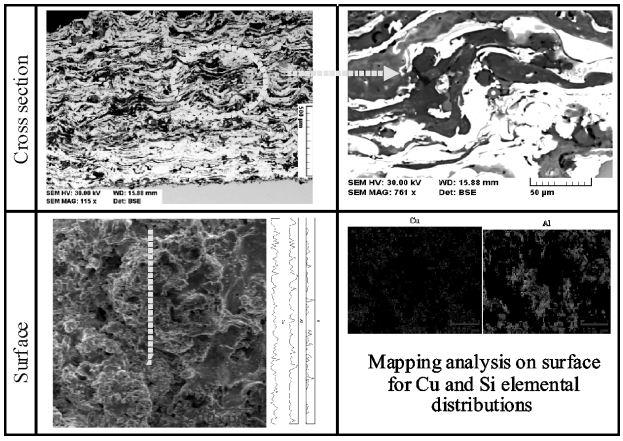

Figure1: Surface and cross-sectional SEM micrographs of the arc-sprayed Cu-Al intermetallic coatings

Slika 1: SEM-posnetki površine in prereza interemetalnih prevlek Cu-Al, napršenih v električnem obloku

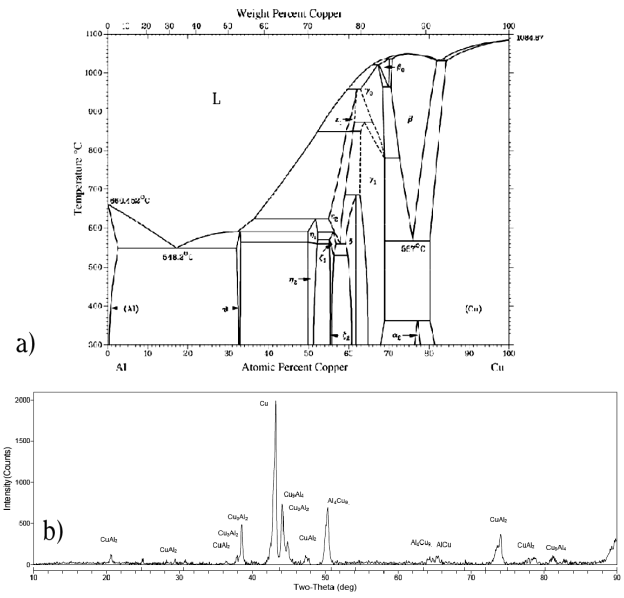

Figure 2: a) Phase diagram of Al-Cu binary system[8], b) XRD pattern of the coating

Slika 2: a) Binarni fazni diagram Al-Cu[8] in b) XRD-spekter prevlek

3.2 Cu-Al intermetallic phases

In the equilibrium phase diagram of Cu and Al (**Figure 2a**) there are five stable intermetallic phases, i.e., Cu_9Al_4, Cu_3Al_2, Cu_4Al_3, CuAl, and $CuAl_2$, with two terminal solid solutions of Cu(Al), which are often designated as αCu and Al(Cu)[8]. In this study different intermetallic phases were identified from XRD patterns. These phases are: 00-025-0012; $CuAl_2$, 00-024-000; Cu_9Al_4, 00-050-1477; Cu_3Al_2, 00-002-1254; Al_4Cu_9 (JCPDS numbers). The main phase content of Cu_9Al_4 and Cu_3Al_2 intermetallics affected the wear resistance of the coating. After a heat treatment at 400 °C for 3 h these phase ratios were increased.

3.3 Comparative wear resistance

The effects of porosity, flattening ratio, oxide content, and splat-to-splat bonding strength play an important role in the coating's antiwear performance. Low cohesion and high porosity generally cause a large piece of the coating to wear away and result in a decrease of the wear resistance

The thickness loss of the specimens was determined by measuring the cross-sectional thickness of the sound material after testing using an optical micrometer to observe accurately a cross-section through the central

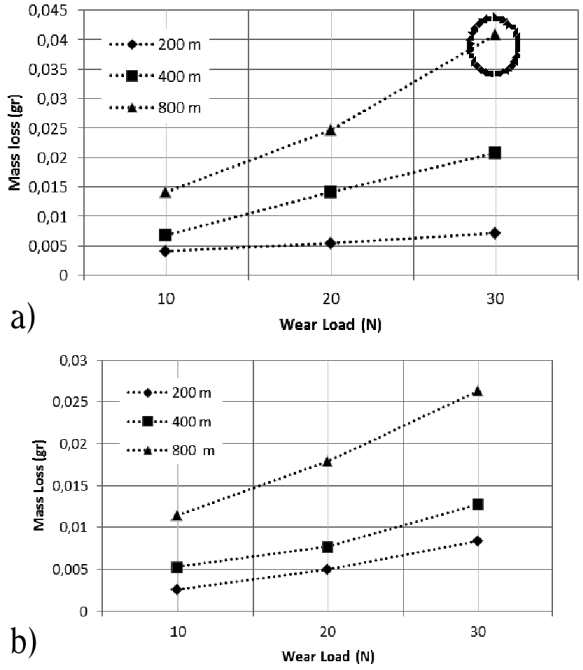

Figure 3: Mass-loss diagram as a function of wear load and sliding distance for samples: a) as-sprayed and b) heat treated

Slika 3: Izguba mase v odvisnosti od obrabne obremenitve in razdalje za vzorce: a) napršene in b) toplotno obdelane

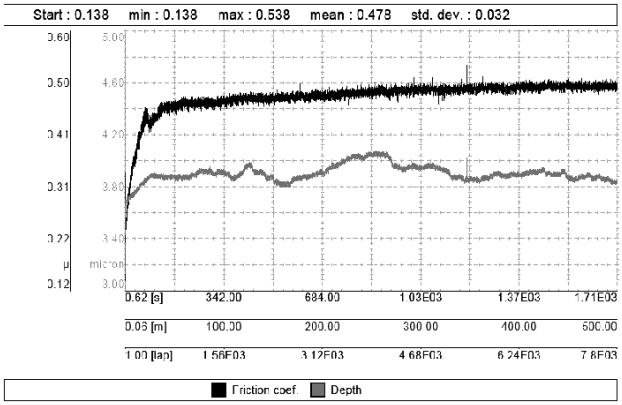

Figure 4: Cof of the coatings
Slika 4: Torni koeficient (*Cof*) prevlek

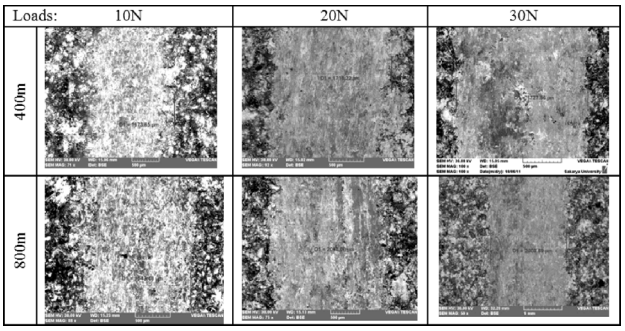

Figure 5: Wear-track profile views
Slika 5: Videz profila obrabnih poti

part of the track zone. The mass losses of the coatings are shown in **Figure 3a**. At a low load of 10 N a very small mass-loss difference was observed for sliding distances between 200 m and 800 m. When the wear load increased, the mass-loss difference increased. The highest wear mass loss on the coating and thickness was observed for 30 N at 800 m of sliding distance. The wear mass-loss change after the heat treatment of the coating is shown in **Figure 3b**. The heat-treated samples showed a lower mass loss. The microstructure and phase content of the coating have been suggested to influence the mass loss. In **Figure 4** the coefficient-of-friction (*Cof*) changes are shown for the Al-Cu coating. As can be seen the *Cof* values changed in the first stage of the test after which a steady state is observed. The *Cof* values were measured between 0.47 and 0.53. The heat-treated samples exhibited lower *Cof* values between 0.41 and 0.45.

Figure 5 shows the wear-track profiles of the coatings, both the track depth and width changed with an increase of the load. The width of the wear tracks varied between 1 650 μm and 1 730 μm at 400 m. When the sliding distance increased to 800 m the width varied between 1 747 μm and 2 015 μm. In both cases, the wear track is rougher than the initial coating surface, which indicates that particle pull-out took place during the sliding. The morphology of the wear tracks of the arc sprayed Al-Cu coatings confirmed that wear primarily arose through cracked particles. The pull-out particles then stayed in the contact area and led to three-body abrasive wear, which was the main wear type in these coatings.

4 CONCLUSION

Intermetallic coatings can be produced easily using the twin-wire arc spray process. A process optimization is required for a better coating quality. As a result of the heat treatment of the Cu-Al arc spray coatings, significant amounts of Cu_4Al_9 and Cu_3Al_2 intermetallic phases were identified by XRD analysis. These phase contents affected the wear mass loss and wear track-profile width. The comparative mass loss as a function of the wear load and sliding distance for both of the heat treated coatings and original coatings were determined. With the heat treatment we were able to improve the wear resistance of the coating by a factor of two.

5 REFERENCES

[1] C. Bartuli, T. Valent, F. Casadei, M Tului, Advanced thermal spray coatings for tribological applications, Proc. IMechE Part L: J. Materials: Design and Applications, 221 (**2007**), 175–185

[2] H. Pokhmurska, V. Dovhunyk, M. Student, E. Bielanska, Tribological properties of arc sprayed coatings obtained from FeCrB and FeCr-based power wires, Surf. Coat. Tech., 151–152 (**2002**), 490–494

[3] S. Dallaire, Hard arc-sprayed coating with enhanced erosion and abrasion wear resistance, Journal of Thermal Spray Technology, 10 (**2001**) 3, 511–519

[4] H. Liao, B. Normand, C. Coddet, Influence of coating microstructure on the abrasive wear resistance of WC/Co cermet coatings, Surf. Coat. Technol., 124 (**2000**), 235–242

[5] J. Voyer, B. R. Marple, Tribological performance of thermally sprayed cermet coatings containing solid lubricants, Surf. Coat. Technol., 127 (**2000**), 155–166

[6] T. Sato, A. Nezu, T. Watanabe, Preparation of Ti-Al intermetallic compund by wire arc spraying, Transactions of Materials Research Society of Japan, 25 (**2000**) 1, 301–304

[7] S. D. Sartale, M. Yoshitake, Investigation of Cu–Al surface alloy formation on Cu substrate, J. Vac. Sci. Technol. B, 28 (**2010**), 353–360

[8] Binary Alloy Phase Diagrams, edited by T. B. Massalski, H. Okamoto, P. R. Subramanian, L. Kcprzak, ASM International, Metals Park, OH, 1990

[9] B. Q. Wang, M. W. Seitz, Comparison in erosion behavior of iron-base coatings sprayed by three different arc-spray processes, Wear, 250 (**2001**), 755–761

UDK 621.762.5:669.14.018.8
Professional article/Strokovni članek

ISSN 1580-2949
MTAEC9, 46(2)185(2012)

EFFECT OF SINTERING PARAMETERS ON THE DENSITY, MICROSTRUCTURE AND MECHANICAL PROPERTIES OF THE NIOBIUM-MODIFIED HEAT-RESISTANT STAINLESS STEEL GX40CrNiSi25-20 PRODUCED BY MIM TECHNOLOGY

VPLIVI PARAMETROV SINTRANJA NA GOSTOTO, MIKROSTUKTURO IN MEHANSKE LASTNOSTI Z NIOBIJEM LEGIRANGA NERJAVNEGA OGNJEVZDRŽNEGA JEKLA GX40CrNiSi25-20, IZDELANEGA Z MIM-TEHNOLOGIJO

Samir Butković[1], Mirsada Oruč[2], Emir Šarić[1], Muhamed Mehmedović[1]

[1]University of Tuzla, Faculty of Mechanical Engineering, Univerzitetska 4, Tuzla, BiH
[2]University of Zenica, Institute of Metallurgy, Kemal Kapetanović Zenica, Travnička cesta 7, 72000 Zenica, BiH
samir.butkovic@untz.ba

Prejem rokopisa – received: 2011-10-20; sprejem za objavo – accepted for publication: 2011-12-22

Properties of heat-resistant, stainless-steel parts produced by the metal-injection-molding (MIM) process depend mostly on the sintering parameters. The effect of these sintering parameters on the densification, microstructure, hardness and tensile properties of the niobium-modified, heat-resistant stainless steel GX40CrNiSi25-20 were investigated. The prepared feedstock was injection molded to obtain tensile test specimens (ISO 2740). The debinding of the molded parts was performed using the catalytic debinding method, while the residual binder was removed by thermal debinding. The sintering was performed at 1200 °C and 1310 °C, in argon (Ar), hydrogen (H_2) and nitrogen (N_2) atmospheres, with the sintering times between 3 h and 6 h. It was found that sintering in a nitrogen atmosphere increased the strength and reduced the ductility. The mechanical properties were also enhanced by a higher sintering temperature (1310 °C), due to the positive effects of the pore rounding and increased density. The prolonged sintering time caused changes in the grain size, but had little effect on the density. Faster sintering and improved ductility was observed for the samples sintered in hydrogen and argon atmospheres.

Keywords: metal injection molding, heat-resistant stainless steel, sintering parameters, density, microstructure, mechanical properties, metal powder

Lastnosti izdelkov iz ognjevzdržnega nerjavnega jekla, izdelanih s tehnologijo brizganja praškastih materialov (MIM) so v največji meri odvisne od parametrov sintranja. Vplivi parametrov sintranja na zgoščevanje, mikrostrukturo, trdoto in trdnostne lastnosti z niobijem legiranega nerjavnega ognjevzdržnega jekla GX40CrNiSi25-20 so opisani v tem članku. Iz pripravljenega surovega materiala so bili nabrizgani vzorci za preizkuse z injekcijskim ulivanjem. Sintranje je bilo izvedeno pri temperaturah 1200 °C in 1310 °C v argonski (Ar), vodikovi (H_2) in dušikovi (N_2) atmosferi v trajanju med 3 h in 6 h. Ugotovljeno je bilo, da sintranje v dušikovi atmosferi povzroči utrjevanje materiala in zmanjšanje duktilnosti. Mehanske lastnosti so bile povečane tudi pri višji temperaturi sintranja (1310 °C) zaradi zaokroževanja por in povečanja gostote. Podaljšan čas sintranja je povzročil spremembe v velikosti zrn, vendar je imel majhen vpliv na gostoto sintranih delov. Hitrejše sintranje in izboljšana plastičnost je bila pri vzorcih, ki so bili sintrani v vodikovi in argonski atmosferi.

Ključne besede: praškasti materiali, ognjvzdržno nerjavno jeklo, sintranje, gostota, mikrostruktura, mehanske lastnosti

1 INTRODUCTION

The metal-injection-molding (MIM) process combines the advantages of polymer injection molding with the material flexibility of powder metallurgy. MIM technology enables the mixing of different metal powders with different binders and allows the processing of materials with complex mechanical, thermal, wear and magnetic properties. It is a cost-effective process in the high-volume production of small and complex-shaped parts.[1–3] The application of MIM technology in the production of complex-shaped components from heat-resistant stainless steel represent a very attractive solution to reduce manufacturing costs and overcome the machinability problems.

Heat-resistant stainless steels are selected for a wide range of applications because of their superior resistance to creep, corrosion and oxidation. Heat-resistant stainless steel GX40CrNiSi25-20 modified with niobium belongs to the group of precipitation-hardened steels. This high-temperature alloy provides strength and oxidation resistance at temperatures up to 1200 °C and it is generally used in the presence of combustion gases that may be generated from exhaust and pollution-control equipment.

There are four main steps that make up the MIM process: preparation of feedstock (mixing of metal powder with binder), injection molding, solvent/chemical debinding and sintering.[4] The most complex step of MIM technology in producing stainless-steel parts is sintering. Sintering parameters, such as, heating and

cooling rate, sintering time, sintering atmosphere, sintering temperature, partial pressure of sintering atmosphere, affect the mechanical and physical properties, as well as corrosion and the heat resistance of sintered parts.[5] The wrong sintering parameters can lead to a low density, the absorption and desorption of some elements, deteriorated mechanical properties, reduced corrosion and oxidation resistance and a reduced service time.[5] Also, if the optimal parameters are not selected, increased sintering costs can be expected.

In this regard, the effect of sintering temperature, time and atmosphere on the physical and mechanical properties of metal-injection-molded heat-resistant stainless steel GX40CrNiSi25-20 modified with niobium was investigated in this work.

2 EXPERIMENTAL WORK

2.1 Material

Niobium-modified GX40CrNiSi25-20 is a heat-resistant stainless steel with a high resistance to creep and oxidation. A higher percent of chromium provides superior oxidation resistance, while a higher percent of carbon, compared to ordinary austenitic stainless steel, provides high strength and creep resistance.[6,7] The niobium addition gives structural stability and precipitation hardening. The austenitic structure provides the strength and structural stability at elevated temperatures. This steel is intended for high-temperature applications, up to 1200 °C, e.g., turbine blades or furnace parts. The production of feedstock involved the mixing of pre-alloyed metal powder with a suitable binder. The typical chemical composition after sintering is presented in **Table 1**.

Table 1: Typical chemical composition after sintering niobium-modified GX40CrNiSi25-20 in mass fractions, *w*/%
Tabela 1: Tipična kemična sestava sintranega jekla GX40CrNiSi25-20 s povišanim niobijem v masnih deležih, *w*/%

C	Cr	Ni	Si	Nb	Fe
0.2–0.5	24–26	19–22	0.75–1.3	1.2–1.5	Bal

2.2 Injection molding

The injection molding of the prepared feedstock was made in a machine for the injection molding of metal powders type ALLROUNDER 320 C 600–100. The shape of the mold cavity corresponds to a standard specimen for tensile tests used in powder metallurgy (ISO 2740).

At the beginning of the injection-molding process the material is heated to 185 °C at the nozzle of the barrel and with a screw rotation transported at the barrel top. The back pressure of the accumulated material was 30 bar. After the accumulation of a sufficient quantity of material, the screw stops rotating and moves forward, pushing the melted material into the tool cavity at a tool temperature of 110–115 °C. The holding pressure of 900 bar and its duration of 3 s provide for complete cavity filling. After the injection molding, the parts were cooled for 27 s.

The average density of the injection-molded parts was 5.5 g/cm^3.

2.3 Catalytic debinding

After the injection molding the parts were debound by a catalytic debinding method. Polyacetal, as a main component of the feedstock, was decomposed by nitric acid at a temperature below the melting point of polyacetal, preventing the parts from deformation during the debinding. Usually, a small concentration of a backbone polymer, that is unaffected by the catalyst, is included to hold the particles together until the material is ready to start forming necks between the particles by diffusion (often polyethylene).

The debinding was performed at 120 °C, where vaporized acid exists in the atmosphere. A nitrogen flow rate of 50 L/min was used to spread the nitric acid over the debinding furnace chamber. The nitric acid flow rate was 3.4 mL/min. The preheating time and the debinding time used during the debinding were 30 min and 4 h, respectively. A purging time of 30 min was used to remove the residual acid to the combustion chamber, where it was burned by propane gas.

2.4 Thermal debinding and sintering

The thermal debinding and sintering were performed in the same furnace type MIM 3045. The parts were gradually heated to 600 °C, where the residual binder starts to degrade and annealed for 2 h. After the residual binder was totally removed the parts were heated to the sintering temperature. The sintering is a process with the temperature, time and sintering atmosphere as influential factors. The thermal cycle of the debinding was the same for all the experiments (**Figure 1**). The sintering temperatures were 1200 °C and 1310 °C and the sintering

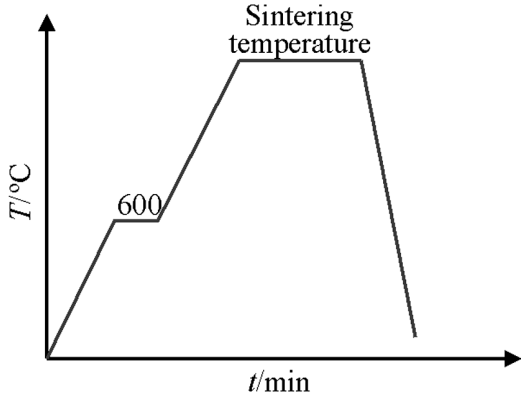

Figure 1: Thermal cycle of sintering and debinding
Slika 1: Termalna cikla sintranja in odstranjevanja veziva

times were 3 h and 6 h. The atmospheres used during the experiments were hydrogen, nitrogen, and argon.

3 RESULTS AND DISCUSSION

3.1 Density

The density of the sintered parts was measured by Archimedes' immersion method. The influence of the sintering atmosphere, temperature and time on the density of the investigated material was performed and analyzed using a general full factorial experiment. Analysis of variance (ANOVA) was used to demonstrate the significance level of the variables, as well as the effect of the sintering variables on the sintered density. The influential factors, their levels and average density for a selected set of parameters are presented in **Table 2**.

Table 2: Sintering conditions and density of sintered alloy
Tabela 2: Pogoji sintranja in gostota sintrane zlitine

Atmosphere (A)	Temperature, °C (B)	Time, h (C)	Average density, g/cm^3
Ar	1 200	3	6.89
H_2	1 200	3	7.27
N_2	1 200	3	6.59
Ar	1 310	3	7.71
H_2	1 310	3	7.80
N_2	1 310	3	7.75
N_2	1 310	6	7.66
H_2	1 310	6	7.77
Ar	1 310	6	7.72
N_2	1 200	6	7.16
H_2	1 200	6	7.44
Ar	1 200	6	7.17

Generally, all the sintering variables have a significant effect on the sintered density. The ANOVA (**Table 3**) showed that the sintering temperature has the highest influence on the sintered density (72.6 %), followed by the sintering atmosphere (9.3 %), the sintering time (4.1 %) and the two-factor and three-factor interactions. The influence of the sintering temperature, time and atmosphere on the density of the sintered parts is shown in **Figure 2**. It was found that sintering time has a significant effect on the sintered density only at 1200 °C, increasing the average sintered density from 6.91 g/cm^3 to 7.26 g/cm^3. A longer sintering time at 1310 °C caused insignificant changes to the density, which has to be taken into account during the sintering-costs analysis.

Higher sintering temperatures caused a more intensive atomic diffusion, resulting in faster sintering and higher resulting densities. Increasing the sintering temperature from 1200 °C to 1310 °C resulted in the average density increasing from 7.09 g/cm^3 to 7.73 g/cm^3 (average of all runs). Statistical data indicated that the sintering atmosphere also has a significant effect on the sintered density. Sintering in hydrogen gave a density higher than the sintered densities achieved in the nitrogen and argon atmospheres. This difference is particularly emphasized at a temperature of 1200 °C and a time of 3 h, where sintering in hydrogen gave a density of 7.27 g/cm^3, while sintering in nitrogen and argon gave densities of 6.59 g/cm^3 and 6.89 g/cm^3, respectively. Small hydrogen atoms diffuse into the metal lattice and do not inhibit the elimination of final porosity[1]. Argon and nitrogen remains in the final pores and build the internal pressure, whereby the elimination of the porosity in the final stage of sintering is inhibited.

For the nitrogen samples the sintering activity was probably impeded by the absorbed nitrogen, which

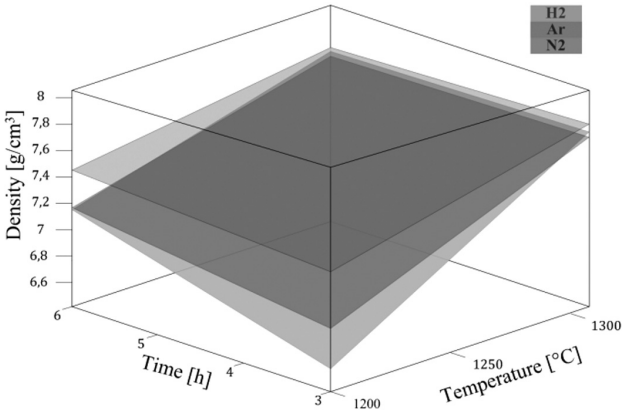

Figure 2: Influence of sintering temperature, time and atmosphere on the density of the sintered parts
Slika 2: Vpliv temperature, časa in atmosfere sintranja na gostoto sintranih delov

Table 3: Analysis of Variance for density
Tabela 3: Analiza variance za gostoto

Term	DOF	SumSqr	MeanSqr	P	F	Contribution, %
A	2	0.324213	0.162106	< 0.0001	111.5602	9.355652
B	1	2.516833	2.516833	< 0.0001	1732.064	72.62707
C	1	0.142913	0.142913	< 0.0001	98.35132	4.123965
AB	2	0.159606	0.079803	< 0.0001	54.9198	4.605679
AC	2	0.032124	0.016062	0.0019	11.05376	0.92699
BC	1	0.211313	0.211313	< 0.0001	145.4236	6.097752
ABC	2	0.060982	0.030491	0.0001	20.98351	1.759717
Pure Error	12	0.017437				0.503171
Residuals	12	0.017437	0.001453			

obviously reduces the mass-transport mechanism during sintering.[5] Also, it is well known that hydrogen is the most effective reducing atmosphere causing effective oxide removal, which results in a longer sintering dwell time. The highest density of 7.8 g/cm^3, which is 98.7 % of theoretical density, was achieved using a hydrogen atmosphere and a temperature of 1310 °C.

3.2 Mechanical properties

Parameters of sintering at the final stage of the MIM (Metal Injection Molding) process have a decisive influence on the mechanical properties of the produced parts. The characteristics of the residual porosity, chemical composition, structure after sintering and the density of the sintered parts are factors that make heat-resistant stainless steel very sensitive to the sintering parameters. Tensile tests were made on standard tensile tests samples used in powder metallurgy.

Table 4 shows the tensile and elongation results of the samples sintered in nitrogen, hydrogen and argon atmospheres at 1200 °C and 1310 °C. All the samples were sintered for 3 h in an atmosphere with 400 mbar of partial pressure.

It was found that the tensile and yield strengths increased with an increase of the temperature. The average tensile strength for parts sintered in argon and nitrogen was increased from 317 MPa to 680 MPa with a change of the sintering temperature from 1200 to 1310 °C. The tensile strength increase is the result mainly of increased density and a significant reduction of porosity. Also, a reduction of porosity by increasing the temperature caused a substantial improvement in the elongation of the sintered parts (**Figure 3**).

The reduction of the temperature leads to a large drop in the elongation and strength of the material. It is evident that sintering at a temperature of 1200 °C and in a nitrogen atmosphere gives an elongation of 2.2 %, while sintering in argon achieved a maximum elongation of 3.5 %. A slight improvement was observed for the samples sintered in hydrogen atmospheres (5.3 %), because of the higher density compared to the densities of samples sintered in argon and nitrogen. The low density and the sharp edges of the residual porosity of the parts sintered at lower temperatures caused a stress concentration during the tensile test, making the material very brittle. Analyzing and comparing the tensile test results, it is evident that the samples sintered in a nitrogen atmosphere experienced strengthening during the sintering. The best tensile strength of 777 MPa and yield strength of 412 MPa were achieved using a nitrogen atmosphere and a sintering temperature of 1310 °C

Sintering in a nitrogen atmosphere caused the absorption of nitrogen, resulting in the solid solution strengthening of the material. Also, based on previous research, the formation of NbCrN and precipitation strengthening were also possible[8]. The strengthening of the material was avoided using an argon atmosphere, where the average tensile strength and yield strength of 583 MPa and 223 MPa were achieved, respectively. A substantial elongation improvement was also observed on samples sintered in an argon atmosphere and temperature 1310 °C.

In order to see the effect of nitrogen absorption on the mechanical properties of the sintered parts, additional experiments were made. The main condition for intensifying the absorption and increasing the nitrogen content in the steel is to increase the partial pressure of the nitrogen atmosphere. In this regard, the partial pressure of nitrogen in the sintering furnace chamber was increased from 400 mbar to 600 mbar. After sintering, the hardness was measured and the results are presented in **Table 5**. The increasing of the partial pressure of nitrogen caused an increasing of the hardness of the sintered parts (**Figure 4**). A higher nitrogen level contained in the steel after sintering, as a result of the increased partial pressure of the nitrogen atmosphere, caused a more intensive strengthening of steel. It can be concluded that the change in the mechanical properties of the sintered heat-resistance stainless steel is possible through the partial pressure of the nitrogen atmosphere.

It was also observed that the sintering temperature has a very significant effect on the hardness of the sintered parts. The hardness increased with a higher sintering temperature and the average hardness increased

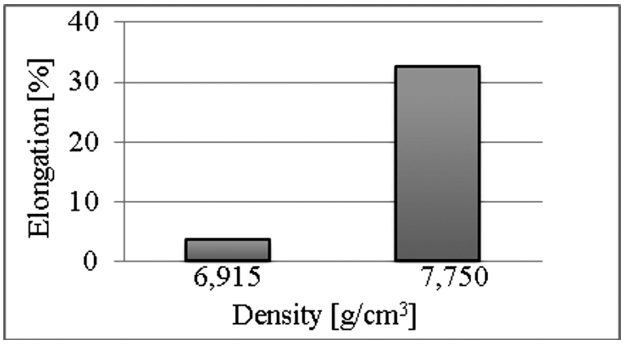

Figure 3: Influence of density on the elongation of the sintered parts
Slika 3: Vpliv gostote na raztezek sintranih kosov

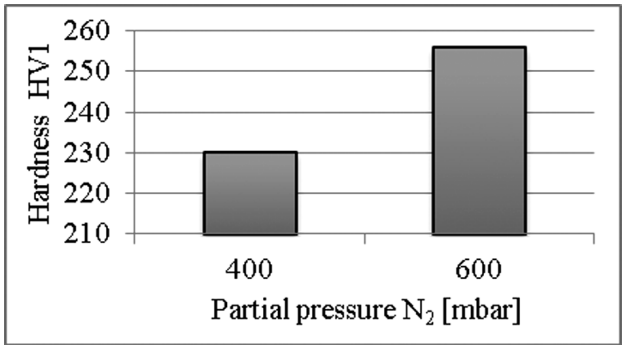

Figure 4: Influence of nitrogen partial pressure on the hardness of the sintered parts
Slika 4: Vpliv parcialnega tlaka dušika na trdoto sintranih delov

from 180 HV1 to 230 HV1 with a temperature increase from 1200 °C to 1310 °C.

Table 4: Mechanical properties after sintering
Tabela 4: Mehanske lastnosti po sintranju

Temperature /°C	Atmosphere	Partial pressure /mbar	Average tensile strength R_m/MPa	Average yield strength R_e/MPa	Average elongation A/%
1310	Ar	400	583	223	38
1310	N_2	400	777	412	27
1200	H_2	400	359	245	5.3
1200	N_2	400	292	–	2.2
1200	Ar	400	291	217	3.5

Table 5: Comparison of the hardness for different partial pressures of the nitrogen atmosphere and temperatures
Tabela 5: Primerjava trdote za različne parcialne tlake dušika in temperature

Partial pressure /mbar	Temperature /°C	Hardness /HV1
400	1200	180
400	1310	230
600	1310	255

3.3 Microstructure

The microstructure of the samples sintered at a temperature of 1200 °C and an argon atmosphere (**Figure 5a**) reveals an insufficient degree of sintering with a noticeable residual porosity and a very small grain size with a density of 6.89 g/cm^3. Insufficient connection between the grains caused a tensile and yield strength reduction and the elongation of parts sintered at 1200 °C. Micrograph of the parts sintered at a temperature of 1310 °C (**Figures 5b, d** and **e**) reveal grain growth and a fully austenitic microstructure with a minimal residual porosity and a density of 7.71 g/cm^3. A small percent of residual porosity indicates that the material reached almost theoretical density with well connected grains and better mechanical properties.

The parts sintered in hydrogen and argon experienced a more intensive grain growth compared to the parts sintered in nitrogen. Clean grain boundaries facilitate grain-boundary movement, resulting in effective pore absorption, higher density and larger grains compared to the parts sintered in nitrogen. Impeded sintering activity and reduced mass transport caused slower motion of the grain boundaries of the parts sintered in nitrogen, resulting in a reduced sintering density. The microstructure of parts sintered at 1310 °C is comparable to the microstructure of the wrought material.

A prolonged sintering time caused a slight grain coarsening (**Figures 5c** and **f**). Also, some of the pores observed on the samples sintered for 6 h coarsened maybe as a consequence of an extended sintering time and vacancy diffusion from smaller to bigger pores.[9,10] The micrographs of parts sintered in nitrogen reveal an austenitic microstructure with Cr_2N regions created as a consequence of nitrogen absorption.

4 CONCLUSION

The density of the heat-resistant stainless steel GX40CrNiSi 25–20 produced by the MIM process depends mostly on the sintering temperature. Increasing the average density from 7.09 g/cm^3 to 7.73 g/cm^3 was achieved by increasing the sintering temperature from 1200 °C to 1310 °C. Sintering in hydrogen and argon resulted in higher densities and better ductility of the sintered parts compared to the nitrogen atmosphere.

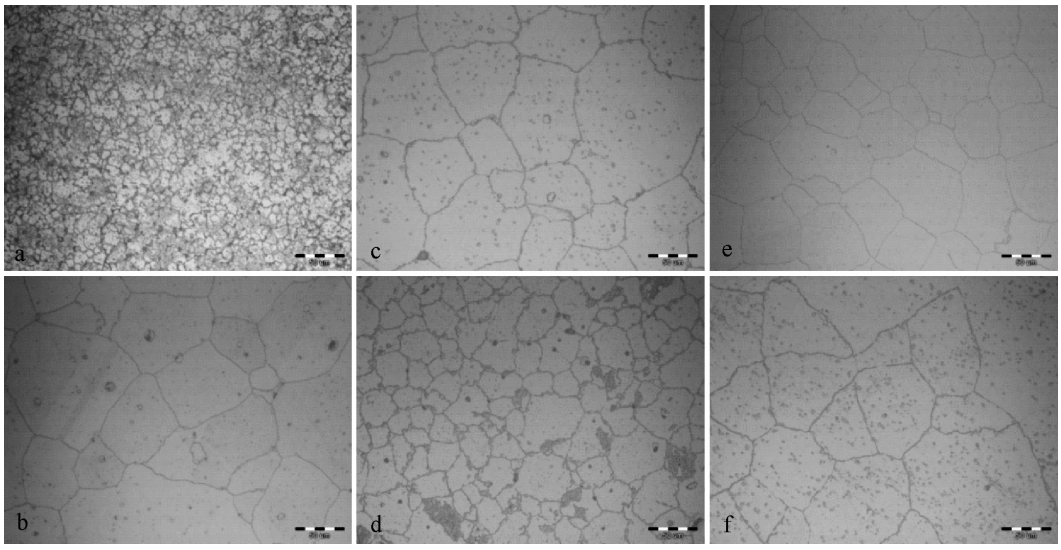

Figure 5: Microstructure of sintered parts for different conditions: a) argon, 1200 °C, 3 h, b) argon, 1310 °C, 3 h, c) argon, 1310 °C, 6 h, d) nitrogen, 1310 °C, 3 h, e) hydrogen, 1310 °C, 3 h, f) hydrogen, 1310 °C, 6 h, glyceregia
Slika 5: Mikrostruktura sintranih kosov pri različnih razmerah: a) argon, 1200 °C, 3 h, b) argon, 1310 °C, 3 h, c) argon, 1310 °C, 6 h, d) dušik, 1310 °C, 3 h, e) vodik, 1310 °C, 3 h, f) vodik, 1310 °C, 6 h, glyceregia

Insufficient density of parts sintered at a temperature of 1200 °C caused brittleness of the steel with a maximum elongation of 5.3 %. A superior tensile and yield strength were obtained by sintering in a nitrogen atmosphere. The maximum tensile strength of 777 MPa and yield strength of 412 MPa were achieved using a nitrogen atmosphere with 400 mbar of partial pressure and a temperature of 1310 °C. Strengthening also depended on the nitrogen partial pressure. The hardness was increased by 10 % when the nitrogen partial pressure was changed from 400 mbar to 600 mbar. It was found that a longer sintering time at a temperature of 1310 °C had a minor effect on the density of the sintered parts. Also, it is very important to emphasize that the prolongation of the sintering time at a temperature of 1200 °C, from 3 h to 6 h, increased the sintered density from 6.91 g/cm^3 to 7.26 g/cm^3, which is still much less than the density achieved at a temperature of 1310 °C. This is very important during the optimization of the sintering profile and indicates the importance of using a higher temperature to reduce the sintering time and the sintering costs.

5 REFERENCES

[1] ASM Handbook, Powder Metal Technologies and Applications, Vol. 7, 1998

[2] E. Klark, P. Samal, Powder metallurgy stainless steel, processing, microstructure and properties, ASM International, Ohio 2007

[3] G. Schlieper, G. Dowson, B. Williams, Metal Injection Molding, Shrewsbury, UK, EPMA, 2000

[4] R. M. German, Injection Molding of Metals and Ceramics, New Jersey, 1997

[5] R. W. Stevenson, P/M Stainless Steels, Powder Metallurgy, Metals Handbook, 9th, American Society for Metals, Vol. 7, 1985, 729

[6] H. K. D. H. Bhadeshia, T. Sourmail, Stainless Steels, University of Cambridge, 2001

[7] T. Sourmail, Precipitation in creep resistance stainless steel, University of Cambridge, Doctoral thesis, 2001

[8] S. Iqbal, Tensile Properties of Austenitic Stainless steel, Master's thesis, University of Cambridge, 2002

[9] D. Nikolić, Metalurgija praha, Beograd, 1998

[10] R. M. German, Sintering theory and practice, New York, 1996